Non-Oxide Ceramic Composites Prepared by Sol-Gel and Spark Plasma Sintering Processes

Manyuan Zhou

Supervisor: Professor Yi-Bing Cheng

Department of Materials Engineering, Monash University

Declaration

The following thesis contains no materials that have been accepted for the award of any other degree in any institution. To the best of my knowledge, it does not contain material previously published or written by any other persons, except where respectful and due reference is made in the text.

Manyuan Zhou

June 2014

Notice 1

Under the Copyright Act 1968, this thesis must be used only under the normal conditions of scholarly fair dealing. In particular no results or conclusions should be extracted from it, nor should it be copied or closely paraphrased in whole or in part without the written consent of the author. Proper written acknowledgement should be made for any assistance obtained from this thesis.

Notice 2

I certify that I have made all reasonable efforts to secure copyright permissions for third-party content included in this thesis and have not knowingly added copyright content to my work without the owner's permission.

Acknowledgements

First and foremost I want to thank my supervisor, professor Yi-Bing Cheng. He has supported me academically and emotionally through the rough road to finish this thesis, since I began my PhD study at Monash four years ago. He helped me come up with the thesis topic and guided me over the whole period of research. During the period of writing this thesis, he gave me great support and spent a lot of time on reading and commenting. I appreciate all his contributions of time, ideas and funding to make my PhD experience productive and stimulating. The joy and enthusiasm he has for his research was contagious and motivational for me, even during tough times in the PhD pursuit.

I am especially grateful to professor Huanting Wang for his valuable advices and fruitful discussions with his extensive knowledge in sol-gel chemistry. I would like to thank Dr Don Rodrigo for his help on the spark plasma sintering of ceramics as well as his collaboration on writing papers. I wish to thank Dr Tim Williams for his help on doing TEM analysis of zirconium diboride powders coated with silicon carbide nano particles. I am also thankful for Dr Aaron Seeber and Dr Xiaodong Wu for their help on doing XRD analysis of silicon nitride ceramic composites using Topas software. In my attempted measurements of the electrical conductivity of silicon nitride titanium nitride composites, I thank Professor Richard Donelson for his kind help. I also want to thank Dr Colleen Bettles for her help on the measuring materials' densities.

I would like to thank all the staff who helped me during the PhD study at Materials Engineering, Chemical Engineering, Physics and MCEM, in particular, Dr Jianfeng Yao, Irek Kozicki, Silvio Mattievich, Roderick Mackie and Daniel Curtis for their experience and advice. I am also grateful to Jack Wang for his help on demonstrating the undergraduates' prac. The members of the Ceramic group have contributed immensely to my personal and professional time at Monash. I am especially grateful for the

Ceramic group members who have been a source of friendships as well as good advice and collaboration with me: Dr Kun Wang, Dr Jie Zhong, Dr Caen Khim Ang, Xiangjing Wang and Paul Michael Firbas.

I gratefully acknowledge the funding sources that made my PhD work possible. I was funded by the Monash University of MGS/MIPRS scholarships for three and half years.

Lastly, I would like to thank my family for all their love and encouragement. For my children Derek and Daniel who brought me great happiness, joy and motivation in the last few years. And most of all for my loving, supportive and encouraging wife Jun whose faithful and unconditional support all these years is so appreciated. She has given up many things for me to be at Monash and has cherished with me every great moment. Thank you.

Manyuan Zhou

Summary

Ultra High Temperature Ceramics (UHTCs) are the most promising candidates for high temperature applications in extreme environments, such as conditions experienced during re-entry of out space flying objects, for their known high melting points, good chemical and thermal stability and high thermal conductivity. To improve the densification and oxidation resistance of UHTCs, a second phase, such as silicon carbide, is usually added to monolithic UHTCs to form ceramic matrix composites. While UHTCs/composites have many unique advantages for high temperature applications, they are very difficult to densify due to their very strong covalent chemical bonds and very high melting point. Conventional methods for processing UHTCs usually use powders as starting materials. A major issue of the conventional methods is the poor mixing/processing of powders with different densities and sizes, especially for nano-sized powders. Thus more research needs to be focused on improving UHTCs' densification, microstructure and properties.

This thesis studies the development of novel sol-gel techniques for preparation of starting materials and spark plasma sintering (SPS) for densification of UHTCs and composites. The thesis is organized into eight chapters. The First Chapter is an introduction to the thesis structure organization. The Second Chapter is the background of the research and literature review. Chapter Three is a description of the experimental procedures and characterization techniques. In the first result chapter, Chapter Four, silicon nitride ceramic and silicon nitride/titanium nitride composite were fabricated by hot pressing and spark plasma sintering (SPS) respectively to study the effect of the SPS DC current on the densification, microstructure and properties of conductive and non-conductive materials. A sol-gel based approach was investigated to improve the UHTC ceramics/composites with fine microstructures in Chapter Five. Although sol-gel techniques may not be suitable for making large bulk materials, they have unique advantages on modifying or improving the microstructures, properties and surfaces of

materials through the solution chemistry approach. The sol-gel processing technique was used to synthesize TiC/SiC nanocomposites and followed by SPS sintering. Dense TiC/SiC composites were fabricated successfully to form a microstructure consisted of nano TiC and SiC grains. Work in Chapter Six used a sol-gel infiltration technique to fabricate dense TiC/SiC nanocomposites from porous TiC scaffolds. In Chapter Seven, zirconium diboride/silicon carbide composites of fine microstructures were successfully fabricated by sol-gel coating of ZrB_2 powders and SPS sintering. Compared to conventional ceramic processing methods, the sol-gel based wet chemistry process has many unique advantages such as homogeneous mixing of starting materials, infiltration of porous green bodies with complex shapes, avoiding the formation of intermediate transit phase/liquid phase in sintering, restricting grain growth and assisting densification by reaction. Chapter Eight presents the conclusions of the thesis and provides some directions for future work.

Contents

Chapter 1 Introduction

1.1 Background

Ceramics are defined as inorganic, non-metallic materials which are typically crystalline in nature containing metallic and non-metallic elements such as Al_2O_3, ZrO_2, SiC and Si_3N_4. Non-oxide ceramics of borides, carbides and nitrides of transition metals (Ti, Zr, Hf, Nb, Ta) are known as Ultra High Temperature Ceramics (UHTCs). UHTCs are an important category in advanced ceramics. UHTCs are characterized by high melting points (higher than 3000 °C), good chemical and thermal stability, high thermal conductivity and good oxidation resistance in extreme environments. An example of such an environment is the conditions a hypersonic vehicle experiences during re-entry to the atmosphere. In this environment the surface temperature of the vehicle can reach to 2000 °C to 2400 °C[1].

While the UHTCs have many unique advantages for high temperature applications, they have very low atomic diffusivity even at very high temperature and are thus very hard to densify. This arises due to their strong covalent bonding. Conventional methods for processing of UHTC composites involve powder mixing and hot-pressing. The major issue with these conventional methods is the poor mixing/processing of powders with different densities and sizes. This is especially true with nano-sized powders, and more research needs to be focused on improving the materials microstructure and hence the properties.

As a newly developed sintering technology, spark plasma sintering (SPS) can significantly enhance the sinterability of most materials; hence extend the possibilities for developing new advanced materials and tailoring their properties. SPS offers unique advantages, such as, much faster heating rates, lower sintering temperatures and shorter sintering times, compared with conventional sintering techniques. However, the

phenomena and mechanism responsible for the enhanced sintering are still uncertain in most cases. In this thesis, the effect of current in the SPS process is examined first. This is achieved by looking at the densification, microstructure and properties of non-conductive silicon nitride ceramics, and conductive silicon nitride/titanium nitride composites.

A sol-gel process involves the formation of a solid product from a solution. During the conversion from a liquid to a solid, a gel intermediate is formed, where both a solid and a liquid phase are present. Here the reactants are mixed at the molecular level. This allows for fast reactions and lower working temperatures. In turn this leads to more homogeneous products with smaller grain size. Due to this flexibility, sol-gel process is a suitable method for the production of a wide variety of materials. This is especially true for UHTCs, which have very high melting temperatures and are very hard to be synthesized and densified. The sol-gel method offers unique advantages for the production of UHTCs, such as improved microstructures, properties and surfaces of materials, compared with the conventional powder mixing approaches. Even with these advantages, to the best of our knowledge, little research has been done on preparation of dense UHTCs by the sol-gel process. In this thesis, sol-gel based wet chemistry approaches coupled with SPS are used to prepare dense UHTC composites with modified/improved microstructures and properties. Research in this thesis shows that the proposed novel sol-gel based, wet chemistry approaches for synthesizing and modifying UHTC composites are successful. The sol-gel technique has many advantages over the conventional powder mixing technique for the production of UHTC composites, including promoting the retention of a homogeneous fine-grained structure, hindering grain growth, avoiding intermediate transit phase/liquid phase, improving densification, filling pores to improve density, avoiding nano-sized powder handling and allowing infiltration of a complex shaped sample.

1.2 Structure of the thesis

The thesis is organized into eight chapters. Chapter one is introduction and thesis organization. Chapter two provides a broad background and literature review of the research. Chapter three describes the experimental procedures. Chapter four reports a study of the effect of electrical current in the SPS process on the microstructure and properties of electrically conductive and non-conductive ceramics and composites. Chapter five details the synthesis and fabrication of nano-sized, dense TiC/SiC composites by sol-gel processing and SPS. A novel sol-gel infiltration approach is investigated to prepare nano-sized composites, tailor the residual carbon in the matrix phase and modify the microstructure and properties of scaffolds in Chapter six. Chapter seven details fabrication and modification of ZrB_2/SiC composites by sol-gel coating. Chapter eight gives conclusions and directions for future research.

Chapter 2 Literature Review

2.1 Introduction

2.1.1 Advanced ceramics

Advanced ceramics are materials tailored to possess exceptional properties (superior mechanical properties, corrosion/oxidation resistance, thermal, electrical, optical or magnetic properties). This is done by controlling their composition and microstructure. Advanced ceramics represent an important technology, which has considerable impact for a large variety of industries, branches and markets. As an enabling technology, it has the potential to deliver high-value contributions for solving the challenges of our future. From a general point of view the advanced ceramics sector comprises the following categories:

• Functional ceramics: Electrical and magnetic ceramics (i.e. dielectrics, piezoelectrics, ferromagnetics), ionic conductors and superconductive ceramics.

• Structural ceramics: Monoliths and composites, e.g. oxides, nitrides, carbides, borides, and composite materials based on these materials.

• Bioceramics: e.g. hydroxyapatite and alumina.

• Ceramic coatings: Oxides, nitrides, carbides, borides, cermets and diamond-like coatings deposited by technologies such as spraying, vapor deposition and sol–gel coating.

• Special glasses: Processed flat glass, fire resistant glazing and glasses for optoelectronics.

Figure 2.1 gives the expected development of the US market up to 2015, indicating that all sectors will exhibit a continuous growth[2].
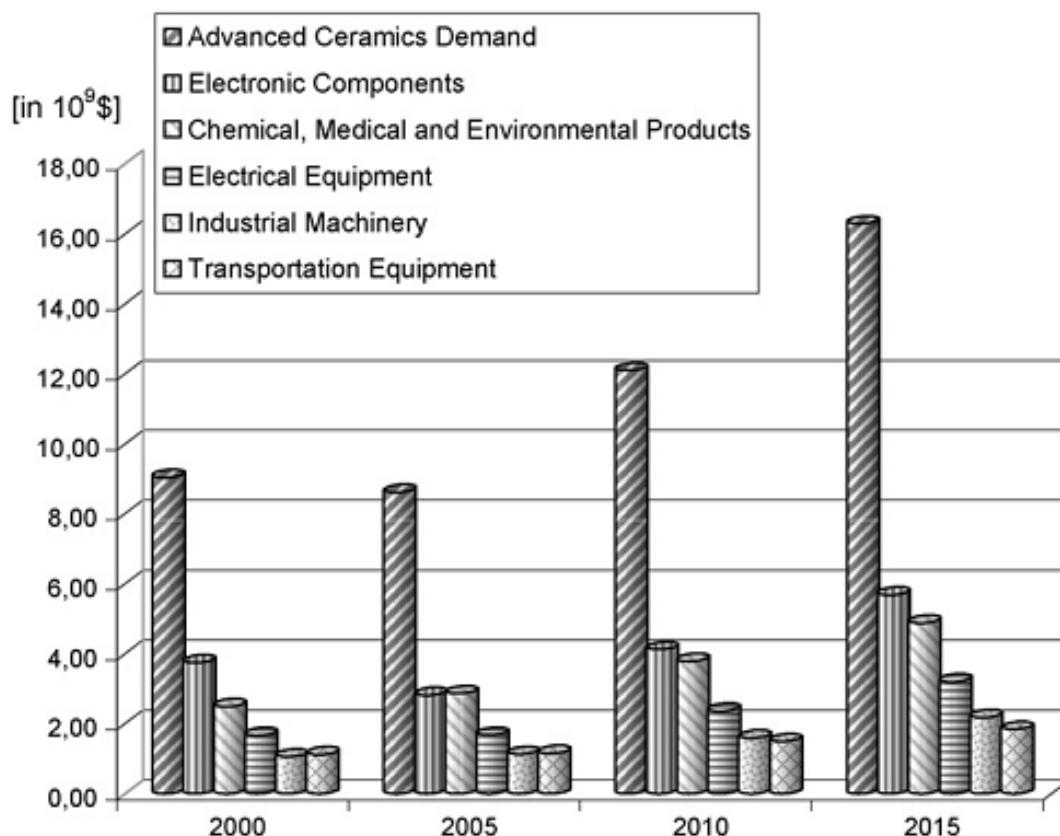
Figure 2.1 Development of the US market for advanced ceramics from 2000 to

2015 [2]

2.1.2 Non-oxide ceramics and ultra-high temperature ceramics

Non-oxide ceramics and ultra-high temperature ceramics (UHTC) are important categories of advanced ceramics. Whereas metals are mostly used as their oxides, however, oxides are just a part of the chemical universe. Boron, carbon and nitrogen are versatile elements that form compounds with most of metals. The bonding between boron, nitrogen or carbon with a less electronegative element such as a transition metal, creates very stable compounds. As compared to oxides, non-oxides' bonding schemes are richer; with more electrons in bonds than localized on the anion lattice, which is also seen in their electronic and optical properties[3].

5

Non-oxide ceramics, especially borides, carbides and nitrides of transition metals (Ti, Zr, Hf, Nb, Ta), are characterized by the highest known melting points (higher than 3000 °C). This is how this group of ceramics became to be known as UHTCs. UHTCs are not only associated with high melting points, but also high hardness, good wear resistance, good mechanical strength, good chemical and thermal stability, high thermal conductivity and relatively good oxidation resistance in extreme environments. One such environment being the conditions hypersonic vehicles experience during re-entry, in which the temperature can reach to 2000 °C to 2400 °C. The need for high temperature materials that can operate with no, or limited oxidation or ablation, at temperatures greater than 2000 °C has driven the development of UHTCs. The potential applications for UHTCs span a wide number of needs arising from future military, industrial and space based projects, such as rocket nozzle inserts, specific engine components, leading edges and nose caps for future hypersonic re-entry vehicles[1].

UHTCs are highly covalent and thus have high thermal stability. This results in correspondingly high thermomechanical strength. However, due to strong bonding, which limits diffusion associated with sintering, processing is very challenging. The ceramic borides, such as HfB_2 and ZrB_2, also benefit from very strong bonding between boron atoms. Although their bonding is not typically as strong as carbides, they have higher thermal and electrical conductivities than carbides and nitrides. The borides also have low coefficients of thermal expansion, which in conjunction with the borides high thermal conductivity, gives them relatively good thermal shock resistance. With these superior properties, the diborides of hafnium and zirconium are of particular interest to the aerospace industry where they would be employed as sharp leading edges, which require chemical and structural stability at extremely high operating temperatures. To improve the oxidation resistance at high temperature, a second phase is added to monolithic UHTCs. This makes a ceramic matrix composite, where silicon carbide is a common second phase addition[4-7]. Silicon carbide additives are used to firstly enhance

the resistance to oxidation, secondly to promote densification by restricting the growth of diboride grains, and lastly to lower their sintering temperature. These ceramic matrix composites exhibit good resistance to oxidation at very high temperatures (>1500°C), due to the formation of a glassy protective layer. Oxygen diffusion is slowed down through this oxide layer and ZrB_2 is then prevented from undergoing further oxidation.

In spite of all their interesting features, UHTCs are mostly known and used as bulk materials. This is likely due to the relatively high temperature required by the classical synthetic procedures. Also the intrinsic difficulty in synthesizing them as nanoparticles, in a systematic and scalable fashion, limits UHTCs uses. This strongly reduces the applications of these materials, indeed nano-sized metal nitrides and carbides could exhibit improved performances. For example in catalysis, their performance can be improved due to a higher surface area[3]. These nano sized UHTCs can also be shaped more easily than corresponding larger grains, for further specific applications. While the UHTCs have many unique advantages for high temperature applications, the fact is that they are very hard to densify. At the same time the UHTCs lack toughness due to their ultra-high melting points and high hardness. Meanwhile conventional methods for processing UHTCs involve powder mixing and fiber toughening. The major issue with these conventional methods is the poor mixing/processing of powders with different densities[8]. And as such more research is needed to improve material microstructure, mechanical properties and oxidation resistance. Recently, sol-gel chemistry has closed this gap and now enables the simple and sustainable production of UHTCs.

2.2 Sintering of non-conductive Si_3N_4 ceramics and Si_3N_4 based electrically conductive composites by conventional sintering techniques and SPS

2.2.1 Conventional sintering and spark plasma sintering

Conventional sintering (CS) of ceramics includes pressureless sintering (PLS), hot pressing (HP) and hot isostatic pressing (HIP)[9-14], as shown in Figure 2.2[15]. Pressureless sintering, which is the oldest method for the sintering of ceramics, is widely used for industrial fabrication of ceramics. The advantages of PLS include low cost, ease of use and flexibility for sintering of products with complex shapes. But pressure sintering (hot pressing and hot isostatic pressing) comes with advantages, even though the pressure sintering techniques are slightly more complex. The major advantage of the pressure sintering techniques is their ability to get fully dense ceramic products at temperatures lower than the pressureless sintering techniques.
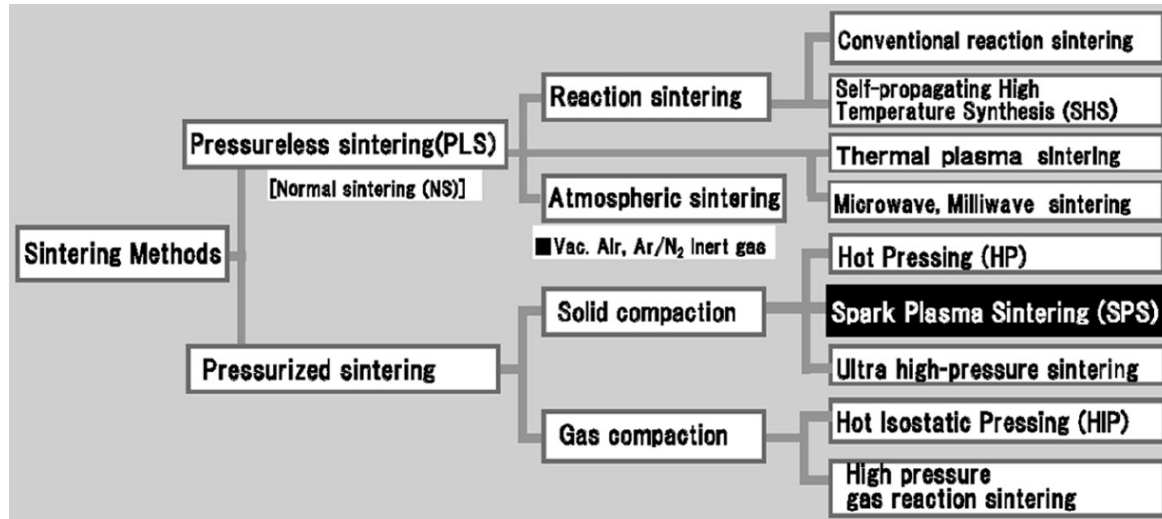
Figure 2.2 Typical classification of sintering methods[15]

Spark plasma sintering (SPS), also called pulsed electric current sintering (PECS) process or plasma activated sintering (PAS), is a newly developed sintering method (about two

decades). It is considered a promising technology for innovative processing in the field of new materials fabrication in the 21st century. The idea to compact metallic and ceramic materials by an electro-discharge process was originally proposed in the 1960s[16]. Based on this concept, three sintering processes have been developed and commercialized during recent years; they are named SPS[17], PAS[18] and PECS[19].

Despite lots of research work concerning the SPS mechanism by many material researchers, the effect of pulsed high current on the generation of spark plasma, peculiar properties in consolidated materials, still remains unclear[9,20-26]. SPS is a synthesis and processing technique which is achieved by charging the powder particles with electrical energy, an electro-magnetic field and/or joule heating by continuous ON-OFF DC pulsed high electric current with a low voltage[15] (Figure 2.3), thus, an existence of high temperature field is suggested locally due to joule heating[27-29].
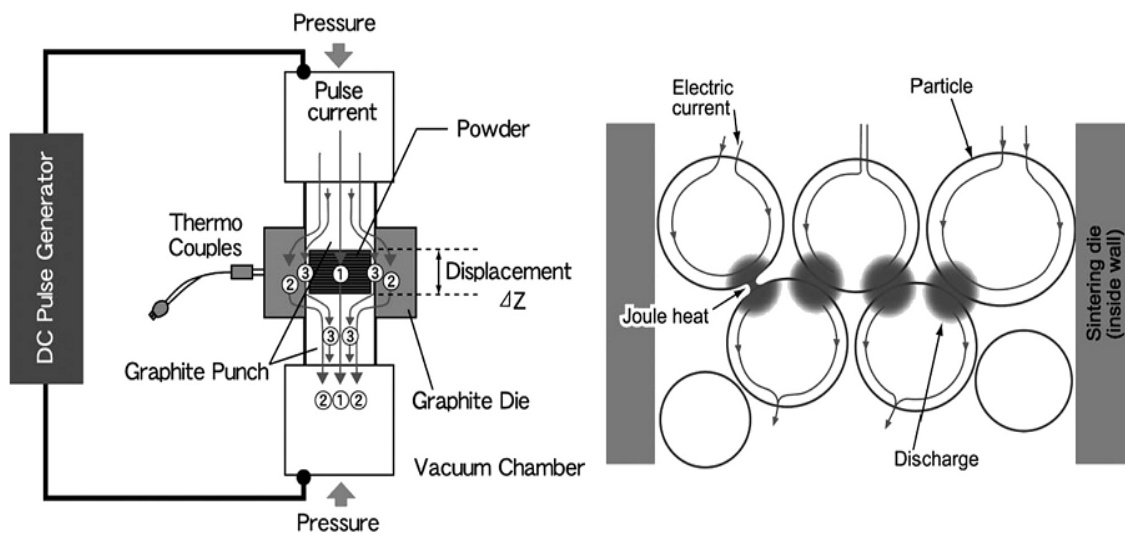
Figure 2.3 ON-OFF DC pulsed current path and pulsed current flow through powder particles[15]

The similarity of SPS and conventional HP is that the powders are loaded in to a die, and then a uniaxial pressure is applied during the sintering. However in the SPS method, no

external heat source is used. Instead a current is allowed to pass through the electrically conducting pressure die and, in appropriate cases, also through the sample. This implies that the die itself acts as heat source, and that the sample is heated from both outside and inside. The schematic diagram of the physical process of SPS is shown in Figure 2.4. The main advantages of SPS compared to CS is the very fast heating rates (up to 600 °C /min or more), very short holding times (minutes) and energy saving (between 1/5 and 1/3 compared with conventional sintering techniques). SPS also has the ability to obtain fully dense samples at comparatively low sintering temperatures, typically a few hundred degrees lower than in HP.
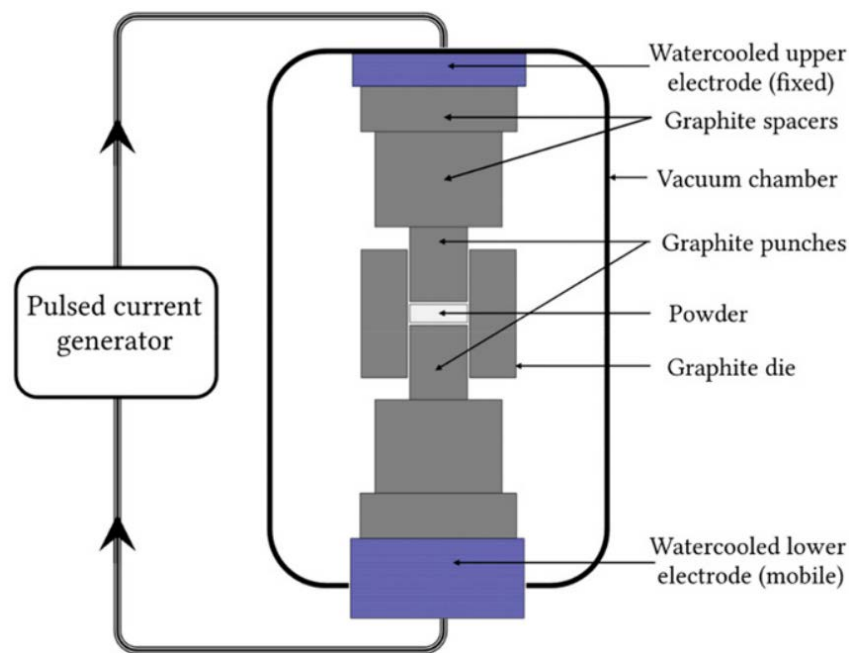
Figure 2.4 Schematic diagram of physical process of the SPS process[30]

SPS is an advanced processing technology to produce a homogeneous highly dense nanostructural sintered compacts, functionally gradient materials (FGMs), fine ceramics, composite materials, new wear-resistant materials, thermo-electric semiconductors, and biomaterials[15]. It is important to note that some of materials can be sintered by SPS only when other consolidation techniques are not effective, e.g. nano-structural

materials and biomaterials. The SPS is fed by pulsed direct current (in various apparatuses, the impulse periodicity varies from 1 ms to 1 s and current amplitude from 0.1 to 10 kA), which is used from the very beginning till the end of the process. An SPS apparatus can be equipped with a vacuum chamber and a computer aided design system. A typical impulse of current in SPS machines causes a magnetic field to be generated. The interaction of the field and the current is accompanied with uniaxial compression.

The heat transfer from the die to the compact is very efficient in SPS, because the die itself and the compressed powder materials act as the heating element. SPS can easily consolidate a homogeneous, highly-dense high-quality sintered compact because of the uniform heating, surface purification, and activation made possible by dispersing the spark points (early stage) and/or joule heat points during sintering[15]. Because of the very high thermal efficiency of SPS, it is able to obtain samples with densities close to the theoretical ones at relatively low temperatures (normally several hundred degrees lower than temperatures employed during HP) and in short period (up to several minutes). The SPS features mentioned above are favorable for sintering, especially of nano-sized powders.

During the last 20 years, the number of papers (including conference proceedings) dealing with the SPS method (Figure 2.5), has shown a seemingly exponential increase[31]. During the 90's, the acquisition of SPS equipment and the fabrication of materials were common research topics. The materials produced via SPS were compared to well-known materials, which were processed by conventional sintering techniques. However, current publication efforts aim to develop new or complex materials, as well as gaining some insight into SPS process.
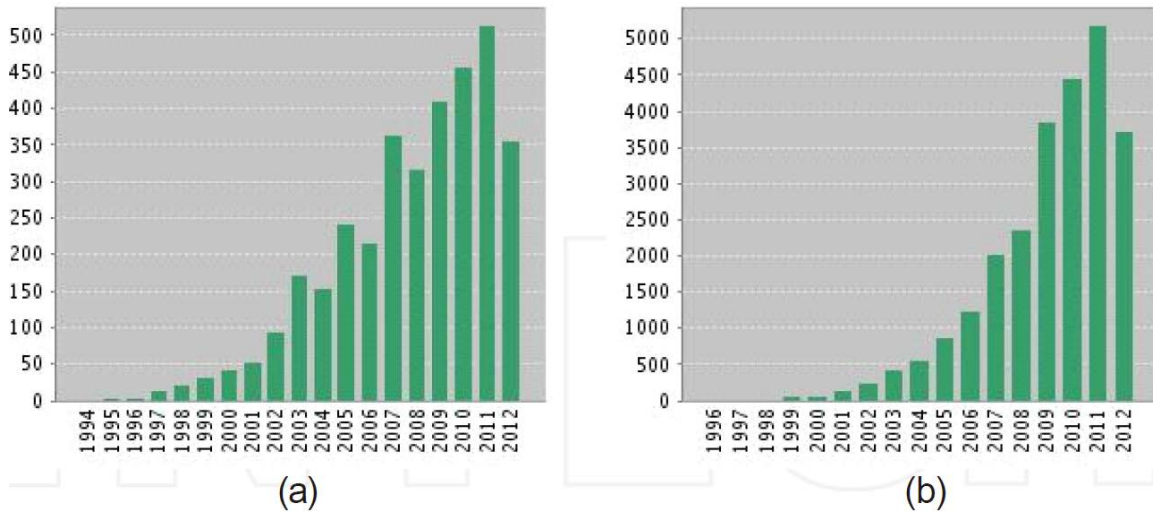
Figure 2.5 Number of publications and citations SPS topic (a) publications (b) citations[32]

2.2.2 Sintering of non-conductive Si_3N_4 ceramics

At present, the phenomena responsible for the enhanced sintering in SPS systems are still under debate. One of the first hypothesis was the local generation of a plasma between particles when current is applied, which would cause the particle surface cleaning and then the improvement of the mass transport[33]. This hypothesis has been particularly controversial because the lack of experimental evidence of such plasma formation. Among the numerous SPS mechanisms proposed, there is a general consensus on the important role of both the rapid Joule heating and the intrinsic electric field effects. For Sialon materials, Nygren's group[34,35] proposed a dynamic ripening mechanism to explain the very fast in situ formation of tough interlocking microstructures by SPS annealing dense compacts. Accordingly, the motion of charged species was enhanced by the electric field and rapid heating, which increased diffusion and homogenization in the liquid phase[35]. This mechanism may be considered as an enhanced solution-precipitation process involving a rapid grain growth. On the other hand, Salamon et al.[36] questioned the influence of electric field on α-phase formation in Sialon materials, claiming that the temperature was the main influence. Most of the

research on the sintering of Si_3N_4 ceramics focuses on the α-β phase transformation, densification, microstructure and properties, which is reviewed in the following sections.

2.2.2.1 *α-β transformation of silicon nitride ceramics by SPS*

Sarin[37] studied the influence of the α-β conversion during liquid phase consolidation on the microstructure of the Si_3N_4-based ceramic and the effects of consolidation time and temperature on the mophorlogy of the β phase. His results indicate that the α-β transformation occurs in the early stages of the liquid phase formation and aids the densification process. Wada et al.[38] found that α-to-β phase transformation of Si_3N_4 was delayed in the surface of the sintered body during both SPS and hot pressing. Kinetic aspects of superfast consolidation of silicon nitride-based ceramics by SPS were studied by Shen and Nygren[34]. The corresponding phase transformation sequences during the initial stages of the sintering process, as well as the consolidation mechanisms, were discussed from the kinetic point of view for Si_3N_4, β-sialon and α-β-sialon composite materials. They confirmed that the formation of a liquid phase is necessary to facilitate the α-β transformation and enhance densification via a solution-precipitation mechanism.

2.2.2.2 *Densification and sintering additives*

The densification of β-silicon nitride powders has been reported by Nishimura et al.[39]. It was found that SPS made possible the preparation of dense materials more rapidly and at much lower temperatures with respect to conventional hot pressing, thus minimizing grain growth during sintering. Using SPS, submicron size, silicon nitride powders were consolidated with Y_2O_3 and $MgAl_2O_4$ additives by Schneider et al.[40]. The SPS technique for silicon nitride/additives mixtures is attractive for retention of fine-grained microstructures favorable for superplastic deformation. The effectiveness of the SPS was thought to be dependent on the dielectric nature of the oxide additives. SPS was also applied by Chen et al.[41] to prepare α-Si_3N_4 ceramics of different densities with

magnesia, silicon dioxide, alumina as the sintering aids. It was shown that the density of obtained samples can be controlled by varying the content of the sintering aids.

2.2.2.3 Microstructure and properties

α-Si_3N_4 ceramics were sintered by Lu et al.[42] using SPS with different heating rates, to study the effect of the heating rate of SPS on the microstructure and the thermal conductivity of Si_3N_4 ceramics. Results showed that the heating rate of SPS had great influence on the phase transformation and the microstructure of the β-Si_3N_4. Suganuma et al. used SPS to densify α-Si_3N_4 powder doped with oxide additives of Y_2O_3 and Al_2O_3[43]. A full density (>99%) was achieved with virtually no transformation to β-phase, resulting in a microstructure with fine equiaxed grains. With further holding at the sintering temperature, the α-to β-phase transformation took place, concurrent with an exaggerated grain growth of a limited number of elongated β-grains in a fine-grained matrix, leading to a distinct bimodal grain size distribution. Xu et al.[44] applied SPS to sinter nano β-Si_3N_4 with additives of Y_2O_3 and Al_2O_3. A non-equilibrium amorphous phase containing a large quantity of well-dispersed nanocrystalline β-Si_3N_4 particles was consolidated at a temperature as low as 1600°C for 5 min at a heating rate of 300°C /min. Submicron-sized α-Si_3N_4 and nanosized amorphous Si_3N_4 powders were also sintered by SPS by Mikinori Hotta and Junichi Hojo[45]. The nanostructure control of liquid-phase sintered Si_3N_4 ceramics was achieved by selecting optimum heating schedules such as temperature, holding time and heating rate. The transformation to β-phase in Si_3N_4 ceramics obtained from the nanosized amorphous Si_3N_4 powder was more greatly accelerated than that from submicron-sized α-Si_3N_4 powder. A multi-layered α-β-Si_3N_4 ceramic composite was prepared by spark plasma sintering[46]. The effects of sintering temperature and time on the strength of the multi-layered α-βSi_3N_4 ceramic composite were determined.

2.2.2.4 Comparison of different sintering techniques for fabrication of Si_3N_4 ceramics

Samples of Si_3N_4 mixed powder with oxide sintering additives were sintered by Wada et al.[47] by SPS and hot pressing with the aim of discussing the characteristic features of the two processing techniques. In contrast, the densification by hot pressing was accompanied by a significant degree of the phase transformation. The apparent activation energy for the phase transformation for hot pressing was almost twice the value for SPS, thereby causing the retention of α-phase during the densification by SPS. The typical low-temperature consolidation and the plasma effect were not confirmed in this work. The rapid consolidation, which enabled the nanometer-scale grain size to be maintained, was shown to be the only advantage of the SPS process with respect to hot pressing. Comparative study of β-Si_3N_4 powders prepared by SHS sintered by spark plasma sintering and hot pressing was carried out by Ling Bai et al.[48]. Well densified Si_3N_4 ceramics with finer and homogeneous microstructure and better mechanical properties were obtained in the case of the SPS technique at 200 °C lower than that of hot press. Similar study also was done by S. Kurama[49]. α- and α/β-SiAlON materials, doped with Y_2O_3 and Nd_2O_3, were sintered using two different sintering processes: SPS and GPS (gas pressure sintering). The results showed that the hardness was not affected by the processing type whereas the toughness values were lower for spark plasma sintered materials than gas pressure sintered materials, which was explained by the changed microstructure of the two different types of material.

SPS was also used to develop new Si_3N_4-based materials by M. Belmonte et al.[31]. They illustrated the capability of SPS for getting continuous functionally gradient materials (FGMs) from a sole homogenous Si_3N_4 mixture just modifying the SPS system punches set-up in order to create a temperature gradient within the specimen.

The densification behavior, resulting microstructure and mechanical properties of hot pressed or SPSed Si_3N_4 with different sintering aids have been the subject of many investigations. Most of them focused on the sintering of α-Si_3N_4. To the best of our knowledge, there is very few research carried out on the comparison of densification behavior and resulting microstructure of α-Si_3N_4 and β-Si_3N_4 sintered by HP or SPS. In the present study, α-Si_3N_4 and β-Si_3N_4 are hot pressed and SPSed comparatively at different temperatures where the densification behavior and resulting microstructure will be discussed.

2.2.3 Sintering of Si_3N_4 based electrically conductive composites by SPS

2.2.3.1 Mechanism and temperature distribution in spark plasma sintering of electrically conductive composites

The experiments carried out for electrically conductive[50-52] and non-conductive powders[52-54] demonstrated such attractive properties/property combination in the compacted materials. It has been believed that at initial stage, the pulsed DC current generates the spark discharge between the powder particles. The gases existing in the sample can be ionized and transformed into plasma. The generated spark discharges and plasma promote the elimination of absorbed gases and oxide layers on the surface of powder particles. Hence, the particle surfaces are cleaned and activated, which provides the favorable diffusion bonding between particles, thus accelerates the densification of the compact. Although, the claim that the pulses generate spark discharges and the existence of plasma between the powder particles explained the reason of the process being called as spark plasma sintering, the experimental evidences for the spark discharge and plasma are still lacking[55-57]. Moreover, the quantification of the effects of pulsed direct current on densification of the conducting powders has not been well-explored yet. The temperature field during sintering becomes an important consideration, because of the high heating rate involved in SPS. When sintering Ni

powder using SPS, the temperature difference is above 130°C from the center of the sample to the inner surface of die (highest temperature is 930°C) [51]. Therefore, it is important to find out the temperature gradient distribution and the associated factors. Zavaliangos et al. also reported the importance of the evaluation of temperature distributions during field activated sintering technique (FAST) [58]. Their study enables a proper comparison between FAST and traditional sintering techniques and also indicates how to optimize processing parameters in larger size specimens. Yucheng and Zhengyi calculated 2D temperature distribution inside the die, and their analysis confirms the temperature difference between the center and edge at the final stage of sintering in SPS system[59]. It was further commented that higher is the thermal conductivity, lower is the temperature difference. Another conclusion of their work is that temperature difference is directly related to heating rate. The higher the heating rate, the greater is the temperature difference which can be as high as 450 °C when sintering temperature at sample center is 1600 °C (Figure 2.6). Hence, it is significant to study the special consolidation mechanisms of SPS process for the sake of optimizing the processing parameters, as well as developing the potential applications of SPS technology.
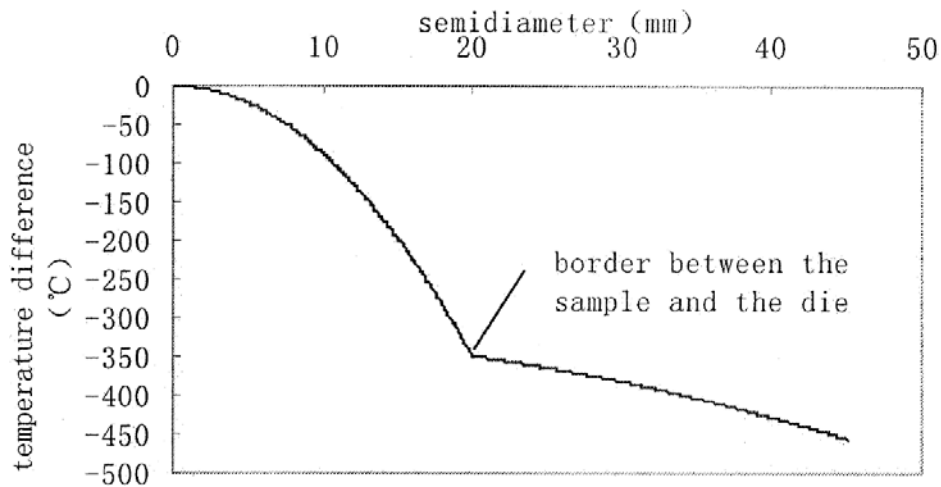
Figure 2.6 Calculation result of temperature field (from the center to 20 mm is the sample, from 20 to 45 mm is the die) [59]

2.2.3.2 Sintering of conductive Si$_3$N$_4$/TiN composites by SPS

TiN/β-sialon composite particles produced ceramics with TiN networks of 0.1–0.5 mm were SPSed at 1500°C[60]. TiN/sialon ceramics (25 vol.%) showed a lower electrical resistivity (of about 10^{-3}Vcm) making these ceramics suitable for electric discharge machining. TiN/ Si$_3$N$_4$ nanocomposites were fabricated by SPS from β-Si$_3$N$_4$ and TiN nanopowders by powder processing routes[61]. The TiN phase grows rapidly and a typical twin structure of TiN can be observed in the composites (Figure 2.7). The grain size and distribution for TiN may affect the electrical resistivity, leading to a pulse current through the sintering compact. The resulting microstructure reveals that grain coarsening behavior for β-Si$_3$N$_4$ based grains is accelerated, and the composite has the highest toughness of 4.9 MPam$^{1/2}$ among all these composites. An effective approach for preparing electrically conductive SiAlON-TiN composites was developed by Ayas et al.[62]. Granules of the designed composition of α-β SiAlON were obtained by spray drying and coated with TiO$_2$ powder by mechanical mixing. The resistivity of the α-β SiAlON (1*10^{11} Ω.m) was drastically reduced down to 2*10^{-4} Ω.m at 5 vol% TiO$_2$ addition. TiN coating on Si$_3$N$_4$ via chemical route were SPSed by Kawano et al. [63,64]. The electrical resistivity was in a wide range of 10^{-4} to 10^{0} Ω.cm for the ceramics sintered at 1400 °C, but increased to the order of magnitude of 10^{-1} and 10^{5} Ω.cm at higher temperatures ≥1500 °C. It was found that the complete transition to β-sialon increased the resistivity to 10^{3} to 10^{5} Ω.cm due to breaking up continuous TiN layers by elongated β-sialon grains. Si$_3$N$_4$/TiN composites were successfully fabricated via planetary ball milling of 70 mass% Si$_3$N$_4$ and 30 mass% Ti powders, followed by SPS at 1250–1350°C[65,66]. The electrical resistivity decreased with increasing sintering temperature up to a minimum at 1250°C and then increased with the increasing sintering temperature. The composites prepared by SPS at 1250–1350 °C could be easily machined by electrical discharge machining. Electroconductive Si$_3$N$_4$/TiN composites were also fabricated by HP and SPS from micron-sized Si$_3$N$_4$ and nano-sized TiN powders by powder processing

routes[67]. High densities (>98%) were obtained by sintering at temperatures ≥1500°C using both sintering methods. The TiN phase grows rapidly during the liquid phase sintering, leading to the increase in electrical resistivity. Dense materials produced by SPS possess significantly higher resistivity than the hot-pressed materials due to the larger TiN grain size and the presence of crystallized grain boundary phase.
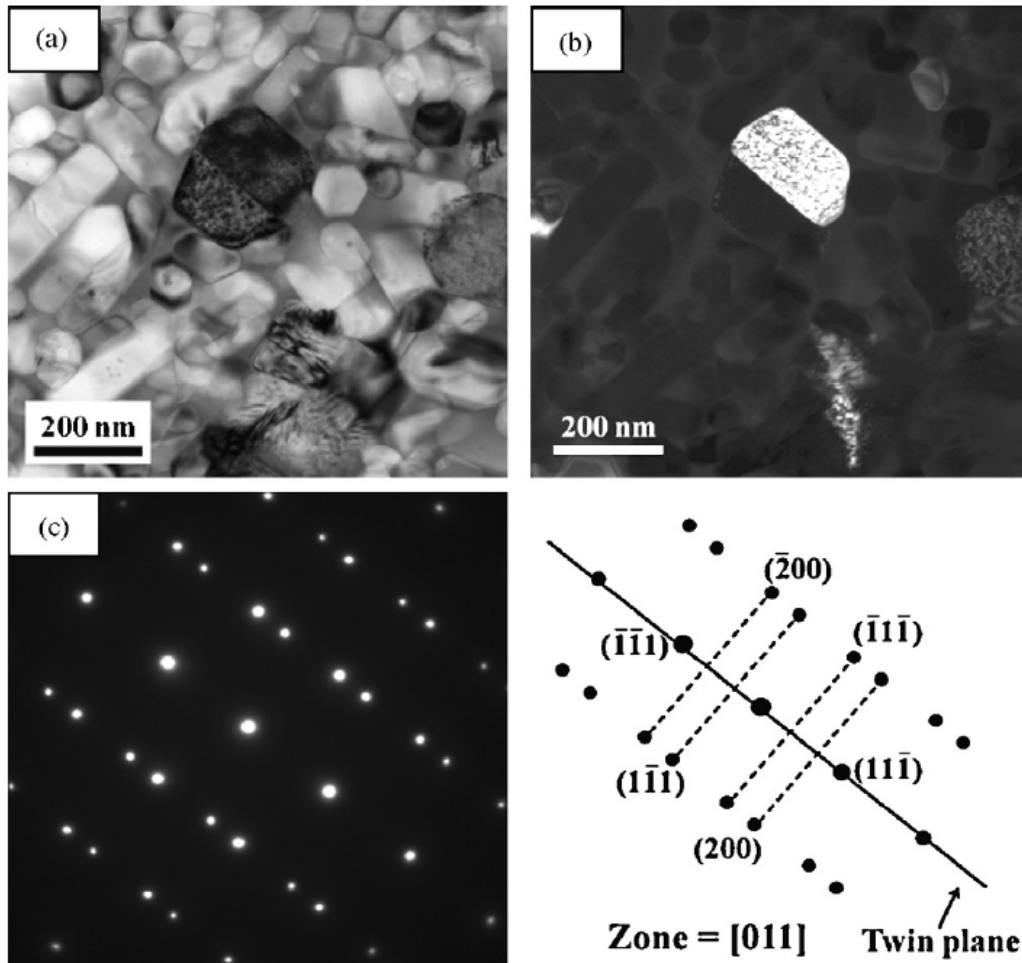
Figure 2.7 Existence of a twin structure of TiN in spark plasma sintered TiN/Si3N4 composite containing 10 wt% TiN (a) Bright field and (b) dark field micrographs, and (c) [0 1 1] selected area diffraction patterns of TiN[61]

Since a current is allowed in SPS to pass through the electrically conducting graphite die and also the sample, a typical impulse of current in SPS machines initiates an electric

and magnetic field. A rational hypothesis is that if the current effects on the densification, phase transformation, microstructure and mechanical properties of conductive materials. At present, the phenomena responsible for the enhanced sintering in SPS systems are still under debate. In this thesis, we will first focus on the effect of electric current on the sintering behavior, microstructures and properties of conductive Si_3N_4/TiN composites by SPS and HP compared with the sintering of nonconductive Si_3N_4.

2.3 Conventional synthesis of non-oxide ceramics and composites

2.3.1 Physical methods

Despite the wide range of current and potential applications, there are not so many ways to prepare non-oxide ceramics on a systematic and scalable fashion, especially when compared to the metal oxides, and some systems are indeed very difficult to make[68]. Synthetic pathways to non-oxide ceramics can be roughly divided into physical and chemical approaches. Physical methods can bring up more defined and chemically pure structures but with a restricted variety of products. Among the physical approaches, the most used are physical vapor deposition[69-71], plasma and laser methods[72-74].

The physical vapor decomposition of solutions has been investigated as an approach for preparing oxide and non-oxide powders. For example, spray pyrolysis is one of the few methods that has given non-agglomerated sub-micrometer particles of high Tc ceramic superconductors[75] and aerosols containing preceramic polymers have been thermally decomposed to obtain non-oxide particles[76].

Preparing powder by thermally induced gas phase reactions requires volatile precursors which are vaporized and thermally decomposed in tube reactors, in plasmas, or by lasers. Wachtmann & Haber[77] reviewed the various methods for making coatings by

CVD techniques, and papers reviewing mechanisms of particle formation[78] and modeling vapor phase reactions[79] has also appeared. These gas phase techniques have most often been used to produce non-oxide powders such as silicon, silicon nitride and silicon carbide[80].

High energy ball milling is also a physical method for synthesis of boride and carbide materials. High-energy ball milling of B-C-Ti mixtures for the fabrication of B_4C and TiB_2 nanocomposite powder was reported[81]. TiB_2 nanocrystalline powder was successfully synthesized by high energy ball milling of a Ti-B elemental powder mixture. The crystallite sizes of TiB_2 decrease with increasing milling time. In the B-C system, B_4C was also formed by high energy ball milling followed by heat treatment above 1000 °C.

2.3.2 Chemical methods

Compared with physical methods, chemical approaches are more versatile and allow the production of a greater range of compounds, however the morphological control is difficult to achieve and toxic precursors have been often used. Classical chemical procedures to non-oxide ceramics involve reactions of parental metals, corresponding metal oxides or any suitable metal precursors with *ad hoc* N/C sources. Synthesis is always performed at high temperature (from 1000 °C up to 2000 °C). Some common examples are: metathesis[82] or other specific chemical conversion[83], thermal decomposition[84], ammonolysis[85-88] and reaction with sodium amide[89].

Recently, more attention has been paid to the selection of tailored precursors, since it has been observed that the starting material plays a crucial role on the features of the final product, and this is especially important when nano-sized material is to be synthesized. Kawaguchi and Nozaki[90] undertook one of the first studies starting from metal chloride toward metal nitrides obtaining AlN from the reaction of aluminium chloride with a triazine based polymer at 1000°C. Among non-classical precursors, there

are also melamine and its close derivative C_3N_4 to TiN nanoparticles[91] or $C_3N_{3.69}$ toward various metal nitrides from the corresponding oxides[92,93].

2.4 Sol-gel based routes for preparing non-oxide ceramic composites

Generally speaking, in a sol-gel process a solid material is formed from a solution passing by a gel intermediate in which reactants are mixed at the molecular level[3]. In the sol-gel process, a solution of metal compounds or a suspension of very fine particles in a liquid (referred to as a *sol*) is converted into a highly viscous mass (the *gel*)[94]. Sol-gel processing allows fast reactions and lower working temperatures, and leads to more homogeneous products with higher surface area. More specifically, a sol-gel process typically involves metal alkoxides that can easily undergo nucleophilic attack due to the presence of the M-O-C bond (readily reactive), e.g. by water. Hydrolysis is coupled with a condensation process that leads to polymerization and then metal oxide formation. Tuning the rate of the condensation process, e.g. by adding a suitable catalyst, a polymeric network (from slow condensation process) or a powder (from fast condensation process) can be obtained[95]. Grain size, morphology (from nanopowders, to films, fibres, etc.) and porosity of the final products can be controlled by adjusting reaction conditions and/or using proper templates or supports[95,96]. The importance of having an ''easy-to-handle'' starting material is especially important for ceramics that, being tougher materials with high melting points and low malleability, are usually difficult to be further processed. Due to this flexibility, sol-gel process is a suitable method for the production of a wide variety of materials. An overview of the sol-gel process and a basic flowchart for sol-gel process are shown in Figure 2.8 and Figure 2.9 respectively.
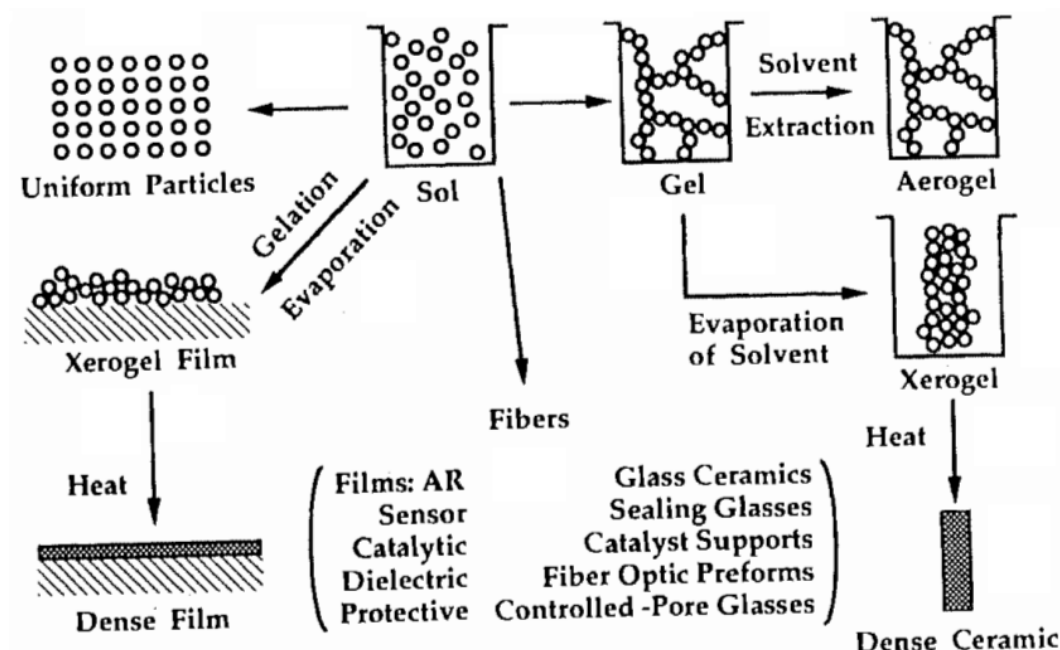
Figure 2.8 Overview of the sol-gel process[97]

First sol-gel experiments date back to 1939, when Geffcken and Berger reported about the preparation of single oxide[98]. Only 15 years later, the first products appeared on the market, and already in the 1980s almost 100 contributions related to the topic were published[99], while nowadays, accordingly to Web of Science®, publications related to the use of sol-gel process exceed 50,000 and the related application market is nowadays wide spread[100]. Success obtained in the synthesis of defined structures of metal oxides by sol-gel process has led scientists to develop similar or related techniques for the synthesis of non-oxide materials.

(a)   (b)
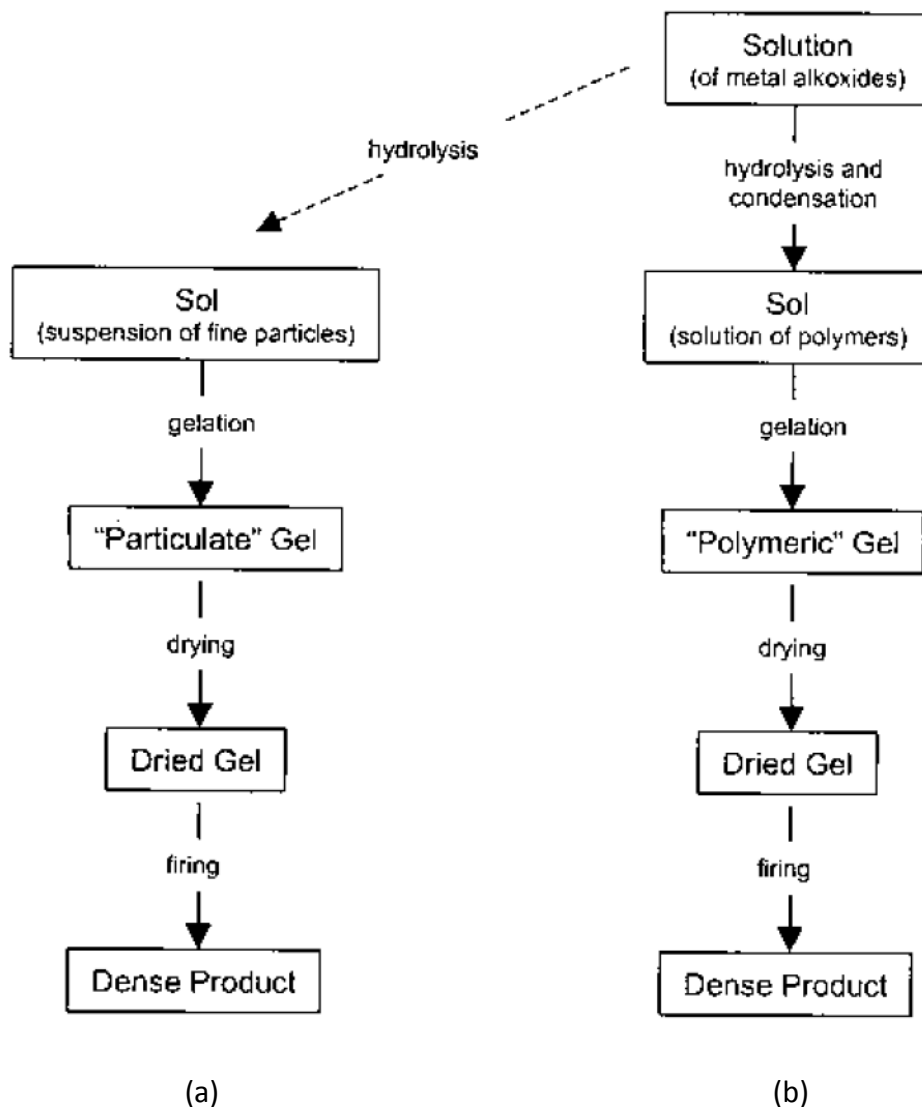
Figure 2.9 Basic flowchart for sol-gel processing (a) a suspension of fine particles (b) a solution[94]

In 1987, Maya reported about the conversion of similar intermediate phases (by ammonolysis of Ti and Nb halides in NH_3) to the corresponding nitrides and carbonitrides, after the reaction of these intermediates with sodium acetylide[101-103]. As for some metal oxides syntheses, sol-gel based routes to nonoxidic materials require a second step treatment where high temperatures are used. The second step can be a solvothermal synthesis, where a sol-gel process is coupled with a solvent-based

structural improvement at elevated temperatures[104-106]. The second step can be also a thermal nitridation or a carbothermal reduction. If a nitrogen source is present, the nitrogen can compete with the carbon in replacing the oxygen bond of the metal, and the process is addressed as ''carbothermal nitridation reaction''[107,108]. With this procedure several materials have been synthesized, including AlN, TiN, SiC, TiC, ZrC, Ti(C,N) TiB$_2$ and ZrB$_2$[109-120]. More unconventional is the procedure known as hydrazide sol-gel process, presented by Kim and Kumta[121]. By a similar hydrazide sol-gel synthesis, AlN was also made[121].

Sol-gel processes have two categories: aqueous and non- aqueous. In general, aqueous sol-gel processes have several advantages compared with solid state reactions such as synthesis at lower temperature, products of higher purity and sensitive process to the reaction conditions which gives this technique a useful versatility. However these advantages in some cases can turn into a disadvantage, for instance when nano-sized materials are synthesized, due to not only the difficulty to get crystalline materials, but also the difficulty to suppress OH- formation, instead of completed Me-O-Me networks, somehow affecting the final product morphology[122]. In contrast, non-aqueous routes allow a better control over the reaction pathways, a direct preparation of crystalline nanoparticles and access to more complex morphologies (such as nanowires and nanorods). Furthermore the absence of surfactants reduces the presence of impurities on the final product that is particularly important for applications as gas sensors or catalysts, where surface processes are involved. The first non-aqueous sol-gel route was developed by Niederberger[123] and addressed as the ''benzyl alcohol route''. In this non-aqueous route, the oxygen is supplied by the organic solvent and/or by the metal precursor. A detailed mechanism and a list of the metal oxide nanoparticles prepared by this route can be found in Ref.[124], where it is also shown how the reaction pathways are related to the nanoparticle formation. Nano-sized metal oxides prepared by the benzyl alcohol route were also shown to be suitable precursors for metal nitrides nanoparticle

synthesis using cyanamide or urea as nitrogen source and upon thermal treatment at 800 °C under nitrogen gas[125].

Transformation of metal oxides into metal nitrides or carbides is usually a ''safe'' way to get well-defined final structures, however the residual amounts of oxygen and carbon are usually not negligible. In addition, the high temperatures required to reduce MOx favor sintering effects and can affect final morphology. In order to skip the crystalline oxide preparation and to speed up the process into a one-step reaction, a urea glass-route was established[126-129]. This sol-gel based procedure is still non-aqueous and surfactant free.

Given the advantages of sol-gel process, it is a suitable method for the production of nano-sized ceramic materials, especially UHTCs, at relatively low temperatures, which is usually prepared at high temperatures.

2.5 Fabrication of UHTC composites by SPS

The SPS of nanoceramics and ceramic nanocomposites attracts much attention due to impeding grain growth and near full densification of ceramics. Both electroconductive and electroisolative composites achieve a poreless state under SPS conditions. Due to the length limitation, only the researches on fabrication of TiC/SiC and ZrB_2-SiC composites are introduced here.

2.5.1 Fabrication of TiC/SiC composite

2.5.1.1 Synthesis of TiC ceramic and TiC/SiC composite

Different mixed organic-inorganic gels as precursors for the synthesis of titanium carbide were prepared in aqueous and organic solutions starting either from rutile or titanium alkoxide by Preiss et al.[130]. The sol-gel processes were controlled by complexing additives such as H_2O_2, acetic acid or ethyl acetoacetate. The synthesis route to the

binary gels could be used to control the elemental composition in the annealed products. Titanium bearing precursor gel and nano carbon particles derived from soot were used to synthesize nano-TiC powder[131]. Both cube shaped particles (~60-140 nm) and hollow rods (diameter ~ 30-185 nm) of TiC were synthesized by heating at 1580 °C (Figure 2.10). TiC and SiC fine-powders were synthesized respectively from organic precursors[116]. Metal alkoxides were used as a metal source and phenolic resin was done as a carbon source. Biedunkiewicz used a sol-gel method to synthesis TiC, TiN and TiC/SiC ceramics/composites[132]. The sol-gel process was carried out in in two stages: low-temperature, in which the raw nC-TiCx product was obtained, and high-temperature in which carbonization of carbides and elimination of excessive organic compounds took place. Rambo et al. produced highly porous, biomorphic (Si,Ti,Zr)-carbide ceramics by vacuum infiltration of low viscosity organo-metallic colloidal suspensions into biologically derived carbon templates[133]. The influence of the initial porosity of the biocarbon template on the final phase composition and morphology of the formed biomorphic MeC/C-ceramic composites was also analysed. TiC–TiB$_2$–SiC ceramics with enhanced yield and microstructure homogeneity were synthesized from hybrid polymer precursors by Li et al.[134]. The authors thought that the key process of phase evolution as well as structure densification was to control the reaction of the C that was redundant for SiC formation with the Ti left after Si-O-Ti cleavage. Hasegawa and Nakamura[135] also synthesized continuous silicon carbide-titanium carbide hybrid fibers through sol-gel processing. Silica-titania-phenolic resin hybrid fibers were first prepared from ethanol solutions of tetraethoxysilane (TEOS), titanium tetrakis (TTP) and novolac-type phenolic resins by sol-gel processing. Carbothermal reduction of both silica and titania components of the hybrid fibers was then taken place at 1500 °C in an Ar flow, resulting in the formation of continuous β-silicon carbide-titanium carbide hybrid fibers with Si-to-Ti atomic ratios varied down to 9.9. Nanostructured silicon carbide hollow spheres, nano spheres and nanofibres were synthesized from mesoporous C–SiO$_2$ nanocomposites by sol-gel processing by Wang et

al.[117,136]. The proportion of nanofibres or nanoparticles can be controlled by tailoring the C/SiO_2 ratio. Zhong and Ang et al. in the same group as Wang also successfully used similar sol-gel processing techniques to synthesize nano-sized TiC, TiC/SiC and ZrC from mesoporous C–TiO_2, C-TiO_2-SiO_2 and C-ZrO_2 respectively[85,111,137]. These researches show that sol-gel processing is an efficient way to synthesize different nanostructured carbide ceramics and carbide composites.
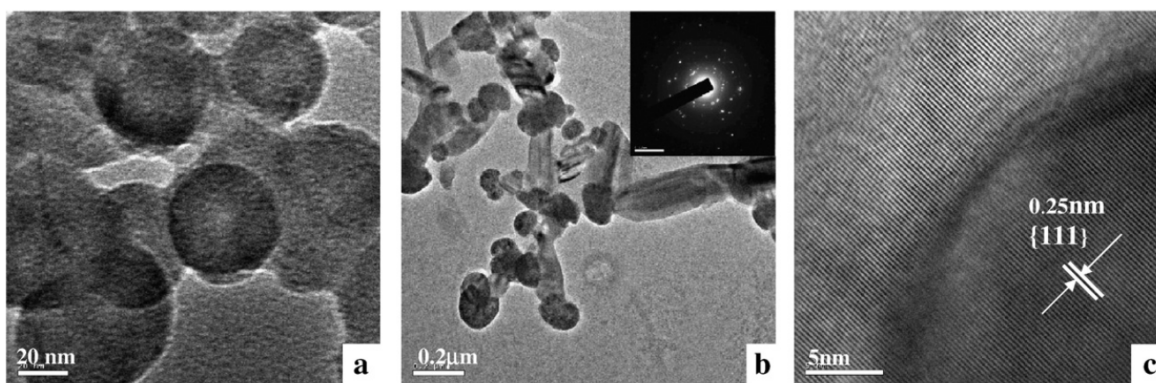
Figure 2.10 HRTEM images of (a) carbon particles synthesized by burning clarified butter, (b) titanium carbide synthesized at 1580 °C. Inset shows selected area diffraction pattern, (c) TiC particle at higher magnification[131]

Besides sol-gel processing, other methods, such as CVD and combustion synthesis, were also investigated to synthesize TiC/SiC composite. SiC/TiC in-situ composites were synthesized by low pressure chemical vapour deposition on graphite with SiC_4, $TiCl_4$, C_3H_8 and H_2 reaction gases to improve the toughness of SiC/TiC ceramics[138]. A dense SiC/TiC deposit without porosity was obtained and only β-SiC and TiC phases were identified in the composite with a dramatic change of the composition at the interface of SiC and TiC grains. SiC/TiC multiphased materials were prepared by thermal chemical vapour deposition under atmospheric pressure from an input gaseous mixture[139]. The morphologies of SiC/TiC composites were strongly dependent on the composition of the input gases leading to either micro- or nanostructures. A combustion synthesis method was also used to prepare TiC/SiC composite powders by coupling strong and

weak exothermic reactions[140]. The reaction temperature and heating rate were found to strongly depend on the Ti/Si ratios in the reactant powder mixture. The authors proposed that the presence of metallic melt phases was important for the formation of the carbide phases.

Although a lot of work have been done on the preparing TiC ceramics and TiC/SiC composites through sol-gel processing, they are all focused on the preparation of ceramic powder or fibers and few work has been carried out on preparing bulk TiC/SiC ceramic materials via sol-gel processing.

2.5.1.2 Fabrication of dense TiC/SiC composites

Hot Pressing is the most conventional sintering technique used for fabrication of UHTCs. The effects of the addition of different amounts of TiC of varying fineness on the mechanical properties and oxidation behaviour of α-SiC were determined and compared with those of single-phase hot-pressed α-SiC[141]. Addition of TiC resulted in a considerable increase in K_{Ic}, however, high-temperature strength and oxidation resistance decreased with temperature and increasing TiC content. Sintering behavior, microstructure and mechanical properties of SiC-TiC composite ceramics sintered by hot pressing was investigated by Endo et al.[142,143]. The room temperature flexural strength of the sintered body increased with the hot pressing temperature and densification was enhanced with the addition of TiC. The composites exhibited superior mechanical properties compared to monolithic SiC and TiC, especially in fracture toughness. The influence of various processing parameters during the fabrication of hot pressed SiC-TiC composites on microstructure and the resulting flexural strength and fracture toughness were investigated in Ref[144]. According to the authors' research, a uniform distribution of the second phase besides a high sintering density is important to achieve high strength and fracture toughness in SiC-TiC composites together with high Weibull moduli. Cho et al. presented a process based on liquid-phase sintering and

subsequent annealing for grain growth to obtain in situ-toughened SiC-TiC composites[145,146]. The β-α phase transformation of SiC in annealing led to the in situ growth of elongated alpha-SiC grains, which caused approximately 60% higher toughness of SiC-30 wt% TiC composites after 6h annealing than that of as-hot-pressed composites. The effects of initial alpha-phase content of SiC on microstructure and mechanical properties were also investigated.
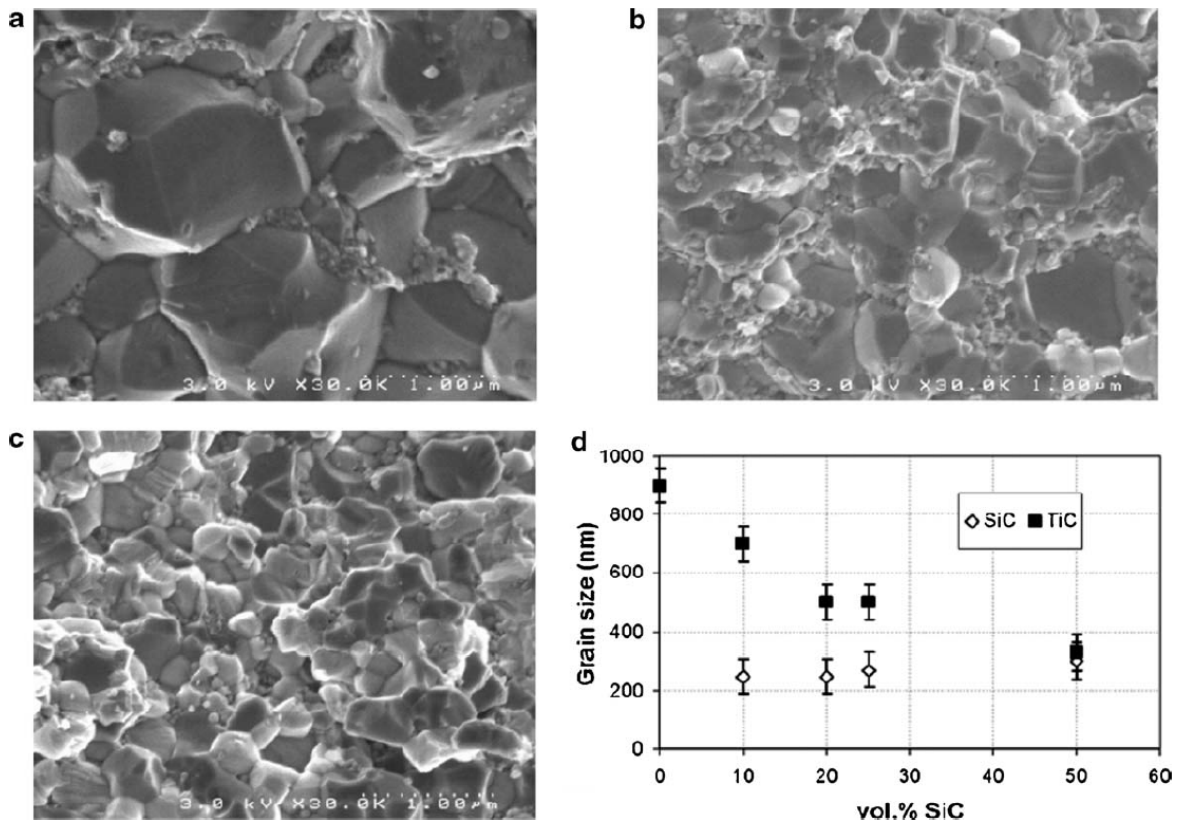
Figure 2.11 SEM images of the fracture surfaces of TiC–SiC composites sintered at 1800 °C (a) 0 vol.%, (b) 25 vol.%, (c) 50 vol.% and (d) grain size of TiC and SiC in several TiC–SiC sintered at 1800 °C for 5 min and under 75MPa[147]

Since the SPS technique was invented about 20 years ago, it has been the most popular sintering technique for fabrication of UHTCs for its unique advantages compared with conventional techniques. Densification of nanocrystalline TiC ceramics by spark plasma

sintering was studied by Chaim et al.[148]. The density linearly increased between 1100 °C and 1500 °C from 72% to 97%. Density of 98% was reached at 1700 °C compared to 76% for the micro-sized reference powder. Cheng et al.[149] investigated the influence of sintering temperature, holding time and pressure condition on densification and mechanical properties of bulk TiC fabricated by SPS. Relative density and Vickers hardness increase with sintering temperature and holding time, but fracture toughness was not significantly influenced by sintering parameters. TiC–SiC composites were fabricated using TiC and SiC powders as starting materials by two step method[150]. TiC and SiC composite powders were first prepared by arc-melting technique and then were sintered by SPS. These TiC–SiC composites prepared by two-step method showed more excellent properties than that prepared by arc-melting technique. The relationship between density, grain growth and temperature of TiC–SiC composites prepared from nano-sized TiC and SiC powders by SPS was studied by Cabrero et al.[147]. The grain size of the TiC/SiC composites sintered at 1800 °C ranged from 300 nm to 700 nm (Figure 2.11). Relative density ranged from 95% to 97%. With the increase of SiC volume contents, Vickers hardness and fracture toughness were improved. Thermal conductivity at room temperature was increased whereas at high temperature it was reduced. Wang et al. investigated the effects of SiC particles on the microstructure and mechanical properties of TiC matrix[151]. The results showed that nano sized SiC particles addition could hinder obviously the coalescence of TiC grains and increase remarkably the fracture toughness of the composites. The grain size of TiC/SiC composites prepared from nano-sized SiC particles was still micron level (a few microns) and some pores could also be found (Figure 2.12). Pressureless sintering and spark plasma sintering of the SiC/TiC laminar ceramic composites were investigated[152] comparatively. The SiC/TiC composites without sintering additives could not be densified using pressureless sintering even at 2000°C. However, SPS could densify the SiC/TiC composites at 1800 °C with a relative density of 98.9%.
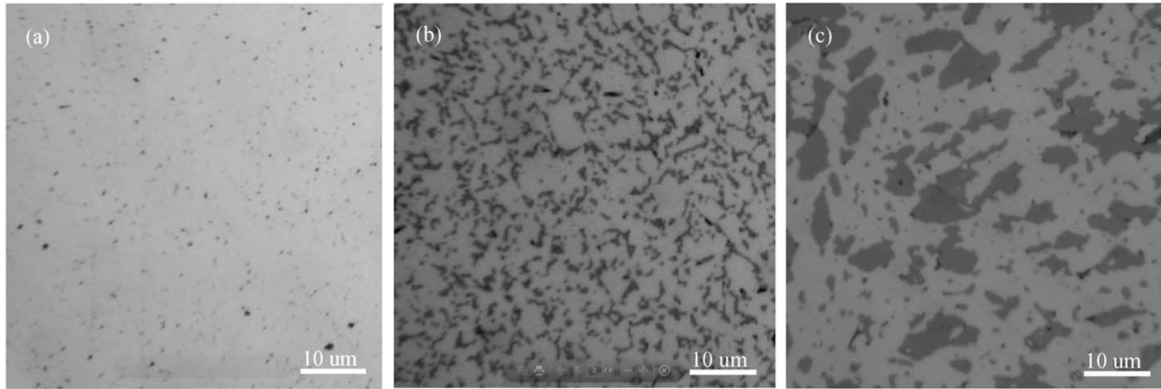
Figure 2.12 Optical microscope observation of samples sintered by SPS at 1600 °C for 1 min: (a) monolithic TiC; (b) TiC/SiC$_{nano}$ composites; (c) TiC/ SiC$_{micro}$ composites[151]

While many researches on the fabrication of bulk TiC/SiC composites materials have been carried out by HP or SPS, they are almost all done via the powder mixing method. Due to the intrinsic disadvantages of powder mixing, it is hard to get dense TiC/SiC composites with homogeneous nanostructure. In this thesis, sol-gel processing and SPS are combined to fabricate dense TiC/SiC composites with nanostructure. The effect of Si/Ti molar ratio and cabon/metal ratio on the densification and microstructure of TiC/SiC composites are also studied.

2.5.2 Fabrication of ZrB$_2$-SiC composites

Within the family of UHTCs, ZrB$_2$ in particular has low theoretical density, which makes it an attractive material for aerospace applications. However, the use of the single-phase material for high-temperature structural applications is limited by its poor oxidation and ablation resistance, as well as its poor damage tolerance. The composite approach has been successfully adopted in order to improve the densification, mechanical properties, physical properties, as well as the oxidation and ablation resistance of the ZrB$_2$ ceramics.

Similar to TiC/SiC composites, some researchers have also prepared ZrB$_2$-SiC composite powders through sol-gel processing. Ultrafine ZrB$_2$–SiC composite powders have been

synthesized *in situ* using carbothermal reduction reactions via the sol–gel method[153]. The powders synthesized had a relatively smaller average crystallite size (<200 nm), a larger specific surface area (~20 m^2/g), and a lower oxygen content (~1.0 wt%). Nano-crystalline ZrB_2-ZrC-SiC ceramics were also synthesized by liquid precursors in a one-pot reaction of polyzirconoxanesal with boric acid and poly(methylsilylene)ethynylene[120]. The pyrolysis of the precursors at 1400 °C in argon led to formation of the nanocrystalline ZrB_2-ZrC-β-SiC powder. The average size of the ZrB_2, ZrC and SiC grains was approximately 100 nm, but there was no report about densification of the powders (Figure 2.13).
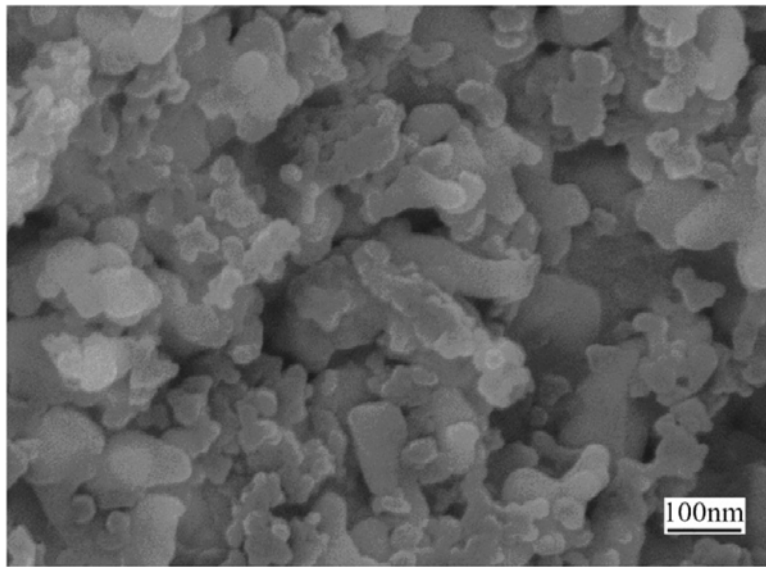
Figure 2.13 SEM micrograph of ZrB_2/ZrC/SiC ceramics[120]

Although only a few researches have been done on the synthesis of ZrB_2-SiC composites, most researches focused on the fabrication, mechanical properties and oxidation behavior of ZrB_2-SiC composites. A hybrid manufacturing process to produce ZrB_2–SiC ceramics by SPS with the SiC phase synthesized in situ by reaction from silicon and carbon was presented by Ortona et al.[154]. The resulting materials had a density ~98% of their theoretical value and presented an interesting microstructure in which SiC was

dispersed within ZrB_2 differently from composites obtained by other reactive processing. High temperature strength of hot pressed ZrB_2-20 vol% SiC ceramics was studied by Zou et al. in which ZrB_2 starting powders were prepared by different carbo/boro-thermal reduction routes[155]. The high temperature flexural strength as well as grain boundary phases of ZrB_2-SiC ceramics were influenced by the different impurity levels of ZrB_2 powder obtained from different boro/carbo-thermal reduction routes. The high temperature strength above 1000 °C can be increased by reducing the grain size. The spark-plasma sintering kinetics of ZrB_2-SiC powder mixtures was investigated as a function of the degree of high-energy co-ball-milling and of the SiC content[156]. As in ZrB_2 without SiC, the crystal size refinement induced by the continued milling progressively enhanced the SPS kinetics of ZrB_2-SiC. The SiC addition further enhanced the SPS kinetics of ZrB_2 and the improved kinetics induced by the SiC addition was identified as being due to the formation of amorphous borosilicate from the oxide passivating layers on the ZrB_2 and SiC particles. The enhanced kinetics induced by the progressive milling was due to the continuous reduction of the diffusion distances and to the development of a greater density of grain boundaries available as faster diffusion paths, together with the greater formation of amorphous borosilicate. The effects of carbon content, SiC volume fraction and SiC particle size on the microstructure and mechanical properties and mechanical behavior of ZrB_2-SiC ceramics at elevated temperature were also studied[157-160]. More researches were focused on the oxidation behavior[4-6,161-163], high temperature strength[155] and creep behavior[164,165] of ZrB_2-SiC ceramics at different temperatures and in different environments.

While the UHTCs have many advantages for high temperature applications, they have a very low atomic diffusion rate and are very hard to densify due to their strong covalent bonding. Conventional methods for processing UHTCs involve powder mixing and fiber toughening. A major issue of the conventional methods is the poor mixing/processing of powders with different densities, especially with nano-sized powders. Thus more

research needs to be focused on improving materials' microstructure and properties. As a wet-chemistry processing method, sol-gel processing is a promising technique to solve this dispersing problem because of its distinct advantage of molecular level solution mixing. Although sol-gel processing has its unique advantages on modifying or improving the microstructures, properties of materials compared with conventional powder mixing approaches, to the best of our knowledge, few researches have been done on preparing dense UHTCs by sol-gel process. In this thesis, sol-gel based approaches are to be investigated to prepare UHTC ceramics/composites with modified/improved microstructures and properties.

2.6 Summary

2.6.1 Summary

In this chapter, an introduction of non-oxide ceramics, ultra-high temperature ceramics and sintering techniques including conventional sintering and spark plasma sintering has been given. The research work on spark plasma sintering of electrically conductive Si_3N_4/TiN composites, and synthesis and fabrication of UHTCs were reviewed.

At present, the phenomena responsible for the enhanced sintering in SPS systems are still under debate. The hypothesis of the local generation of plasma sparks between particles during SPS has been controversial due to the lack of experimental evidence of the plasma formation. Some researchers proposed that the electric field and rapid heating increased diffusion and homogenization in the liquid phase. However, some others questioned the influence of electric field and claimed that the temperature was the main influence. Most of the research on the spark plasma sintering of conductive Si_3N_4/TiN composites focused on increased conductivity and improved mechanical properties, the α-β silicon nitride phase transformation, densification, microstructure and properties. The temperature field during the SPS process becomes an important consideration because of the high heating rate involved in SPS. The temperature

difference between the center and edge of the sample during sintering was confirmed by some researchers. However, the quantification of the effects of pulsed direct current on densification of the conducting powders has not been well-explored yet.

Sol-gel processing has many advantages such as fast reactions, lower processing temperatures and more homogeneous final products, and it has been widely applied to synthesize metal oxides and non-oxide materials. However, it has not been commonly used in synthesizing UHTCs, with most researches being focused on the fabrication, mechanical properties and oxidation behavior of ZrB_2-SiC composites. The densification of ZrB_2 can be enhanced due to the reduction of fusion path by introducing SiC. The high temperature strength of ZrB_2 can also be increased by reducing the grain size. The researches on the oxidation behavior of ZrB_2-SiC composites show that a high SiC content is beneficial for the oxidation resistance at high temperature due to a large amount of silica glass formation as a protective layer to ZrB_2. While the UHTCs have many unique advantages for high temperature applications, the fact is that they are very hard to densify. Meanwhile conventional methods for processing UHTCs involve powder mixing and fiber toughening. The major issue with these conventional methods is the poor mixing/processing of powders with different densities[8]. And as such more research is needed to improve the microstructure, mechanical properties and oxidation resistance of UHTCs. Recently, sol-gel chemistry has shown potential to close this gap and to enable a simple and sustainable approach for the production of UHTCs.

2.6.2 Scope of research

At present, the phenomena responsible for the enhanced sintering in SPS systems are still under debate. More research needs to be carried out on the current effects on the densification, phase transformation, microstructure and mechanical properties of conductive materials. As the quantification of the amount of the current passing though the sample during a SPS process is very difficult to measure, we will focus our study on

the effect of electric current on the sintering behavior, microstructures and properties of conductive Si_3N_4/TiN composites by sintering via SPS and HP respectively. As a comparison, nonconductive Si_3N_4 is also sintered as well. The conductivity, densification, microstructure and mechanical properties of the Si_3N_4/TiN composites with different TiN contents were investigated respectively to figure out the effect of electric current during the SPS process.

As sol-gel processing has many advantages and has not been widely used for producing UHTCs, it was used to synthesize nano-sized TiC/SiC composite precursors first. The effect of the carbon/metal ratio and Si/TiC ratio on the phases and microstructure of the Ti-Si-O-C precursor and TiC/SiC composites were investigated. UHTCs are very hard to densify and usually need to be sintered at high temperatures, resulting in inevitable rapid grain growth. Dense TiC/SiC composites with a nanostructure were investigated via sol-gel processing and SPS in this work.

As a wet chemistry route, the sol-gel method has some unique advantages on processing of UHTCs and functionally gradient UHTCs. A novel sol-gel infiltration approach was developed to modify/improve the surface of the UHTCs. The effect of infiltration cycles on the density and microstructure of TiC/SiC composites and the high temperature ablation of ZrB_2/SiC composites prepared by the sol-gel infiltration were investigated. Sol-gel processing was also be used to combine with powder processing to mix nano-sized secondary phase (SiC) on the surface of UHTCs (ZrB_2) powders to overcome the problem occurred in conventional powder mixing. The effect of the SiC/ZrB_2 molar ratio and the carbon/metal ratio of the sol-gel on the phases, densification and microstructure, as well as the ablation behavior, of the SiC/ZrB_2 composites were investigated in this work.

Chapter 3 Experimental Methods

In this chapter, the starting materials used in this research, experimental procedures including the synthesis and sintering of non-oxide ceramic composites and techniques used for characterization of all samples are introduced.

3.1 Starting materials

3.1.1 Starting powders

The starting powders used in this study are detailed in Table 3.1.

Table 3.1 Raw powders used in this study

Powder	Manufacturer	Grade	Particle size (µm)
α-Si$_3$N$_4$	HC Starck	M11	0.6
β-Si$_3$N$_4$	DENKI KAGAKU KOGYO KABUSHIKI KAISHA	-	-
Al$_2$O$_3$	Aldrich Chemical	99.7%	-
AlN	HC Starck	C	0.8-1.8
BN	HC Starck	B50	-
TiC	Hefei Kaier Nanometer Energy & Technology	99.0%	0.05
TiN	Aldrich Chemical	99%	$<$10
TiN	Hefei Kaier Nanometer Energy & Technology	99.2%	0.02
Y$_2$O$_3$	High purity chemicals	99.99%	-
ZrB$_2$	HC Starck	Grade B	$<$5

3.1.2 Starting chemicals

The starting chemicals used are listed in Table 3.2.

Table 3.2 Chemicals used in this study

Chemical	Manufacturer	Grade
Acetylacetone (AcAc)	Sigma–Aldrich	≥99%
Absolute ethanol (anhydrous)		99.7%
Furfuryl alcohol (FA)	Sigma-Aldrich	98%
Hydrochloric acid (HCl)	Merck, Kilsyth	10M
Tetraethyl orthosilicate (TEOS)	Sigma-Aldrich	≥99%
Titanium tetraisopropoxide (TTIP)	Sigma-Aldrich	≥97%
Poly(ethylene oxide)-b-poly(propylene oxide)-b-poly(ethylene oxide) copolymer Pluronic (P123)	Sigma-Aldrich	Mw=5800
Zirconium npropoxide (ZNP)	Sigma-Aldrich	70 wt% in 1-propanol

3.2 Materials processing facilities

3.2.1 Spark plasma sintering

Spark plasma sintering (SPS) was done by using a Dr. Sinter 950 SPS unit (Figure 3.1) made by SPS Syntex Inc. in Japan. The maximum operation temperature it can go up to is 2100 °C. The maximum force is 100 KN. Maximum sample size is 100 mm in diameter.

Figure 3.1 Dr. Sinter 950 SPS unit

3.2.2 Hot pressing

Hot pressing was performed in a Thermal Technology Group 1400 Laboratory Hot Press machine (Figure 3.2). The maximum operation temperature is 2400 °C.

Figure 3.2 Thermal Technology Group 1400 Laboratory Hot Press machine

3.2.3 Powder mixing and cold pressing

Powder mixing was done via a ball milling machine (Figure 3.3) in a in polyethylene container using Si_3N_4 milling-balls.

Figure 3.3 Ball milling machine

The green body pellets were cold isostatically pressed before sintered by hot pressing. This was done in an ABB Autoclave cold isostatic pressing (CIP) machine (Figure 3.4). The operation pressure is about 200 MPa.

Figure 3.4 ABB Autoclave cold isostatic pressing (CIP) machine

3.2.4 Powder, sol and gel drying

Powder mixture after ball milling was dried in a muffle furnace (Figure 3.5), which has a maximum temperature of 1200 °C. The sol-gel was dried at a vacuum oven (Figure 3.6). It has a maximum operation temperature of 250 °C.

Figure 3.5 Muffle furnace

Figure 3.6 Vacuum oven

3.2.5 Heat treatment facilities for sol-gel process

The carbonization and carbothermal reduction of sol-gel were done in a quartz tube furnace (Figure 3.7) and an alumina tube furnace (Figure 3.8). The maximum operation temperature is 1600 °C.

Figure 3.7 Quartz tube furnace for carbonization of sol-gel

Figure 3.8 Alumina tube furnace for carbothermal reduction of sol-gel

3.2.6 High temperature ablation

The device for the high temperature ablation test of UHTCs is shown in Figure 3.9. Propylene was used as the fuel and the highest temperature of the flame is about 2300 °C.

Figure 3.9 Device for ablation test

3.3 Characterization

3.3.1 X-Ray diffraction

X-Ray diffraction (XRD) was utilized to determine the phases and polymorphic forms of the all samples, for both the sintered samples and original powders. However, it should be noted that the XRD cannot accurately detect the presence of a phase when it is below 5 wt. % of total compositions. The surface layer of each sample was first removed to ensure the bulk material of the specimen was investigated. The samples were then cut for X-Ray diffraction analysis. The analysis was performed using a Philips X-Ray Diffractometer, with a Cu filament operating at 40Kv and 25mA. Standard x-ray diffraction scans for phase identification were taken from 10-80°at 2°/min, with a step of 0.02°.

The β/(α+β) volume fractions of sintered silicon nitride samples were determined by XRD peak-height method. This method was developed by Kall, due to the chemical and crystallite size similarity of their compounds[166]:

$$\beta / (\alpha + \beta) = 100 \times \frac{I_\beta(101)}{I_\beta(101) + KI_\alpha(102)} \qquad (3\text{-}1)$$

Where $I_\alpha(102)$ and $I_\beta(101)$ are the integrated peak intensities (peak area) of the α(102) and β(101) reflections for the α and β phases respectively. K is the normalizing parameter, here it is 1.652. The α(102) and β(101) peaks were chosen because of their high intensity and minimal overlap with peaks from other phases presented in the samples.

3.3.2 Microstructure analysis

The microstructure and structural characterization were made with the aid of scanning electron microscopy (JEOL JSM 7001F), and transmission electron microscopy (FEI Tecnai G2 F20). For scanning electron microscopy, the samples were first ground with SiC paper of progressively finer grades – 180, 600, 1200, 2400 and then polished to a 1 μm finish. The samples were coated with gold, to avoid charging of the insulating ceramic material in the electron microscope. Micrographs were obtained using SEM. Back-scattered imaging provides strong compositional contrast, and so is used to study the microstructural features of different phases of the composites. Secondary electron imaging was used to study the porosity in the samples, because it has a higher resolution and much more sensitive to topological information such as pores.

3.3.3 Thermogravimetric analysis

Thermogravimetric analysis (TGA) on the samples was conducted using a Perkin Elmer DTA/TG 6300 analyser. Experiments were run in air at a heating rate of 5/10 $^\circ$C /min from 50 $^\circ$C to 800/900 $^\circ$C, holding for 60 minutes.

3.3.4 Density and porosity measurement

The density of the samples was determined via the Archimedes principle, using water as the buoyant medium. Samples were first soaked in water for at least 48 hours, ensuring that the surface pores were filled with water. Then they were weighed while immersed in water (W_{immer}). This was followed by the surface being dried by tissue paper; the sample was then weighted, giving W_{wet}. Finally the samples were dried, by placing them in a drying oven set at 120℃, for at least 2 hours so as to completely remove the water from the surface pores. The dry samples were then weighed again (W_{dry}). All weight measurements were performed three times and the average was used to ensure reliability. The bulk density (D_{bulk}) of sample was then determined by:

$$D_{bulk} = \frac{W_{dry}}{W_{wet} - W_{immer}}$$
(3-2)

The relative density (D_{rel}) of sample was determined by:

$$D_{rel} = \frac{D_{bulk}}{D_{th}} \times 100\%$$
(3-3)

where D_{th} is the theoretical density of the sample which comes from the references.

The open porosity (P_{open}) of sample was calculated by:

$$P_{open} = \frac{W_{wet} - W_{dry}}{W_{wet} - W_{immer}}$$
(3-4)

3.3.5 Mechanical properties test

Hardness and toughness values of samples were determined using a Vickers hardness indentation tester. Prior to indentation, the samples were ground flat and then polished to a mirror finish as for SEM analysis. A weight of 10 Kg was applied to the surface of the sample via the Vickers diamond indenter for ~10 seconds. Measurements were taken of

the diagonals of the indentations, and the tip-to-tip distance of the cracks emanating from the corners of the indentations, refer to Figure 3.10. The horizontal and vertical measurements of six indentations were taken on selected points of the sample surface. These results were then averaged to give a reliable distribution. From these values, the hardness and fracture toughness could be calculated using the following equations[167]:

$$H_v = \frac{P}{2a^2} \tag{3-5}$$

$$Kc = 0.016 \sqrt{\frac{E}{H_v}} \frac{P}{c^{3/2}} \tag{3-6}$$

where P is the load, 2a is the diagonal of the diamond, 2c is the distance from one crack-tip to the opposite crack-tip and E is the Young's Modulus of the material.
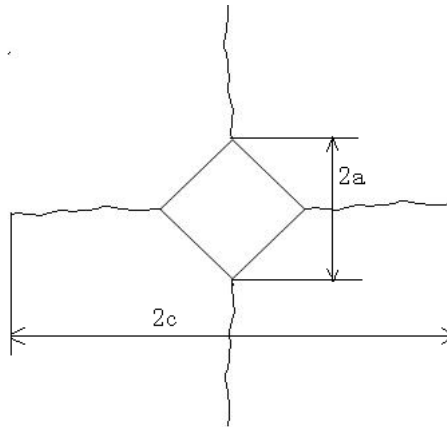
Figure 3.10 Schematic diagram of Vickers indentation for K_{IC} measurement

Chapter 4 Nitride Ceramic Composites Prepared by Hot Pressing and Spark Plasma Sintering

Compared to the traditional sintering techniques, spark plasma sintering (SPS) allows much faster heating rates and shorter sintering times. This would lower sintering temperature and make it suitable for sintering a variety of materials. The SPS technique can significantly enhance the sinterability of most materials. Additionally the SPS can also extend the possibilities for developing new advanced materials and tailoring their properties. Even though SPS uses current to sinter, the technique is not limited to electrically conductive powders. SPS has the ability to sinter non-conductive powders as well. However the conductivity of the powder does influence how the powder is heated. Conductive materials are heated by both Joule heating (self-heating), caused by the direct current passing through the sample, and thermal conduction from the container (usually a graphite die); whereas non-conductive materials are heated only through thermal conduction[168].

Therefore an obvious difference between the SPS and traditional sintering methods, such as hot pressing (HP), is the heating mode. This is because the materials sintered by HP are heated exclusively by thermal conduction from the container, irrespective of whether the material is electrically conductive or not. The differences in heating techniques gives the SPS an extra layer of complexity, this being the pulsed current. Understanding the effect of the pulsed current in the SPS process is important for controlling the resulting microstructure, and properties of sintered products. Given its importance, however, the effect of the current through the samples of such conductive materials has not been well understood.

In this chapter, I will focus on the study of the effect of the pulsed DC current applied during the SPS process. Variables to be investigated are densification, phase transformation, microstructure and mechanical properties of non-conductive ceramics

(both α-Si_3N_4 and β-Si_3N_4) and conductive composites (Si_3N_4/TiN). This will be achieved by sintering Si_3N_4 ceramics and Si_3N_4/TiN composites using HP and SPS respectably. These two materials are chosen in this study because Si_3N_4 is nonconductive and TiN is electrically conductive. They are suitable for studying the effect of current in the SPS process, and its influence on the microstructure and properties of materials. These materials also have widespread industrial application prospects. The weight fraction of each material in the starting powders used in this study is detailed in Table 4.1.

4.1 Experimental procedure

4.1.1 Starting powders

The silicon nitride samples used in this study had different weight fractions of titanium nitride with the sintering aids of Y_2O_3, Al_2O_3 and AlN. As well as being sintered via SPS, the composites were also sintered using HP as comparison. The starting powders, which are detailed in Table 3.1 in Chapter 3, used in this study were mixed in the weight fraction indicated in Table 4.1. The powders were mixed into 100 gram batches and milled for 48 hours using Si_3N_4 milling-balls and 200 ml of isopropanol. The milling mixture was then dried off in a drying oven at 80 °C. This dried powder was then remixed for 10 minutes using a porcelain mortar and pestle in order to ensure complete homogeneity of the powder mixture.

Table 4.1 Weight fractions of raw powders (wt%)

Samples	TiN%	α-Si$_3$N$_4$	β-Si$_3$N$_4$	Al$_2$O$_3$	AlN	Y$_2$O$_3$
1	0	90		3	2	5
2	10	81		2.7	1.8	4.5
3	30	63		2.1	1.4	3.5
4	50	45		1.5	1	2.5
5	0		90	3	2	5
6	10		81	2.7	1.8	4.5
7	30		63	2.1	1.4	3.5

4.1.2 Green body preparing and sintering

The sample size used in hot pressing was 25mm in diameter and about 5 mm in thickness. The green body pellets were formed first by uniaxially pressing ~10 grams of powder in a 25 mm steel die at a pressure of ~15 MPa. The pellets were then vacuum sealed in polyethylene bags and cold isostatically pressed (CIP) for 3 minutes under a pressure of ~200MPa. The final diameter of the green body was approximately 22.5 mm after CIP. In hot pressing, sample pellets were sintered in a graphite die; which was coated with boron nitride to avoid contact between the graphite and Si$_3$N$_4$/TiN raw powders. The boron nitride also provided lubrication during densification. A small amount of boron nitride was also used as packing powder surrounding the pellet so as to separate the pellet and the graphite rams. Hot pressing was performed under a flowing high-purity nitrogen atmosphere. Samples were heated to designed temperature (1300-1800°C) at 20 °C /min and held for 1 hour under an applied pressure of 20MPa. The samples were lastly cooled down naturally in the chamber to room temperature. The temperature was measured using an optical pyrometer.

For SPS, the sample size was with diameter of 20mm and height of about 5 mm. In SPS the sample powder was packed directly into a graphite die. The die and punches were separated from the powder by 0.2 mm thick graphite sheets; this was to aid removal of the sample after sintering. The graphite die was covered with a heat insulating carbon fibre mat to avoid heat wastage from the external surface of the die. For sintering first the chamber was evacuated to a pressure less than 6 Pa. The heating profile was then carried out as follows; the sample was first heated to 600 °C in 4 min, then heated to the sintering temperature (1300–1600 °C) at 100 °C /min and held for 10 min. This was done under a uniaxial pressure of 20 MPa in a SPS unit (Dr. Sinter 950, SPS Syntex Inc., Japan). The sample was then allowed to cool naturally in the die and the initial cooling rate was about 200 °C /min. The final sintered sample was a 20 mm diameter disc with a thickness of about 5 mm.

4.2 Electrical conductivity of the starting materials and Si_3N_4/TiN composites

In this study, α-Si_3N_4 and β-Si_3N_4, with different weight percentages of TiN (0 wt%, 30 wt% and 50 wt%) were used. The compositions contained sintering aids, namely Y_2O_3, Al_2O_3 and AlN. The composites were sintered by HP and SPS at the same temperatures ranging from 1300 °C to 1600 °C under the pressure of 20 MPa holding for 60 and 10 minutes respectively. To study the current effect on the microstructure and properties of Si_3N_4/TiN composites, with varying TiN, the electrical conductivity data of the composites and graphite die used in SPS process must be obtained first. The electrical resistivity data, which were measured by the 4-probe method at different temperatures, are given in Table 4.2. The electrical resistivity data of the samples at the temperature higher than 500 °C are not given here, due to the experiment limitation.

Table 4.2 Electrical resistivity of samples and graphite die (unit: ohm.cm)

Material	Temperature(°C)					
	25	100	200	300	400	500
Graphite die[a]	0.1×10^{-3}	\	\	\	\	\
100% Si_3N_4[b]	approx. 10^{14}	\	\	\	\	2×10^{13}
70%Si_3N_4+30%TiN[c]	$> 2\times10^5$	\	\	\	$> 2\times10^5$	\
50% Si_3N_4+50%TiN	4.6×10^{-3}	4.2×10^{-3}	3.9×10^{-3}	3.4×10^{-3}	3.0×10^{-3}	\
TiN[d]	$20\pm10\times10^{-6}$	\	\	\	\	\

[a] According to the data from the graphite die manufacturer; [b] http://www.siliconfareast.com/sio2si3n4.htm; [c] This value is the upper limit of the instrument used. The resistivity of this composition should be less than that for 100% silicon nitride. [d] Pierson, H.O. (1996). Handbook of Refractory Carbides and Nitrides. William Andrew Publishing/Noyes. charpter 11. pp187

According to the results, the 100% Si_3N_4 sample is non-conductive, and the composite sample with 30% TiN is moderately conductive. The sample with 50 wt% TiN is the most conductive one produced, which is almost as conductive as the graphite die (the same order of magnitude). The higher conductivity of the 50 wt% TiN sample means that a large pulse current will pass through the sample, as well as the graphite die during the SPS process. The electrical resistivity of Si_3N_4/TiN composite with 50 wt% TiN decreases by about 35%, from 25 °C to 400 °C. Electrical conductivity of Si_3N_4 increases with temperature, from about 10^{-15} (ohm.cm)$^{-1}$ at room temperature, to about 10^{-7} (ohm.cm)$^{-1}$ at 1500 °C[169]. Because of this, we can reasonably infer that the electrical conductivity of the Si_3N_4/TiN composite, with 50 wt% TiN, at the sintering temperatures (1300–1600 °C) will be higher than the room temperature conductivity. This increasing electrical conductivity will allow a large current to pass through the sample, rather than the graphite die, during the SPS process.

4.3 Effect of electric current on the densification of Si$_3$N$_4$ ceramic and Si$_3$N$_4$/TiN composites

4.3.1 Effect of current on the density of Si$_3$N$_4$/TiN composites

4.3.1.1 Densities of Si$_3$N$_4$/TiN composites prepared from α-Si$_3$N$_4$ sintered by HP and SPS

The relative densities of the composites of α-Si$_3$N$_4$, with 0 wt%, 30 wt% and 50 wt% TiN respectively, obtained at different temperatures, using both HP and SPS, are shown in Table 4.3 and Figure 4.1. The relative density was calculated by dividing the density of the sintered Si$_3$N$_4$/TiN composite samples with its theoretical density, which was calculated as the average theoretical density of silicon nitride and titanium nitride with their weight percentage respectively. At 1600°C, Si$_3$N$_4$ based composites sintered by either HP or SPS, are almost fully densified. The exception to this was the 50% TiN, sintered via HP, which only achieved a relative density of 96.9%. The results also indicate that the relative density of Si$_3$N$_4$/TiN composite is lower, than that of monolithic Si$_3$N$_4$ in HP at higher temperatures (1500°C and 1600°C). This means the presence of TiN hinders the densification of silicon nitride when sintered by HP. However, in SPS, the relative density of electrically conductive Si$_3$N$_4$/TiN composite, with 50% TiN, is clearly higher than non-conductive monolithic Si$_3$N$_4$, after being sintered at all temperatures. In addition, the sample with 30% TiN, which is moderately conductive, also has higher relative density than the one without any TiN. It means the densification of silicon nitride is improved significantly, with increasing electrical conductivity in materials.

Table 4.3 Relative densities of α-Si_3N_4 with different contents of TiN sintered by HP and SPS

Temperature (°C)	100%Si$_3$N$_4$+0%TiN		70%Si$_3$N$_4$+30%TiN		50%Si$_3$N$_4$+50%TiN	
	HP	SPS	HP	SPS	HP	SPS
1300	62.4±0.1	57.8±0.1	64.5±0.1	59.0±0.1	62.6±0.1	61.5±0.1
1400	68.8±0.1	64.6±0.1	71.9±0.1	71.4±0.1	71.0±0.1	72.8±0.1
1500	97.0±0.1	84.7±0.1	95.0±0.1	89.2±0.1	88.5±0.1	91.3±0.1
1600	100±0.1	98.6±0.1	99.2±0.1	99.6±0.1	96.9±0.1	100±0.1

From the results in Figure 4.1, the relative densities of the samples with 0% and 30% TiN, are obviously higher in HP than in SPS. The differences in relative densities are because of much longer holding time in HP (60 minutes) than in SPS (10 minutes). However, the sample with 50% TiN, which is electrically conductive, has higher density in SPS than in HP at all temperatures except 1300°C. From this it can be observed that densification is aided by electrically conductive materials in SPS, whereas HP shows no such increase in densification when a conductive phase is added to the composite. The SPS technique experiences better densification with the addition of a conductive phase, due to the electric current passing through the sample. This is because of the over heating effect of the conductive materials during the SPS process.
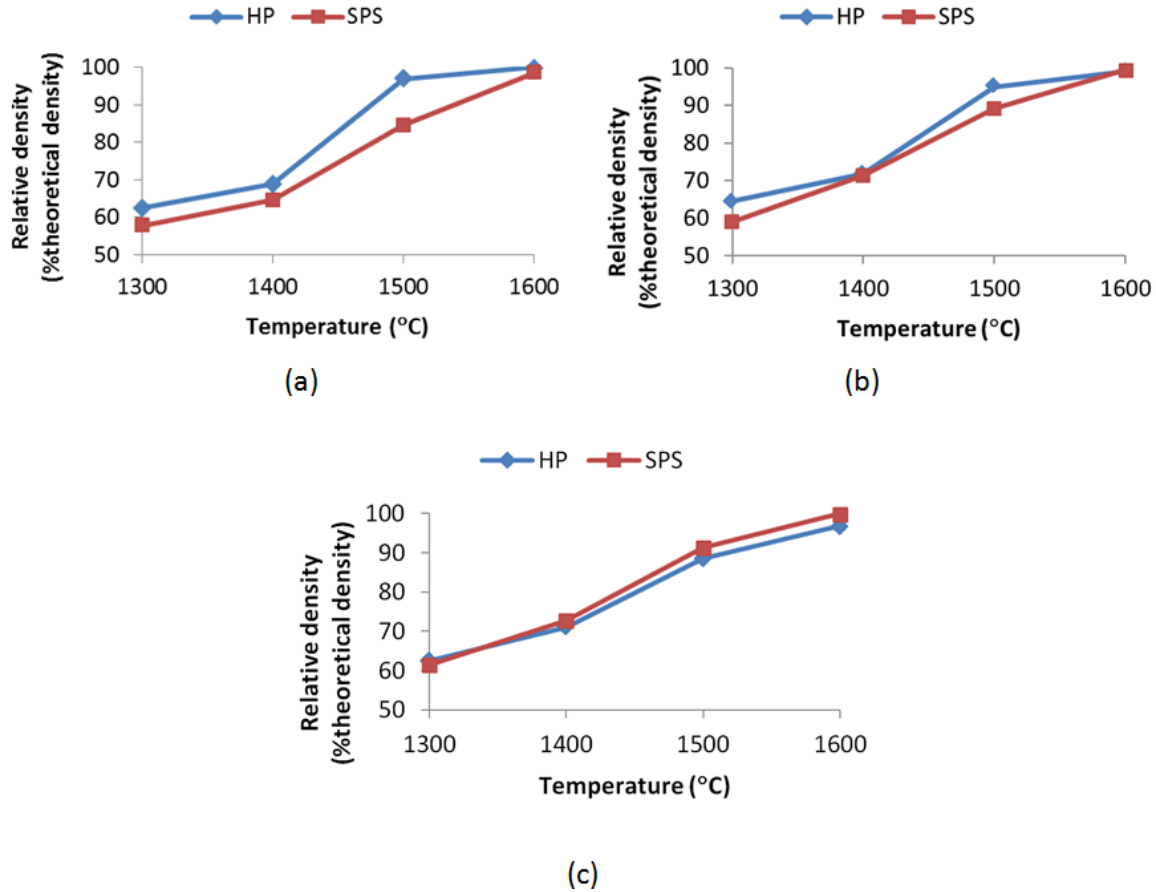
Figure 4.1 Relative density of Si_3N_4/TiN composites sintered by HP and SPS (a)

100%Si_3N_4+0%TiN (b) 70%Si_3N_4+30%TiN (c) 50%Si_3N_4+50%TiN

4.3.1.2 Densities of Si_3N_4/TiN composites prepared from both α-Si_3N_4 and β-Si_3N_4 sintered by SPS

The relative densities of α-Si_3N_4 and β-Si_3N_4, with 0%, 30% and 50% TiN, sintered by SPS at different temperatures, are also compared and shown in Figure 4.2. At 1600°C, both α-Si_3N_4 and β-Si_3N_4 based composites are almost fully densified after being sintered for 10 minutes. Even 0% TiN samples are densified to a similar extent at this temperature. The results also indicate that the relative densities of the conductive samples (50%Si_3N_4+50%TiN), are higher than those of the non-conductive ones, (α-Si_3N_4 and β-Si_3N_4 with no added TiN) after sintering at all temperatures. In addition, the samples with 30% TiN, which are moderately conductive, also have higher densities than those

without any TiN. One main reason for the observed trends in the densification of these materials is the variation in conductivity of the composites. This will affect how the pulse current passes through the specimen, during the SPS sintering. The other may be a chemical effect of the varying amounts of TiN added. TiN itself may also improve the densification of Si_3N_4 besides its effect on improving the electrical conductivity of Si_3N_4.
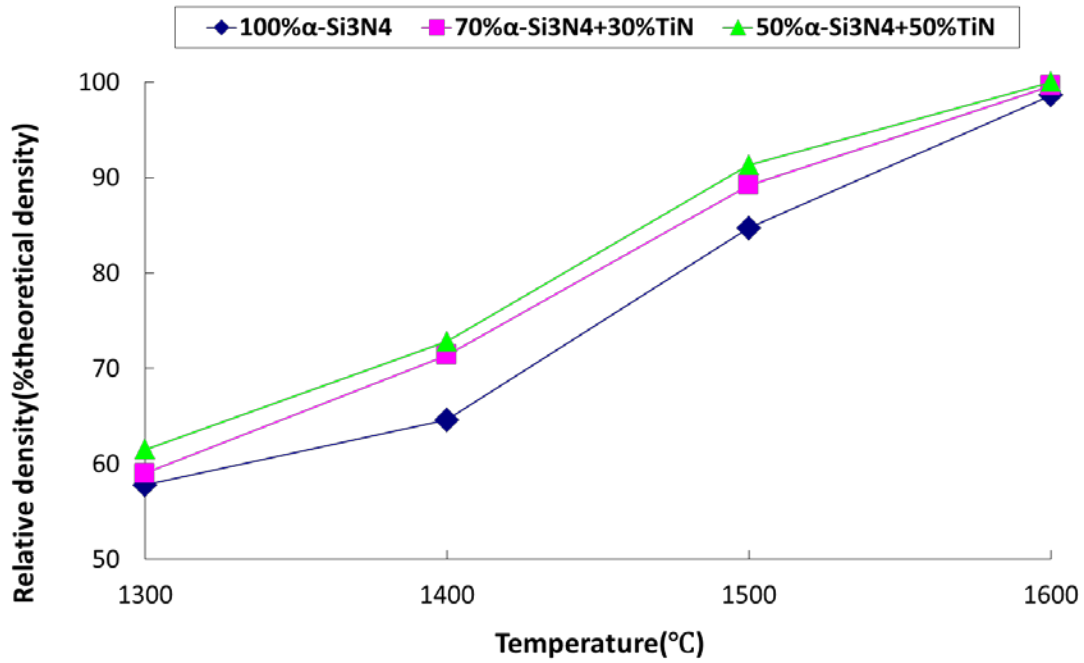
(a)
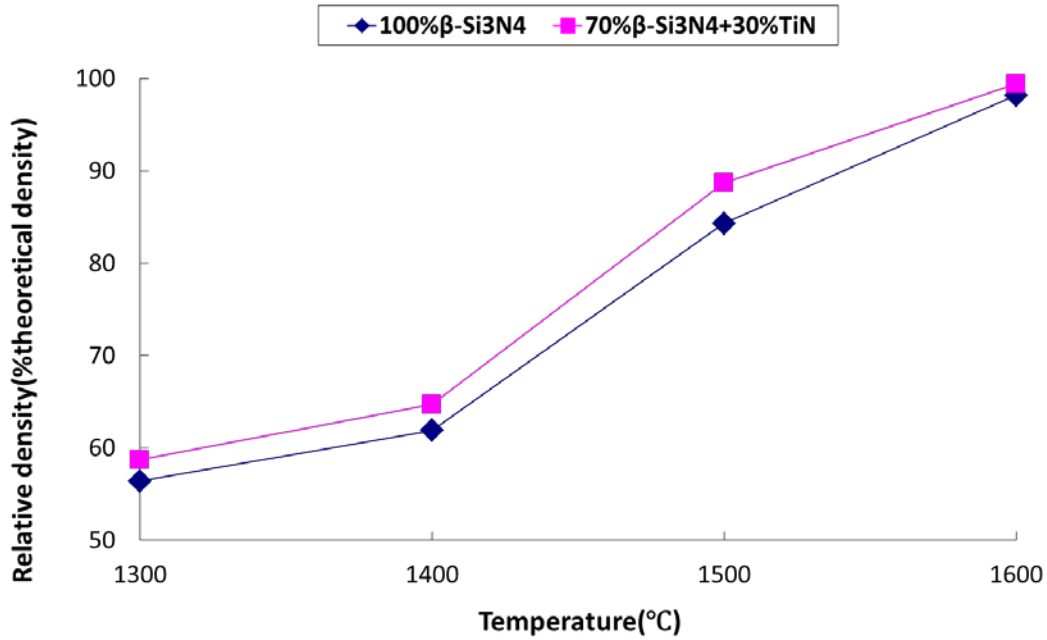
(b)

Figure 4.2 Relative densities of Si_3N_4/TiN composites sintered by SPS at different temperatures: the starting powders were (a) α-Si_3N_4 and (b) β-Si_3N_4 respectively.

4.3.1.3 Densities of monolithic Si_3N_4 and Si_3N_4/TiN composite sintered by HP and SPS

To separate these two variables on the densification of the composite, monolithic Si_3N_4 and Si_3N_4/TiN composite samples were sintered, by both hot pressing and SPS, at 1500°C. The relative densities of the sintered samples are given in Table 4.4. These results show that, in the case of hot pressed samples, the presence of TiN suppressed the densification of α-Si_3N_4 because the TiN grains hinder the elongation of β-Si_3N_4 and consequently the α-β transformation and densification of α-Si_3N_4. This is because the TiN is a foreign phase for the Si_3N_4 and it has a Zener pinning effect on the grain boundaries. As for β-Si_3N_4 no noticeable effect on the densification occurred. But in the case of SPSed samples, the introduction of the conductive TiN phase, improved the densification of α-Si_3N_4 and β-Si_3N_4 samples by 6.6 percent and 4.4 percent respectively.

59

This is because the Joule heating effect is increased with the addition of TiN, and hence a large current can pass through samples. Antonio's research also showed that the final density of samples, (aluminium powder) with electric current flowing through them, is about 5% higher than that of ones without electric current passing[168].

Table 4.4 Comparison of the relative densities (%) of conductive and non-conductive samples sintered by HP and SPS at 1500 °C

50%α-Si$_3$N$_4$+50%TiN		100%α-Si$_3$N$_4$		70%β-Si$_3$N$_4$+30%TiN		100%β-Si$_3$N$_4$	
HP	SPS	HP	SPS	HP	SPS	HP	SPS
88.5±0.1	91.3±0.1	97.0±0.1	84.7±0.1	79.7±0.1	88.7±0.1	79.5±0.1	84.3±0.1

4.3.2 Effect of current on the shrinkage of Si$_3$N$_4$/TiN composites

The shrinkage curves for α-Si$_3$N$_4$ and β-Si$_3$N$_4$ based composites with 0%, 30% and 50%TiN, sintered by SPS at 1600°C, are shown in Figure 4.3a and 4.3b respectively. It should be noted that the dimensional changes of the samples are not directly comparable, due to the differences in the particle size, and the amount of the raw powder used in sample preparations. However, the temperature at which the shrinkage, due to sintering, exceeds the thermal expansion of the assembly (the lowest point on the displacement curve), can be easily identified for each composition by intersecting the displacement curve with the horizontal tangent line. The results in Figure 4.3a show that this happened when the temperature of the die wall (measured by the pyrometer) was about 120°C lower for the electrically conducting specimen than for the non-conducting specimen. Similarly, the corresponding temperature was about 70°C lower for the moderately conducting specimen, than for the non-conducting specimen. The result is also true for β-Si$_3$N$_4$ (Figure 4.3b), the corresponding temperature was about

80°C lower for the moderately conducting specimen, than for the non-conducting specimen.

(a)

(b)
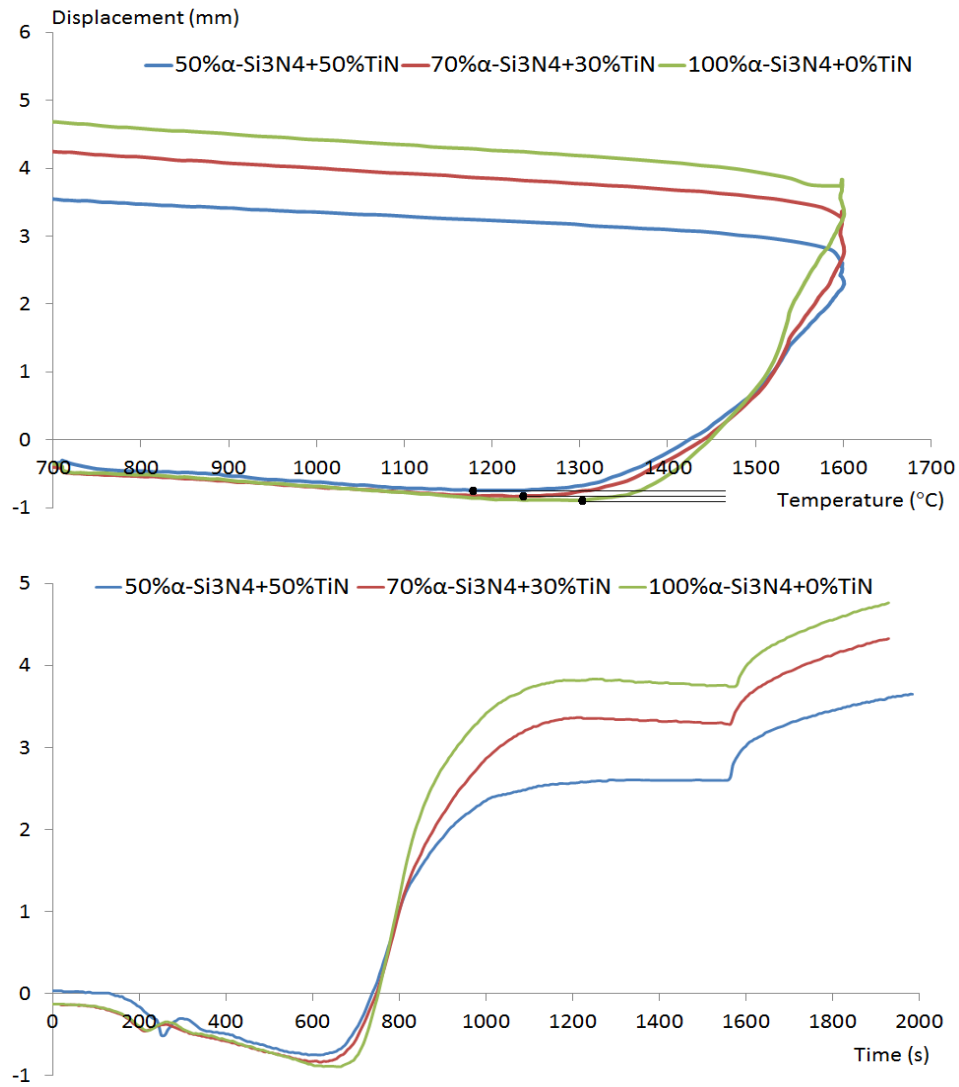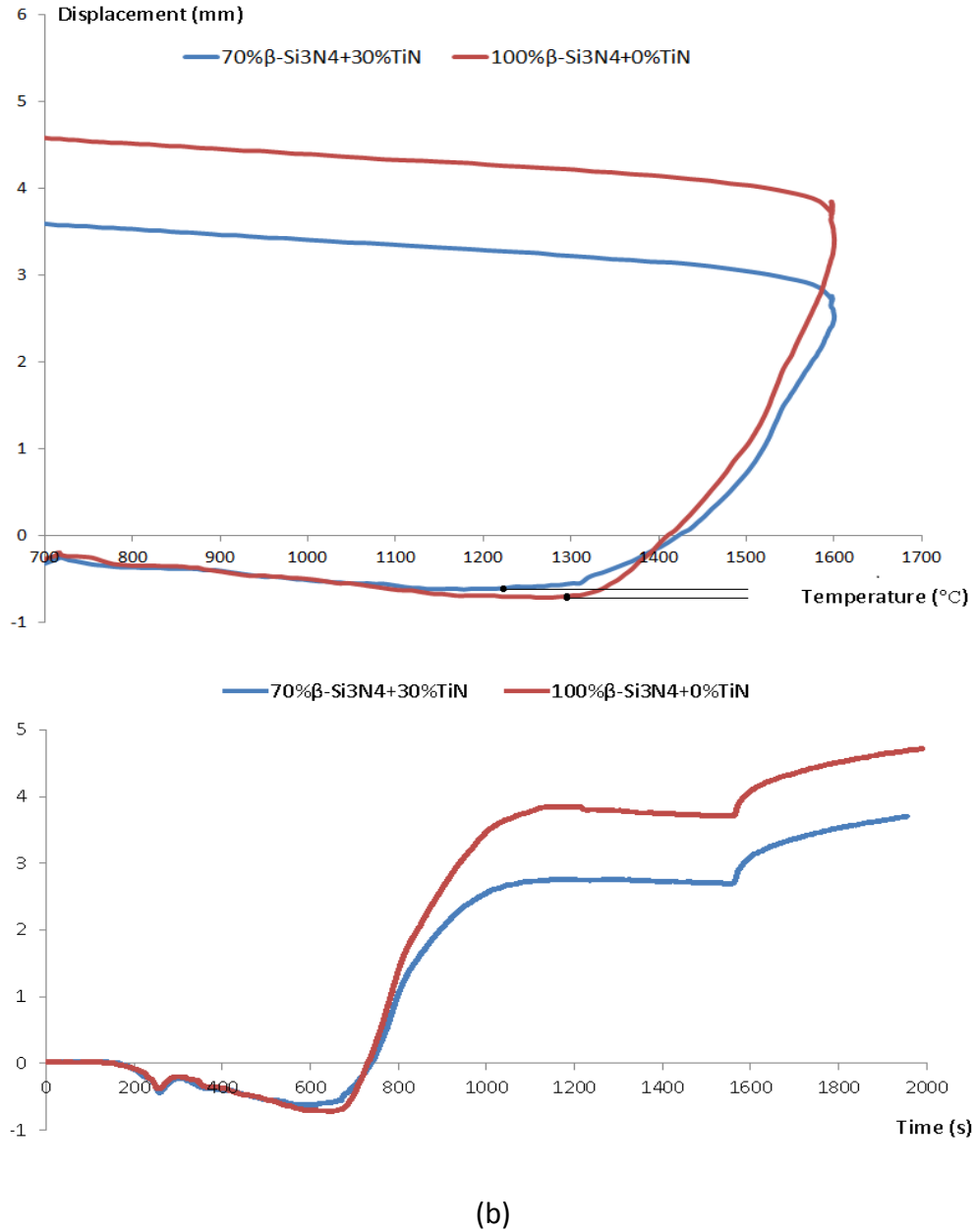
Figure 4.3 Shrinkage curves for Si_3N_4/TiN composites SPSed at 1600°C, the starting powders were (a) α-Si_3N_4 and (b) β-Si_3N_4 respectively

The hot pressed composites show no beneficial chemical effect on densification from the addition of TiN, as discussed earlier. Therefore the commencement of sintering of composites in SPS at apparently lower temperatures than for monolithic Si_3N_4 can be

attributed to a physical effect arising from the presence of conductive TiN, which is the temperature difference between the die and the core of the sample. For the non-conducting, monolithic Si_3N_4 sample, the core of the sample is at a lower temperature than that measured on the surface of the die. Whereas, for the conducting composites, which can be self-heated to some extent by Joule heating, the temperature of the core of the sample can be higher than that measured on the surface of the die. This is also known as the overshooting effect, which is a very important behaviour during the SPS process. Previous studies have also presented some evidence to support this overshooting effect[35,36,43,59,170]. The measured temperature (on the surface of the die) is about 140°C hotter and 170°C cooler for non-conducting silicon nitride and conducting tungsten carbide respectively than the actual temperature (on the surface of the samples)[170]. According to Wang Yucheng's research, the measured temperature on the surface of the die for conducting material (TiB_2 and BN) can be even up to 345°C cooler than the actual temperature (the core of the sample)[59].

4.4 Effect of current on the phase transformation of silicon nitride

4.4.1 Phases of the sintered Si_3N_4/TiN composites

The XRD patterns of Si_3N_4/TiN mixtures with different percentages of TiN, SPSed at 1600 °C, are compared in Figure 4.4. The results show that there is still some α-Si_3N_4 in all the three samples, which means the α-Si_3N_4 has not fully transformed to β-Si_3N_4 at 1600 °C.
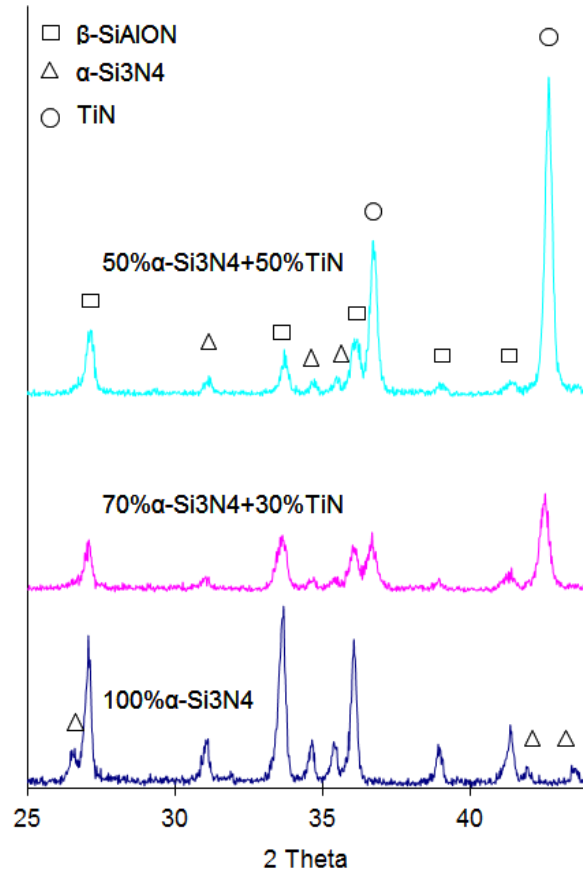
Figure 4.4 XRD patterns of Si_3N_4/TiN composites spark plasma sintered at 1600 °C

4.4.2 β-ratios of Si_3N_4/TiN composites prepared from α-Si_3N_4 sintered by HP and SPS

The β-ratios (β/(α+β)) of Si_3N_4 with different weight percentage of TiN, sintered by HP and SPS, at different temperatures, are listed in Table 4.5. The β-ratio here is used to describe the extent of α-β phase transformation of silicon nitride. We can see that, in SPS, the β-ratio of the conductive sample containing 50% TiN is much higher than that of the non-conductive one (100% Si_3N_4). This is especially true in the liquid phase sintering stage (1500-1600 °C), when α-β transformation occurs. In addition, the moderate conductive samples containing 30% TiN, also have higher β-ratios than those without TiN. From this it can be concluded that the α-β transformation of silicon nitride is

promoted with the increase of conductivity of the sample. This is because a rapid Joule heating effect is taking place within the sample, caused by the large pulse current passing through the conductive powders. The current passing through leads to a temperature difference between the actual temperature at the center of the conductive sample, and the nominal temperature measured on the outer surface of the graphite die. The situation just described agrees well with the shrinkage curves of the samples (Figure 4.3) obtained. On the contrary, in HP, the β-ratio of the conductive Si_3N_4/TiN composites is lower than that of the non-conductive monolithic Si_3N_4, because the presence of TiN suppresses the growth and elongation of β-Si_3N_4 grains, and hence the α-β transformation of Si_3N_4, due to the Zenner pinning effect of TiN on the grain boundaries of Si_3N_4.

Table 4.5 β-ratios in α-Si_3N_4 samples with different mass fraction of TiN sintered by HP and SPS at different temperatures

Temperature (°C)	100%Si_3N_4+0%TiN		70%Si_3N_4+30%TiN		50%Si_3N_4+50%TiN	
	HP	SPS	HP	SPS	HP	SPS
1300	10.1±0.5	10.6±0.3	10.1±0.6	10.9±0.5	9.7±0.2	10.6±0.8
1400	12.8±0.5	11.0±0.3	12.2±0.6	11.0±1.2	9.8±0.9	13.0±1.2
1500	32.3±0.8	12.6±0.3	23.3±0.8	13.0±0.9	18.0±1.1	26.4±2.1
1600	73.9±0.8	70.7±1.8	72.0±0.6	76.8±0.7	70.8±1.5	81.8±1.8

The comparison of β-ratios of α-Si_3N_4 with 0%, 30% and 50% TiN, sintered by HP and SPS at different temperatures, is shown in Figure 4.5. The results indicate that, for the samples with 0% TiN, the β-ratios are higher in HP than in SPS because the holding time in HP is much longer than in SPS, and the solution-diffusion-precipitation involved in the α-β phase transformation of silicon nitride, is a time-consuming process[171]. However, for the electrically conductive sample with 50% TiN, the β-ratio is higher in SPS than in HP,

at all temperatures. Even for the moderately conductive sample with 30% TiN, the β-ratio is also higher in SPS than in HP at 1600 °C where the α-β transformation of silicon nitride proceeds more completely than at lower temperatures. Considering that the sintering time in SPS is 10 minutes compared to 60 minutes in HP, even if the β-ratios were the same between the two samples sintered by SPS and HP, the effect of current on the conductive material is still significant. In HP, the existence of TiN grains suppresses the α-β phase transformation as stated in the last paragraph; while in SPS, the introduction of the conductive phase, TiN, assists the α-β phase transformation because the elevated temperatures the sample experienced. Combining these two points, it can be said that the introduction of a conductive phase, such as TiN, promotes the α-β phase transformation of silicon nitride. This is due to the Joule heating effect of the large current during the SPS process, compared with no current passing through samples in HP.
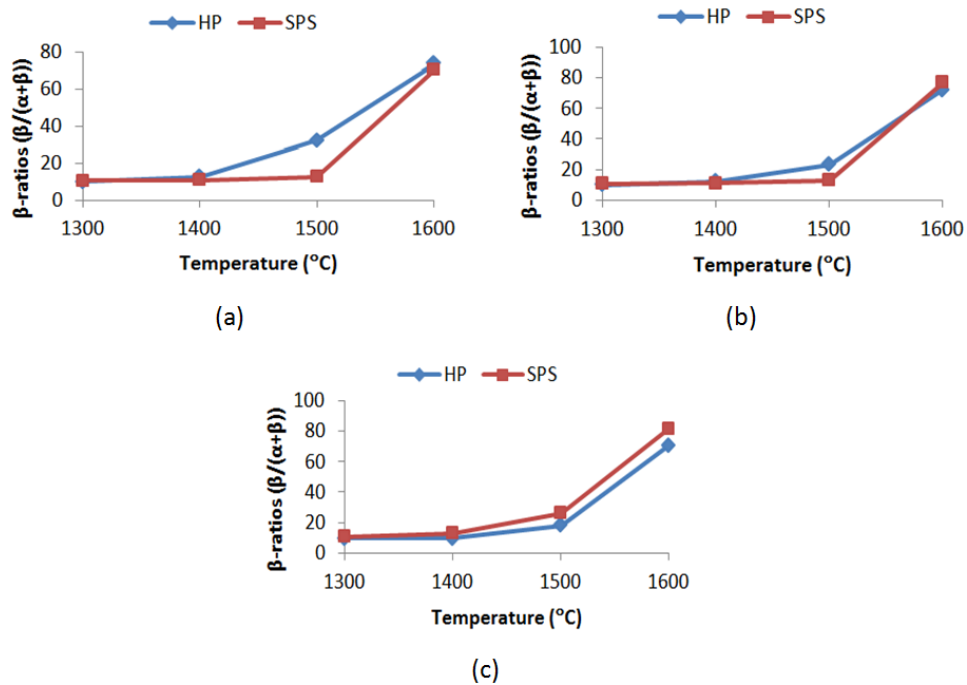
Figure 4.5 Comparison of β-ratio of α-Si₃N₄/TiN composites sintered by HP and SPS (a) 100%Si₃N₄+0%TiN (b) 70%Si₃N₄+30%TiN (c) 50%Si₃N₄+50%TiN

4.4.3 β-ratios of Si_3N_4/TiN composites prepared from both α-Si_3N_4 and β-Si_3N_4 sintered by SPS

The β-ratios of Si_3N_4/TiN composites based on α-Si_3N_4 and β-Si_3N_4 with different weight percentages of TiN, sintered by SPS at different temperatures, are shown in Figure 4.6. It can be seen that the β-ratio of the sample with 50% TiN, based on α-Si_3N_4, is much higher than that of the non-conductive one (100% α-Si_3N_4) at 1500-1600°C. This temperature range is significant because this is when the α-β transformation occurs. This means that the α-β transformation of silicon nitride is promoted, by the presence of TiN, which enhances the conductivity of the sample. Previous research also shows that the β/α ratio of silicon nitride composites, can be used to monitor the real temperature distribution during the SPS process. During this process, the β/α ratio is higher in the higher temperature region, (the out surface of the sample) than that in the lower one (the core of the sample)[170]. For the samples based on β-Si_3N_4, however, the Si_3N_4/TiN composite samples have slightly lower β-fractions than monolithic Si_3N_4 samples at 1400 and 1500°C. These differences are not significant, since they are well within the errors of measurements. Also there is very little α-β transformation occurring in predominantly β samples, at these low sintering temperatures. On the contrary, at 1600°C, the Si_3N_4/TiN composite samples have higher β-fractions, than monolithic Si_3N_4 ones. This can also be attributed to the enhanced Joule heating effect in conductive composites containing TiN. In addition, TiN itself may also promote the α to β transformation and densification of Si_3N_4.

(a)

(b)
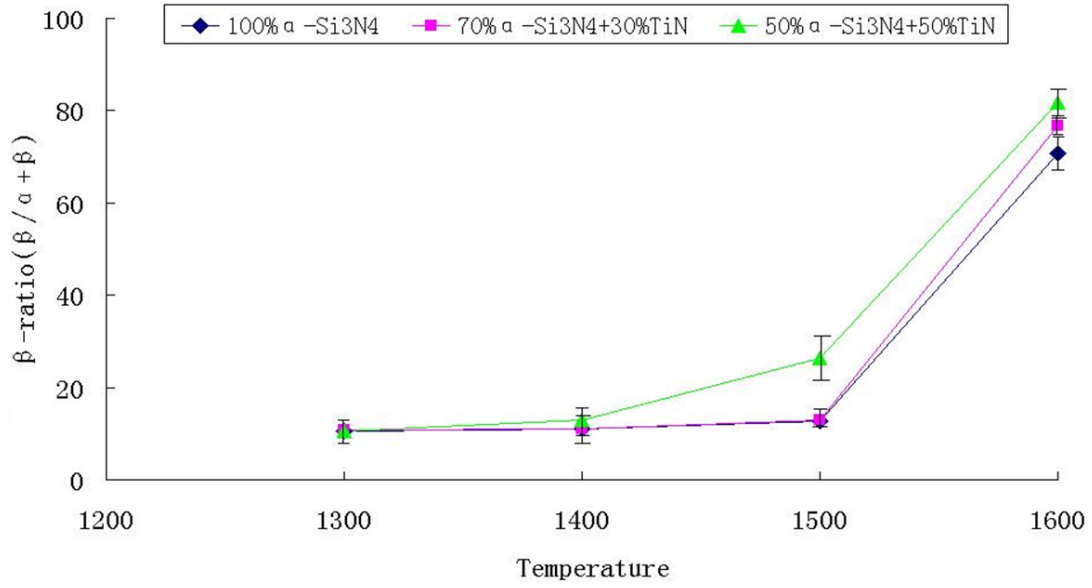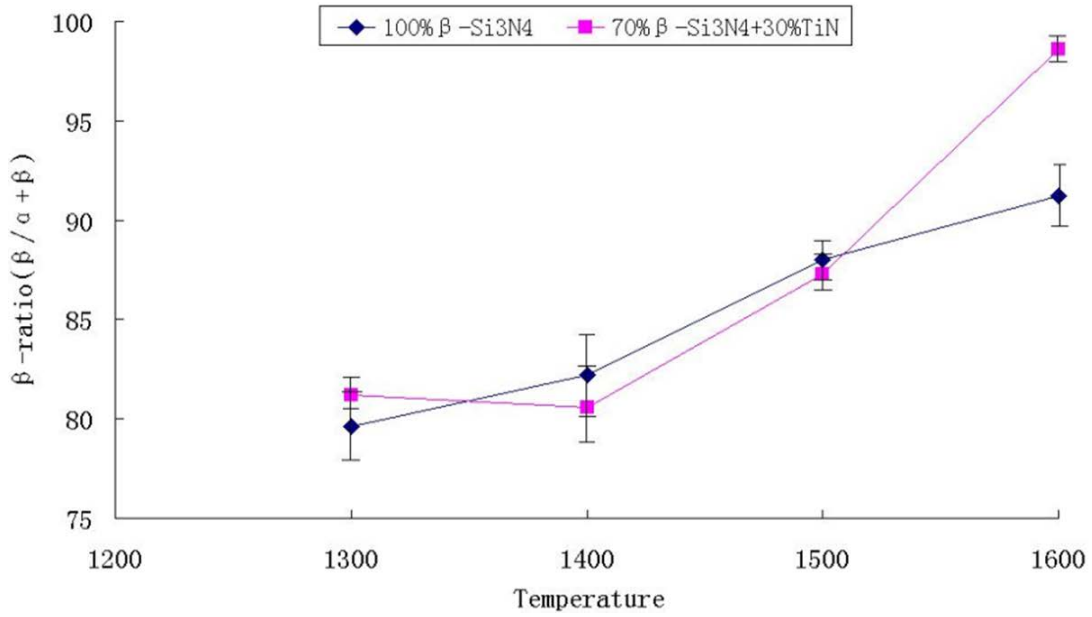
Figure 4.6 β-ratios of Si_3N_4/TiN composites based on α-Si_3N_4 and β-Si_3N_4 SPSed at different temperatures: (a) α-Si_3N_4 and (b) β-Si_3N_4

4.5 Effect of current on the microstructure of Si_3N_4/TiN composites

4.5.1 Microstructures of the α-Si_3N_4 and β-Si_3N_4 based Si_3N_4/TiN composites sintered by SPS

The microstructures of the α-Si_3N_4 and β-Si_3N_4 based composites, sintered by SPS at 1300 °C and 1600 °C, are shown in Figure 4.7 and 4.8 respectively. The results show that the Si_3N_4/TiN composite samples sintered at 1300 °C (Figure 4.7b, 4.7c and 4.7e), have higher densities than the monolithic Si_3N_4 ones (Figure 4.7a and 4.7d), irrespective of whether the starting material is based on α-Si_3N_4 or β-Si_3N_4. The porosity of Si_3N_4/TiN composites at 1600 °C (Figure 4.8b, 4.8c and 4.8e) is slightly less than that of monolithic Si_3N_4 (Figure 4.8a and 4.8d). In these images the dark grains are Si_3N_4, and the bright ones are TiN, because Ti has heavier atomic weight than Si. This observation is in agreement with the density data in Table 4.4 in Section 4.3.1, in which the introduction of the conductive phase, TiN, promotes the densification of Si_3N_4 during spark plasma sintering. Again this is due to the improved Joule heating effect, in the presence of conducting TiN.
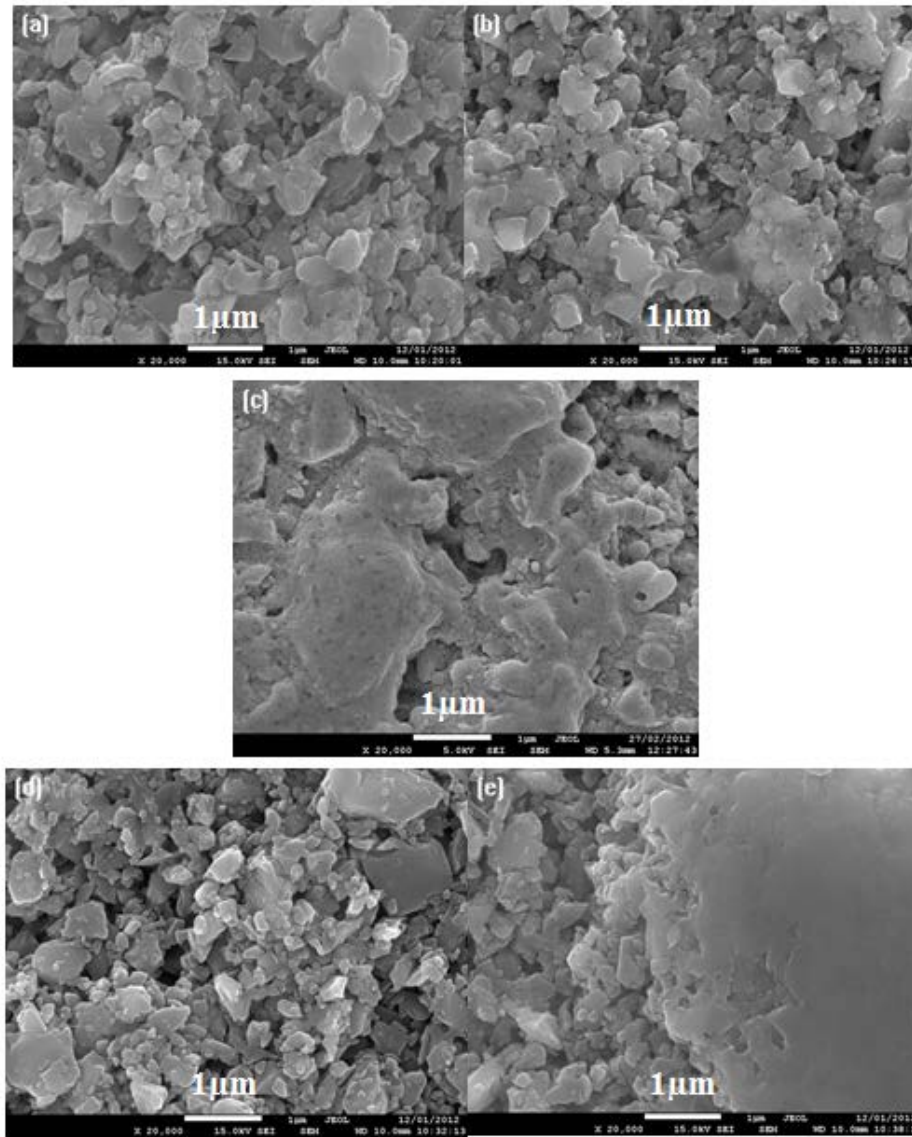
Figure 4.7 SEI micrographs of Si$_3$N$_4$/TiN composites SPSed at 1300°C (a)100%α-Si$_3$N$_4$ (b)70%α-Si$_3$N$_4$+30%TiN (c)50%α-Si$_3$N$_4$+50%TiN (d)100%β-Si$_3$N$_4$ (e)70%β-Si$_3$N$_4$+30%TiN
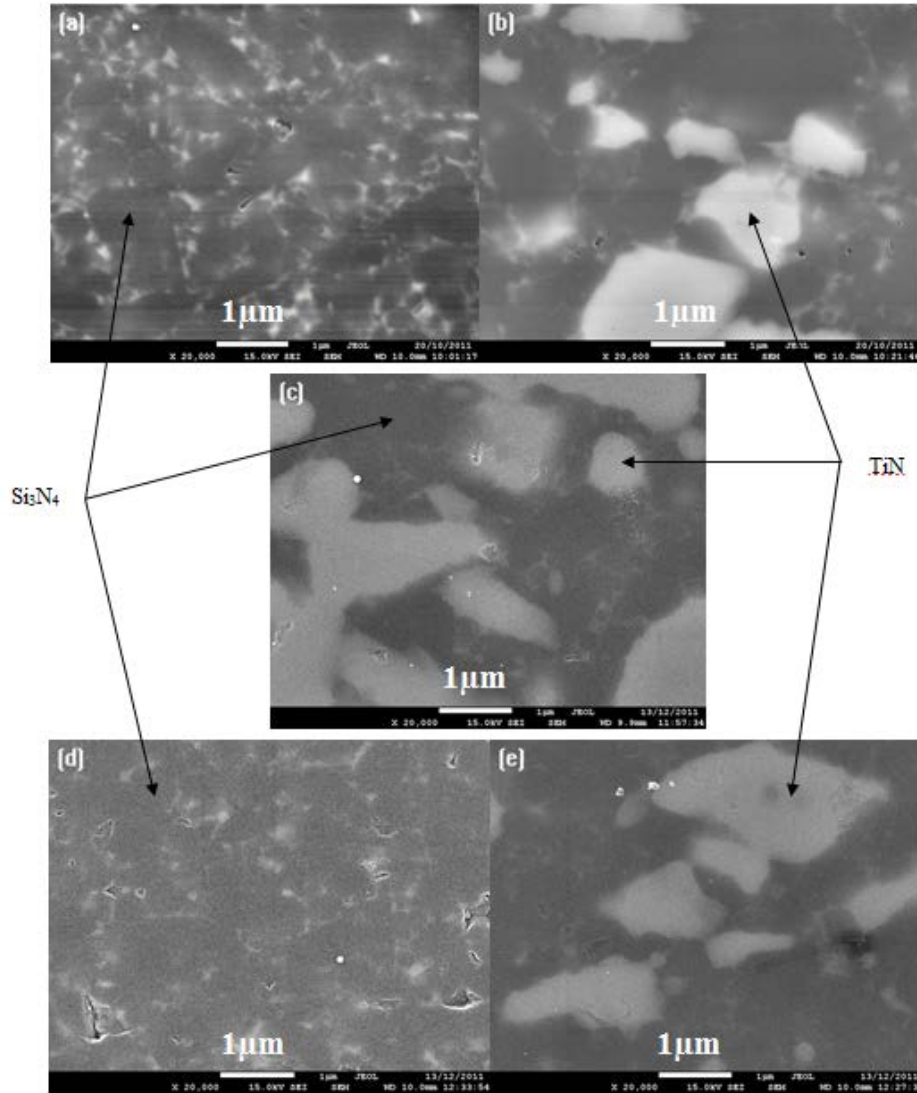
Figure 4.8 SEI micrographs of Si_3N_4/TiN composites SPSed at 1600°C (a)100%α-Si_3N_4 (b)70%α-Si_3N_4+30%TiN (c)50%α-Si_3N_4+50%TiN (d)100%β-Si_3N_4 (e)70%β-Si_3N_4+30%TiN

4.5.2 Microstructures of the α-Si_3N_4 based Si_3N_4/TiN composites sintered by HP and SPS

The microstructures of Si_3N_4/TiN composites, sintered by SPS and HP at 1600°C, are compared in Figure 4.9. The results show that there is a minor difference in the porosity between the monolithic Si_3N_4 and the Si_3N_4/TiN composites. The porosity of the Si_3N_4/TiN composites (Figure 4.9b, 4.9c) is slightly reduced when compared to the

monolithic Si_3N_4 (Figure 4.9a), when sintered via SPS. This is because the conductive phase of TiN promotes the densification of Si_3N_4, through the Joule heating effect. On the other hand, the porosity of Si_3N_4/TiN composites (Figure 4.9e, 4.9f), is a little bit higher than that of monolithic Si_3N_4 (Figure 4.9d) in HP due to the presence of TiN, which hinders the densification of silicon nitride. This result is also in agreement with the density data in Table 4.3.
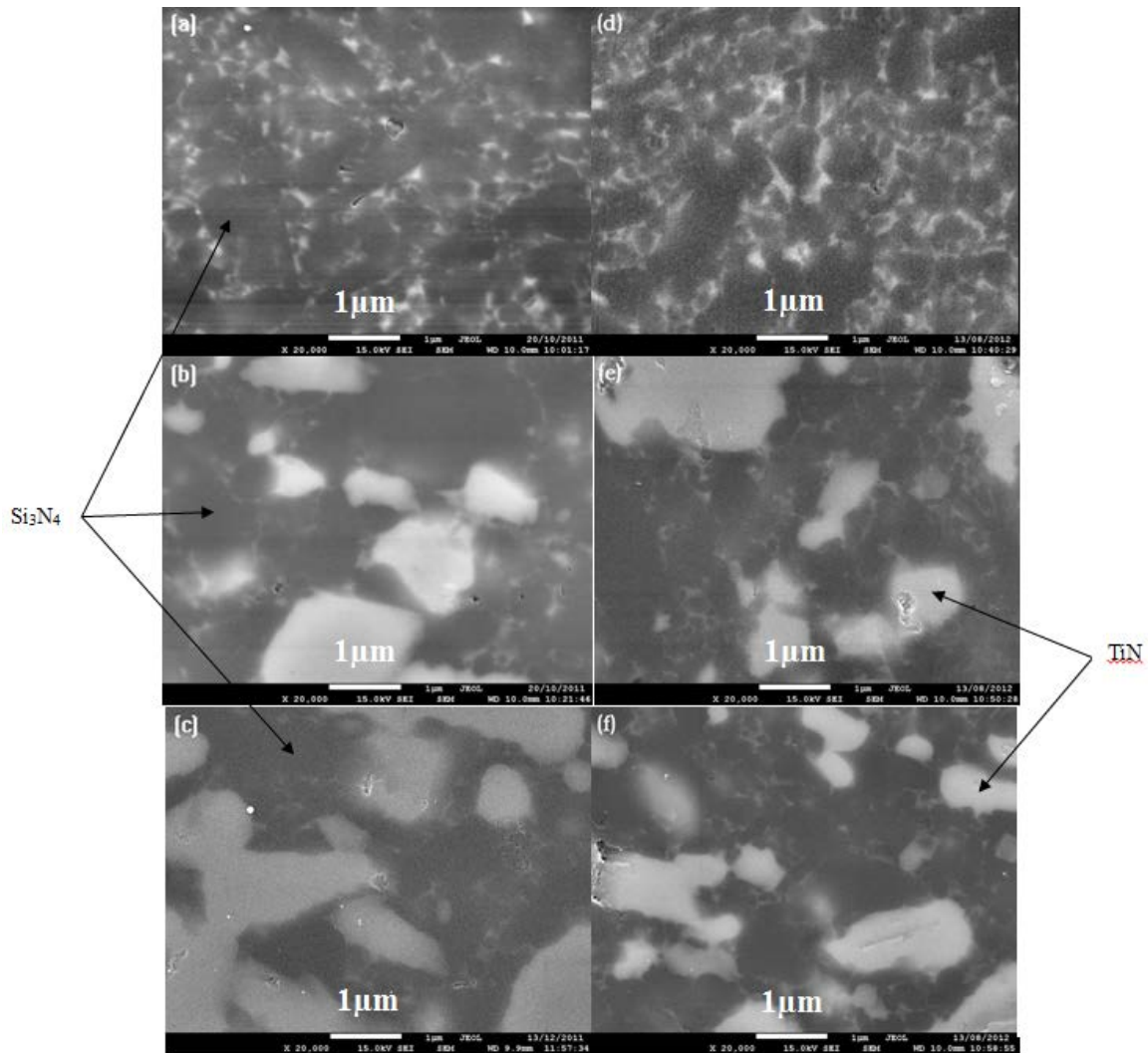
Figure 4.9 SEI micrographs of α-Si_3N_4/TiN composites sintered at 1600°C by SPS: (a) 100% α-Si_3N_4 (b) 70% α-Si_3N_4+30%TiN (c) 50 α-%Si_3N_4+50%TiN, and by HP: (d) 100% α-Si_3N_4 (e) 70% α-Si_3N_4+30%TiN (f) 50% α-Si_3N_4+50%TiN

The average grain size and aspect ratio of the Si_3N_4/TiN composites, sintered by HP and SPS at 1600°C, are shown in Table 4.6. We can see that, for the SPS sintered samples, the average grain size of Si_3N_4/TiN composites is bigger than that of monolithic Si_3N_4, in both α-Si_3N_4 and β-Si_3N_4 as the starting powder. However the aspect ratio in both α- and β-Si_3N_4/TiN composites is smaller than that seen in the monolithic α- and β-Si_3N_4. It indicates that the difference between the actual temperature of conductive Si_3N_4/TiN composites, and the nominal temperature measured on the surface of the die due to the Joule heating effect of the conductive samples, promotes the solution-diffusion-precipitation process involving the α-β phase transformation and the β-Si_3N_4 grain growth in the Si_3N_4/TiN composites. However, the presence of TiN suppresses the elongation of β-Si_3N_4 grains, which leads to the smaller aspect ratio of β-Si_3N_4 in Si_3N_4/TiN composites. It can also be found that the aspect ratio for α-Si_3N_4 based samples is bigger than that of β-Si_3N_4 based ones, this is because there is fewer α phase and less α-β phase transformation during SPS in β-Si_3N_4 based samples.

Table 4.6 Average grain size and aspect ratio of the α-Si_3N_4/TiN composites sintered by HP and SPS at 1600°C

	SPS					HP		
	100%α-Si_3N_4	70%α-Si_3N_4+30%TiN	50%α-Si_3N_4+50%TiN	100%β-Si_3N_4+0%TiN	70%β-Si_3N_4+30%TiN	100%α-Si_3N_4	70%α-Si_3N_4+30%TiN	50%α-Si_3N_4+50%TiN
Grain size (µm)	0.3	0.5	0.6	0.4	0.6	0.3	0.35	0.35
Aspect ratio	9	3	2	5	2	8	4	3

From the results in Table 4.6 and Figure 4.9, it can be found that there is not much difference between the average grain sizes of the monolithic Si_3N_4 samples, sintered

either by SPS (Figure 4.9a) or by HP (Figure 4.9d). However, the grain sizes of the Si_3N_4/TiN composite samples sintered by SPS (Figure 4.9b, 4.9c) are larger than those sintered by HP (Figure 4.9e, 4.9f). This is due to the difference between the actual temperature and the measured temperature in SPS, which does not happen in HP.

4.6 Effect of current on the mechanical properties of Si_3N_4/TiN composites

4.6.1 Hardness of Si_3N_4/TiN composites sintered by HP and SPS

The hardness of monolithic Si_3N_4 and Si_3N_4/TiN composites, sintered by HP and SPS are shown in Table 4.7 and Figure 4.10 respectively. It should be pointed out that the hardness of monolithic Si_3N_4, and the Si_3N_4/TiN composite with 30%TiN sintered by SPS at 1500°C, is obviously lower than by HP (Figure 4.10a and 4.10b), because they possess much lower density (Figure 4.1a and 4.1b).

Table 4.7 Vickers Hardness of Si_3N_4 with different fractions of TiN sintered by HP and SPS at 1600°C (Kg/mm^2, Load=10Kg)

Sintering method	Compositions				
	100%α-Si_3N_4+0%TiN	70%α-Si_3N_4+30%TiN	50%α-Si_3N_4+50%TiN	100%β-Si_3N_4+0%TiN	70%β-Si_3N_4+30%TiN
HP	1741±29	1589±13	1311±15	1623±11	1438±11
SPS	1735±9	1602±40	1509±28	1591±34	1509±21

The results show that the hardness of the non-conductive sample, with 0%TiN, and moderately conductive sample, with 30%TiN, sintered by SPS are lower than that sintered by HP (Figure 4.10a and Figure 4.10b). However, the hardness of the electrically conductive sample with 50%TiN, sintered by SPS, is higher than that sintered by HP (Figure 4.10c). This means that the hardness of the conductive composite material is

improved with the addition of the second conductive phase - TiN. This is because the relative density of the Si_3N_4/TiN composite is increased due to joule heating effect of the electrical current passing through the composite during the SPS process (refer to section 4.2).
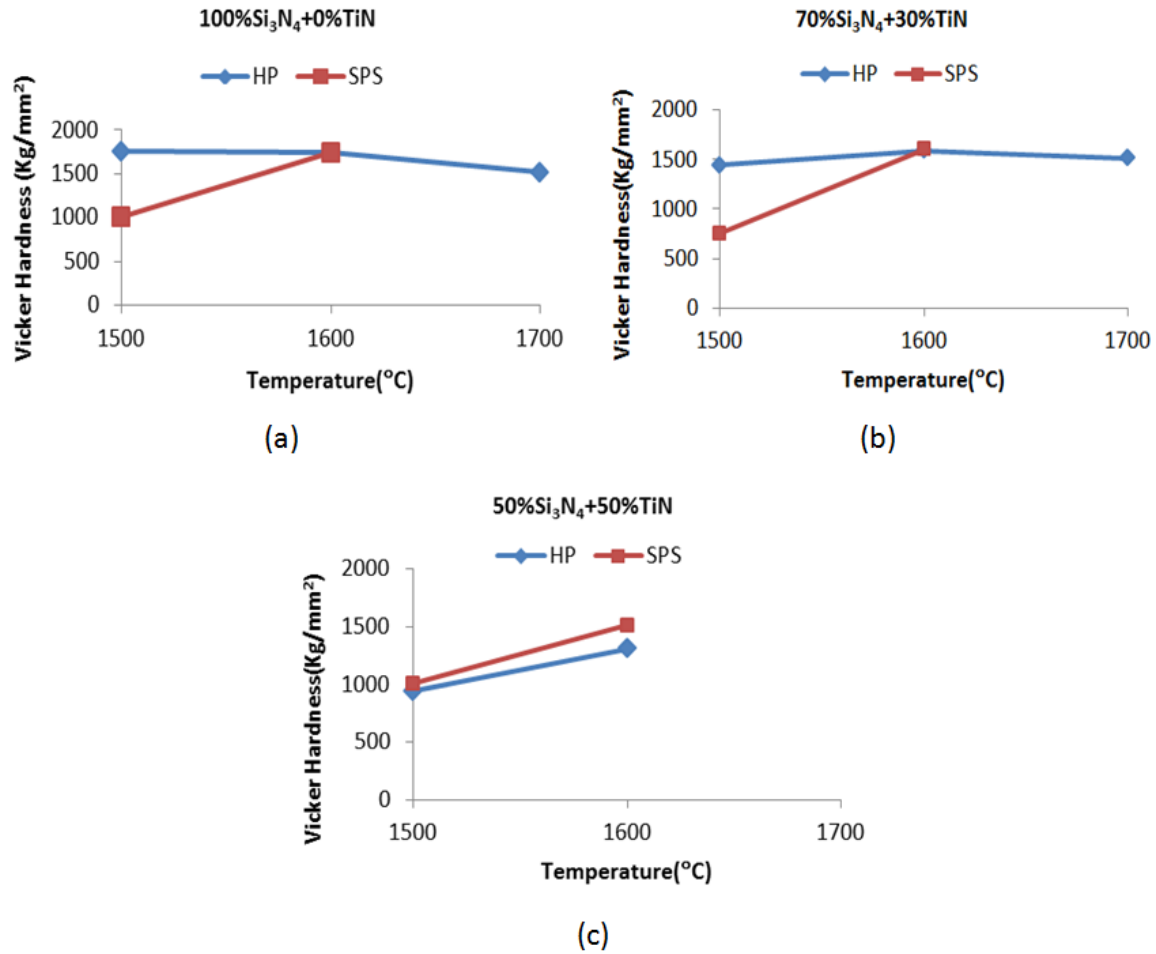
Figure 4.10 Vickers hardness of Si_3N_4/TiN composites sintered by HP and SPS at different temperatures (a) 100%Si_3N_4 (b) 70%Si_3N_4+30%TiN (c) 50%Si_3N_4+50%TiN

4.6.2 Fracture toughness of Si_3N_4/TiN composites sintered by HP and SPS

The fracture toughness of monolithic Si_3N_4 and Si_3N_4/TiN composites, sintered by HP and SPS are shown in Table 4.8 and Figure 4.11 respectively. The fracture toughness of

both the monolithic Si_3N_4 and Si_3N_4/TiN composites, sintered by SPS, is higher than the composites sintered by HP at all temperatures. This means that the effect of current during the SPS process can also improve the fracture toughness of the materials. It can also be found that the Si_3N_4/TiN composites have significantly higher fracture toughness than monolithic Si_3N_4, especially the sample with 50%TiN.

Table 4.8 Fracture toughness of Si_3N_4 with different fractions of TiN sintered by HP and SPS at 1600°C ($MPa.m^{1/2}$)

Sintering method	Compositions				
	100%α-Si_3N_4+0%TiN	70%α-Si_3N_4+30%TiN	50%α-Si_3N_4+50%TiN	100%β-Si_3N_4+0%TiN	70%β-Si_3N_4+30%TiN
HP	4.6±0.1	5.2±0.1	7.4±0.1	4.8±0.1	5.7±0.1
SPS	4.7±0.1	7.7±0.1	8.1±0.1	4.2±0.1	6.0±0.1

The hardness and fracture toughness data show that the introduction of TiN in Si_3N_4/TiN composite samples, with 50% TiN, increases the fracture toughness significantly, (Figure 4.11a and 4.11c) without decreasing the hardness of the Si_3N_4 (Figure 4.10a and 4.10c). The results in Table 4.7 and Table 4.8 also show that the mechanical properties (both hardness and fracture toughness) of Si_3N_4/TiN composites sintered by SPS are improved, compared with those of the HP sintered samples, because of the Joule heating effect during SPS process. This effect is again generated by the electrical current passing through the conductive composite samples, which is the most significant difference between the SPS and HP processes.

The pictures of the indentations on the monolithic Si_3N_4 and Si_3N_4/TiN composites in Vickers hardness tests are shown in Figure 4.12. The bright phase in Figure 4.12b is TiN. We can find that cracks in the monolithic Si_3N_4 are generally straight and intragranular, but cracks in the Si_3N_4/TiN composite are deflected and mostly not through but around

TiN grains. That means the TiN grains hinder the crack propagation, which is the main reason why the addition of TiN increases the fracture toughness of Si_3N_4/TiN composite.

(a)

(b)

(c)
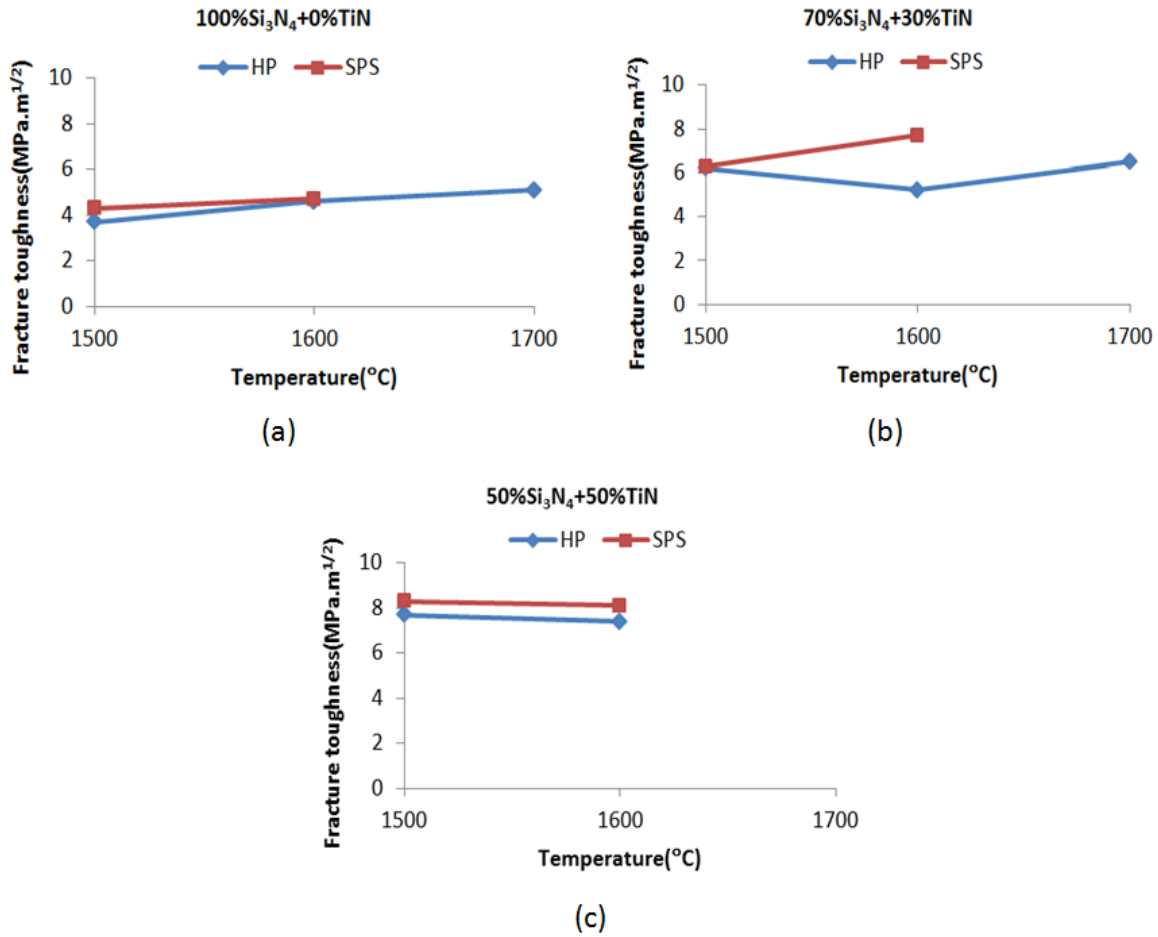
Figure 4.11 Fracture toughness of Si_3N_4/TiN composites sintered by HP and SPS at different temperatures (a) 100%Si_3N_4 (b) 70%Si_3N_4+30%TiN (c) 50%Si_3N_4+50%TiN
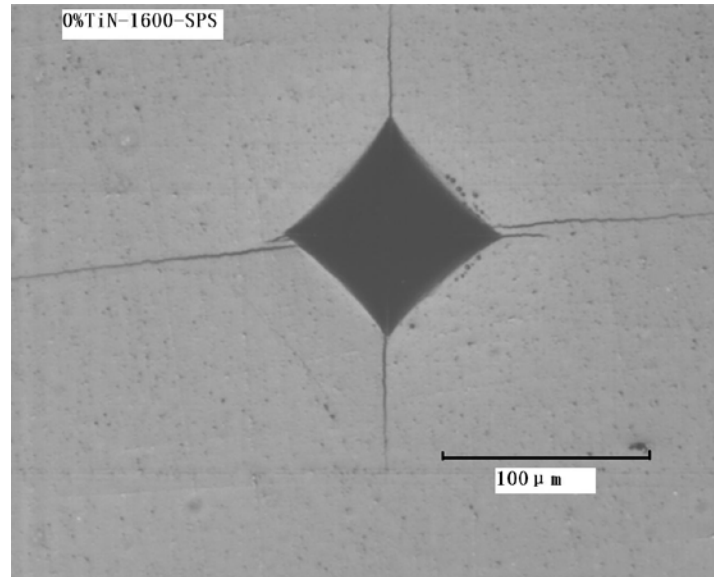
(a)
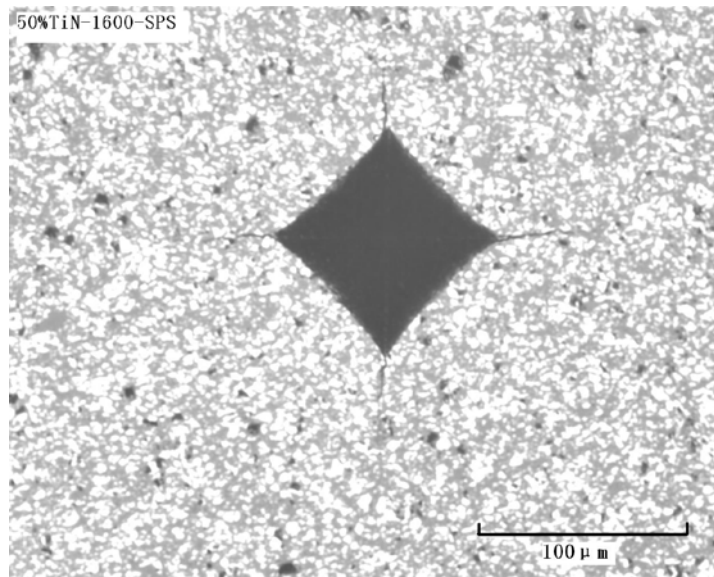
(b)

Figure 4.12 SEM micrographs of Vickers indentation on (a) monolithic Si_3N_4 and (b) 50%Si_3N_4-50%TiN composite

4.7 Discussion

Understanding the effect of the pulsed current in the SPS process is important for controlling the densification, resultant microstructure and properties of sintered products. However, the effect of the current through the samples of conductive materials has not been well understood possibly because of the difficulty on direct measurement of the current. In this chapter, the effect of current has been studied indirectly by comparing the densification, phase transformation, microstructures and mechanical properties of nonconductive monolithic Si_3N_4, semi-conductive and conductive Si_3N_4/TiN composites sintered by HP and SPS.

The densification and the α-β phase transformation of α-Si_3N_4 are closely related during the sintering because the α-β phase transformation can improve the densification of Si_3N_4. In the HP sintering, the densification and the α-β transformation of Si_3N_4 are suppressed by the presence of TiN. This arises because the TiN grains on the grain boundary of Si_3N_4 suppress the grain growth and elongation of β-Si_3N_4, and consequently the α-β transformation and densification of α-Si_3N_4, due to its pinning effect[172]. In the SPS sintering, on the other hand, the densification (relative density) and the α-β transformation of Si_3N_4 are improved by the addition of the electrically conductive phase, TiN, especially for the Si_3N_4/TiN composite with 50 wt% of TiN (0% porosity), which is almost as conductive as graphite. The studies on the porosities, grain sizes and aspect ratios of monolithic Si_3N_4 and conductive Si_3N_4/TiN composites also come to the same conclusion. To separate the chemical effect of the varying amounts of TiN in the materials from the electric current effect on the conductive specimens, insulated monolithic Si_3N_4 and conductive Si_3N_4/TiN composites were sintered by both hot pressing and SPS respectively. The results show that the current effect is the main reason that makes the improvement for the relative density and the α-β transformation of Si_3N_4. On top of that, In addition, TiN itself may also promote the α to β transformation and densification of Si_3N_4.

In addition, the shrinkage of the conductive Si_3N_4/TiN specimen took place at the temperature about 120°C lower than that of the nonconductive Si_3N_4 in the SPS sintering. This indicates that the actual temperature of the conductive Si_3N_4/TiN sample is higher than the nonconductive Si_3N_4 ceramic in the SPS sintering. The intrinsic reason for this difference is that the large pulse current passing through the conductive materials during the SPS sintering generates a large amount of heat due to the Joule heating effect so that the temperature of the sample can be higher than that measured on the surface of the die. This is known as the overshooting effect, which is a very important behavior during the SPS process. Previous studies have also presented some evidence to support this overshooting effect[35,36,43,59,170]. The understanding of this effect is quite important for our studies in the following chapters, where different ultra-high temperature ceramics (UHTCs) and composites are prepared with the SPS technique. Most of these UHTC materials are in fact electrically conductive.

4.8 Summary

The introduction of TiN into Si_3N_4 increases the electrical conductivity of the composite materials and leads to the passing through of electrical current from the sample as well as the graphite die during the SPS process. The sample is then heated intrinsically by the joule heating effect of the current besides being heated extrinsically by the graphite die, and consequently affects their sintering behavior, microstructure and mechanical properties. In the HP sintering, the densification and the α-β transformation of Si_3N_4 are suppressed by the presence of TiN because the TiN grains hinder the elongation of β-Si_3N_4 and consequently the α-β transformation and densification of α-Si_3N_4 due to its pinning effect on the Si_3N_4 grain boundaries. However, in the SPS process, the densification and the α-β transformation of the Si_3N_4/TiN composites are significantly improved by the passage of a large pulse current through the samples. From the microstructural analysis, the grain aspect ratio in the Si_3N_4/TiN composites is less than that in the monolithic Si_3N_4, both for HP and SPS sintered samples because the presence

of TiN suppresses the elongation of the β-Si$_3$N$_4$ grains. The porosity of Si$_3$N$_4$/TiN composites is higher than that of monolithic Si$_3$N$_4$ in HP sintered samples, but in the SPS sintered samples, the result is the reverse. This is consistent with the results of the measured relative density dada. The results of the mechanical property tests show that the introduction of TiN increases the fracture toughness without causing a decrease to the hardness of the Si$_3$N$_4$. Although TiN suppresses the formation of elongated β-Si$_3$N$_4$ grains, the Si$_3$N$_4$/TiN composites sintered by SPS, compared with that by HP, still experience improved fracture toughness and hardness with improved densification. This study shows that increasing the DC current that is passing through a conductive ceramic sample is a possible means of improving the sintering efficiency of the SPS process.

Chapter 5 Sol-Gel Processing of Nano Carbide Ceramic Composites

TiC ceramics have been widely used in cutting tools, machining materials and nuclear power industry because of its high melting temperature (3260 ∘C), high chemical and thermal stability and good corrosion resistance. However, the modest fracture toughness and low oxidation resistance of TiC ceramics limit their use under severe conditions and thus it is usually used as a second dispersive phase to improve the mechanical properties and oxidation resistance of TiC based ceramic composite materials[145,173,174]. SiC has very high hardness and wear resistance, excellent corrosion, thermal shock and oxidation resistance and good high temperature strength, which allow the use of SiC for numerous structural and wear applications, e.g. heat exchanger, metal working parts and nozzles. Especially SiC is usually used as a second phase to improve the oxidation resistance of other ceramic matrices, because SiC-based ceramics are oxidation resistant up to ~1600 °C, due to the formation of a protective SiO_2 surface film[175,176]. Compared with other UHTCs such as ZrC and HfC, SiC has the lowest theoretical density so that it can help to make the composites lighter, which would be an advantage for some applications like aerospace in which the weight of parts is an important factor in the design.

TiC/SiC composites are usually prepared through mixing nano or micron-sized TiC and SiC powders. However, difficulties in dispersing of nano-sized powders lead to sintered composites with non-uniform microstructures[8]. As a wet-chemical processing method, sol-gel processing is a promising technique to solve this dispersing problem, due to its distinct advantage of solution mixing at a molecular level to make ceramic composites with homogenous compositions and nano microstructures. As such some research has been carried out on the synthesis of nano-sized TiC/SiC powder and fibre by sol-gel processing[132,135,177]; but to the best of our knowledge, no research has been reported on the direct fabrication of bulk TiC/SiC nanocomposites, from sol-gel processing. From the study of this chapter, bulk TiC/SiC composites with uniform nanostructures are

fabricated directly by sol-gel processing and spark plasma sintering. The effects of the carbon/metal ratio in the sol-gel process, residual carbon, firing temperatures and Si/Ti mole ratio on the phases and microstructures of the TiC/SiC composites after carbothermal reduction, densification and microstrcutures of the sintered TiC/SiC composites are studied. As well as the solution casting method studied in this chapter, solution infiltration and surface coating techniques will be investigated in the next two chapters to evaluate the charateristics of the sol-gel processing for UHTC composites.

5.1 Experimental procedure

For the work in this chapter, mesoporous TiC/SiC composites with uniform nanostructure were first prepared by sol-gel processing followed by sintering via SPS to get dense TiC/SiC nanocomposites. The chemicals used are detailed in Table 3.2. The commonly used titanium tetraisopropoxide (TTIP, Ti(OCH(CH$_3$)$_2$)$_4$) and tetraethyl orthosilicate (TEOS, Si(OC$_2$H$_5$)$_4$) were employed as titania and silica precursors respectively. The molar percentage of TEOS in total metal precursors in this composite system ranged from 0 to 50 atomic %. Amphiphilic triblock copolymer P123 was used as a surfactant with a molar ratio of 0.2 to the metal precursors. Furfuryl alcohol (FA) was chosen as the carbon source. To study the effect of carbon content on the microstructures of TiC/SiC composites, the molar ratio of carbon to metal precursors was designed to range from 3.5 to 5 (FA molar ratio from 0.7 to 1). Carbonization, to remove organic components, and carbothermal reduction, to produce carbides, were carried at 550°C and 1450 °C respectively. The TiC/SiC nano-powders formed 1450°C were ground and sieved, before being sintered by SPS. The sol-gel process, sintering behavior and microstructures of TiC/SiC nano-composites have been studied.

Sol–gel processes were carried out as follows (Figure 5.1). P123 was first dissolved in absolute ethanol to form a solution under continuous stirring. Then TTIP was added. Separately, TEOS was mixed with hydrochloric acid (HCl, 10 M) at a molar ratio of 0.5 to

the metal precursors. Here ethanol was used as the solvent and the solution underwent vigorous magnetic stirring for 15 min. The solution containing TTIP and surfactant was then added into the silica precursor solution under vigorous stirring. After 30 min, FA was added into the TTIP and TEOS mixtures under stirring. The solution turned brown immediately after the addition of FA, indicating the start of FA polymerization. The color of the sol became dark brown after continuous stirring for 6 h. The solution was then aged for 3 days at 25°C, with its color becoming very dark at the end. The aged solution was lastly poured into a petri dish and dried in an oven at 80°C to form a gel. The as-synthesized gel was put in an alumina boat and inserted into a quartz tube to be heat treated. The conditions employed were as follows; 550°C at 5°C/min under nitrogen atmosphere and kept for 5h at 550°C. The heating and cooling rate were 5°C/min. The aim of the heat treatments was to decompose the organic components and obtain Ti–Si–O–C composites. The Ti–Si–O–C composites were then heat treated at 1450°C in an alumina tube under argon for 5h; aiming to fully reduce the TiC/SiC composites. The heating and cooling rate were 2°C/min.
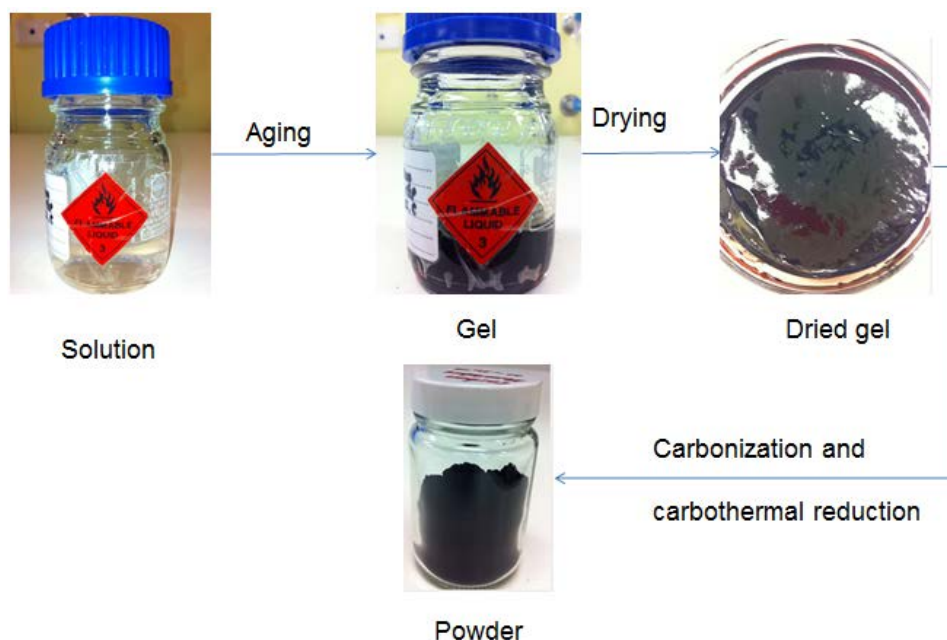
Figure 5.1 Sol-gel process for synthesizing of TiC/SiC composites

The porous TiC/SiC composites were ground into powder and sieved before SPS sintering for densification. Approximately 1 g of TiC/SiC powder was packed into a 10 mm graphite die. The weight of the powder was calculated based on the mole percentages and theoretical densities of TiC and SiC to make sure that the thickness of the sintered samples was about 5 mm. The green powder was separated from the die body by a 0.2 mm thick graphite sheets lined between them. The graphite die was covered with a heat insulating carbon fibre mat to avoid heat radiation loss from the external surface of the die. First the SPS furnace chamber was evacuated to a pressure less than 6 Pa, then the sample was heated to 600 °C in 4 min and then heated to the sintering temperature (1500-1800 °C) at 100 °C /min, where it was held for 5 min under a uniaxial pressure of 40 MPa. The sample was allowed to cool naturally in the die and the initial cooling rate was about 200 °C /min above 1000°C.

5.2 Effect of Si/Ti ratio on the phases and microstructures of the Ti-Si-C-O precursor and TiC/SiC composites

5.2.1 XRD analysis of the phases of Ti-Si-O-C precursors and TiC/SiC composites

Different Si/Ti molar ratios (0:100, 10:90, 30:70 and 50:50), were designed to study the effect of Si/Ti ratio on the phases and microstructures of the Ti-Si-O-C composites. The study of the composites was undertaken after carbonization and carbothermal reduction respectively. The XRD spectra of the Ti-Si-O-C composites, with different Si/Ti molar ratios, after carbonization at 550°C, are shown in Figure 5.2. The results show that TiO_2 (the anatase phase) is the single crystal phase in all the Ti-Si-O-C composites. The grain size of TiO_2 is about 3~5 nm, calculated from Scherrer formula[178]. The intensity of the XRD peaks of TiO_2, which represents the degree of crystallinity, decreases with the increase in the concentration of Si. This means the existence of amorphous SiO_2 suppresses the crystallization of TiO_2.

The XRD spectra of the TiC/SiC composites, after carbothermal reduction at 1450°C, are shown in Figure 5.3. The results indicate that only titanium carbide and silicon carbide exist in all TiC/SiC composites. No oxides are detected in the composites, which means that the titanium oxide and silicon oxide have been completely reduced and reacted with carbon to form titanium carbide and silicon carbide at this carbothermal reduction temperature. The silicon carbide phase (β-SiC) can only be detected in the TiC/SiC composites with a high SiC content (e.g. 50 at% SiC and 30 at% SiC), but can't be seen by the XRD with the low SiC content (10 at%SiC) composite after the carbothermal reduction process. This is not to say SiC does not exist in this composite, but rather due to the high degree of overlap between TiC and SiC XRD peaks, and the relatively low intensity of SiC peaks compared with the TiC ones, the SiC peaks are hidden at low concentrations. There is a line shift of peaks at 35 degrees (2 theta), which may indicate solid solution of SiC in TiC.
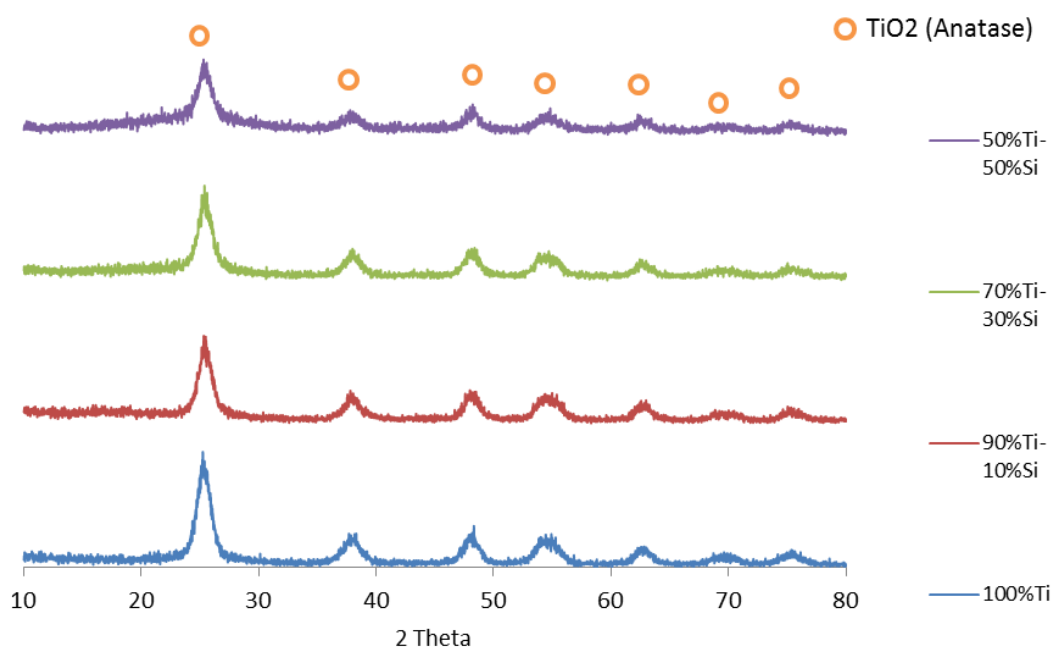
Figure 5.2 XRD spectra of the Ti-Si-O-C precursors after carbonization at 550°C
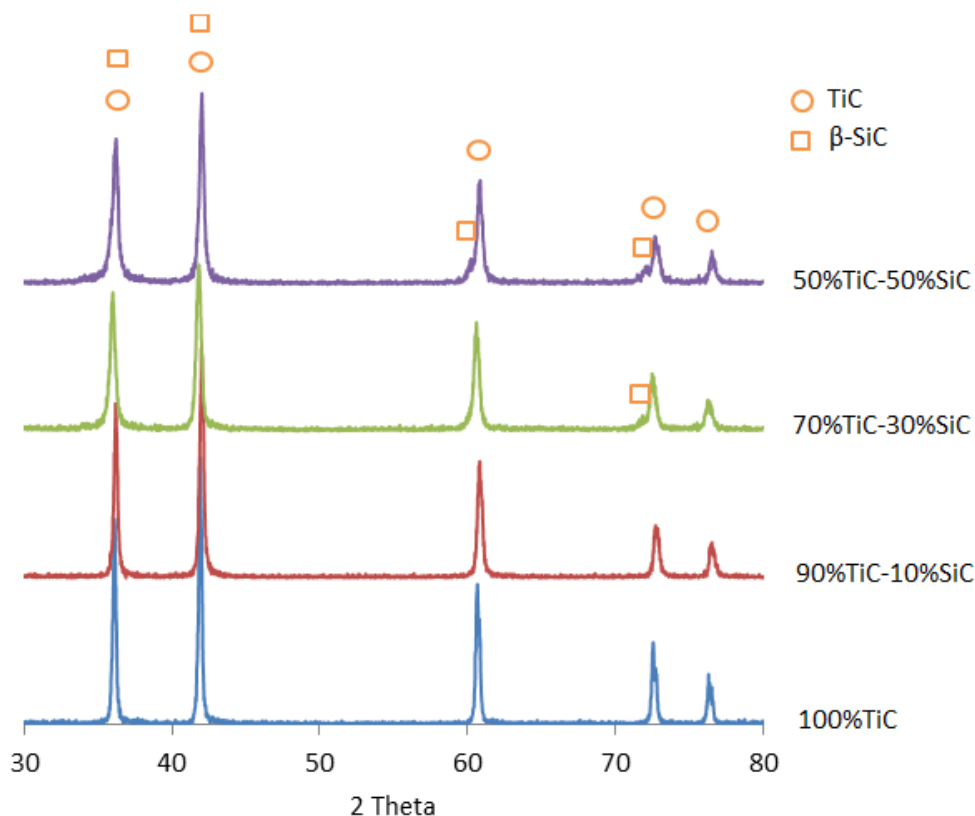
Figure 5.3 XRD spectra of TiC/SiC composites after carbothermal reduction at 1450°C

5.2.2 Microstructures of the Ti-Si-O-C composites and TiC/SiC composites

The SEM micrographs of the Ti-Si-O-C composites are shown in Figure 5.4. The microstructures of the Ti-Si-O-C composites with different Si/Ti molar ratios after carbonization at 550°C are similar. The size of the anatase nanocrystal is about 3~5 nm. The SEM micrographs of the TiC and TiC/SiC composites with different Si/Ti molar ratios, after carbothermal reduction at 1450°C, are shown in Figure 5.5. The microstructures show that the grain size of monolithic TiC is about 100~500 nm (Figure 5.5a), which is about 10 times that of the 50 at% TiC - 50 at% SiC composite (less than 50 nm) (Figure 5.5d). The grain size of the TiC decreases obviously with the increase of SiC content (from a few hundred nanometres in Figure 5.5a to less than 50 nanometres in Figure 5.5d), this indicates that the presence of SiC hinders the grain growth of TiC particles

due to the large Zenner pinning effect of nano SiC particles. Some grains bonded together can also be seen in the monolithic TiC after carbothermal reduction (Figure 5.5a), which means some sintering of TiC has commenced at 1450°C. However, there is no bonding between TiC grains in the TiC/SiC composites (Figure 5.5b, 5.5c and 5.5d). This also indicates that the introduction of SiC can hinder the grain growth of TiC.
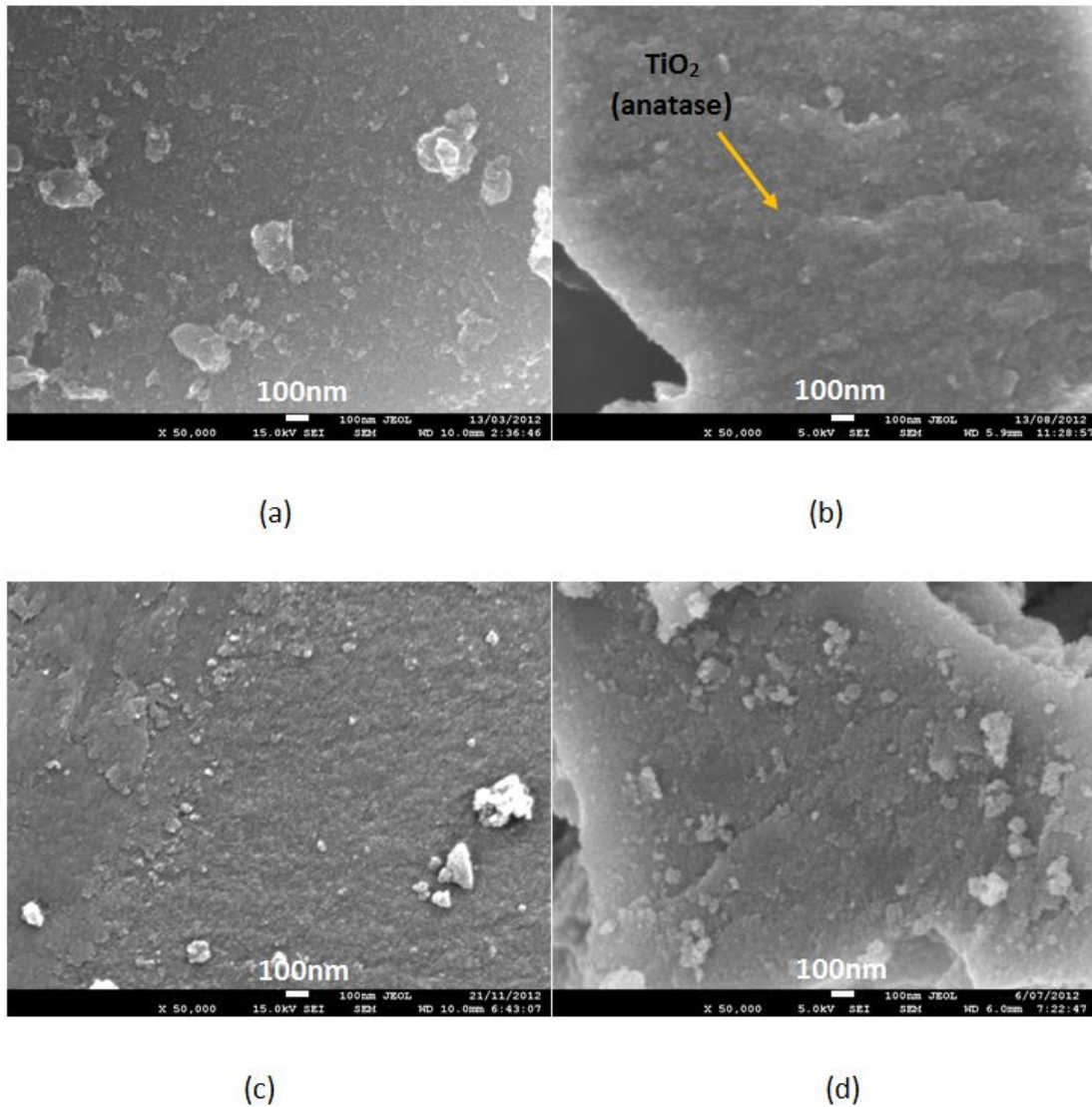
Figure 5.4 SEM micrographs of the Ti-Si-O-C composites with different Si/Ti molar ratios after carbonization at 550°C (a) 100%Ti (b) 90 at%Ti-10 at%Si (c) 70 at%Ti-30 at%Si (d) 50 at%Ti-50 at%Si
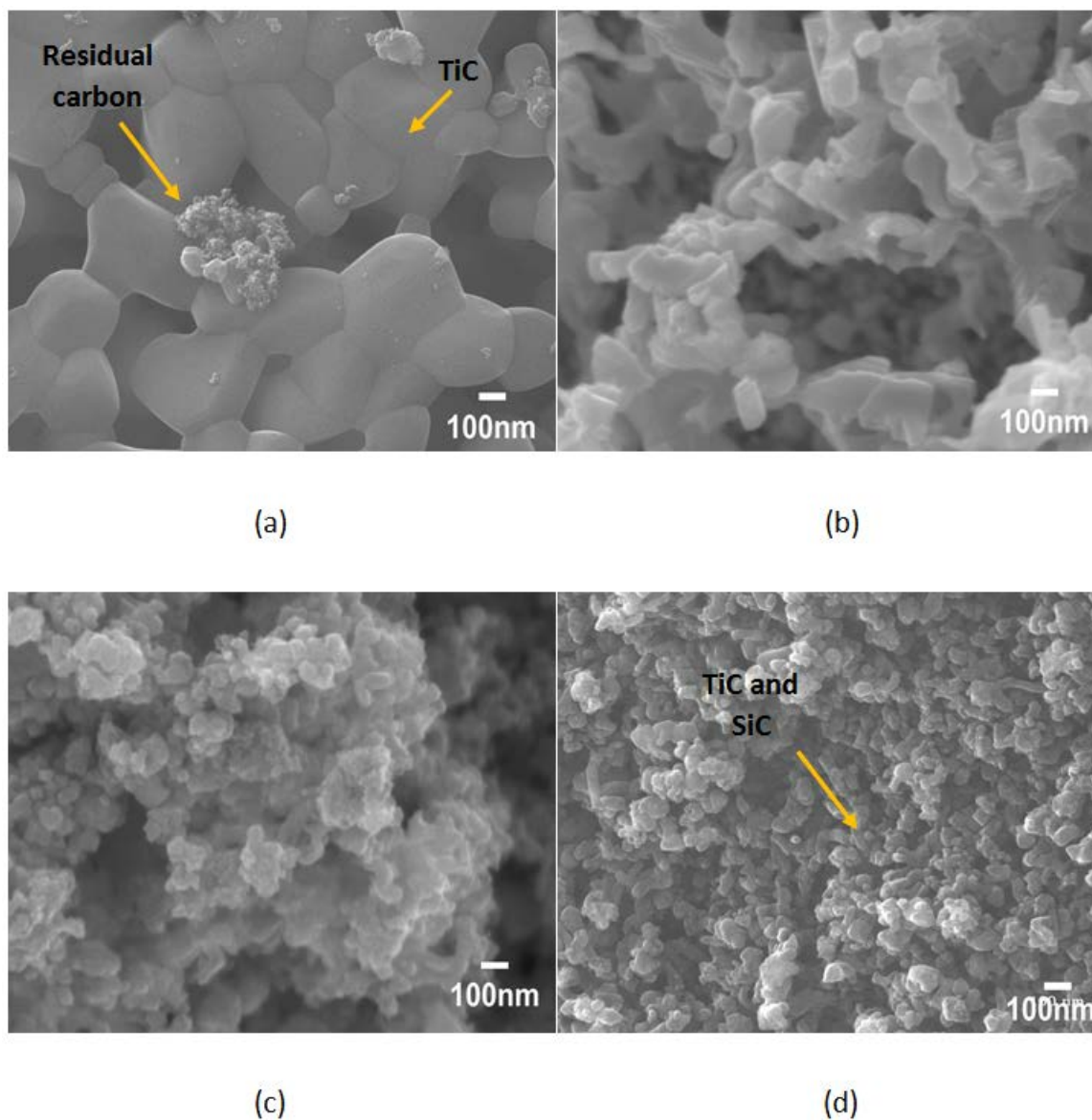
Figure 5.5 SEM micrographs of the TiC and TiC/SiC composites with different Si/Ti molar ratios after carbothermal reduction at 1450°C (a) 100%TiC (b) 90 at%TiC-10 at%SiC (c) 70 at%TiC-30 at%SiC (d) 50 at%TiC-50 at%SiC

5.3 Effect of carbon/metal ratio on the microstructure of TiC/SiC composites

5.3.1 Effect of carbon/metal ratio on the residual carbon of TiC/SiC composites

To achieve the desired TiC/SiC composites using the sol-gel processing technique, controlling the amount of residual carbon in the composite is important, because the residual carbon in the final composite may retard the densification of the composite.

To achieve the desired TiC/SiC composite, first the TiO_2-SiO_2-C composite is heated in an inert atmosphere. In this elevated temperature environment, the following carbothermal reduction reactions could take place, from a thermodynamic point of view:

$$TiO_2(s)+3C(s)\rightarrow TiC(s)+2CO(g) \tag{5-1}$$

$$SiO_2(s)+3C(s)\rightarrow SiC(s)+2CO(g) \tag{5-2}$$
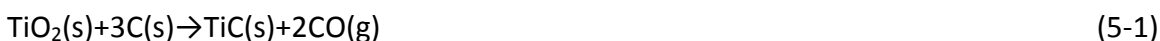
The temperatures for the reactions 5-1 and 5-2 to take place are 1567K and 1781K respectively according to the free energy calculation of the two reactions[179]. The minimum theoretical carbon to metal molar ratio (C/M ratio) required is 3 for the completion of the above carbothermal reactions. However, the actual carbon/metal ratio in the initial mixture of reactants should be higher than 3, due to the loss of carbon during the sol-gel and heat treatment processes. To determine the optimal C/M ratio and study its effect on the microstructure of TiC/SiC composite, C/M ratios of 3.5, 3.6, 4 and 5 were used in the sol-gel compositions respectively.
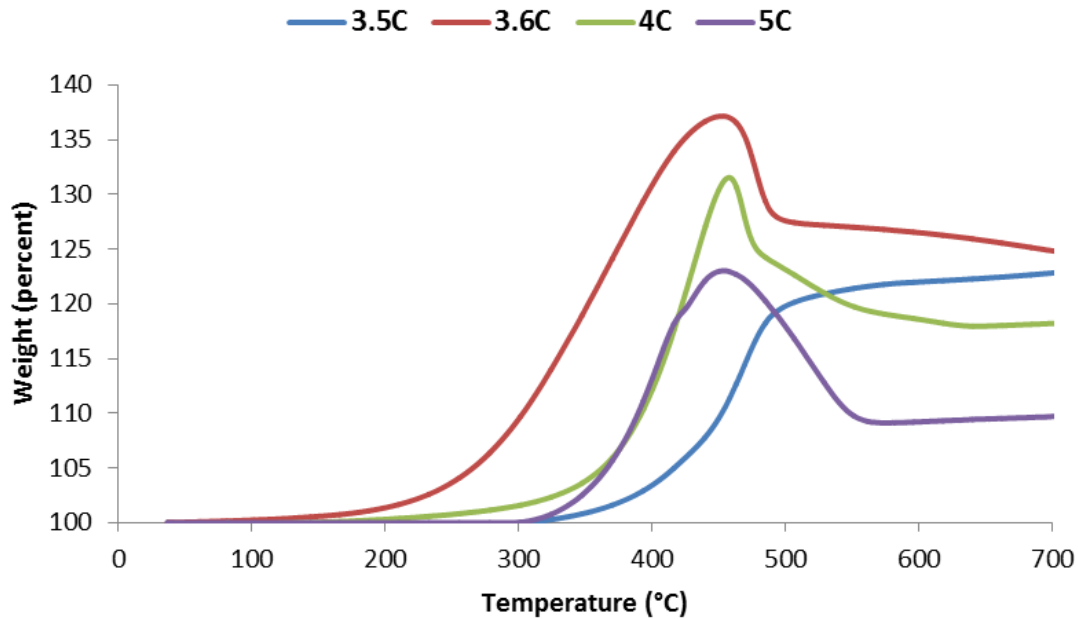
Figure 5.6 Thermogravimetric analyses of the TiC ceramics with different carbon ratios

To simplify the process, thermogravimetric analysis was done on the monolithic TiC ceramics which were prepared through the same sol-gel process as TiC/SiC composites except removing TEOS, with different C/M ratios. The TGA results of the TiC prepared with different starting carbon ratios, ranging from 3.5 to 5, are shown in Figure 5.6. The total weight changes on the TGA curve in Figure 5.6 are contributed by two reactions. One is due to the oxidation of TiC which will gain weight, while the other is caused by the oxidation of the free carbon which will loss weight. We can assume that the free carbon in the TiC-C composites have been fully oxidized at 700 ^{o}C because there is very little change of weight at temperatures higher than 600 ^{o}C from the TGA curve. So we can calculate the approximate amount of residual carbon in the composites according to the weight change of the composites at 700 ^{o}C. The amount of residual carbon in the composites with 4C and 5C are 0.45C and 1.05C respectively according to the calculation with the TGA data.

A weight gain corresponding to the oxidation of TiC (TiC+3/2O$_2$→TiO$_2$+CO) appears in the TGA curves above 300 ^{o}C, which can be seen in Figure 5.6. Then a weight loss associated with the oxidation of residual carbon was recorded for all TiC samples that contained carbon ratios ≥3.6, this can be seen above 400 ^{o}C. This is a clear indication of the presence of free carbon in the TiC samples with a carbon ratio equal to 3.6 and above. The weight gain of the TiC sample with 3.5C is only about 24 percent and the weight gain for complete oxidation of TiC without free carbon should be 33 percent according to the change of molecular weight from TiC to TiO$_2$, which are about 60 and 80 respectively. This means that this TiC sample includes some TiO$_2$ and the 3.5C is not sufficient for the completion of the reduction of TiO$_2$.Therefore, the optimum value for the starting C/M ratio for the TiC/SiC composites should be 3.6. This ratio will allow for complete carbothermal reduction of the oxides, while leaving the minimum amount of residual carbon in the TiC/SiC composite.

5.3.2 Effect of carbon/metal ratio on the microstructure of TiC/SiC composites before sintering

The microstructures of TiC/SiC composites with different starting C/M ratios are shown in Figure 5.7. The results show that there is a little difference in the microstructures of TiC/SiC composites with different starting C/M ratios. The grain size of the samples decreases in some degree, with the increase of C/M ratio. This means that the presence of residual carbon, suppresses the grain growth, of TiC/SiC composites. For the sample with C/M ratio=3.5, some unreacted oxides can still can be found, due to the insufficient carbon in the composite for complete carbothermal reduction (Figure 5.7a). This is also consistent with the TGA result showed in the last section. There are no oxides left in the composites according to the XRD after carbothermal reaction at 1450°C for 5 hours (Figure 5.3).
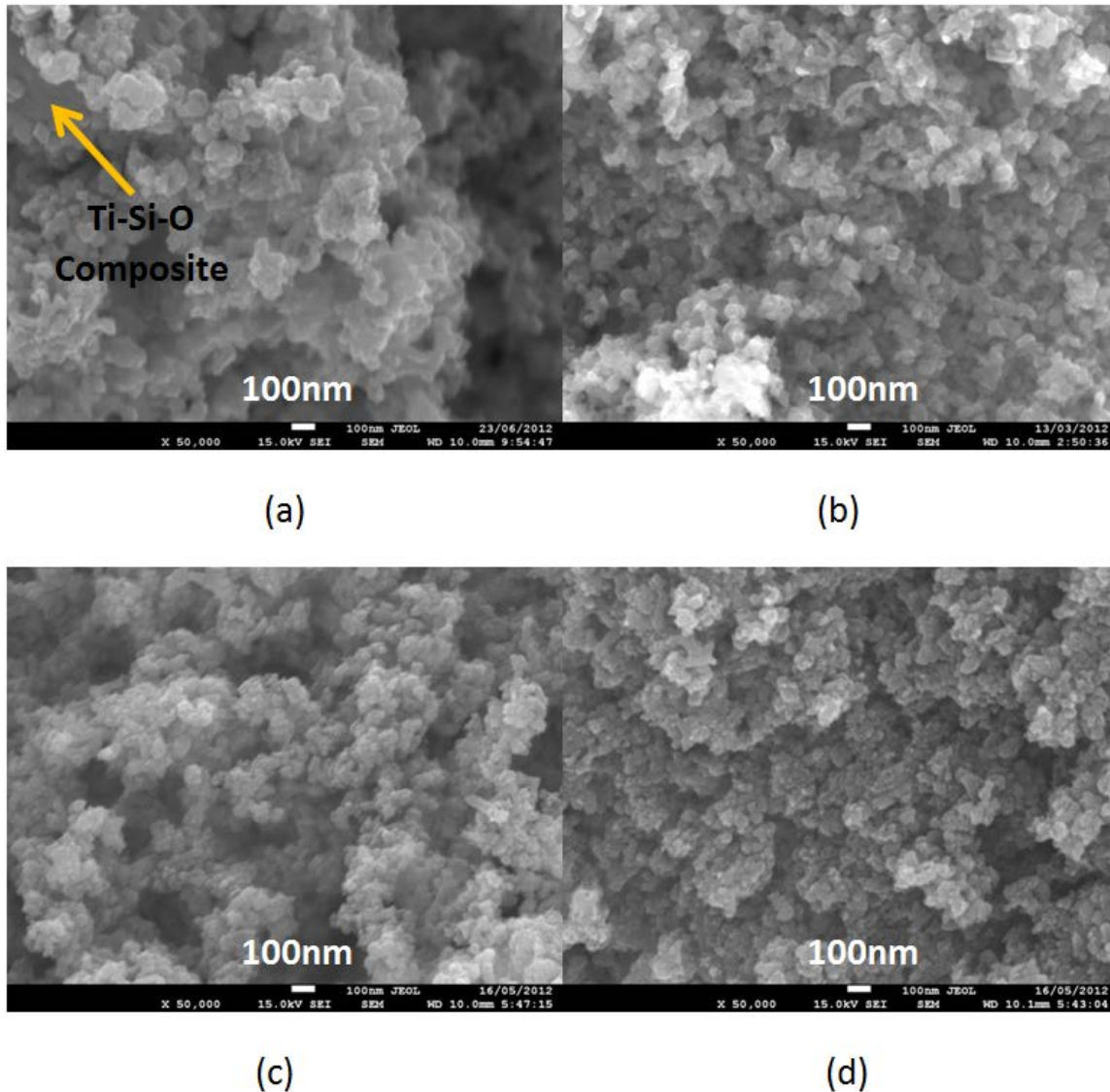
Figure 5.7 Microstructures of TiC/SiC composites with different carbon/metal ratios after carbothermal reduction at 1450°C (a) C/M=3.5 (b) C/M=3.6 (c) C/M=4 (d) C/M=5

5.3.3 Effect of carbon/metal ratio on the microstructures of SPSed TiC/SiC composites

To study the effect of the carbon/metal (C/M) ratio on the micrstructures of sintered TiC/SiC composites, 70 at%TiC-30 at%SiC composites were prepared with different C/M molar ratios. These composites were then sintered by SPS at 1700°C for 5 minutes,

under a uniaxial pressure of 40 MPa. The SEM micrographs of the composites are shown in Figure 5.8. The results show that the sample with C/M ratio of 3.5 has very few pores. This means that the TiC/SiC composite can be almost fully densified at 1700°C by SPS. Some white flake-shaped residual carbon can be found in the TiC/SiC composites with C/M=4 and 5 (Figure 5.8b and 5.8c) because carbon is conductive and will be brighter in a dielectric matrix under the electronic beam[180]. EDS analysis also shows that the white flakes are carbon because there is a relatively strong carbon peak (Figure 5.8d). This is also consistent with the TGA analysis (Figure 5.6). It can also be found that the porosity of the TiC/SiC composite increases with increasing the C/M molar ratio, especially the sample with a C/M ratio of 5. This sample in particular has much higher porosity than the other two samples presented here. This means that high C/M ratios, which resulted in more residual carbon in the composite after carbothermal reduction reaction, hinders the densification of TiC/SiC composites because residual carbon on the grain boundaries retards the surface diffusion of TiC and SiC grains. However, the grain size of TiC/SiC composites with different C/M ratios does not change much. This indicates that the C/M ratio does not have an obvious effect on the grain growth of sintered TiC/SiC composites.
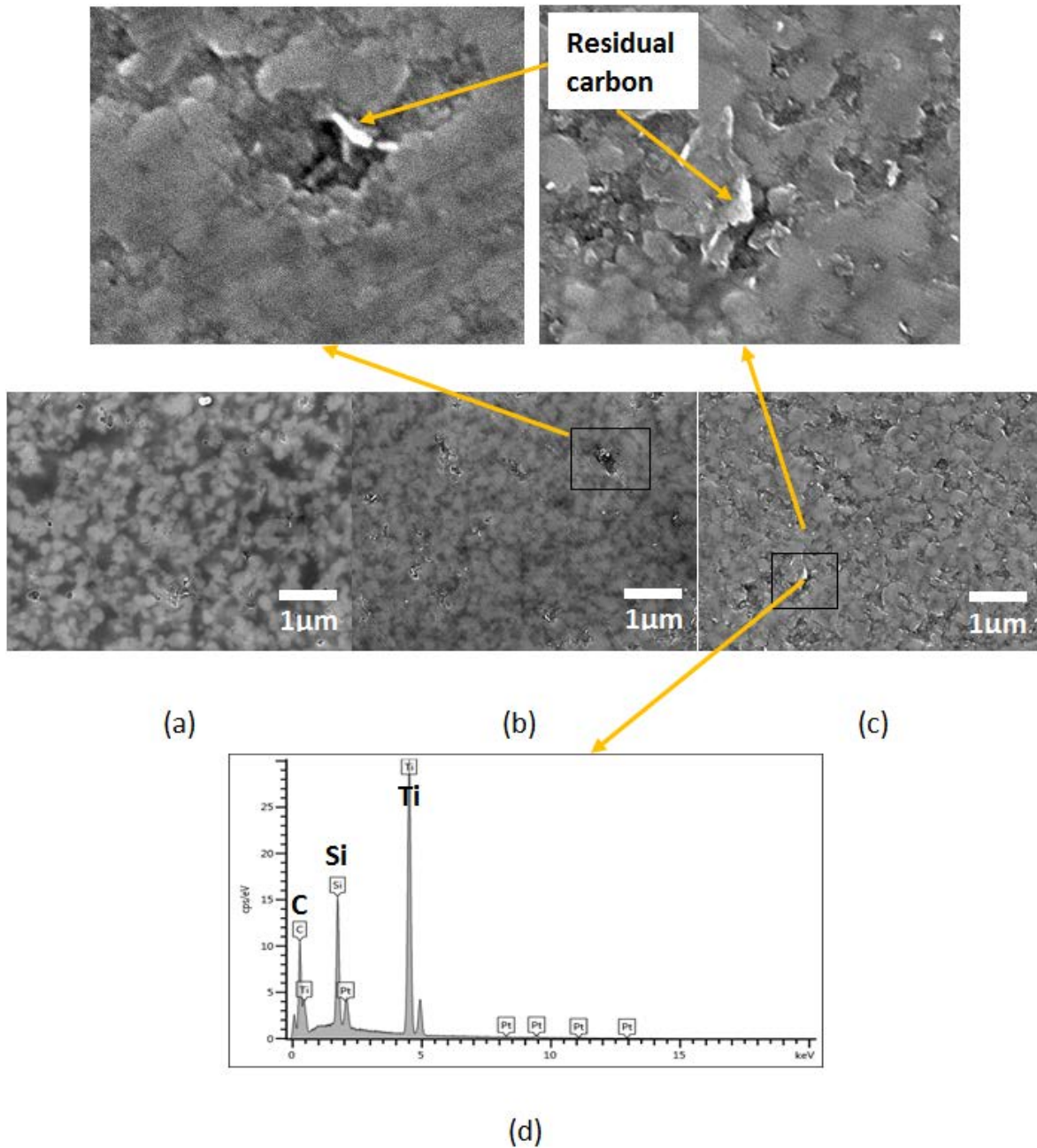
Figure 5.8 Microstructures of 70%TiC-30%SiC composites prepared using precursors with different carbon/metal ratios SPSed at 1700°C (a) C/M=3.5 (b) C/M=4 (c) C/M=5 (d) EDX result at the spot in (c)

5.4 Effect of the sintering temperature on the microstructures of SPSed TiC/SiC composites

5.4.1 Microstructures of the monolithic TiC

To study the effect of sintering temperature on the microstructures of TiC/SiC composites, monolithic TiC and 50%TiC-50%SiC composite samples were sintered by SPS at temperatures ranging from 1500°C to 1800°C for 5 min in vacuum under a uniaxial pressure of 40MPa respectively. The heating rate was 100 °C/min. The microstructures of the SPSed monolithic TiC are shown in Figure 5.9. To see clearly the grain boundaries, low magnification micrographs were used for the two TiC samples SPSed at 1700 and 1800°C due to their very large grain size of TiC. We can find that the grain growth of monolithic TiC is very significant with the increase of sintering temperature (from about 700 nm at 1500 °C to larger than 10 μm at 1800 °C), especially at the temperatures of 1700 °C and above (Figure 5.9c and 5.9d). The monolithic TiC is not fully densified and still has some pores even at 1800 °C (Figure 5.9d). This is because some excess carbon comes from PFA may exist in the sample during the sol-gel process.
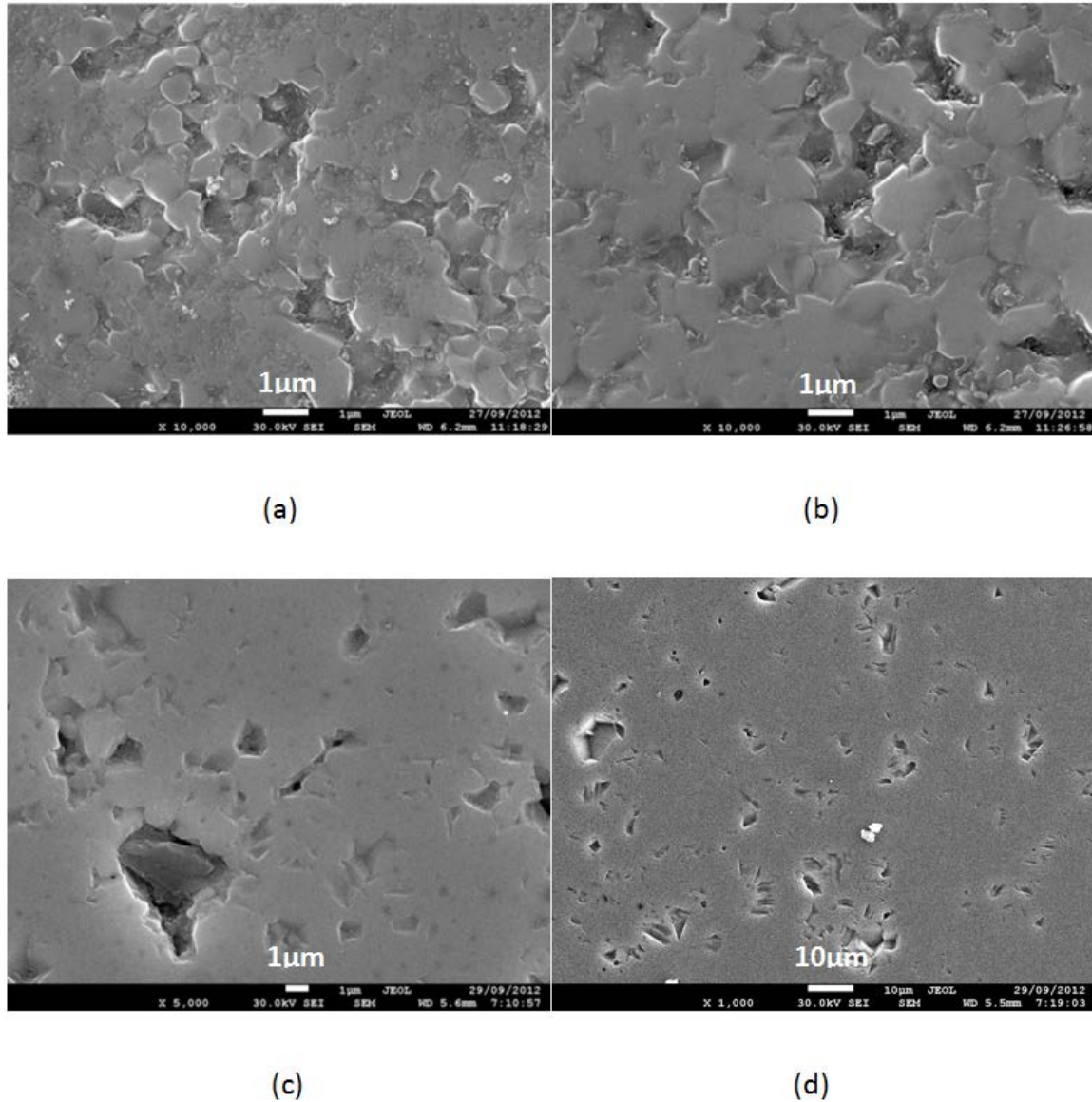
Figure 5.9 SEM micrographs of monolithic TiC SPSed at (a) 1500 °C (b) 1600 °C (c) 1700 °C (d) 1800 °C

5.4.2 Microstructures of the TiC/SiC composites

The microstructures of the SPSed TiC/SiC composites are shown in Figure 5.10. The light grains are TiC, and the dark ones are SiC. This is because the atomic weight of titanium is heavier than silicon and the larger the atomic weight the stronger the electron repulsion. Compared with monolithic TiC, the TiC/SiC composites are fully densified at

1700°C and above, with a uniform nano structure (Figure 5.10c and 5.10d). Grain size of the TiC/SiC composites doesn't grow as much as monolithic TiC, with increasing sintering temperature. The grain sizes of TiC/SiC composites for both the TiC and SiC phases are about 200 nm, even after being sintered at 1800 °C (Figure 5.10d). This figure is much finer than that of monolithic TiC ceramics, which has grain sizes larger than 10 μm (Figure 5.9d). These results show that the presence of SiC not only improves the densification of TiC due to the formation of a solid solution of TiC and SiC[143] and the nano size of the particles, but also significantly hinders the grain growth of TiC because of the great pinning effect of SiC grains on the grain boundaries of TiC. In the commonly used nano-powder mixing approach[147], relative densities achieved for TiC/SiC composites SPSed at 1800°C are around 95%, with TiC grain sizes ranging from 270nm to 700nm and SiC content varying between 10% and 50%. This sol-gel processing approach has, however, demonstrated its unique advantages, achieving a much smaller grain size, higher final density, and more uniform microstructures for the fabrication of the ceramic composites at the same sintering condition.
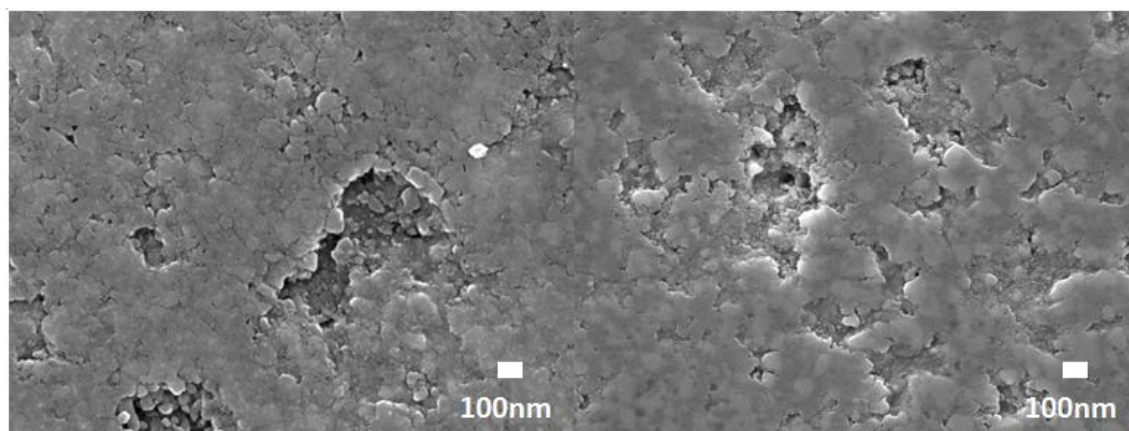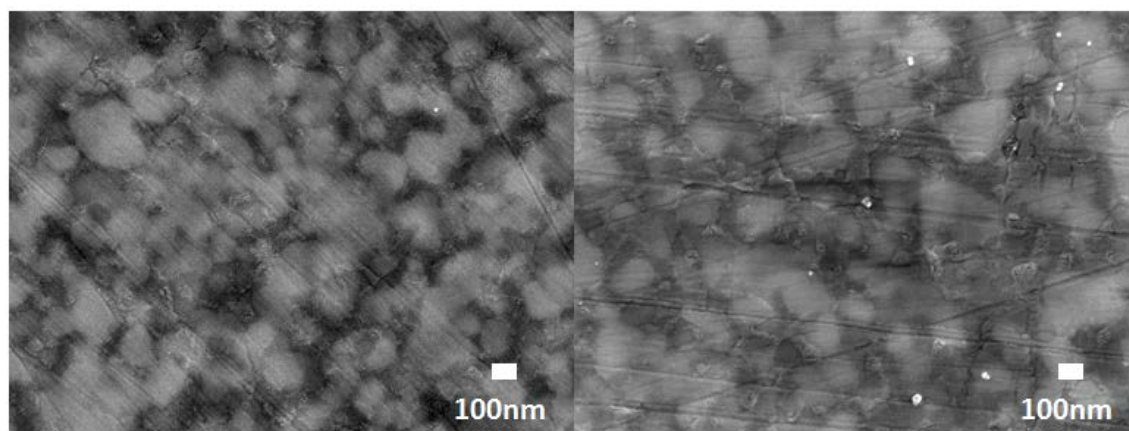
Figure 5.10 SEM micrographs of 50%TiC-50%SiC composites SPSed at (a) 1500 °C (b) 1600 °C (c) 1700 °C (d) 1800 °C

5.5 Effect of the concentration of SiC on the densification and microstructure of the TiC/SiC composites after SPS

5.5.1 Effect of the concentration of SiC on the densification of the TiC/SiC composites during SPS

To study the effect of the SiC content on the densification of the TiC/SiC composites, four samples with different concentrations of SiC ranging from 0 to 50 at% were sintered via SPS at 1700 °C for 5 min. The shrinkage curves of these samples are shown in Figure 5.11. The temperature at which the shrinkage due to sintering exceeds the thermal expansion of the graphite die assembly can be identified for each composition from the lowest point on the displacement curve (refer to the arrows in Figure 5.11). The displacement here means the distance of the movement of the graphite plungers during the SPS process from its initial position before sintering. A bigger displacement means a greater shrinkage of the sample during the sintering process. The results in Figure 5.11 show that the shrinkage happens at about 1280 °C for monolithic TiC sample and at about 1180 °C for the composite with 10 at% SiC. For the composites with 30 at% SiC and 50 at% SiC, the start of shrinkage begins at about 1120 °C and 1140 °C respectively. It should be noted that the dimensional changes of the samples are not directly comparable due to the differences in the amount of the raw powder used in sample preparations. However, the amounts of the raw powder for the four sintered samples with different concentrations of SiC were calculated and adjusted based the different theoretical densities of TiC (4.93 g/cm^3) and SiC (3.21 g/cm^3) so that the final thicknesses of the four sintered samples were similar, about 5 mm, which means the dimensions of the four samples after sintering can be compared relatively. From the results in Figure 5.11, we can see that the total shrinkage of the sample at the direction of pressing increases with the increasing SiC content from about 2.7 mm for 100% TiC to about 5.3 mm for 50% TiC-50% SiC. All these results indicate that the densification of the TiC/SiC composites is improved with the increase of SiC content, indicating an

increased diffusion between TiC and SiC grains. The improved atomic diffusion may be caused by the formation of a solid solution between TiC and SiC grains in some degree[143]. The β-SiC has a cubic crystalline form of 3C with a lattice parameter of a = 0.436 nm and TiC is also in a cubic form with a = 0.433 nm. The crystalline form and the lattice parameter of both phases are similar to each other, assisting the formation of a solid solution.
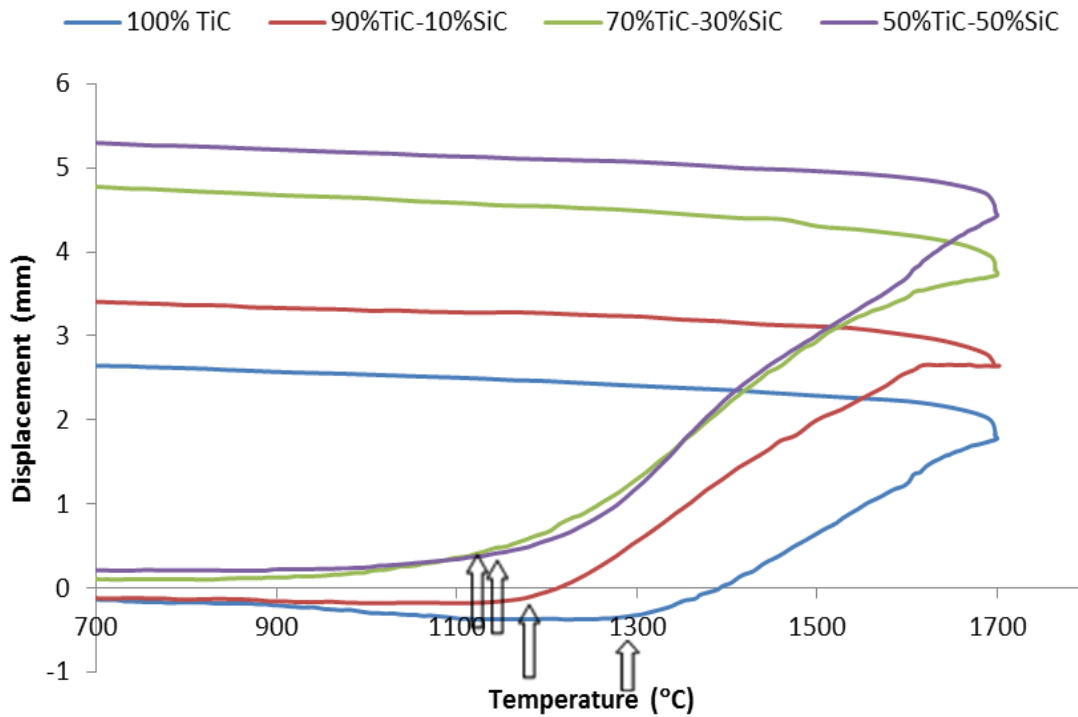
Figure 5.11 Shrinkage curves for TiC/SiC composites SPSed at 1700 °C with different concentrations of SiC

5.5.2 Effect of the concentration of SiC on the microstructures of the TiC/SiC composites after sintering

The microstructures of TiC/SiC composites, with different concentrations of SiC ranging from 0 to 50% (0, 10%, 30% and 50%), sintered by SPS at 1700°C, are shown in Figure 5.12. The light grains are TiC and dark ones are SiC. We can see that the microstructures

of TiC/SiC composites with 30% SiC and above (Figure 5.12c and 5.12d), have uniform nano structures. The results also indicate that the grain size decreases dramatically, from larger than 1 μm in monolithic TiC (Figure 5.12a) to about 150 nm in 50%TiC-50%SiC (Figure 5.12d). The porosity of the TiC/SiC composites also decreases in some degree with the increase of the SiC content. Especially, the pore size of the TiC/SiC composites decreases markedly with the increase of the SiC content. The large pore in the monolithic TiC sample (Figure 5.12a) may not be a real pore, but a hole left after a TiC grain was pulled off during the grinding process due to the low fracture toughness of TiC, as its shape is irregular and its boundary is not smooth. To the extent that the 50%TiC-50%SiC composite is almost fully densified at 1700 °C (Figure 5.12d). All these results further illustrate that the grain growth of TiC is greatly suppressed by the presence of SiC due to its pinning effect on the boundaries of TiC grains. The densification of TiC/SiC composites also experiences improvements with the increase of SiC content because of the diffusion of TiC and SiC grains as stated in the above section. Through this work, dense TiC/SiC composites, with a uniform nanostructure, were prepared successfully by sol-gel processing and SPS at 1700 °C.
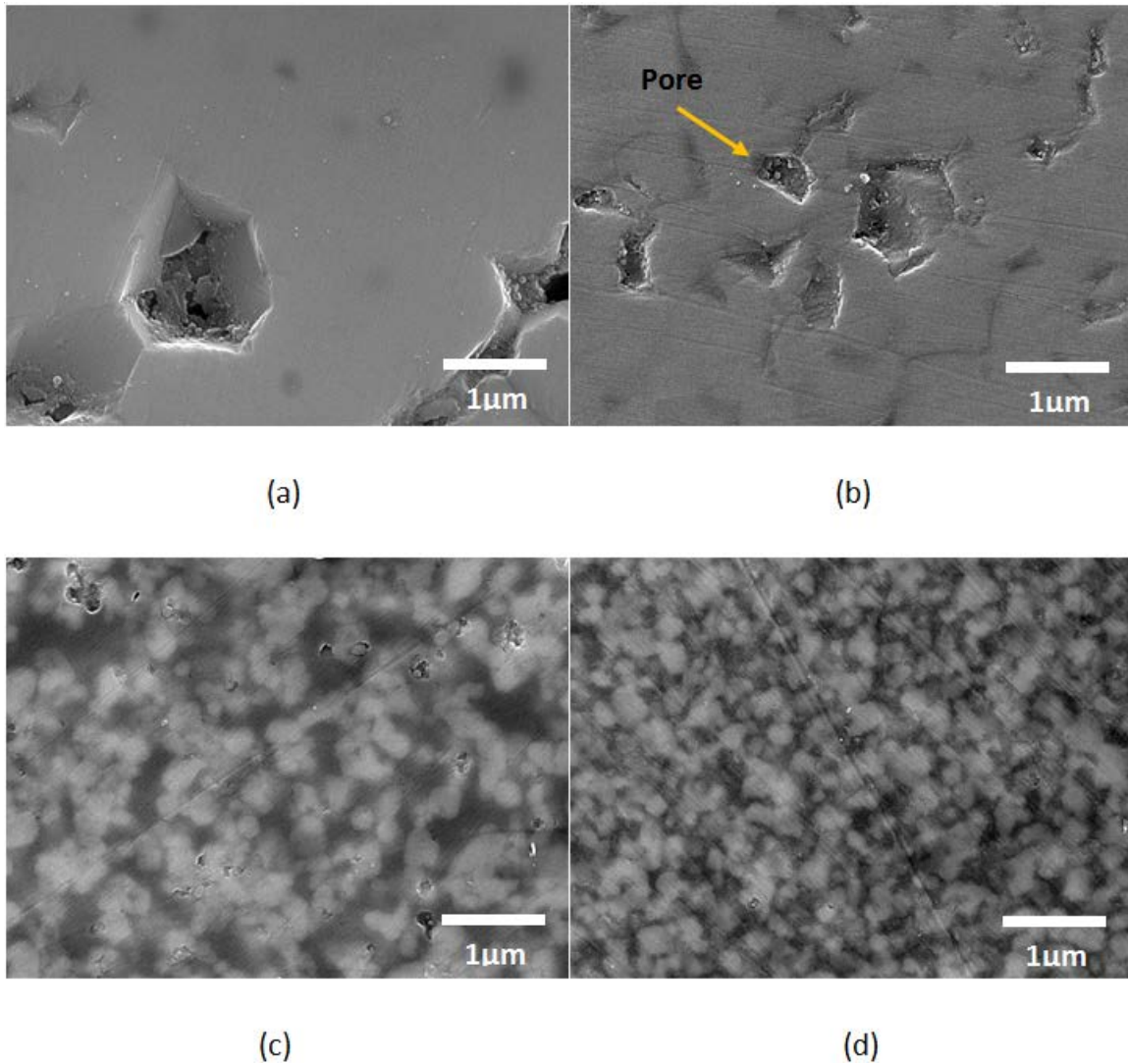
Figure 5.12 SEM micrographs of TiC/SiC composites with different Si/Ti mole ratios SPSed at 1700 °C (a) 100%TiC (b) 90%TiC-10%SiC (c) 70%TiC-30%SiC (d) 50%TiC-50%SiC

5.6 Discussion

5.6.1 Effect of carbon on the densification of TiC/SiC composites

The effect of carbon in the ceramic-carbon composites is quite complex. It can suppress the grain growth, bond grains, improve or hinder (exceeding its certain critical level) the

densification of the ceramics. The critical level of carbon required in the composition depends on what the matrix material is and how much oxygen exists in the matrix.

Nano-sized carbide grains can be bonded into bulk materials by poly(furfuryl alcohol) derived nanocrystalline carbon framework in terms of "bridge," "entanglement," and "adhesive" effects[178]. The bonding of graphitic carbon layers on carbide grains supports the nanostructure and also results in the desired combination of functional and mechanical properties. Carbon (graphite) can also be used as a retarder of recrystallization of ceramics. Graphite introduced into TiC at a concentration of 20 vol.% makes it possible to reduce the average grain size of the matrix by a factor of 2-2.5[181]. The presence of low-modulus graphite inclusions can retard the recrystallization of titanium carbide matrix. It was found that the observed microstructure of the hot-pressed TiC–C hetero-modulus ceramics could be well described by a formula, which was analogous to the classical Zener pinning equation for stable grain size[182]. This means that the retardation of the grain growth of the monolithic carbide ceramics is due to Zener pinning effect of the graphite/carbon.

The changes of apparent density of the sintered materials caused by carbon addition have similar characters. Initially, density increases with carbon content. Exceeding a certain critical level, 4 wt% (weight percentage of carbon in the starting metarial for all the compositions)[183,184], the apparent density decreases because the unreacted residual carbon limits the mass transport mechanisms between ceramic grains during the sintering process. However, below this critical level, carbon can eliminate the oxide impurities and facilitate the sintering process. Thus the apparent density increases with the initial increase in carbon concentration was due to the pore elimination. This is because carbon reduces concentration of oxygen (oxide impurities) at temperatures lower than 1400 °C. Carbon addition below the critical level was also found to lower weight loses on sintering and decrease the size of pores by preventing thermal decomposition of SiC and evolution of gaseous products of chemical reactions[183].

At higher contents of carbon addition, the densification rates decreased rapidly due to increased volume fraction of carbon that acts as a diffusion barrier. Beyond a certain concentration, the excess free carbon does not positively take part in the sintering process, rather it hinders the mass transport processes. According to the calculation based on the TGA results in section 5.3.1 (Figure 5.6), the amounts of residual carbon in the composites with 4C and 5C are 0.45C (14 wt%) and 1.05C (27 wt%) respectively, which are much higher than the generally accepted critical level (4 wt%)[183,184] for carbon addition. The reduction of the density of TiC–SiC-C composites observed with increase of carbon (graphite) content is explained by the effects of several factors, such as the reduction of graphite interlayer spacing during sintering, the diffusion difficulties for metal atoms in the normal direction to the basal planes (0 0 l), and the high value of anisotropy of thermal expansion and compressibility for graphite microcrystals[182]. Difference in electron structure of carbides and graphite cause considerable discrepancy in self-diffusion coefficients of carbon in these phases, which leads to some difficulties in the formation of interphase contact between carbide and carbon in the initial stage, but also in its extension during subsequent stages of sintering[182].

In general, the residual carbon in the carbide-carbon composites can be positively involved in the sintering process and effectively retard the grain growth of the carbide grains if the amount of the carbon is controlled to below a certain critical level. However, excess free carbon does hinder the densification of carbide ceramics because of the reduced mass transport and boundary diffusion mechanisms.

5.6.2 Effect of the SiC on the densification of TiC/SiC composites

Since both TiC and SiC are refractory materials and have high melting points (3160 °C and 2730 °C respectively), the sintering of TiC/SiC composites without additives in this research is a solid state sintering process. The sinterability of SiC is also lower than TiC[152]. However, the densification of the TiC/SiC composites is improved in some degree with

the increase of SiC contents (section 5.5). There are two reasons which may account for this.

Firstly, as thermal conductivity of SiC is much higher than that of TiC at room temperature (17 W/mK for TiC and 120 W/mK for SiC), the introduction of SiC could lead to an increase of thermal conductivity of TiC/SiC composites. According to the research carried out by Taylor[185] and Lezhenin[186], the thermal conductivities of TiC and SiC at high temperature (1700 °C) increase by about 20% and 6 times respectively compared with those at room temperature. Therefore the difference of the thermal conductivities between TiC and SiC is even higher at high temperatures than at room temperature and the introduction of SiC could significantly increase the thermal conductivity of TiC/SiC composites during the SPS sintering at 1700 °C. Many models aim to estimate the thermal properties of two phase materials from the characteristics of each component and their volume fractions[187]. Commonly, the experimental thermal conductivity of a two-phase-material is reported as the arithmetic average (linear):

$$K_{arithm.} = K_1 V_1 + K_2 (1 - V_1) \hspace{3cm} (5\text{-}3)$$

with K_1 and V_1 the thermal conductivity and volume fraction of the dispersed phase and K_2 the matrix thermal conductivity[188]. With the increase of thermal conductivity of TiC/SiC composites, heat would be conducted faster and the actual temperature distribution in the sample during the SPS sintering process would be more uniform for the samples with higher thermal conductivities (higher SiC content). This effect may become more significant for the SPS sintering because the sintering time is usually very short (5 min in this work). The difference in heat conduction and temperature distribution between the samples with different SiC contents can make a contribution to the different densities (porosities) of the TiC/SiC composites, that is the TiC/SiC composite with higher SiC content has lower porosity.

In addition, the solid solution between TiC and SiC may also improve the densification of

the TiC/SiC composites even though their solubility is limited in some degree[189]. Although no phases other than SiC and TiC were detected by X-ray diffraction (Figure 5.3), the results of more detailed energy dispersive analysis of X-rays (EDX) study suggested some possibility that formation of a solid solution between SiC and TiC had occurred. The line shifts of peaks at 35 degrees (2 theta) in XRD patterns may also indicate solid solution of SiC in TiC. Figure 5.13 shows the EDX spectra obtained from SiC and TiC grains in the TiC/SiC composite with 50 at% SiC SPSed at 1700 °C. Peaks representing Ti and Si were detected from the spectra for β-SiC (3C) and TiC phases, respectively. The Pt peaks is caused by the Pt coating on the sample before doing SEM because the low electrical conductivity of the SPSed TiC/SiC composites and coating of Pt can increase the samples' conductivity. Although the grain size for both phases may be too small to avoid the influence to the EDX spectra from the surrounding grains, it may be used to indicate the possibility of a solid solution of SiC and TiC in the composite. The similarity of the crystalline form and the lattice parameter of both phases would facilitate the formation of a solid solution between them. This is also consistent with Endo's result[143]. This possible solid solution between TiC and SiC can lead to better diffusion between them and improve the densification of TiC/SiC composites.

(a)   (b)
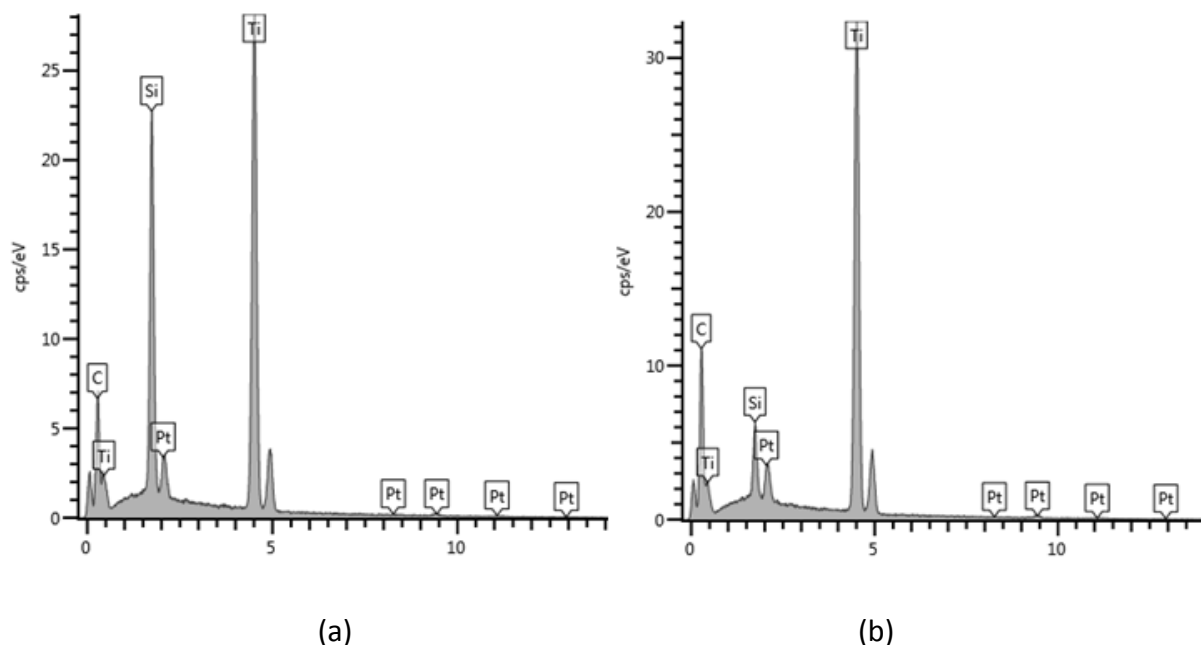
Figure 5.13 EDX spectra obtained from (a) SiC and (b) TiC grains in the TiC/SiC composite with 50 at% SiC SPSed at 1700 °C

5.6.3 Effect of the SiC on the grain growth of TiC/SiC composites

In our system, although TTIP (source of Ti) and TEOS (source of Si) in the sol were immiscible because TTIP was hydrophilic and TEOS was hydrophobic, amphiphilic triblock copolymer P123 was used as a surfactant which could bond the TTIP and TEOS together in the sol-gel process. Incorporation of silica into the titania system could inhibit crystallization of anatase which will enhance the homogeneity of M-O-C precursor[190] so that a nanostructure is formed.

Compared with the effect of SiC on the densification of TiC/SiC composites, its effect on retarding grain growth of TiC during the SPS sintering is much more marked. Silicon carbide is a more effective inhibiter for recrystallization and grain growth than excessive carbon (graphite). 20 vol% graphite in a TiC composite reduced the average grain size of matrix by a factor of 2-2.5[181], whereas silicon carbide added at 20 vol.% resulted in the

108

reduction of TiC grain size by a factor of 5-7[191]. Our result is very consistent with literature. The average grain size of monolithic TiC was larger than 1 μm and the grain size of TiC/SiC composite with 50 at% was only about 150 nm after SPS sintering at 1700°C (Figure 5.12).

The effect of SiC on retarding grain growth of TiC is mainly due to the Zener pinning effect. Our results have shown clearly that the TiC grain size reduced with increasing SiC nano particles, which can pin the boundaries of TiC grains. The average grain size of the SPSed TiC/SiC composites can be calculated according the following modified Zener pinning equation[192]:

$$R'_p = \frac{4}{3}\frac{r}{f_v^{2/3}} \tag{5-4}$$

where R'_p is the average matrix (titanium carbide) grain size, r is the nominal drag radius of pinning force (the grain size of the dispersed particle) and f_v is the volume fraction of the dispersed second phase. According to this equation, the grain size of the matrix ceramic decreases with the increase of the volume fraction of the dispersed second phase and the decrease of grain size of the dispersed phase. Because the grains of the dispersed second phase SiC was nano-sized, the introduction of SiC retarded the grain growth of TiC more significantly (Section 5.5.2). While the SiC retarded the grain growth of TiC, it did not hinder the densification because the dominated densification mechanism of the TiC was surface diffusion instead of boundary diffusion[192] and the reasons explained in the above sections.

5.7 Summary

Dense TiC/SiC composites with uniform nanostructures are successfully prepared by the sol-gel processing and spark plasma sintering. UHTCs usually need to be sintered at temperatures close to 2000 °C or even higher to get dense microstructures due to their extremely high melting point and low lattice diffusivity. The grain growth of UHTCs at

such high temperatures is significant. Compared with conventional powder mixing approaches, the sol-gel processing has shown its advantages on fabrication of UHTC composites with a much smaller grain size, higher final density, and more uniform nano-sized microstructures due to its unique solution mixing at a molecular level. The results in this chapter indicate that the sol-gel processing is a unique and useful technique for fabrication of UHTCs.

A very important parameter for the sol-gel process is to control the carbon concentration in the composition, which is different form the conventional powder mixing, because excessive carbon in the composition retards the densification of ceramics. The major role of the carbon in the sol-gel process is to reduce the oxides to form carbides at elevated temperatures. However, both a too high and a too low carbon concerntrations are undesirable for making UHTCs because a too high carbon concerntration would lead to too much residual carbon after carbothermal reduction, which will retard the densification during sintering, and a too low carbon concerntration would leave some oxides unreacted during the carbothermal reduction process.

Chapter 6 Carbide Ceramic Composites Prepared by Sol-Gel Infiltration

To improve/modify the microstructures and properties of ceramics/composites, the sol-gel processing technology is one possible option. The sol-gel method has its unique advantages due to its liquid phase processing compared to other conventional powder approaches, such as avoiding nano-sized powder handling, allowing infiltration of complex shape samples and making functionally gradient materials. Densification of ultra-high temperature ceramics often requires sintering at very high temperature, 2000 °C or above, which is usually accompanied inevitably with significant grain growth[8,193]. In many cases, full densification of the materials is very difficult to achieve despite of prolonged sintering at elevated temperatures[8]. In this chapter, the study of preparing dense or functionally gradient carbide nanocomposites was undertaken. These samples were prepared via infiltrating porous scaffolds with a sol, then sintered by SPS to obtain the dense or functionally gradient composites while maintaining fine grain sizes. Within this chapter, the microstructures and chemical analyses of the produced carbide composites were also investigated.

As a typical and widely applied ceramic composite, TiC/SiC system was first studied in this chapter. Porous TiC scaffolds were prepared in one of two ways. They were either prepared via direct carbothermal reduction of a monolithic Ti-O-C precursor obtained from a controlled sol-gel process, named Scaffold G, or obtained via spark plasma sintering of nano-sized TiC commerical powder named Scaffold S. The scaffolds prepared by either technique were then infiltrated with a Si-O-C sol in a vacuum container. After the Si-O-C sol became a gel, the infiltrated scaffold was then heated at 550°C in N_2 to remove the organic components. Then the scaffold was heat treated at 1450°C in Ar, to convert the Si-O-C gel to SiC by the carbothermal reduction reaction. The cycle of infiltration and heat treatment was repeated several times, until further infiltration was impossible, to ensue relatively dense TiC/SiC composites were obtained.

After this sample preparation, the TiC/SiC composites were at last sintered by SPS to achieve dense materials. The schematic process of the sol-gel infiltration is shown in Figure 6.1.
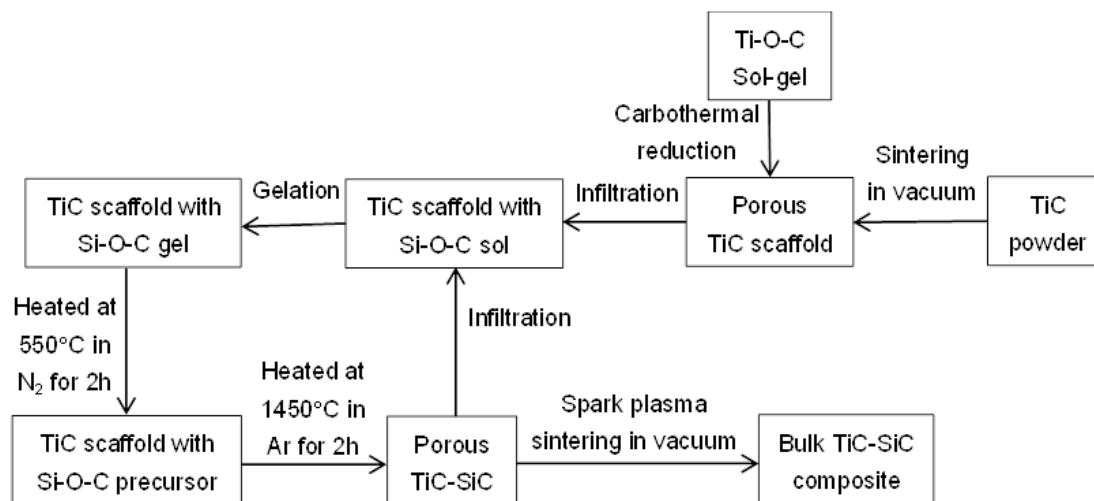
Figure 6.1 Schematic process of the fabrication of TiC/SiC nanocomposites prepared by sol-gel infiltration

6.1 Experimental procedure

6.1.1 TiC scaffold G prepared by sol-gel processing

Sol-gel infiltration has its unique advantages to modify/improve the surface of UHTCs compared with the conventional techniques. In this chapter, infiltration of SiC sol-gel will be carried out to prepare functionally gradient TiC/SiC nanocomposites from porous TiC scaffolds. The sol-gel process for preparing porous TiC scaffold G was carried out as following. The molar ratio of FA to TTIP ranged from 0.7 to 1.2 to adjust the strength of the TiC scaffolds. A solution of P123 and TTIP was prepared by first dissolving P123 in anhydrous ethanol under continuous stirring. The TTIP was then added to this P123

solution. Separately a solution of 10M HCl and ethanol was prepared by mixing them in a 1:2 weight ratio, using vigorous stirring for 15 min. The acid and ethanol solution was then added into the TTIP solution under vigorous stirring. After 30 min, the FA was added into the TTIP mixture with continuous stirring. This solution was then aged for 3 days at 25°C before it was poured into a petri dish. The petri dish was then placed in an oven at 80°C to allow a gel to form. The as-synthesized gel was then calcined in an alumina boat, inside a quartz tube furnace, at 550°C for 5h under nitrogen atmosphere. This was to obtain a Ti-O-C precursor. The Ti-O-C precursor was finally heat treated in an alumina tube furnace, at 1300°C/1450°C for 5h under argon atmosphere. This achieved a porous TiC scaffold through carbothermal reduction.

6.1.2 TiC scaffold S prepared by SPS

Another route for preparing TiC scaffold S was by spark plasma sintering of nano-sized TiC powder. TiC powder was packed into a 30 mm graphite die, then SPSed at 1500 °C for 5 min at a uniaxial pressure of 40 MPa. This was performed in vacuum. The sintered sample was cut into a few pieces of about 10 mm size before being infiltrated.

6.1.3 Infiltration of TiC scaffolds with a Si-O-C sol

To make the Si-O-C sol, TEOS was used as a silica source. The molar ratio of furfuryl alcohol to TEOS in the solution was 0.72. This was found to be the optimal value to keep the residual carbon content to a minimum in the final TiC/SiC composite after infiltration. P123 was first dissolved in ethanol, followed by mixing with hydrochloric acid under continuous stirring for 15 minutes. Then TEOS was dropped in the solution mixture and stirred for 15 minutes. Lastly furfuryl alcohol was added in the mixed solution under continuous stirring. This was then aged for 3 days at room temperature, to form a Si-O-C sol. The porous TiC scaffolds were then infiltrated with the Si-O-C sol, after removing the entrapped air in the scaffolds. This was achieved by placing the scaffold in a container and evacuating the container for about 10 min. The final vacuum

pressure for this process was about 21 kPa. The infiltrated TiC scaffolds were kept in the evacuated container for 12 h before being transferred into a petri dish and dried at 80°C for 48 hours until the Si-O-C sol was fully gelled.

Similar to Si-O-C sol, Zr-O sol was also prepared for infiltration. P123 was first dissolved in 99.7% ethanol and acetylacetone (AcAc). Once the P123 was dissolved, zirconium npropoxide (ZNP) 70 wt% in 1-propanol, was added to bring the molar ratios of P123:etOH:AcAc:ZNP in a solution to 0.05:40:1:1. The solution then turned yellow. Solutions were aged for 72 h at room temperature before infiltration.

After gelation, the infiltrated TiC samples were first re-heated to 550°C to remove organic components. This was performed in a quartz tube furnace at 550°C for 2h under nitrogen atmosphere. This was followed up by carbothermal reduction of the Si-O-C gel in an alumina tube furnace where the conditions employed were 1450 ^{o}C for 2h in flowing argon. Both the heating and cooling rate are 2 ^{o}C/min. This process produced TiC/SiC composites. The infiltration and heat treatment cycle was repeated for a number of times. For one of the samples the infiltration cycle was continued until no further infiltration was possible.

6.2 Preparation and characterization of porous TiC scaffolds

6.2.1 Preparation of porous TiC scaffolds via sol-gel processing, Scaffold G

The sol-gel process used for preparing porous TiC scaffolds was described in the above section. The temperature for carbothermal reduction of Ti-O-C precursor to achieve a porous TiC scaffold G ranged from 1300 °C to 1450 °C so that optimized temperature could be taken to obtain finer TiC particles as well as reduce the Ti-O-C precursor to TiC completely. If the temperature for carbothermal reduction reaction is too low, then the reaction will not be complete and some titanium oxide may remain in the scaffold. While too high temperature will lead to coarse TiC particles due to the grain growth,

which is unfavorable for getting a nano-sized structure. To achieve the desired TiC/SiC composites, using the sol-gel infiltration technique, the porous TiC scaffolds should have sufficient strength to withstand the infiltration and heat-treatment processes. So controlling the amount of residual carbon in the TiC scaffold after carbothermal reduction is important. If the residual carbon in the final composite is too high, it would retard the densification. But a low residual carbon would result in a weak TiC scaffold.

The minimum theoretical carbon to metal (C/M) ratio required is 3 for the completion of the carbothermal reduction reaction, according to the formula:

$$TiO_2(s) + 3C(s) \rightarrow TiC(s) + 2\ CO(g) \quad\quad\quad\quad\quad\quad (6\text{-}1)$$

However, the actual C/M ratio in the initial mixture of reactants should be higher than 3, because of the loss of carbon during the sol-gel and heat treatment processes. According to the TGA analysis results in section 5.3.1 Chapter 5, the optimized value of the C/M ratio is 3.6. This value allows for the complete carbothermal reduction reaction of TiO_2 gel, with the minimum residual carbon remaining in the composites. However, the porous TiC scaffold formed at this carbon ratio was very weak, and could not withstand even gentle handling. The weakness this scaffold exhibits is due to the poor bonding, between the TiC particles at the carbothermal reduction temperatures, usually below 1500°C. It was found that the strength of the scaffold increased with an increase in the residual carbon content, producing an adequate strength for subsequent handling achieved at a designed C/M of about 6. This can be attributed to the bonding of nano sized TiC crystals, by the residual poly(furfuryl alcohol) (PFA) derived carbon network. In this carbon network the nanocrystalline graphene sheets, between the nano TiC grains, provide the bonding mechanism for nano TiC grains[111].

6.2.2 Preparation of porous TiC scaffolds via SPS, Scaffold S

The process for preparing porous TiC scaffolds S is similar to the one described in Section 4.1, Chapter 4. Commercial nano-sized TiC powder was sintered by SPS to get

porous scaffolds. The particle size of the TiC powder was about 50 nm. The sintering temperature was 1500 ^{o}C, and the holding time was 5 minutes. The heating rate was 100 ^{o}C /min. Too high of a temperature, leads to insufficient open porosity of the achieved TiC scaffolds, and too low temperature causes inadequate strength of the TiC scaffolds for subsequent handling.

6.2.3 Characterization of porous TiC scaffolds

Figure 6.2 shows the XRD patterns of the TiC scaffolds G obtained by carbothermal reduction of TiO$_2$ sol-gel at 1300°C, and 1450°C respectively without pressure. Only one crystalline phase, TiC, is present in both samples, indicating the completion of the carbothermal reduction reaction at temperatures of 1300°C and above. The intensity of TiC, formed at 1450°C, peaks (Figure 6.2b) is higher than that of the one formed at 1300°C (Figure 6.2a). This means the crystallinity of TiC phase improves, with the increasing carbothermal reduction temperature.

(a)   (b)
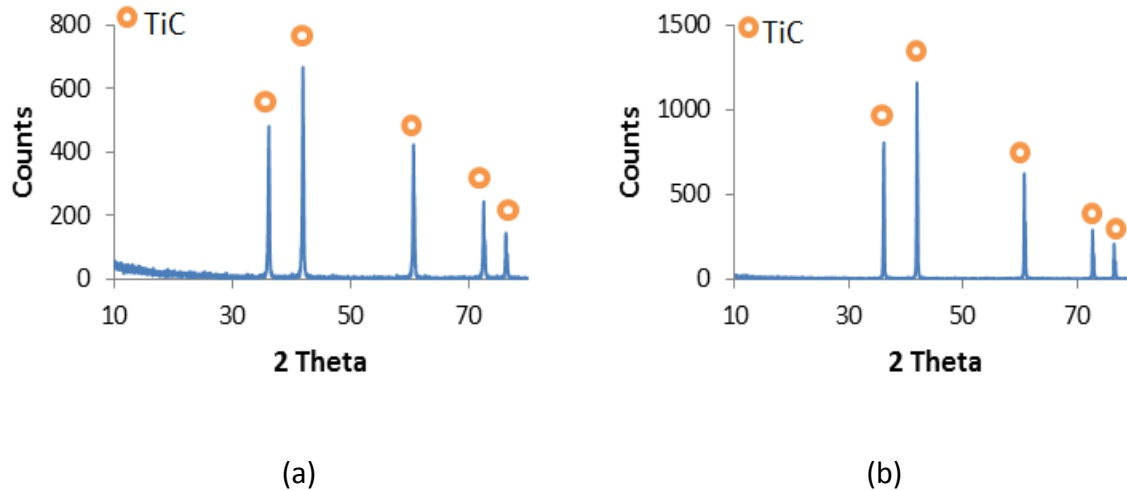
Figure 6.2 XRD patterns of the TiC Scaffold G with a starting C/M ratio of 6 obtained by carbothermal reduction at (a) 1300°C (b) 1450°C

A comparison of the microstructures produced at 1300°C and 1450°C is shown in Figure 6.3. The scaffolds G observed were produced via sol-gel processing, utilizing a carbon ratio of 6. The results show that the TiC scaffold contains a large amount of uniformly distributed open meso/micro-pores. The grain size of the TiC particles in the sample formed at 1450°C, is a few hundred nanometers (Figure 6.3b), whereas the grain size of TiC in the one formed at 1300°C is less than 100nm (Figure 6.3a). It indicates that the carbothermal reduction temperature has a significant effect on the grain size of TiC, with the grain size of TiC increasing significantly with the increase of temperature. If the TiC grains need to be nano-sized, the grain growth of TiC scaffolds must be limited during the carbothermal reduction of the Ti-O-C precursor. To achieve this, a low temperature needs to be employed. For the subsequent infiltration study, TiC Scaffolds G were produced by carbothermal reduction of the Ti-O-C gel at 1300°C.

(a)   (b)
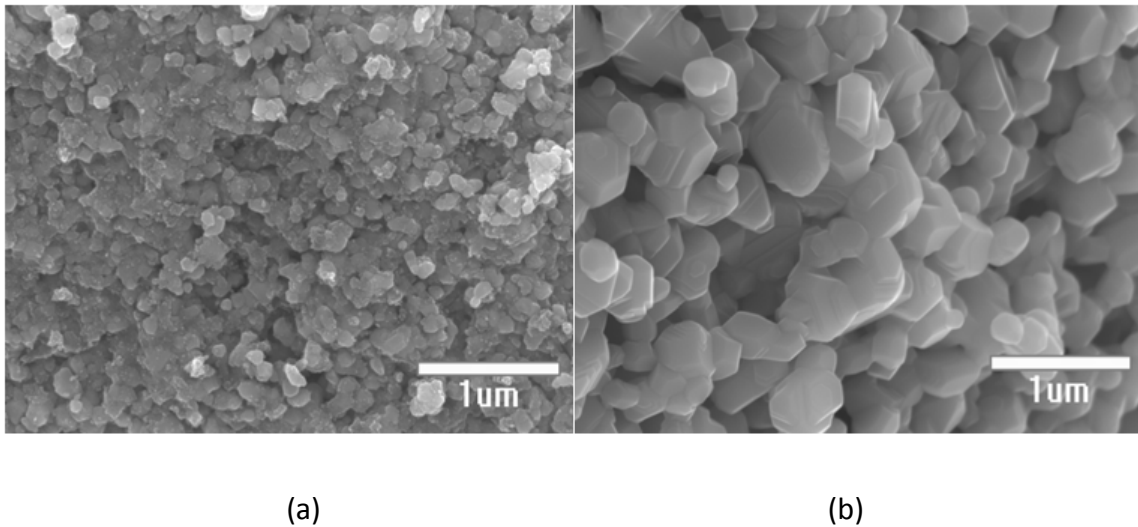
Figure 6.3 Microstructures of the porous TiC Scaffold G obtained by carbothermal reduction of the sol-gel precursor at (a) 1300 $^{\circ}$C (b) 1450 $^{\circ}$C

The microstructure of the TiC Scaffold S prepared through SPS of commercial nano-sized TiC powder at 1500°C is shown in Figure 6.4. The results indicate that the pore size of the TiC scaffold ranges from a few hundred nm to about 1-2 μm. The grain size of TiC is

about 100 nm. The total porosity and open porosity of the TiC scaffold measured via the Archimedes principle are 30% and 14.5% respectively. The open porosity and pore size are the main factors that would affect the surface layer thickness of the composites because the solution can only penetrate from the material's surface into the scaffolds through open pores.
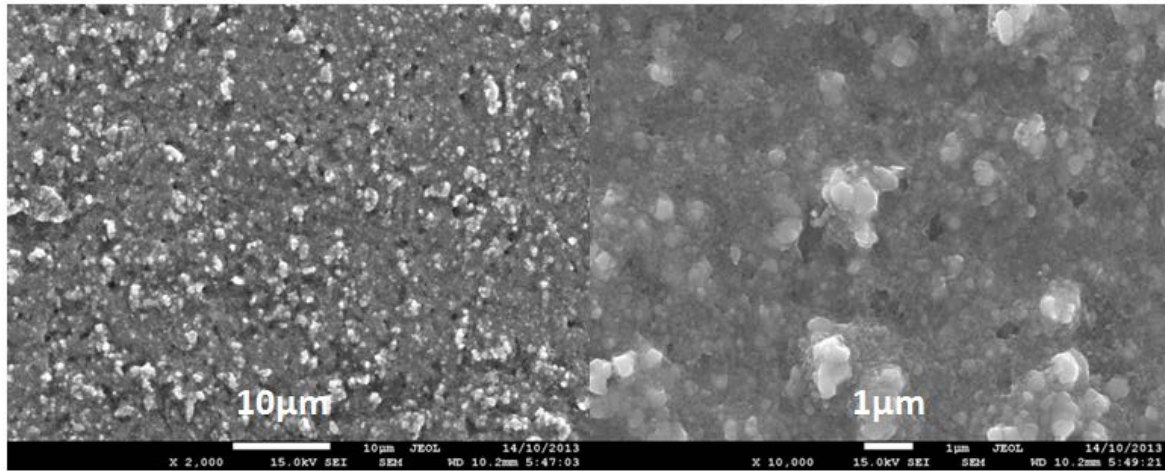
(a)   (b)

Figure 6.4 Microstructures of the porous TiC Scaffold S prepared via SPS at 1500 °C (a) low magnification (b) high magnification

6.3 Effect of the number of infiltration cycles

6.3.1 Infiltration of the TiC scaffolds G prepared via sol-gel processing

To obtain better infiltration of the Si-O-C sol into the porous TiC scaffold, vacuum infiltration was employed. The porous TiC scaffolds G were put in a container and vacuumed for about 10 minutes followed by infiltrating a Si-O-C sol prepared via a controlled sol-gel process which is described in section 6.1. The molar ratio of furfuryl alcohol (FA) to tetraethyl orthosilicate (TEOS) ranged from 0 to 0.72 (equals to

carbon/silicon ratio of 0 to 3.6), which depended on the amount of carbon left in the TiC/SiC composites after each infiltration cycle. The amount of residual carbon left in the TiC/SiC composites was measured and calculated by TGA analysis. The residual carbon in the final TiC/SiC composites can be tuned and kept in the minimum level by this way. The TiC/SiC composites prepared by this sol-gel infiltration route were not fully dense even after a few cycles' infiltration. This is because the decomposition and volatilization of the organic components in the Si-O-C gel during calcination at 550°C and the carbothermal reduction reaction at 1450 °C left a large amount of unfilled voids. So further sintering by SPS is necessary to achieve dense final materials.

The microstructures of the TiC scaffolds G with different numbers of infiltration cycles without any sintering are shown in Figure 6.5. The larger grains are TiC and the very fine ones are SiC. The grain size of SiC is far less than 100 nm. The grain size of TiC in all the samples with different numbers of infiltration cycles is still less than 100nm (Figure 6.5a, 6.5b, 6.5c and 6.5d) and is almost the same as the one of the initial scaffold G before infiltration (Figure 6.3a), while the grain size of monolithic TiC prepared by sol-gel processing is about a few hundred nanometers after fired at 1450 °C for 5 hours (Figure 6.3b). This means that the introduction of SiC via sol-gel infiltration can significantly retard the grain growth of TiC due to the great pinning effect of very fine SiC particles at the grain boundaries. It can also be found from the microstructures that the amount of infiltrated SiC increases and the porosity of the scaffolds decreases with the increasing number of infiltration cycles (Figure 6.5b, 6.5c and 6.5d). This indicates that the infiltration of TiC scaffolds G, which are prepared by sol-gel processing, with SiC sol-gel is successful and effective.
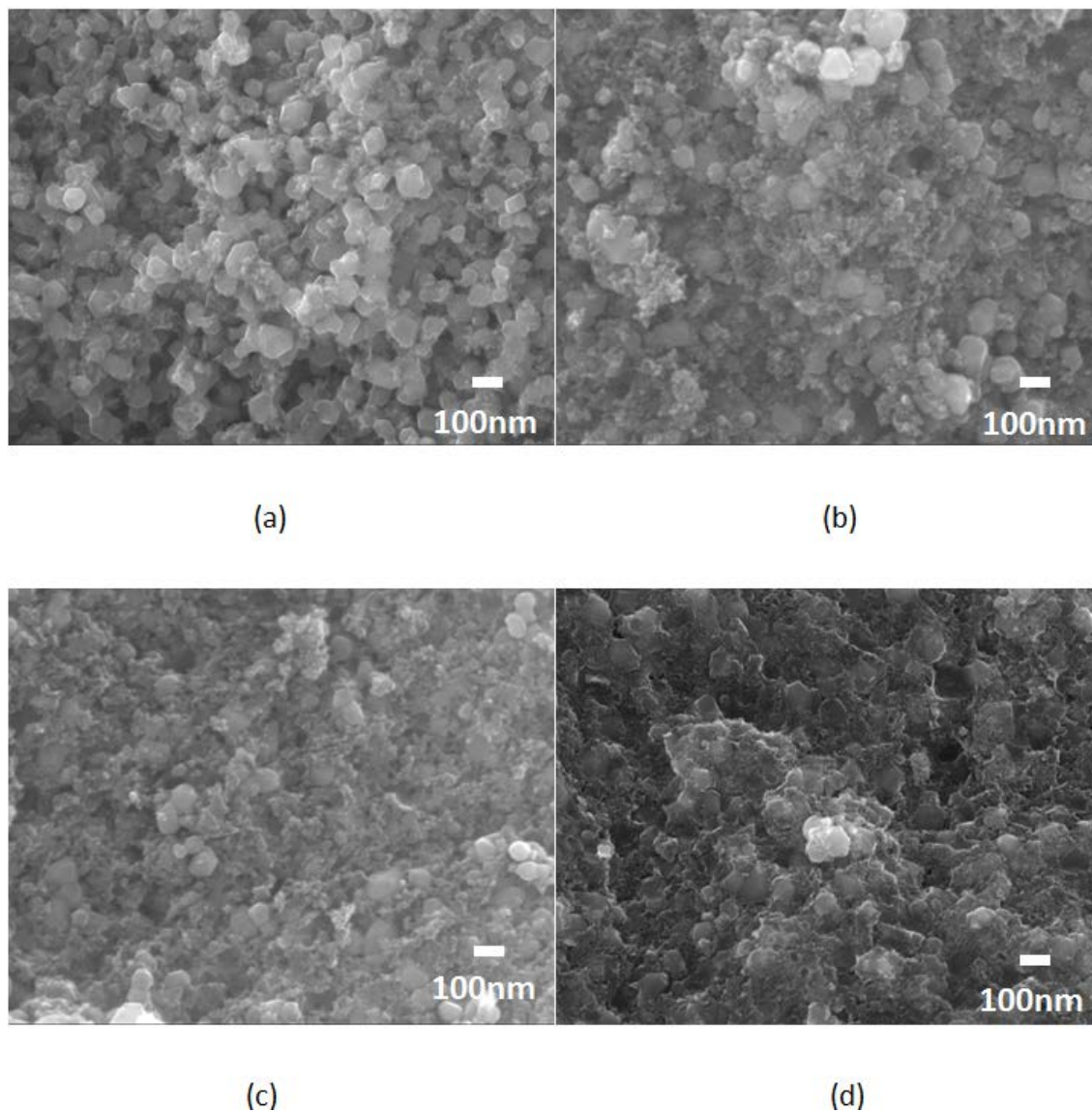
Figure 6.5 Micrographs of the TiC scaffolds G after different numbers of infiltration cycles after fired at 1450 °C for 5 hours in Ar (a) 1 cycle (b) 3 cycles (c) 5 cycles (d) 7 cycles

The relative densities of the infiltrated TiC/SiC composites using TiC scaffolds G with final sintering via SPS at 1800°C with respect to the number of infiltration cycles are shown in Table 6.1. No SPS sintering process was done between each infiltration cycle for the samples with multi-cycle infiltrations. The density of the samples was

determined via the Archimedes principle, using water as the buoyant medium. The theoretical density of the TiC/SiC composite was calculated based on the fractions of TiC and SiC. The weight percentage of SiC in the composite was measured by EDX. The density of the SPSed TiC/SiC composites improved significantly with increasing numbers of infiltration cycles. This sample was near full density after 7 cycles of infiltration, compared with 95.2 percent density achieved with a controlled monolithic TiC sample sintered under the same condition (Figure 6.6). The grain size of the infiltrated TiC/SiC composite sample is about 150 nm (Figure 6.6a), while the one of the monolithic TiC sample is larger than 1 μm (Figure 6.6b). From this result, it indicates that infiltration of porous scaffolds prepared via sol-gel processing is a promising technique to fabricate dense UHTC composites with homogeneous nanostructures.

Table 6.1 Relative densities of the SPSed TiC/SiC composites and TiC ceramic at 1800°C for 5min. The Scaffold G samples were infiltrated by a Si-O-C sol-gel for a number of cycles prior to the SPS sintering.

	TiC/SiC with different numbers of infiltration cycles				TiC
	1	3	5	7	
Relative density (%)	68.2±0.1	82.6±0.1	92.3±0.1	99.5±0.1	95.2±0.1
SiC content (wt%)	6.5	16.3	24.2	29.7	0

(a)   (b)
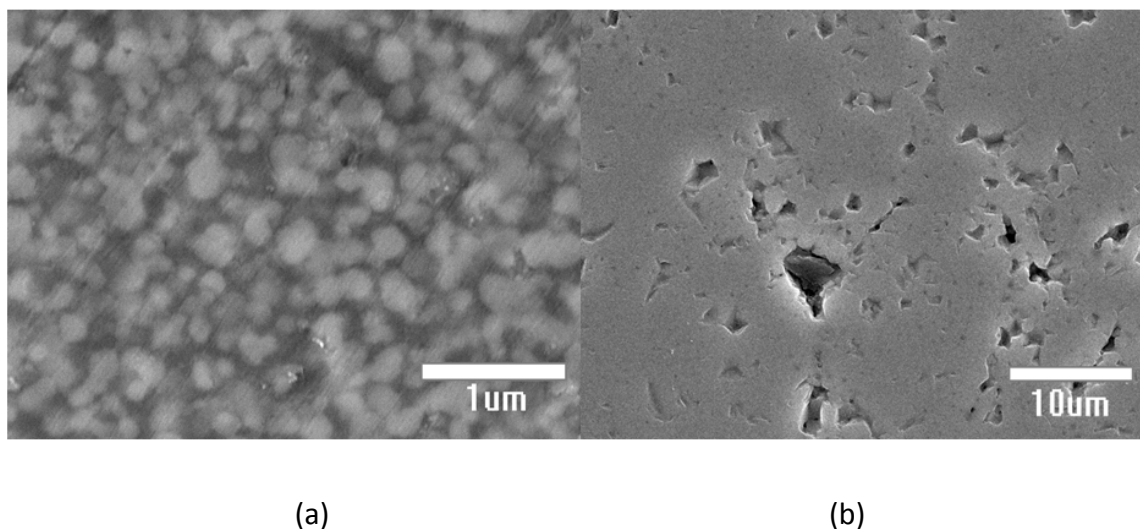
Figure 6.6 Microstructures of (a) TiC/SiC composite using TiC scaffolds G with 7 cycles of infiltration and (b) monolithic TiC. Both samples were sintered by SPS at 1800 °C.

6.3.2 Infiltration of TiC scaffolds S prepared via SPS

The porous TiC scaffolds S can also be prepared by partially sintering at a relatively low temperature. Another advantage of sol-gel infiltration is that functionally graded ceramic composites can be formed by infiltrating such porous scaffolds with a sol. After infiltration, the surface of the scaffold becomes dense and the center still keeps some porosity. This kind of functionally gradient ceramic composites have many advantages such as high hardness, strength and oxidation resistance on the surface and very good thermal shock resistance and thermal insulation at the center[194], which, for example, could be a material with a dense SiC/ZrB$_2$ composite on the surface and a porous ZrB$_2$ in the centre.

TiC scaffolds S were prepared via SPS at 1500°C with a heating rate of 100 ^{o}C/min and a uniaxial pressure of 40 MPa, and were held for 5 min. The total porosity and open porosity of the SPSed TiC scaffold S were 30% and 14.5% respectively after sintering at these conditions. The scaffolds were then infiltrated with a Si-O-C sol, prepared via a controlled sol-gel process, for up to 5 cycles. After each cycle of infiltration, the scaffolds

were not sintered because they were expected to be infiltrated with SiC as much as possible before final sintering to get dense TiC/SiC composites. The molar ratio of furfuryl alcohol (FA) to tetraethyl orthosilicate (TEOS) was 0.72, equal to carbon/silicon ratio of 3.6. At this point, no further infiltrations were possible. After each cycle of infiltration, the scaffold was put into water to check if there were bubbles coming out. When the scaffold with 5 cycles of infiltration was put into water, there was no bubble coming out, suggesting that no more solution could be infiltrated. Images in Figure 6.7 show the surface layers of the TiC scaffolds S after infiltration. The size of the scaffolds was about 10 mm in diameter and 8 mm in thickness. These scaffolds were infiltrated with SiC without any further sintering. The crack in the scaffold in Figure 6.7e was caused by the thermal stress during the heat treatment of carbothermal reduction reaction. The microstructures of the surface layer and core of the scaffold with one cycle of infiltration are shown in Figure 6.7c and 6.7d respectively. After the infiltration, the surface layer becomes a relatively dense layer of the TiC/SiC composite and the core of the sample is mostly porous TiC. The thickness of the surface layer increases with the number of infiltration cycles (Figure 6.7a, 6.7b and 6.7e). The thickness of the surface layer is about 500 nm after 1 infiltration cycle (Figure 6.7a), and increases to about 800 nm after 2 cycles (Figure 6.7b). It reaches its maximum value of about 1 mm after 3 cycles and above (Figure 6.7e, 6.7f and 6.7g). The maximum thickness of the surface layer achievable will depend on the pore size and the open porosity of the starting scaffold.

(a)

(b)

(c)   TiC   SiC   (d)

(e)   (f)

(g)
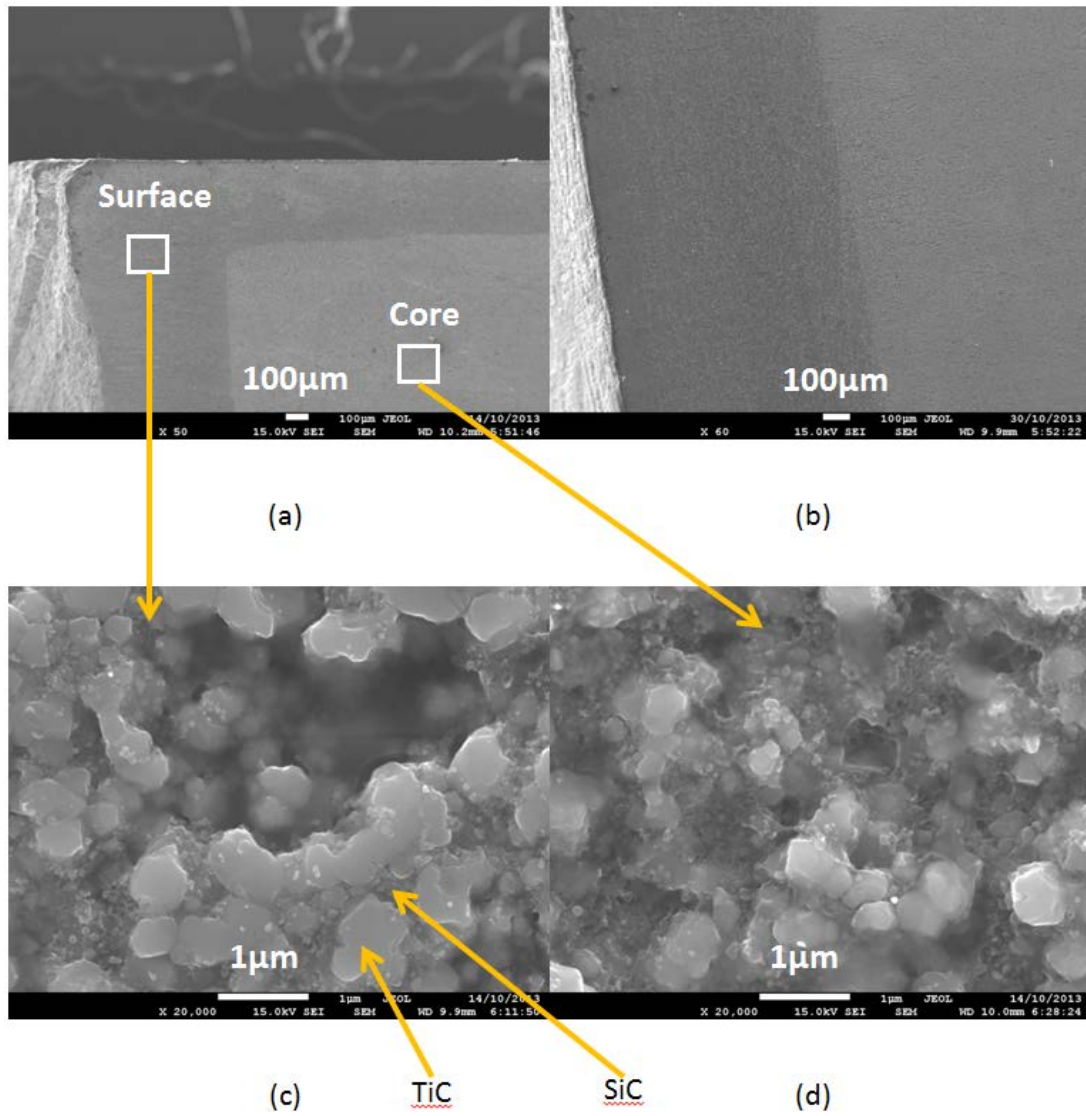
Figure 6.7 Micrographs of the TiC scaffold S after different numbers of infiltration cycles without sintering. (a) 1 cycle (b) 2 cycles (c) surface layer of the sample with 1 infiltration cycle (d) core of the sample with 1 infiltration cycle (e) 3 cycles (f) 4 cycles (g) 5 cycles

The results of the EDX analysis of the surface layer and core of TiC scaffold S after 1 cycle of infiltration (Figure 6.7a) are shown in Figure 6.8. The white grains are TiC and dark ones are SiC. The blue, green-yellow and cyan lines in Figure 6.8a represent Ti, Si and C respectively. While the green-yellow, green and red lines in Figure 6.8b represent

Ti, C and Si respectively. From the EDX results, SiC can be found both within the surface layer and at the core of the sample even with one cycle of infiltration. The concentration of SiC (Si element) in the surface layer (Figure 6.8a) is much higher than that at the core (Figure 6.8b) of the sample. This is consistent with the microstructures of the scaffold in Figure 6.7c and 6.7d, which show the sol is mostly infiltrated into a limited thickness of the sample surface, and has difficulty to reach the center of the scaffold. The thickness of the surface layer depends on the size and amount of the open pores in the initial scaffold S.

(a)

(b)

Figure 6.8 EDX analysis of the TiC scaffold after 1 cycle of infiltration without sintering in (a) surface layer (b) center of the composite in Figure 6.7a

The microstructures of the surface layer and core of TiC scaffolds S after different numbers of infiltration cycles without any further sintering are shown in Figure 6.9. The results indicate that the porosity in the infiltration surface layer (Figure 6.9a, 6.9c, 6.9e and 6.9g) of the scaffold is significantly lower than that at the center (Figure 6.9b, 6.9d, 6.9f and 6.9h). This again shows that the sol is mainly infiltrated into the outer layers

and does not get to the center of the sample during infiltration. The porosity at the infiltration surface layer decreases dramatically with the increase in the number of infiltration cycles. From the microstructures in Figure 6.9, we can see that the porosity at the surface layer of the scaffold (Figure 6.9a, 6.9c and 6.9e) decreases significantly after the initial few infiltration cycles compared with that of the scaffold before infiltration (Figure 6.4b). However, the porosity at the center of the scaffold does not change much with the increase in the number of infiltration cycles because the infiltrating mainly fills the pores in the surface layer. The grain size of the TiC scaffold changes little with the increase in the number of infiltration cycles, with the TiC grain size maintaining submicron levels.

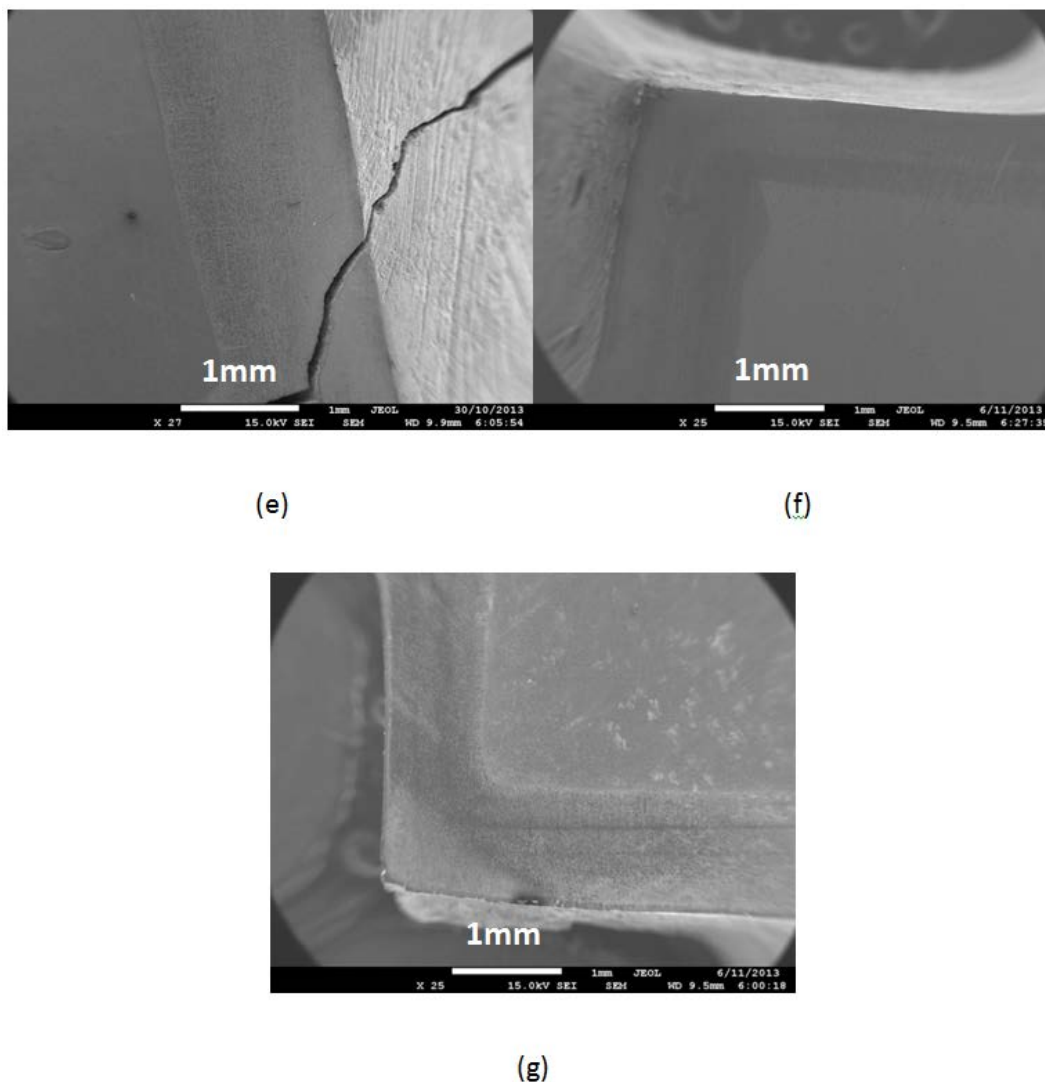(a)   (b)

(c)   (d)
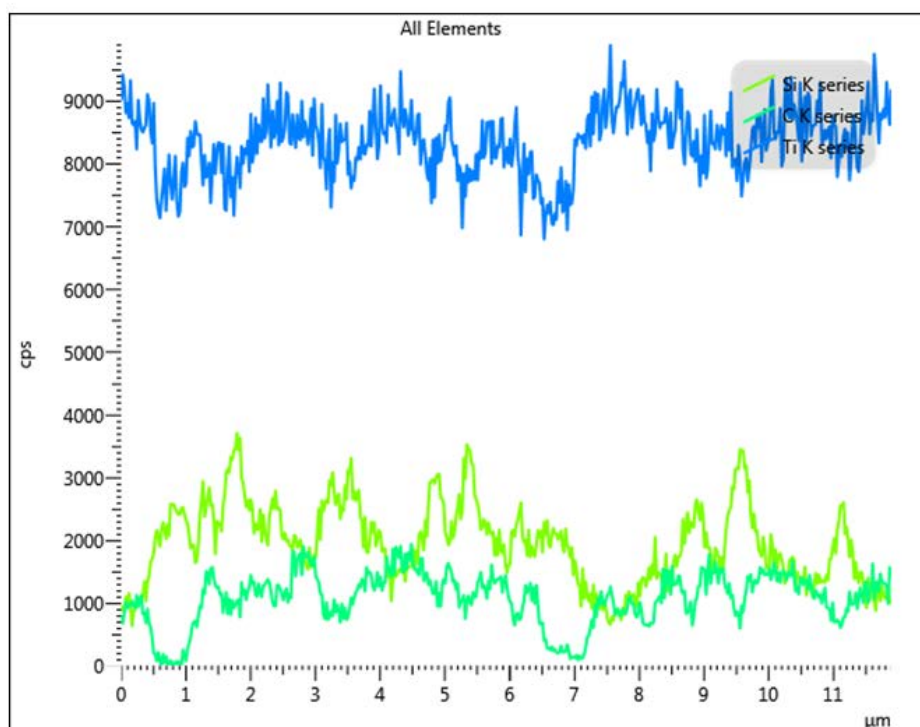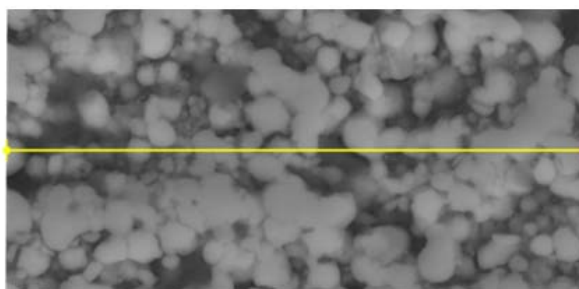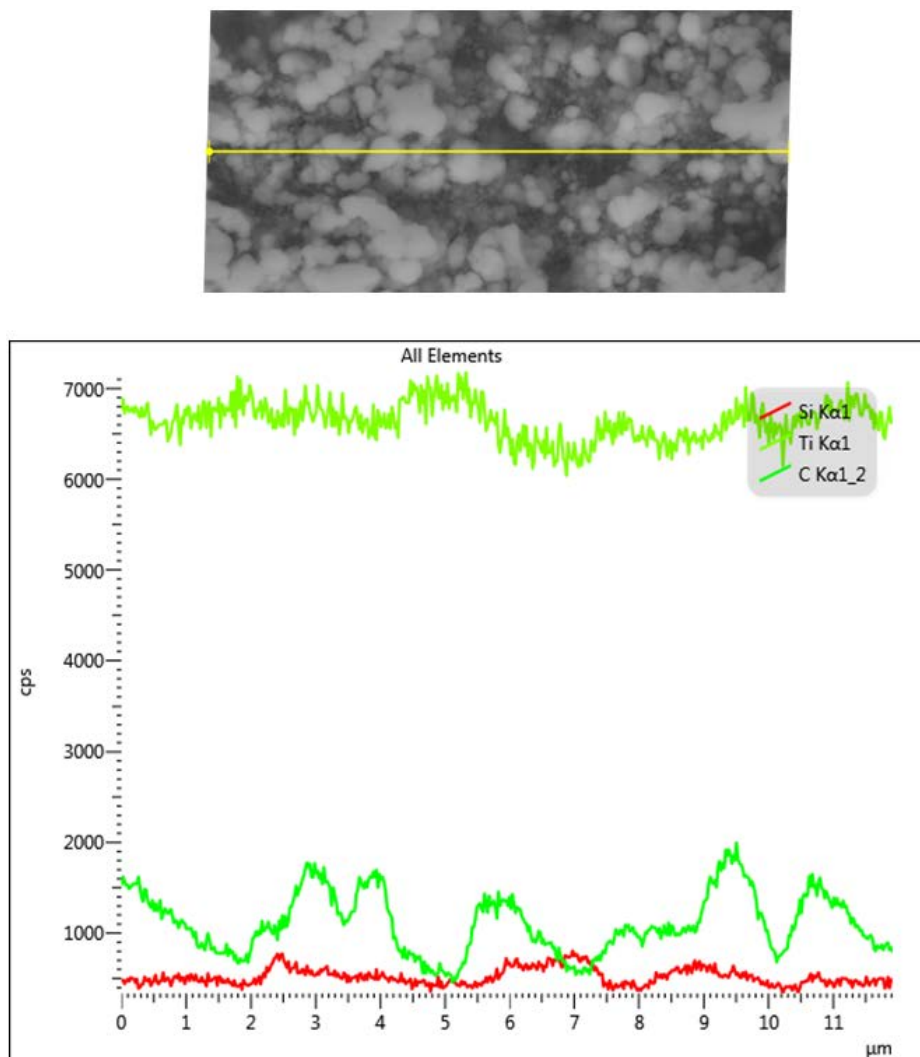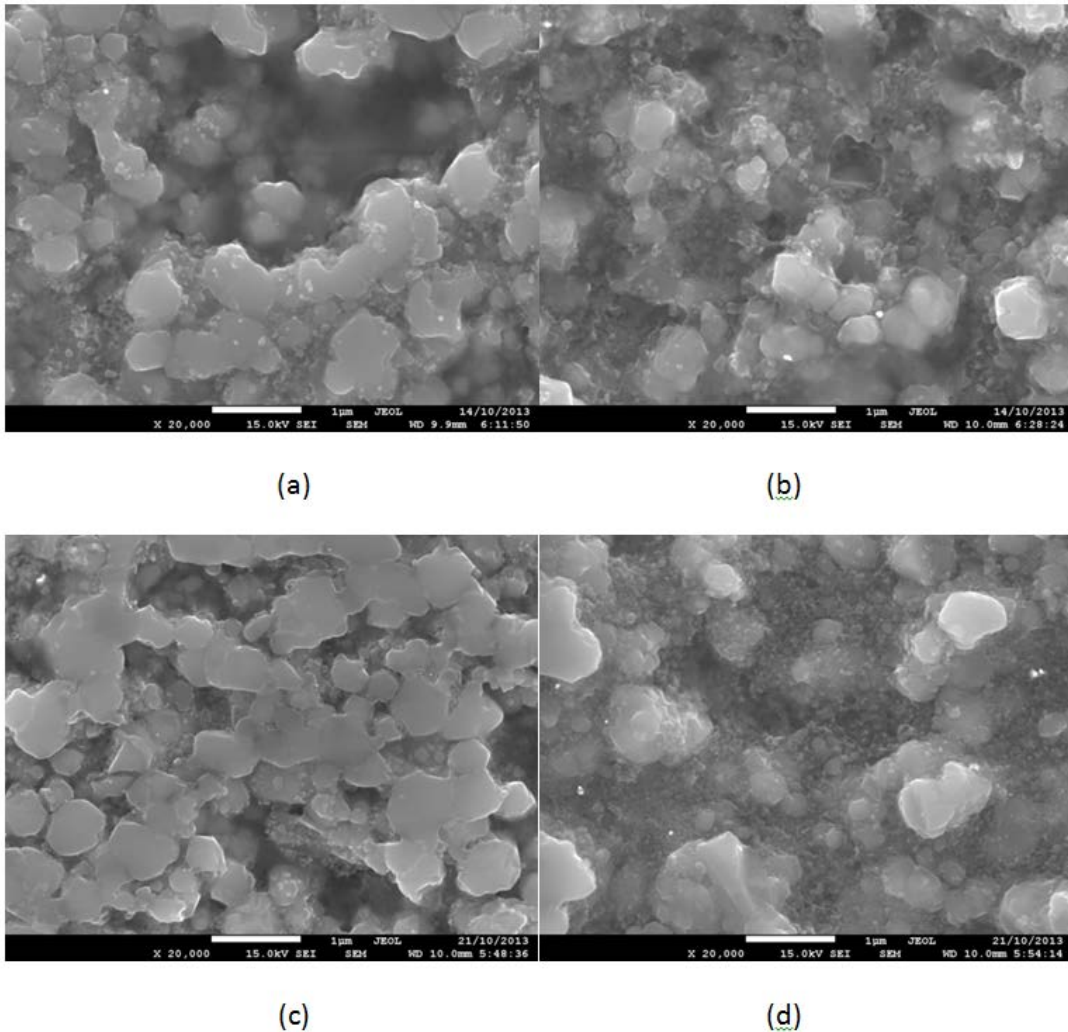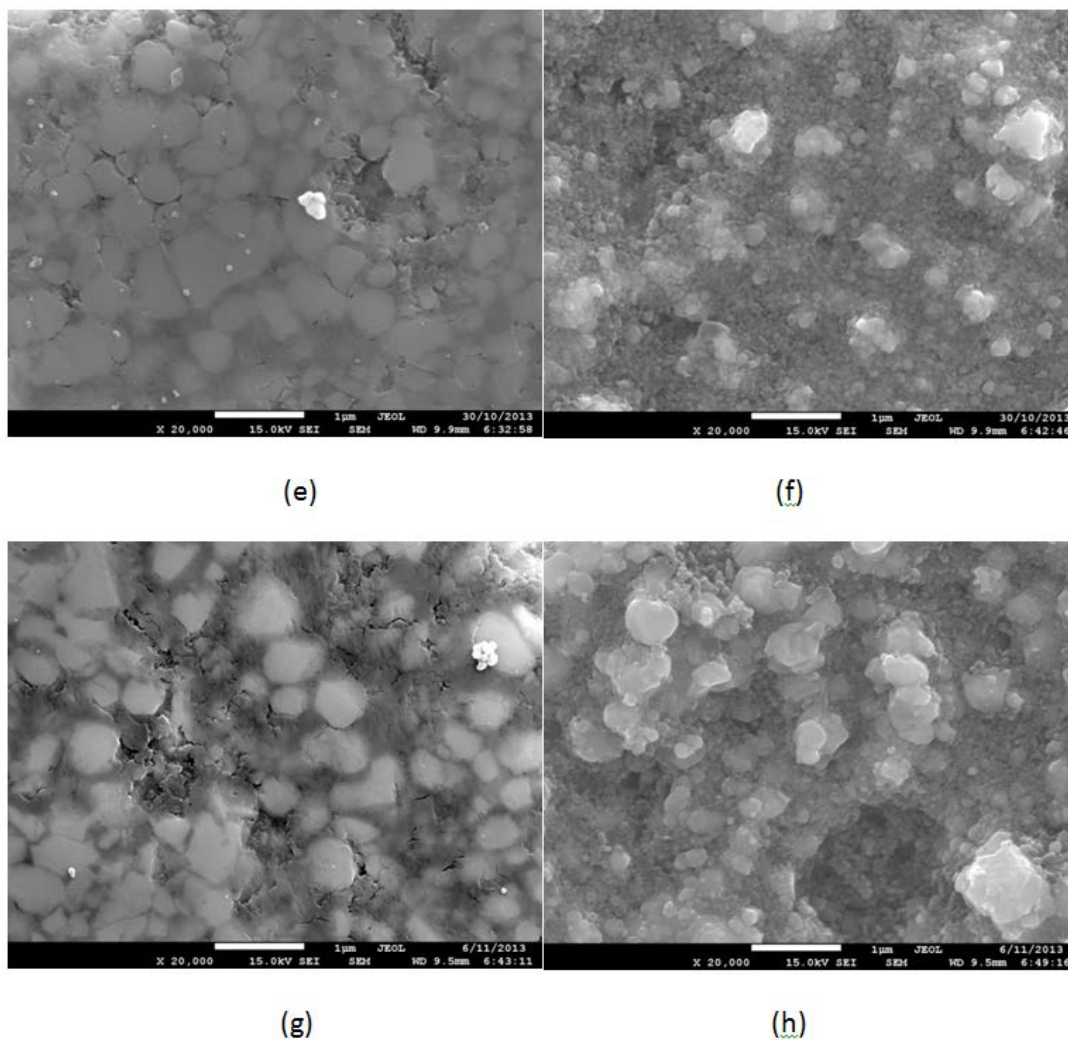
Figure 6.9 Microstructure of the TiC scaffold after different numbers of infiltration cycles without sintering (a) 1 cycle at surface layer (b) 1 cycle at core (c) 2 cycles at surface layer (d) 2 cycles at core (e) 3 cycles at surface layer (f) 3 cycles at core (g) 5 cycles at surface layer (h) 5 cycles at core

6.4 Chemical analysis and microstructures of the TiC/SiC composites prepared by sol-gel infiltration and SPS

6.4.1 Chemical analysis of the TiC/SiC composites

XRD results of the infiltrated TiC/SiC composite SPSed at $1800^{o}C$ are presented in Figure 6.10. The pattern is similar to that of the original TiC scaffold (Figure 6.2), even though SiC has been infiltrated to this composite. The presence of SiC is not distinguishable from the XRD pattern, due to the small fraction of SiC, and the heavy overlap of XRD peak positions between SiC and TiC. The approximate SiC fraction of the sample prepared with 7 cycles of infiltration is about 30% (Table 6.1). According to the study on the TiC/SiC composites prepared by the sol-gel processing in Section 5.2.1 in Chapter 5, composites with SiC fractions less than 50% have difficulties in detecting the SiC. This is due to the strong overlap of the TiC and SiC XRD peaks and the relative low intensity of SiC peaks, compared with the TiC peaks. This is also consistent with Cabrero's work[147]. However, the surface microstructures of the TiC/SiC composites (Figure 6.11), without surface preparations, confirmed the presence of two intimately mixed phases, with distinct compositional contrast. This is especially true for the sample prepared with 7 cycles of infiltration in Figure 6.11d, due to its elevated levels of SiC.
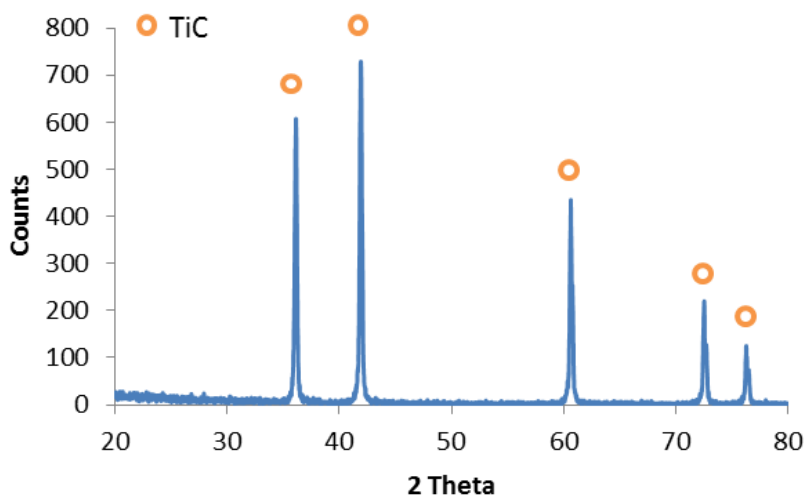
Figure 6.10 XRD pattern of the TiC/SiC composite sample SPSed at 1800 ^{o}C

6.4.2 Microstructures of the TiC/SiC composites using scaffolds G after SPS sintering

The SEM micrographs of the TiC/SiC composites using scaffolds G after different numbers of infiltration cycles with final sintering by SPS 1800 ^{o}C in vacuum under 40 MPa uniaxial pressure for 5 min are listed in Figure 6.11. The heating rate during the SPS process was 100 ^{o}C/min. The result shows that the porosity of the TiC/SiC composites decreases with the increase in the number of infiltration cycles. The porosity evolution of the samples is described via density measurements, shown in Table 6.1 in section 6.2.1. During each infiltration cycle, the samples were infiltrated and heat treated at 550 ^{o}C and 1450 ^{o}C for carbonization and carbothermal reduction respectively. The infiltration step was repeated for multiple times. No sintering process was done between each infiltration cycle. The final sintering process for all the samples with different numbers of infiltration cycles was done via SPS at 1800°C for 5min in vacuum. The grain growth of the composites may be expected during this process. However, the grain size of the TiC/SiC composites in SEM images does not change as much as the porosity with the increase in the number of infiltration cycles (Figure 6.11). The relative

densities of these samples were listed in Table 6.1 in Section 6.3.1. Both TiC (light and bigger grains) and SiC (dark and smaller grains) phases consist of nano-sized grains (Figure 6.11d). The overall average grain size of the TiC/SiC composite is about 150 nm after 7 cycles of infiltration (Figure 6.11d). The sample prepared with 7 infiltration cycles is almost fully densified (99.5% relative density) and has very few pores (Figure 6.11d).

(a)   (b)

(c)   (d)
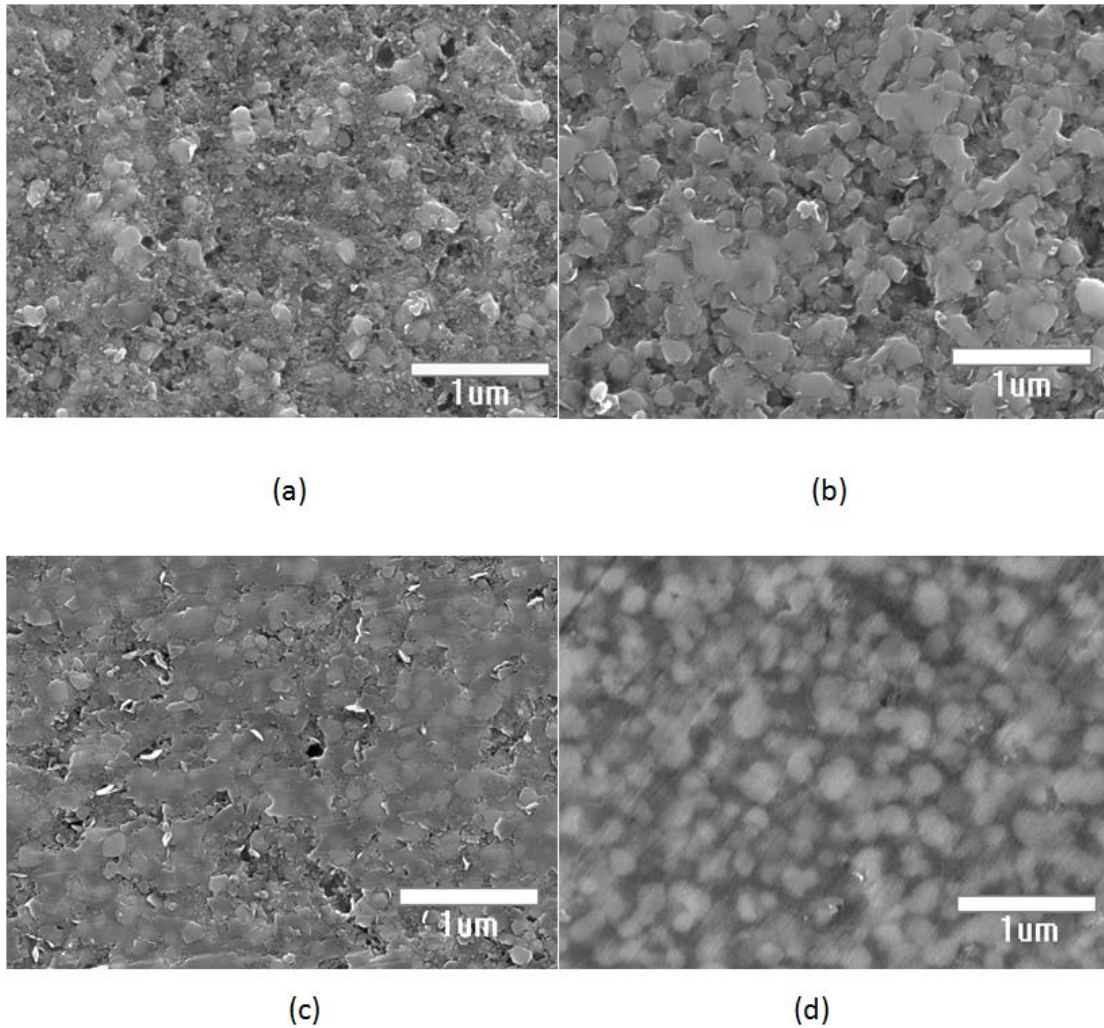
Figure 6.11 Microstructures of TiC/SiC composites prepared with different numbers of infiltration cycles of SiC and SPSed at 1800°C for 5min. (a) 1 cycle (b) 3 cycles (c) 5 cycles (d) 7 cycles

These results indicate that near fully dense TiC/SiC nano-composites can be produced by the sol-gel route described here, followed by spark plasma sintering. From the results in Figure 6.11, we can also find that there is only a small amount of grain growth with the increase in the number of infiltration cycles. The grain size of TiC increases from 100 nm for the sample with 1 infiltration cycle, to 150 nm for the one with 7 infiltration cycles. This means that this novel sol-gel infiltration approach can be used to improve the densification of TiC/SiC composites efficiently, without promoting obvious grain growth.

As a comparison, a monolithic TiC control sample, prepared by sol-gel processing, was also sintered by SPS under the conditions identical to those employed in sintering of the TiC/SiC composites (Figure 6.12). The relative density and grain size of the monolithic TiC are 95.2% and larger than 1 μm respectively. This means that sintered monolithic TiC has much bigger grains and larger porosity than the TiC/SiC composites. Therefore, it can be concluded that the introduction of fine SiC particles by sol-gel infiltration significantly hinders the grain growth of TiC and successfully fabricates dense TiC/SiC composites with a uniform nanostructure (Figure 6.11d). There are two main reasons supporting this conclusion. One is that the scaffolds prepared by sol-gel processing have a very high uniformly distributed open meso/macro-porosity and are very suitable for infiltration with a second phase material to achieve dense composites. Another is that the infiltrated second phase material with nano size at the grain boundaries of the scaffold grains greatly suppresses the grain growth of the matrix due to the pinning effect and thus helps to create fine composites with nanostructure. Improving densification while retaining a nano-sized grain structure can significantly increase the fracture strength and toughness of ceramic composites[147,151]. Compared with the commonly used nano-powder mixing approach[147], where relative densities achieved for TiC/SiC composites SPSed at the same temperature (1800°C) are only around 95% with TiC grain sizes ranging from 270nm to 700nm, the sol-gel infiltration approach has demonstrated some advantages, being a much smaller grain size, higher final density,

and more uniform microstructures for the fabrication of the composites with a nano-structure.

(a)   (b)
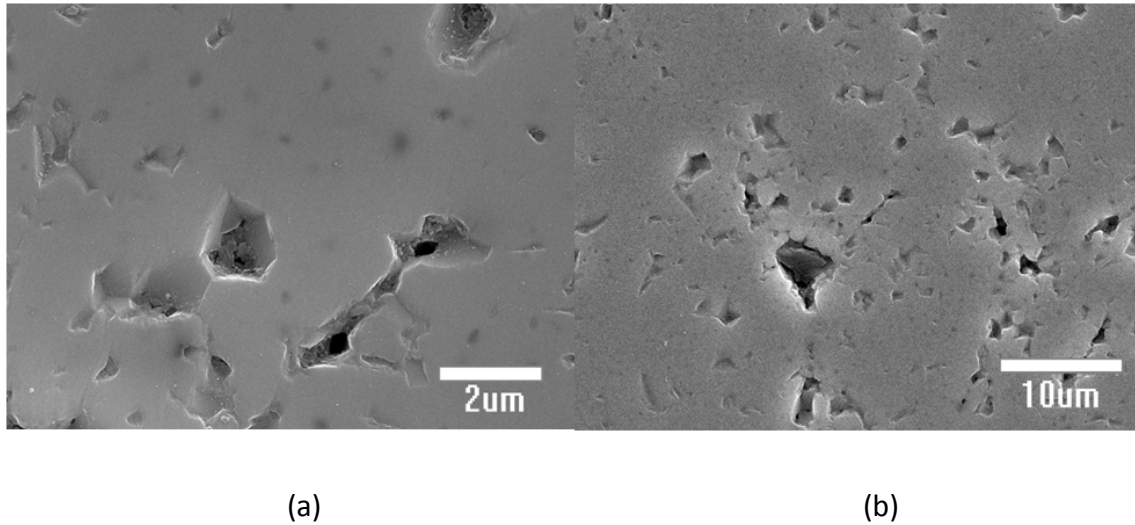
Figure 6.12 SEM micrographs of the monolithic TiC SPSed at 1800 °C. (a) high

magnification image; (b) low magnification image.

6.5 Tailoring residual carbon in the TiC scaffolds G by sol-gel infiltration

It is usually very difficult to remove the residual carbon in the materials prepared by sol-gel processing. However, another advantage of the sol-gel infiltration technique is that it can be used to tailor residual carbon in the scaffold, as well as to make composites. In this section, porous TiC scaffolds G, prepared by sol-gel processing with some residual carbon in them, are infiltrated with a ZrO_2 sol. This is followed by carbonization and carbothermal reduction of the scaffold at 550 °C and 1450 °C respectively for 2h after each cycle of the infiltration. Here a ZrO_2 sol was used instead of a SiO_2 sol, because the carbothermal reduction of SiO_2 is a gas phase reaction (Section 5.3.1 in Chapter 5) and a part of silicon will escape in the form of SiO gas during the carbothermal reduction reaction. Thus, a solid reaction phase, such as ZrO_2, will be more effective to consume

(remove) the residual carbon because the amount of the ZrO_2 that can react with the carbon will be more than that of SiO_2 with the same amount of addition in the starting sol-gel process during the carbothermal reduction process.

6.5.1 Effect of the number of infiltration cycles on the amount of residual carbon in the scaffolds

The initial residual carbon to metal ratio in the as-prepared TiC scaffold G was 0.31 after the carbothermal reduction at 1450°C, according to the calculation from the TGA analysis (Figure 6.13). The samples were tested in air and two reactions occurred in the temperature range, an initial weight gain due to TiC oxidation and the subsequent weight loss due to oxidation of residual carbon. From the TGA results, the amount of weight loss (the circle part on the TGA curve) decreases with the increasing number of infiltration cycles, until the fifth infiltration where little weight loss is found. This means that the residual carbon left in the TiC scaffold decreases with the increasing number of infiltration cycles, and almost no residual carbon is left in the scaffold after 5 cycles' infiltration.
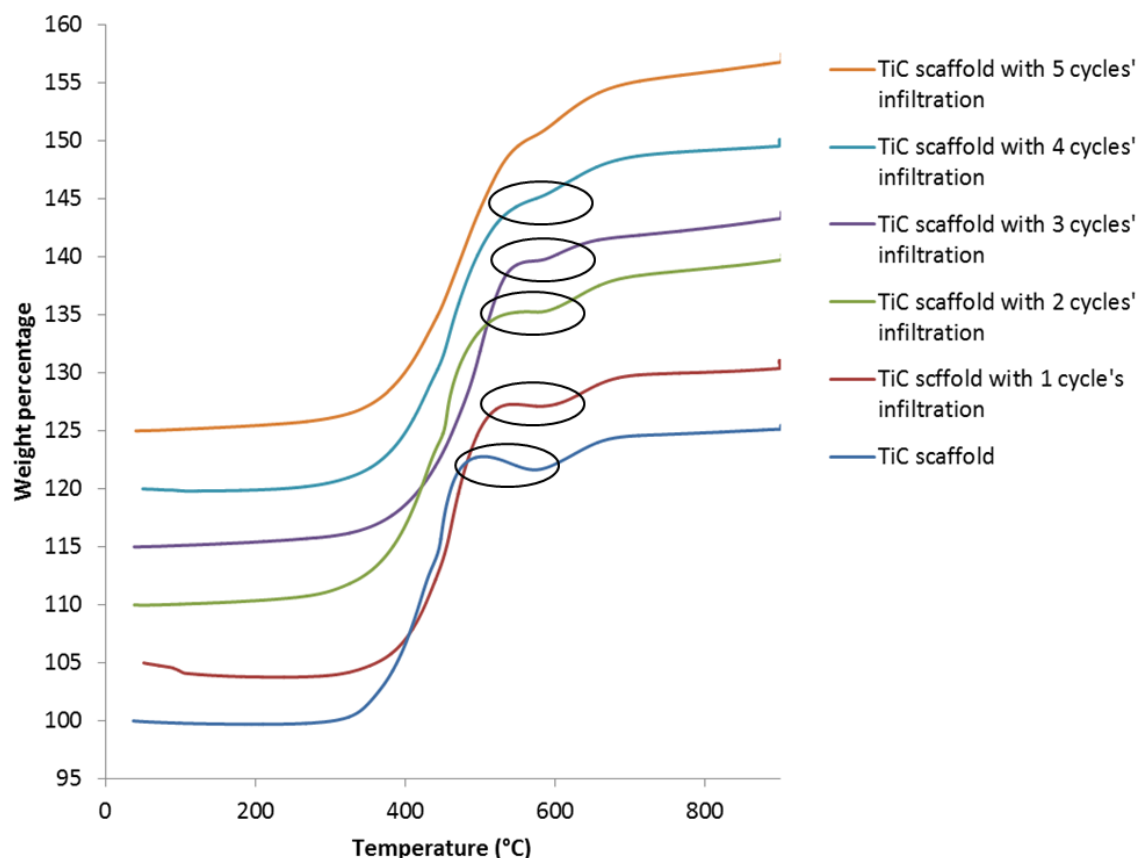
Figure 6.13 TGA analysis of TiC scaffolds with different numbers of infiltration cycles

6.5.2 Chemical analysis of the scaffolds with different numbers of infiltration cycles

The XRD patterns of the TiC scaffolds after different numbers of cycles of infiltration with ZrO_2 are shown in Figure 6.14. The results show that ZrO_2 is reduced to ZrC successfully, by reaction with the residual carbon in the scaffold during the carbothermal reduction at 1450 °C. All the ZrO_2 has fully reacted with the carbon in the scaffold during each infiltration cycle, because no ZrO_2 was found from the XRD patterns up to four cycles. The intensity of the ZrC peaks increases with the increasing number of infiltration cycles, which means more ZrC is present after each infiltration cycle. TGA analysis also indicates that the amount of residual carbon in the scaffold decreases with the number of infiltration cycles of the Zr-O sol. The XRD pattern of the TiC scaffold with

5 cycles' infiltration is shown in Figure 6.15. This result indicates that monoclinic zirconia phase was detected in the composite, along with TiC and ZrC, for the fifth number of infiltrations. This means that all the carbon in the scaffold had reacted with the infiltrated ZrO_2, and there was still some ZrO_2 left in the composite, after 5 cycles' of infiltration. Both XRD and TGA results show that the residual carbon has fully reacted with ZrO_2 after 5 cycles of infiltration, where the initial residual carbon to metal molar ratio in the scaffold is 0.31.
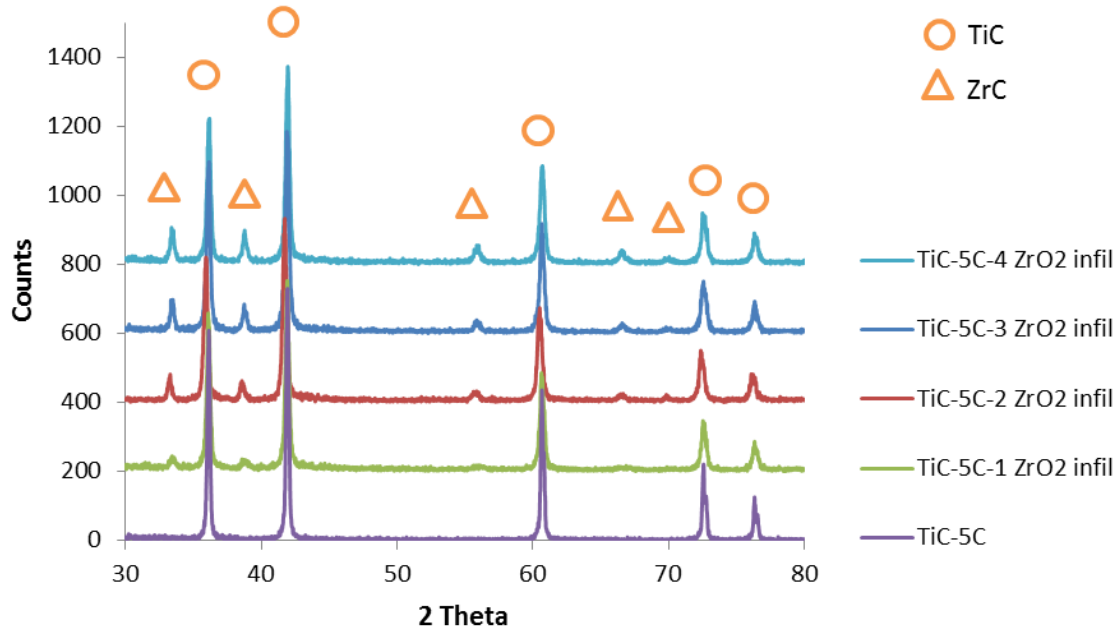
Figure 6.14 XRD patterns of the TiC scaffolds after different numbers of cycles of infiltration with ZrO_2
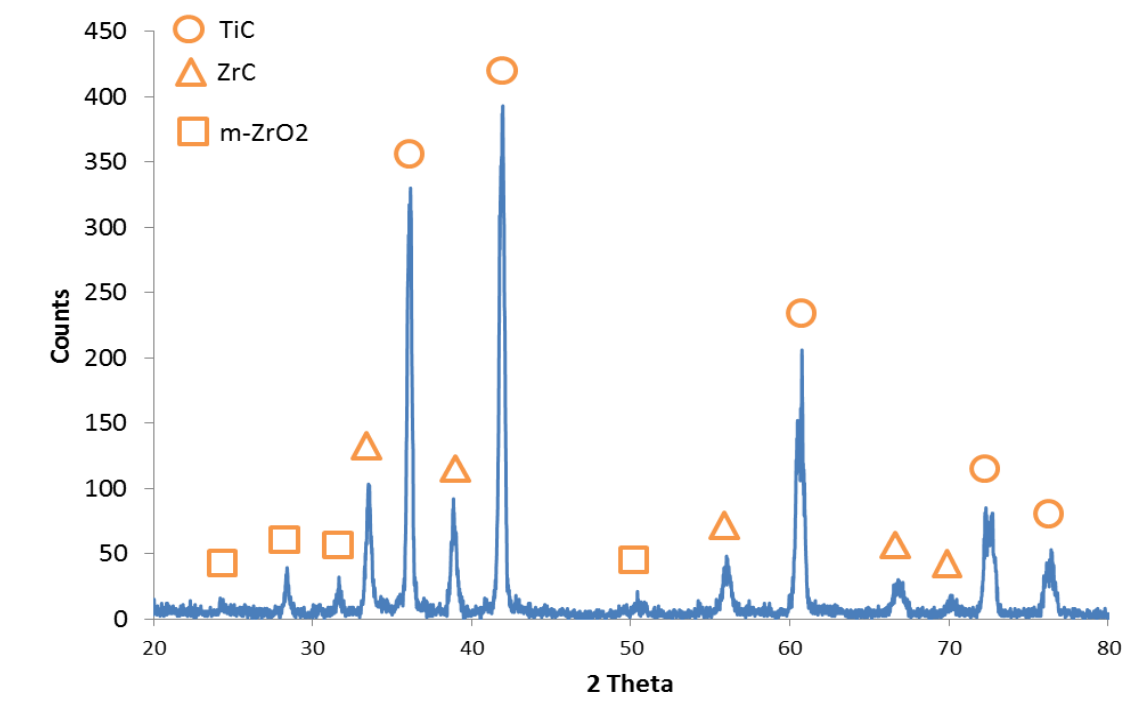
Figure 6.15 XRD pattern of the TiC scaffold with 5 cycles of infiltration with ZrO_2

6.6 Preparation of ZrB_2/SiC composites by sol-gel infiltration

ZrB_2 has been considered as a very attractive candidate for components used in aerospace applications due to its low theoretical density compared to HfB_2, excellent thermal shock resistance and high thermal conductivity. However, the oxidation resistance of ZrB_2 is not good enough for most high temperature applications, especially at temperatures above 1200 ^{o}C due to volatilization of the B_2O_3 liquid at these temperatures[195,196]. Researchers in the field have discovered that the addition of SiC to ZrB_2 and HfB_2 increases the oxidation resistance as well as the densification and thermal shock resistance of the composites[196-199]. In this section, the preparation of ZrB_2/SiC composites by sol-gel infiltration is studied and the oxidation resistance of the infiltrated ZrB_2/SiC composites was studied together with pre-coated ZrB_2/SiC composites

prepared by sol-gel coating and a monolithic ZrB_2 control sample in the following chapter.

The process for preparing porous ZrB_2 scaffolds is similar to the one described in Section 4.1 Chapter 4. Micro-sized commercial ZrB_2 powder (<5μm) was sintered by SPS to form porous scaffolds. The particle size of the ZrB_2 powder was less than 5μm. The sintering temperature was 1500 ^{o}C, and the holding time was 5 minutes. The heating rate was 100 ^{o}C /min. The dimension of the sintered ZrB_2 scaffolds is 10 mm in diameter and about 8 mm in thickness. The preparation of Si-O-C sol and the infiltration process are the same as the one described in Section 6.1. After infiltration, the ZrB_2 scaffolds were finally sintered again by SPS at 1900 ^{o}C for 5min under a uniaxial pressure of 40 MPa. The final sample was about 5 mm in thickness.

6.6.1 Microstructure of the ZrB_2 scaffold infiltrated with a Si-O-C sol

The microstructures of the surface layer of the final ZrB_2 composite after two cycle infiltrations and SPS sintering are shown in Figure 6.16. The results show that a functionally gradient ZrB_2/SiC composite is successfully fabricated by the proposed novel sol-gel infiltration technique. The thickness of the surface layer after two cycles of infiltration is about 500 μm (Figure 6.16a). The EDX analysis indicates that SiC is successfully infiltrated into the surface layer of the ZrB_2 scaffold (Figure 6.16c), but the core only has a small amount of SiC (Figure 6.16d). The weight percentage of SiC is about 3.5% in the surface layer according to EDX result. The oxygen in the surface layer may come from two sources. One is from the oxygen impurity of the initial ZrB_2 powder and the other is from the incomple carbothermal reduction of the infiltrated SiO_2 sol-gel. The microstructure shows that the surface layer of the infiltrated ZrB_2 scaffold is quite dense, while the core is still porous. The dark grains in Figure 6.1b are SiC and grey ones are ZrB_2. The grain size of ZrB_2 remains about 3~5μm after being sintered at 1900 ^{o}C, showing little grain growth compared to the original powder size (less than 5μm) (Figure 6.16b). The porosity of the surface layer is only about 3 percent.
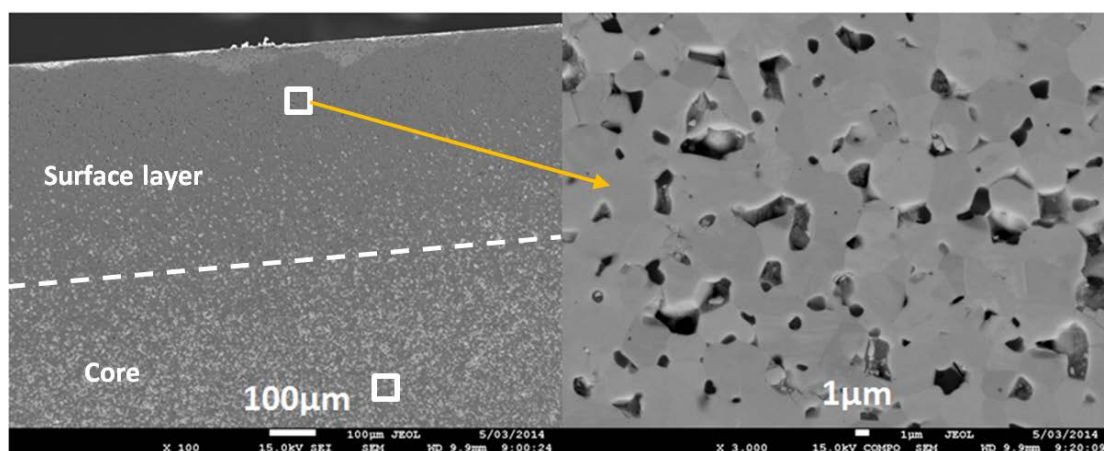
(a)   (b)
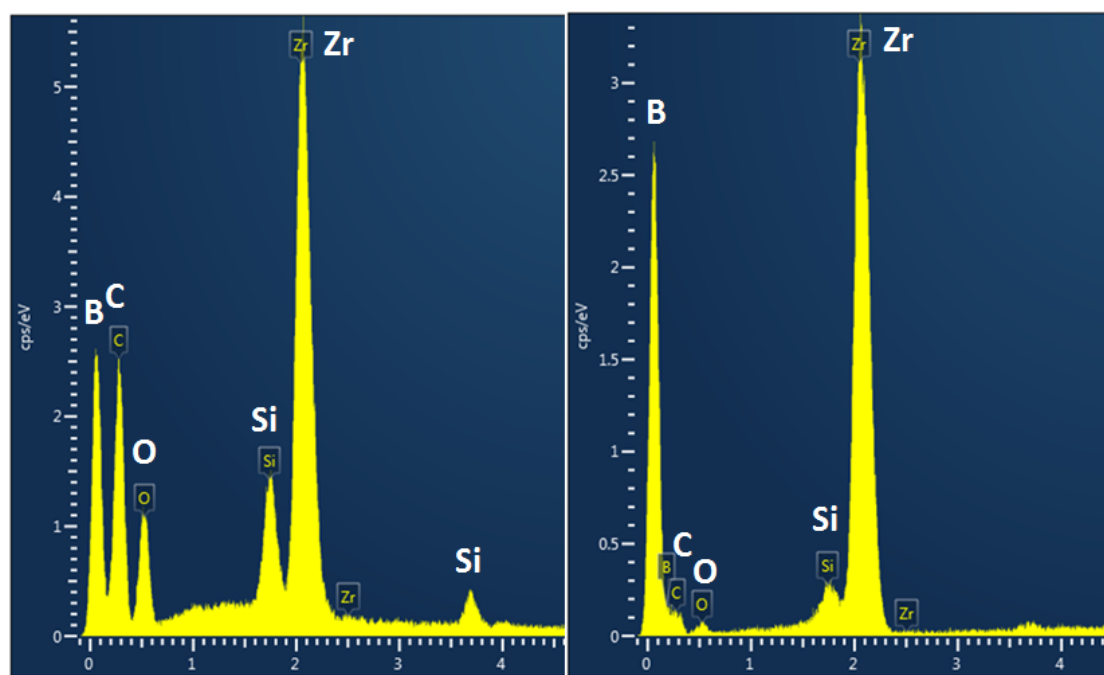
(c)   (d)

Figure 6.16 Microstructures and EDX of the ZrB$_2$ scaffold with infiltration of SiC sintered by SPS at 1900 $^\circ$C (a) cross section of surface layer and core of the composite; (b) a high magnification microstructure of the surface layer; EDX results of the (c) surface layer and (d) core.

6.6.2 Chemical analysis of the ZrB2 scaffold infiltrated with a Si-O-C sol

The XRD spectrum of the final ZrB_2 scaffold after sintering is shown in Figure 6.17. The result shows that only ZrB_2 and SiC phases exist in the infiltrated scaffold after sintering. The existence of SiC phase again clearly indicates the infiltration of ZrB_2 scaffold through the SiC sol-gel process is successful and effective.
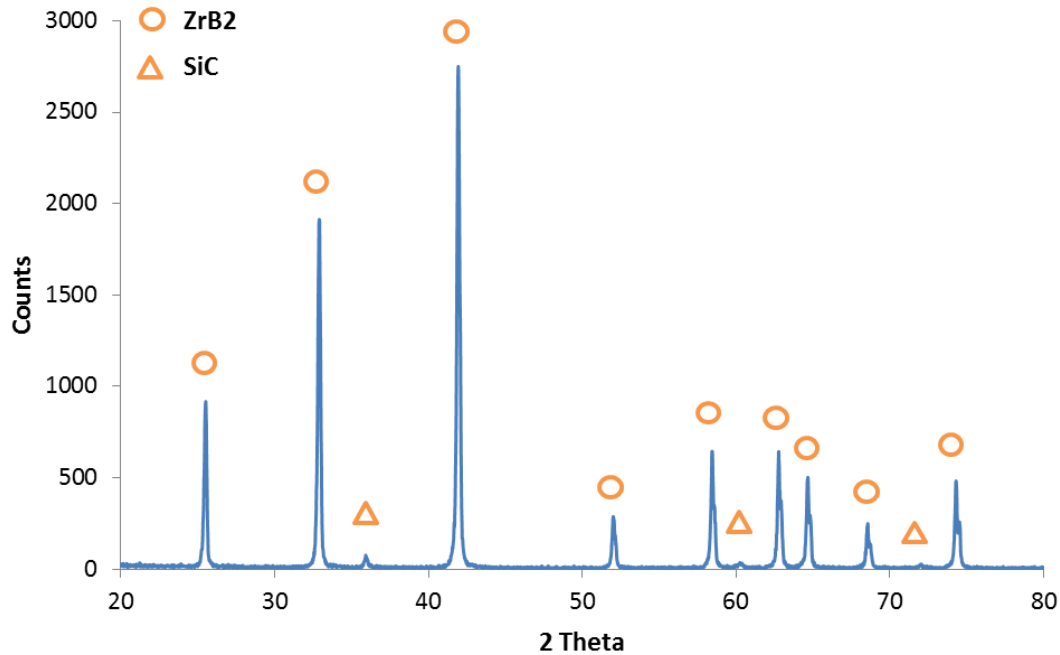
Figure 6.17 XRD spectrum of the ZrB_2 composite formed by infiltration of a Si-C-O sol and sintered by SPS at 1900 ^{o}C

Both the phases and microstructures of the infiltrated ZrB_2 scaffold show that this sol-gel infiltration technique is a promising and efficient approach for preparing functionally graded UHTC composites This unique gradient microstructure with a dense ZrB_2/SiC composite on the surface and a porous ZrB_2 in the core would improve not only the thermal shock resistance of the ZrB_2/SiC composite due to its high thermal conductivity at the dense surface, but also the oxidation resistance at high temperature, as well as high mechanical properties due to its dense fine microstructure in the surface layer. The

oxidation test of the infiltrated ZrB_2/SiC composites have been done and the results will be presented together with those of the pre-coated ZrB_2/SiC composites prepared via sol-gel coating in the next chapter.

6.7 Discussion

The introduction of SiC to TiC by sol-gel infiltration improves the densification of the TiC/SiC composites during spark plasma sintering compared with the monolithic TiC ceramic prepared at the same sintering conditions. There are several sintering mechanisms for the improvement in densification by the introduction of SiC via sol-gel infiltration besides those discussed in Section 5.6.2 in Chapter 5.

Residual carbon in the sol-gel derived TiC scaffold is a main obstacle preventing the materials densification[178,200]. The introduction of silica by the sol-gel infiltration can effectively reduce the amount of residual carbon in the TiC scaffold through the carbothermal reduction reaction of silica with the carbon. Tailoring the residual carbon left in the scaffolds has been proved successful in Section 6.5. As discussed in Section 5.6.1 in Chapter 5, a carbon concentration exceeding a certain critical level (4 wt% in this study) would hinder the densification of TiC/SiC composites, while the carbon concentration below this critical level would improve the densification. Thus, the introduction of a controlled amount of SiO_2 by sol-gel infiltration can effectively improve the densification of TiC/SiC composites by reducing the carbon concentration level in the material below the critical level.

The carbothermal reduction reaction during the SPS sintering process can also improve the densification of TiC/SiC composites by facilitating the mass transport process[201]. A small amount of oxides and carbon may still exist in the scaffolds after the initial carbothermal reduction at 1450 ^{o}C. These oxides and carbon will further react at the elevated temperature during the SPS sintering process and this chemical reaction can facilitate the mass transport, so to improve densification. From the carbothermal

reduction reactions described in Section 5.3.1 (equations 5-1 and 5-2), gas products were produced during the reactions. The SPS sintering was carried out under vacuum, but an increase in the chamber pressure was observed from 700 ^{o}C and became more significant above 1200 ^{o}C, and reached the maximum at about 1600 ^{o}C (Figure 6.18). For this particular system, this temperature range corresponds to the carbothermal reduction reactions (1567K and 1781K), in which gas products are generated so to increase the chamber pressure. The chamber pressure decreased above 1600 ^{o}C where the reactions completed gradually. The sharp decrease of the chamber pressure at 1700 ^{o}C was due to the termination of the sintering at the temperature.
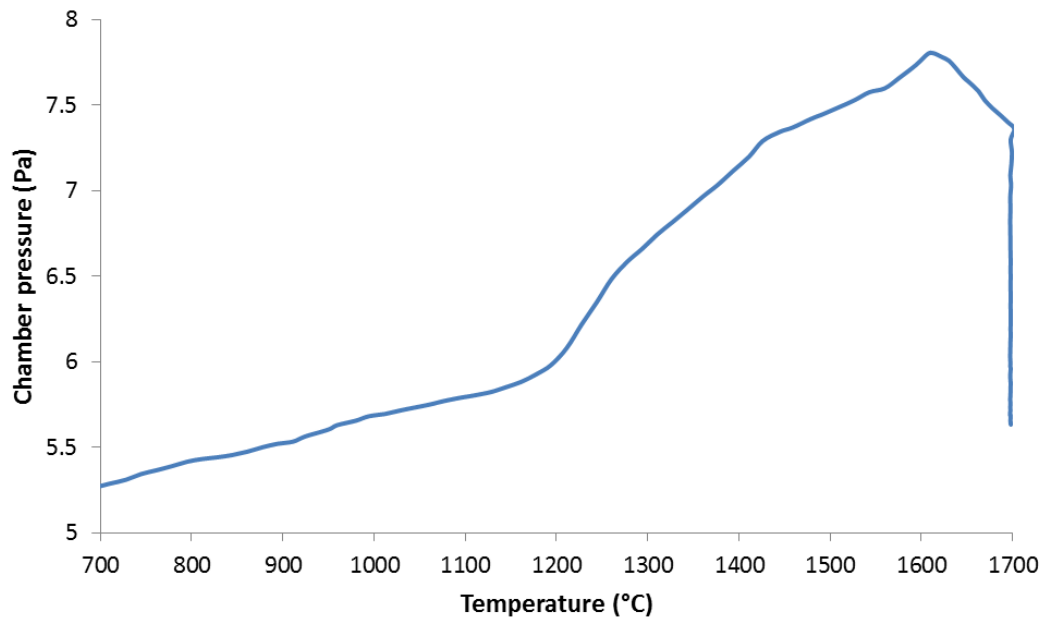
Figure 6.18 Change of the chamber pressure during the sintering process of the TiC scaffold infiltrated with SiC SPSed at 1700°C

In addition, the pinning effect of the SiC nano particles introduced by the sol-gel infiltration not only significantly hinders the grain growth of TiC, but also helps to form and keep channels along the TiC grain boundaries during the sintering process. These channels help the elimination of the air left in the scaffolds and the gas products of the

carbothermal reduction reactions so that facilitate the densification of TiC/SiC composites.

6.8 Summary

The sol-gel infiltration technique for preparing dense, or functionally gradient, TiC/SiC nanocomposites from porous TiC scaffolds is studied in this chapter. Near fully dense TiC/SiC composites with uniform nano-sized microstructure after 7 cycles of infiltration was successfully formed via SPS sintering at 1800 $^{\circ}$C. The grain size was only about 150nm. This compares favorably with the 95% density achieved with a monolithic TiC control sample with a grain size of larger than 1μm prepared at the same condition. Furthermore, compared with the conventional powder mixing approach[147], where relative densities achieved for TiC/SiC composites SPSed at the same temperature are only about 95% with grain sizes of a few hundred nanometers, this novel sol-gel infiltration approach also shows its advantages such as much smaller grain size, higher final density, and more uniform microstructures for the fabrication of the composites with a nano-structure. It is anticipated that the fine-grain microstructure of TiC/SiC composites would lead to improved mechanical properties. This sol-gel infiltration technique is also successfully used to tailor the residual carbon in the scaffold, which helps to facilitate densification of the composites.

The sol-gel infiltration is a useful technique to produce functionally gradient UHTC composites. Both TiC/SiC and ZrB_2/SiC systems were investigated and functionally gradient TiC/SiC and ZrB_2/SiC composites were produced by the Si-O-C sol-gel infiltration, followed by SPS sintering. For the TiC system, a dense TiC/SiC nanocomposites layer was formed on the surface of porous TiC scaffolds prepared by spark plasma sintering of commercial TiC nano powders. The thickness of the surface layer increased with the number of infiltration cycles, until it reached a maximum thickness of about 1 mm after 3 cycles of infiltration. The thickness of surface layer on a ZrB_2 scaffold was about

500µm after two cycles of infiltration, created a gradient microstructure with dense ZrB$_2$/SiC composite on the surface and porous ZrB$_2$ at the core. It is anticipated that the functionally gradient UHTC composites would have improved thermal shock resistance due to its high thermal conductivity and porosity. The dense SiC/ZrB$_2$ surface layer with nano sized grains is also expected to result in improved mechanical properties and better oxidation resistance at high temperature.

The sol-gel infiltration approach presented here not only has the advantages demonstrated above, but also offers some additional benefits for manufacturing. By utilizing the sol-gel infiltration approach, nano-sized powder handling can be avoided. The sol-gel infiltration approach will allow for the infiltration of complex shaped samples to produce functionally gradient material parts, which would be difficult to produce using conventional powder mixing approaches.

Chapter 7 Sol-Gel Coating of Powders for Carbide Ceramic composites

With a melting point of ~3200 °C, zirconium diboride is one of the leading candidates for thermal protection systems in hypersonic flight and refractory materials due to its low density (6.09 g/cm^3) compared to HfB$_2$ (11.2 g/cm^3) and high thermal conductivity and excellent thermal shock resistance. However, its densification is challenging. Densification of ZrB$_2$ powders can be improved by additives. Higher melting point metals such as Ir, W, Nb and Mo, as well as silicides of Zr, Ta and Mo, are often selected as sintering additives[202-204]. However, these methods have reported reduced refractory performance, due to the metal or residual metal oxides and glassy phase remained in the sintered material. As a similar refractory ceramic, silicon carbide is the most commonly reported additive in zirconium diboride[205,206]. Silicon carbide is commonly added due to its high melting point, high hardness and especially, good oxidation resistance.

ZrB$_2$/SiC composites have been generally produced via powder mixing. However, during green body preparation and sintering of the composites, challenges remain for mixing the second phase evenly at the boride grain boundaries. This is especially true for fiber, whisker or nanoparticle additions, as these methods may not be easily integrated into powder processing.

The sol–gel process is one of the leading techniques for producing different morphologies and nanostructures of ceramic composites. In this chapter, a method of integrating powder and sol-gel processing for the fabrication of ZrB$_2$/SiC composites is investigated. Nano-sized SiC particles were integrated onto ZrB$_2$ powders evenly by coating commercial ZrB$_2$ powders with a SiC sol-gel precursor followed by sintering via SPS to prepare dense ZrB$_2$/SiC composites.

7.1 Experimental procedure

7.1.1 SiC sol-gel precursor preparation

The SiC sol-gel precursor was first prepared. The process of making Si-O-C sol is similar to the one described in Section 6.1 in Chapter 6 except for the molar ratio of furfuryl alcohol to TEOS, which ranges from 1.2 to 3 (i.e. 6C to 15C) depending on the SiC/ZrB_2 molar ratio. The molar ratio of SiC to ZrB_2 was designed ranging from 0.1 to 0.3. Although the optimized molar ratio of furfuryl alcohol to TEOS for minimized residual carbon left in the carbides after carbothermal reduction is 0.72 (refer to Section 5.3.1 in Chapter 5), excess carbon is used here due to the oxide impurity in the ZrB_2 commercial powder. Previous work showed that there were two carbothermal reactions in the system during the carbothermal reduction process[207], one to reduce the surface oxide films on ZrB_2 and the other to convert the sol–gel oxides. To produce composites with different SiC ratios, the FA content will need to be varied. This is to ensure complete carbothermal reduction. Another reason for using a large range of molar ratio of furfuryl alcohol to TEOS is to determine the minimum amount of carbon required to minimise oxide existing in the materials. If sufficient carbon was provided, this would result in only carbides and diborides after carbothermal reaction at elevated temperatures.

7.1.2 Coating of ZrB_2 powders with the SiC sol-gel precursor

After solutions were prepared and aged for 72 h at room temperature, they were transferred to open containers. Here the commercial ZrB_2 powder was added during stirring. Coating the sol on the ZrB_2 powder should take place while the powder was immersed, as it was extremely adhesive to any surface. The ZrB_2 powder was added based on the designed SiC/ZrB_2 molar ratio (0.1~0.3) in the composite. Alcohol drying resulted in rapid gelation of the powder–gel composite, at which point no mechanical stirring was possible. Further drying occurred at $80^{o}C$ for 24h to completely remove ethanol. The gel often formed a gray green body. This powder-gel cast in the container

often shrank, and maintained green body cohesion during furnace transfers. The powder-gel cast was mixed with acetone and crushed by an agate pestle and mortar and dispersed ultrasonically. Then the crushed powder was dried in an oven at 80 ^{o}C. The dried powder-gel cast was calcined in a quartz tube furnace. This was performed under flowing nitrogen at a heating rate of 5 ^{o}C /min to a maximum temperature of 550 ^{o}C. This occurred over a time frame of 5 h to allow the decomposition of the surfactant, and to remove any residual monomer, FA. After calcination, the powder-gel was heated in an alumina tube furnace at 2 ^{o}C /min to 1450 ^{o}C and kept at that temperature for 5 h, under an argon atmosphere. This allowed for carbothermal reduction. After carbothermal reduction, the powder-gel was crushed by an agate pestle and mortar, and then finally sieved before sintering. No milling was used in order to minimize oxygen uptake. The ZrB_2/SiC composite was lastly sintered, via spark plasma sintering (SPS), to achieve the consolidated composite.

Through the method described, nano-sized SiC particles were coated on the surface of ZrB_2. This leads to uniform and dense ZrB_2/SiC composites with homogenous microstructures after the SPS sintering. A schematic diagram of the synthesis and sintering process is shown in Figure 7.1. The elemental impurities in the ZrB_2 powder are listed in Table 7.1.

Table 7.1 Impurities in ZrB_2 powder from H.C. Starck

Impurity	Mass fraction
Carbon	0.2% max
Oxygen	1.5% max
Nitrogen	0.25% max
Iron	0.1% max
Hafnium	0.2%-2.5%
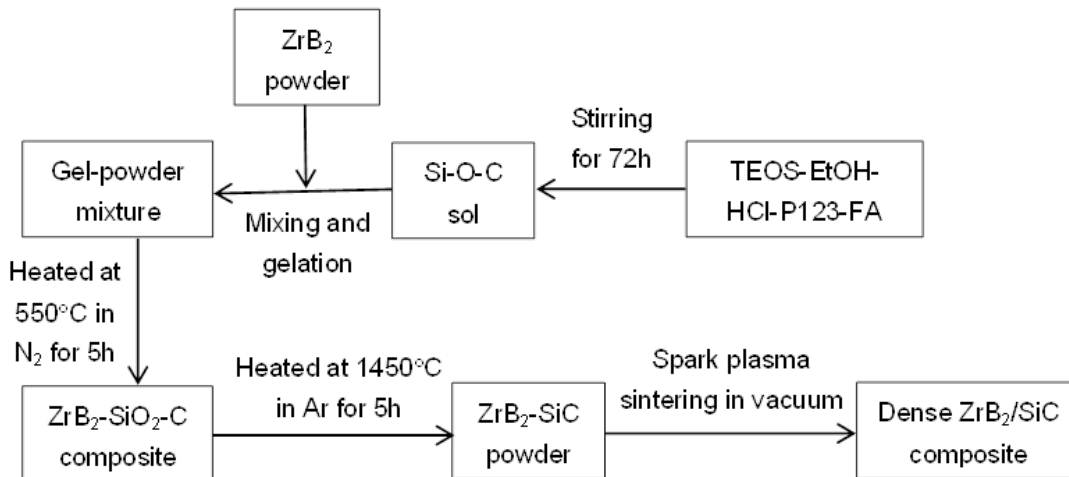
Figure 7.1 Schematic process of the preparation of ZrB$_2$-SiC composites by sol-gel coating and spark plasma sintering

7.2 Chemical analysis and microstructure of the ZrB$_2$ powder coated with SiC

SEM micrographs of the starting ZrB$_2$ powder are shown in Figure 7.2. The particle size of ZrB$_2$ is about 3-5 μm. EDX result shows that some oxide impurity can also be found on the surface of the ZrB$_2$ particles (Figure 7.2c). This is because of the initial oxygen impurity (Table 7.1). The weight percentage of oxygen is about 2.5%, which is a bit higher than the initial oxygen impurity, possibly because the EDX analysis was not so precise and the ZrB$_2$ powder was further oxidized during the storage process after first usage. This is also why the carbon/silica ratio of 6 to 20 (excess carbon) was designed during the sol-gel processing. The excess carbon was introduced not only for reducing the silica precursor to silicon carbide, but also for removing the oxygen impurity in the as-received ZrB$_2$ powder.
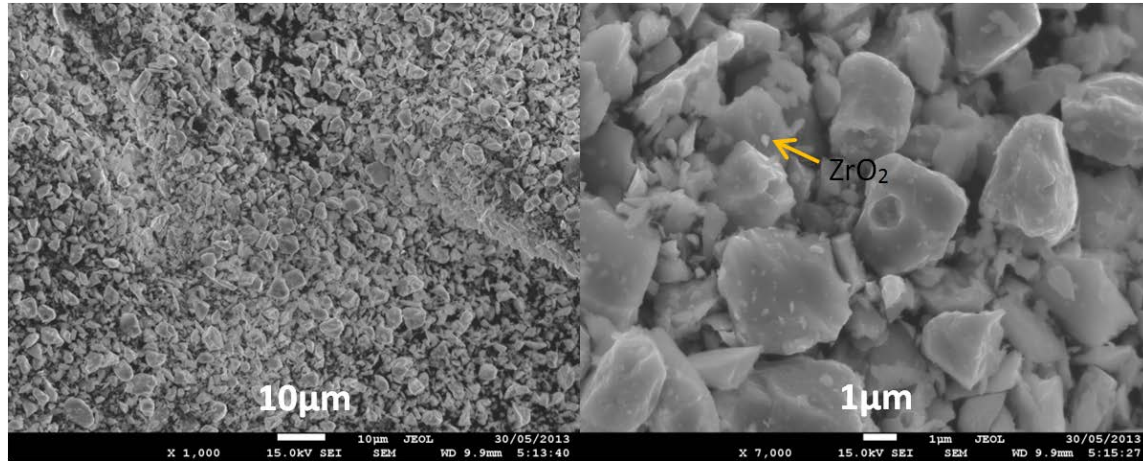
(a)   (b)
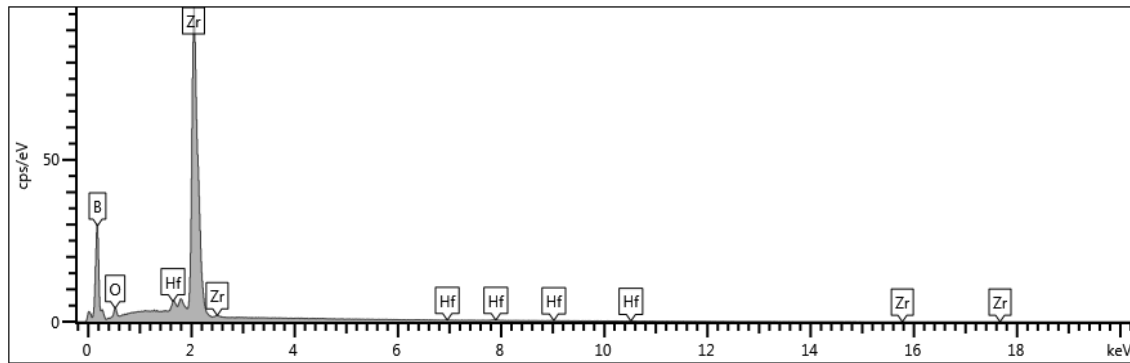
(c)

Figure 7.2 Micrograph of the starting ZrB_2 powder (a) low magnification (b) high

magnification (c) EDX result at the spot labeled by the arrow in (b).

7.2.1 Chemical analysis of the ZrB_2 powder coated with SiC

XRD pattern of the ZrB_2 powder coated with SiC by the sol-gel process after

carbonization at 550^oC in N_2 for 5 hours and carbothermal reduction at $1450\,^oC$ in Ar for

5 hours is shown in Figure 7.3. The molar ratio of SiC to ZrB_2 is 0.3 here. The result

clearly indicates the existence of the SiC phase along with the ZrB_2 phase. No oxide is

detected in the ZrB_2/SiC composite, which means all the oxides have been reduced to

carbides after being heat treated at 1450 °C due to the excess carbon introduced by the sol-gel processing.
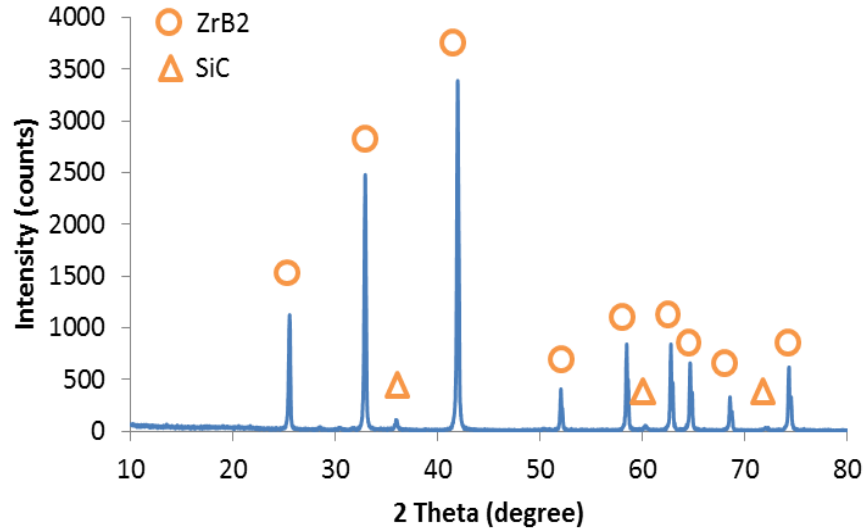
Figure 7.3 XRD pattern of the ZrB_2 powder coated SiC (SiC/ZrB_2=0.3) after carbothermal reduction at 1450 °C in Ar for 5h

7.2.2 Microstructure of the ZrB₂ powder coated with SiC

The SEM micrographs of the ZrB_2 powder coated with SiC are displayed in Figure 7.4. We can find that the grain size and morphology of the ZrB_2 do not change after heat treatment at 1450 °C (Figure 7.2 and Figure 7.4). Fine SiC particles are coated on the surface of ZrB_2 grains evenly (Figure 7.4b). The grain size of SiC is about 150 to 200 nm. The morphology of SiC grains looks more like elongated grains or short whiskers than equiaxed particles (Figure 7.4b). When a Si-O-C composition is heated in an inert atmosphere, the following carbothermal reduction reactions could take place from a thermodynamic point of view:

$SiO_2(s) + C(s) \rightarrow SiO(g) + CO(g)$ (7-1)

$SiO(g) + 2C(s) \rightarrow SiC(s) + CO(g)$ (7-2)

$$SiO(g) + CO(g) \rightarrow SiC(s) + CO_2(g) \tag{7-3}$$

The first two reactions are more common in an environment where there is a sufficient amount of carbon. In an environment with insufficient carbon, the third reaction could also take place. During the carbothermal reduction reaction, the ZrB_2 particles may act as seeds for the formation of SiC and the morphology of SiC tends to be short nano-fibres (whiskers) rather than equiaxed particles[136]. In addition, as a product of the gas phase reactions (equation 7-2 and 7-3), SiC particles tend to stick together to form elongated shapes to reduce their surface energy.
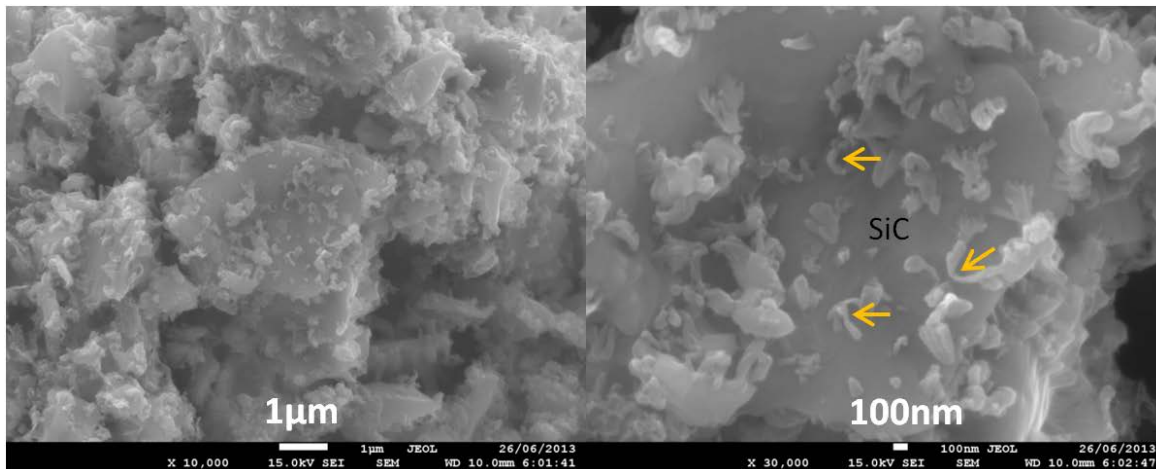
(a)   (b)

Figure 7.4 SEM micrographs of the ZrB_2 powder coated with SiC (SiC/ZrB_2=0.3) after firing at 1450 °C for 5 hours in Ar. (a) low magnification (b) high magnification

To confirm the fine particles on the surface of ZrB_2 grains, TEM was done on the ZrB_2 powder sample coated with SiC. The results of the TEM analysis, the micrographs and EDS are shown in Figure 7.5. The size of the ZrB_2 particle is about 500nm. The small ZrB_2 particle is chosen for the TEM analysis because the electron beam can only penetrate a thickness of a few hundred nanometers. The TEM mapping shows that the big dark green grain is ZrB_2, and the small orange ones surrounding the ZrB_2 grain are SiC (Figure

7.5a). The grain size of SiC is about 200nm, which is consistent with the SEM observation (Figure 7.4b). The dark field image also confirms that the big white grain in the core is ZrB_2 due to the heavy atomic weight of zirconium, and the grey grains surrounding the ZrB_2 grain are SiC (Figure 7.5b). There are also some small zirconium oxide particles left on the surface of ZrB_2 grains (Figure 7.5a and 7.5b). This indicates that a small amount of oxides still remained in the ZrB_2 powders even after the carbothermal reduction process, which can be further reduced to carbides during the following SPS sintering at elevated temperature. The overall amount of oxygen in the ZrB_2 powder was very small (Figure 7.2c), thus no oxide peaks can be found from the XRD spectrum. Finally the EDS result also indicates the existence of silicon element. All these results show that the nano-sized SiC particles are evenly coated on the surface of the ZrB_2 grains successfully using this sol-gel coating technique.
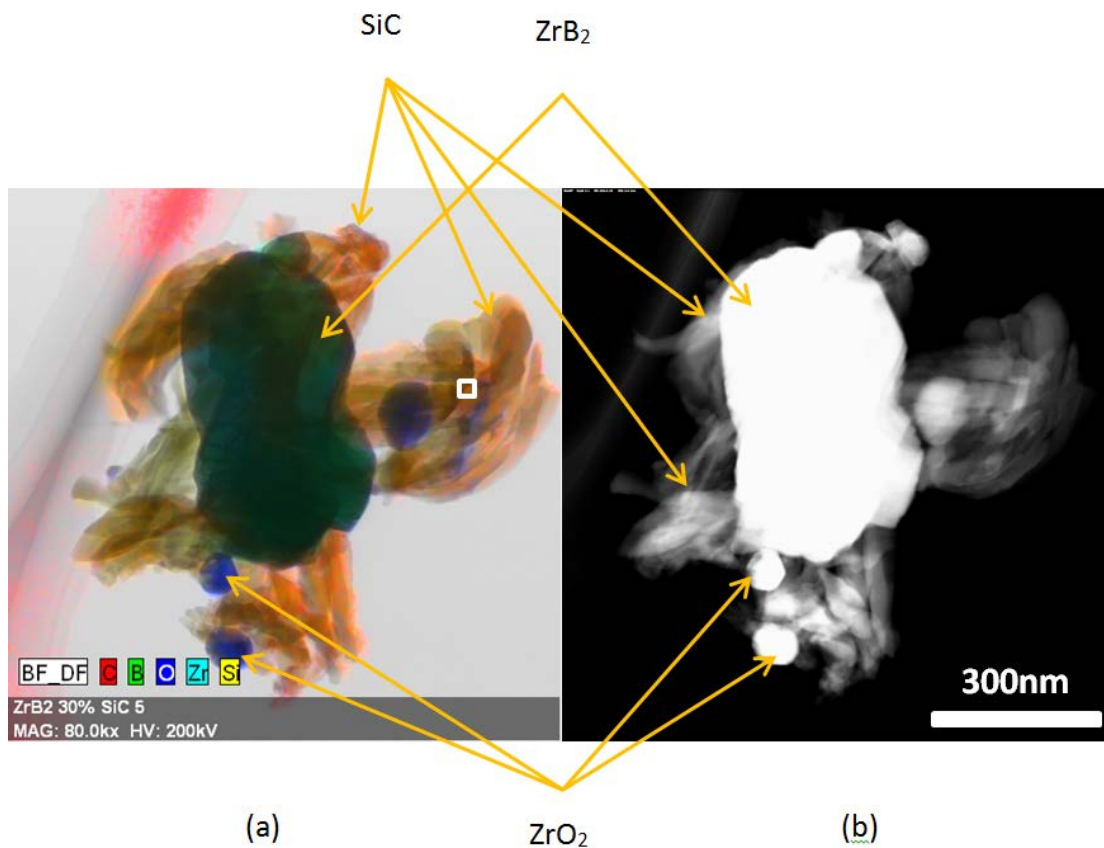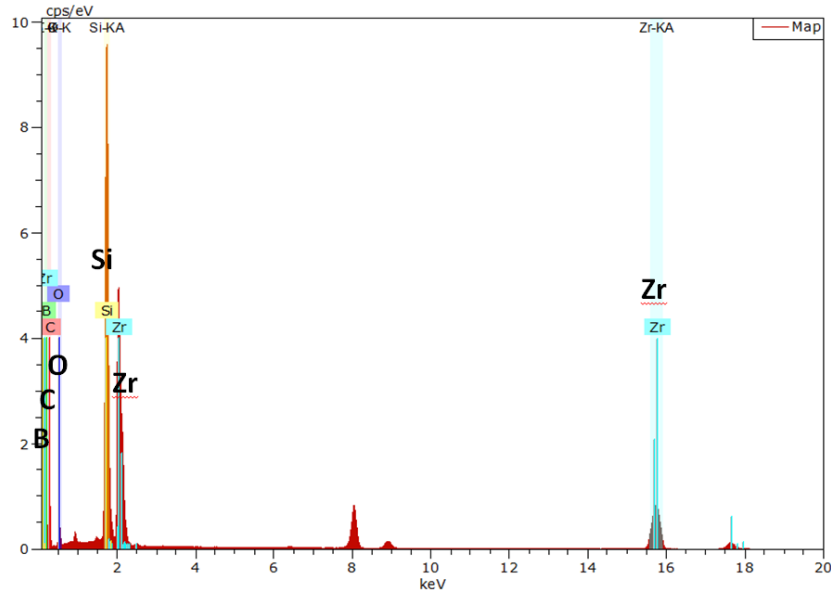
(c)

Figure 7.5 TEM micrographs and EDS analysis of the ZrB_2 powder coated with SiC (SiC/ZrB_2=0.3) after firing at 1450 °C for 5 hours in Ar. (a) map of the elements (b) dark field image (c) EDX result at the spot labelled by a square in (a)

7.3 Effect of the SiC/ZrB_2 molar ratio on the phases, microstructure and densification of the ZrB_2/SiC composites

To study the effect of SiC on the microstructure and densification of the ZrB_2/SiC composites, different SiC/ZrB_2 molar ratios ranging from 0 to 0.3 were designed. According to the study in chapter 5, the optimized carbon/metal ratio for the SiC sol-gel should be 3.6. The 3.6 ratio gives the minimum amount of residual carbon in the carbide after the carbothermal reduction reaction. However, the starting ZrB_2 powder contains some oxygen impurities. Therefore the carbon/metal ratio of the SiC sol-gel precursor for the coating should be higher than 3.6 for completely reducing all the oxides to carbides. The actual carbon/metal ratio for the SiC sol-gel precursors ranged from 6 to

20, depending on the SiC to ZrB_2 molar ratio and the estimated oxygen impurity of the ZrB_2 powder. The lower the SiC/ZrB_2 molar ratio in the composition, the higher the carbon/metal ratio was used because the carbon introduced by the sol-gel precursors was used not only to reduce the silica precursor to silicon carbide but also to remove the oxygen impurity of the ZrB_2 powder.

7.3.1 Effect of the SiC/ZrB₂ molar ratio on the phases of the ZrB₂/SiC composites

The XRD patterns of the ZrB_2/SiC composites with four SiC/ZrB_2 molar ratios, 0.1, 0.15, 0.2 and 0.3, are displayed in Figure 7.6. The carbon to metal ratios in these four compositions are 8C, 10C, 12C and 15C respectively due to the different SiC/ZrB_2 ratios. The XRD results find no oxide phases in the samples, which means that all the oxides have been reduced to carbides completely, after the heat treatment at 1450 °C for 5 hours in Ar. The intensity of SiC peaks increases with increasing SiC/ZrB_2 molar ratio. This confirms that more SiC is coated on the surfaces of the ZrB_2 particles, with increasing SiC content in the sol-gel powder mixture. ZrC phase can also be found in the composites with lower SiC/ZrB_2 ratios (0.1 and 0.15). This is because of the overestimate of the oxygen impurity in the ZrB_2 powder, which leads to a high carbon/metal ratio being used. In these composites with excess carbon, some ZrB_2 is first oxidized and becomes zirconia, followed by reducing from zirconia to ZrC by excess carbon during the carbothermal reduction process at 1450°C, so that the amount of ZrC is higher than those without excess carbon.
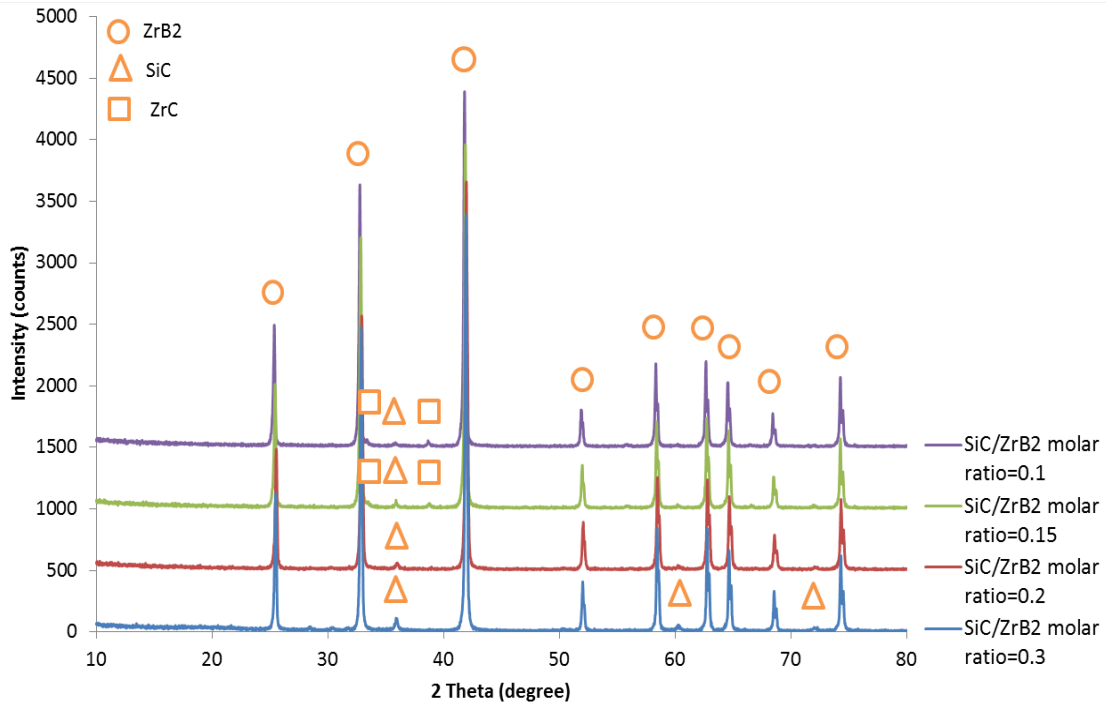
Figure 7.6 XRD patterns of the ZrB_2/SiC composites with different SiC/ZrB_2 molar ratios after firing at 1450 °C for 5 hours in Ar.

7.3.2 Effect of the SiC/ZrB_2 molar ratio on the microstructure of ZrB_2/SiC composites

The SEM micrographs of the ZrB_2/SiC composites with different SiC/ZrB_2 ratios, after carbothermal reduction, are shown in Figure 7.7. The carbon to metal ratios in these four compositions are 8C, 10C, 12C and 15C respectively. We can find that there are very few SiC particles on the surface of the ZrB_2 grains in the composite with SiC/ZrB_2=0.1, and some residual carbon can be found instead (Figure 7.7a). This is also because of the overestimate of the oxygen impurity in the ZrB_2 powder, leading to a high carbon/metal ratio to be used for the composites with lower SiC/ZrB_2 ratios. With too little silica, the carbon just reacted to form silicon monoxide and evaporated off, leaving some residual carbon behind. The quantity of the SiC particles coated on the surface of ZrB_2 grains increases greatly with the increase of SiC content in the

composites (Figure 7.7b, 7.7c and 7.7d). Nano-sized SiC particles can be found more clearly in the composites with high SiC/ZrB$_2$ ratios. This is because the carbothermal reduction between SiO$_2$ and carbon in the sol-gel precursor is a gas phase reaction. Only a part of SiC particles can be coated on and stuck to the surface of ZrB$_2$ grains and the rest reacted to form monoxide and just evaporated off. The morphology and size of the SiC grains also changed with increasing SiC content.

The morphology of SiC grains is mostly particles in the composites at low SiC contents (Figure 7.7a, 7.7b and 7.7c), however it becomes short elongated shape at high SiC contents (Figure 7.7d). The grain size of SiC also increases from about 100 nm in the sample with a low SiC content (Figure 7.7a and 7.7b), to larger than 300 nm in the one with SiC/ZrB$_2$=0.3 (Figure 7.7d). These differences are due to the nature of the gas phase reaction of the carbothermal reduction of SiC gel, in which the SiC grains grow up along the direction of gas evaporation.
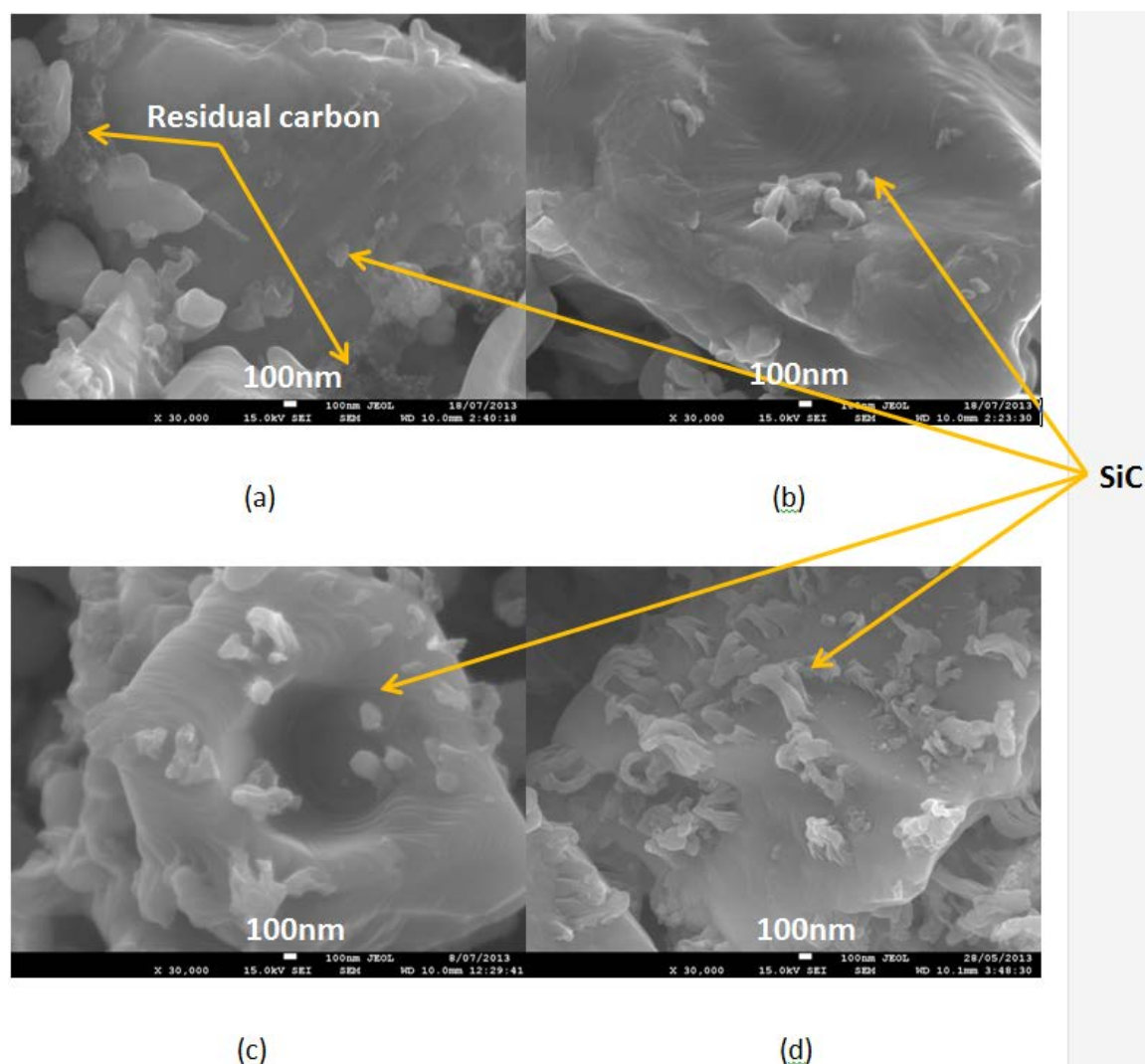
Figure 7.7 SEM micrographs of the ZrB_2/SiC composites with different SiC/ZrB_2 ratios after firing at 1450 °C for 5 hours in Ar. (a) SiC/ZrB_2 =0.1 (b) SiC/ZrB_2 =0.15 (c) SiC/ZrB_2 =0.2 (d) SiC/ZrB_2 =0.3

7.3.3 Effect of the SiC/ZrB_2 molar ratio on densification of the ZrB_2/SiC composites

To study the effect of the SiC content on the densification behavior of the sol-gel coated ZrB_2/SiC composites during spark plasma sintering, four ZrB_2/SiC composite samples were prepared. The SiC/ZrB_2 molar ratio of these samples were 0, 0.15, 0.2 and 0.30,

respectively. These samples were sintered via SPS at 1900 °C for 5 min. The heights of the original green body samples are all about 10mm. The shrinkage curves from the SPS process are shown in Figure 7.8. The temperature at which the shrinkage due to sintering exceeds the thermal expansion of the graphite die assembly is identified for each sample as the lowest point on the displacement curve (refer to the arrows in Figure 7.8). These results show that the shrinkage/sintering starts at about 1480 °C for the control ZrB_2 sample (SiC/ZrB_2 molar ratio=0). For the composite samples with the SiC/ZrB_2 molar ratio of 0.15, 0.2 and 0.3, the temperatures that the shrinkage begins are much lower than that of the control sample. The shrinkage/sintering for the composite samples begin around 1360 °C, 1260 °C and 1220 °C respectively. The total shrinkage of the sample at the pressing direction also increases with increasing SiC content from about 3.4 mm for the control ZrB_2 sample to about 4.2 mm for the ZrB_2/SiC composite with a SiC/ZrB_2 molar ratio of 0.3. These results indicate that the densification of the ZrB_2/SiC composites via SPS is improved with the increase of the SiC content due to the agglomeration of nano-SiC particles coated on the surface of ZrB_2 powders[201] and the dissolution between SiC and ZrB_2 at elevated temperature (Figure 7.11).
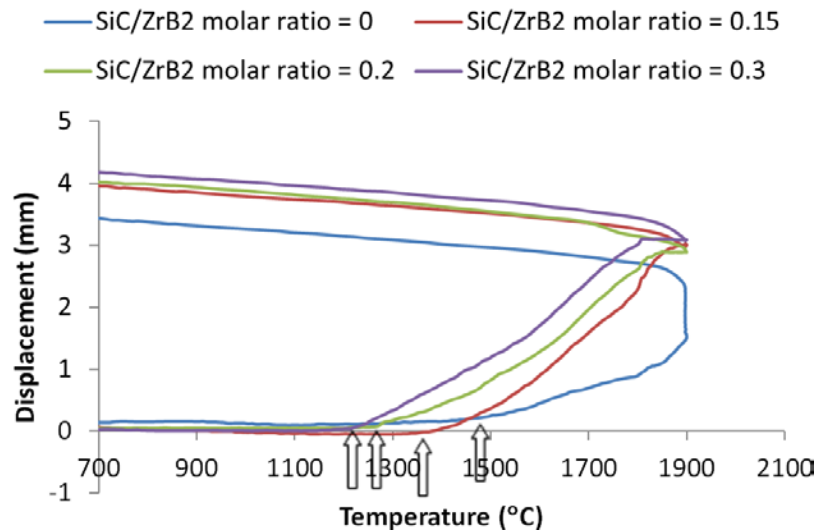
Figure 7.8 Shrinkage curves of the ZrB_2/SiC composites SPSed at 1900 °C with different concentration of SiC

7.3.4 Effect of SiC on the microstructures of SPSed composites

SEM micrographs of the ZrB_2/SiC composites, with different SiC/ZrB_2 ratios, sintered by SPS at 1900 °C are shown in Figure 7.9. As a control sample, ZrB_2 was also sintered at the same temperature. The big grey particles are ZrB_2 grains and the small dark ones are SiC. We can see that the grain size of the ZrB_2 control sample is 6-7 μm, and the porosity is about 10 percent according to the SEM image (Figure 7.9a). There is some grain growth for the control sample after being sintered at 1900 °C, compared with the size of less than 3-5 μm for the starting ZrB_2 powder (Table 3.1 in Chapter 3).

However, there are only a few pores in the ZrB_2/SiC composites, and there is not much grain growth (Figure 7.9b, 7.9c and 7.9d). The grain size of ZrB_2 in the ZrB_2/SiC composites is about 5 μm, and even lower in the composite with SiC/ZrB_2 molar ratio of 0.3 (Figure 7.9d). The grain size in this composite is approximately the similar size of the original ZrB_2 powder. So with the changing of the SiC/ZrB_2 ratio, the grain size of the ZrB_2/SiC composite decreases from about 5 μm to 3 μm (Figure 7.9b, 7.9c and 7.9d). These results indicate that the sol-gel coated ZrB_2/SiC powders can be almost completely densified without obvious grain growth after being SPS sintered at 1900 °C without any sintering additives. This means that the introduction of SiC by sol-gel coating can improve the densification of ZrB_2 and greatly suppress its grain growth.
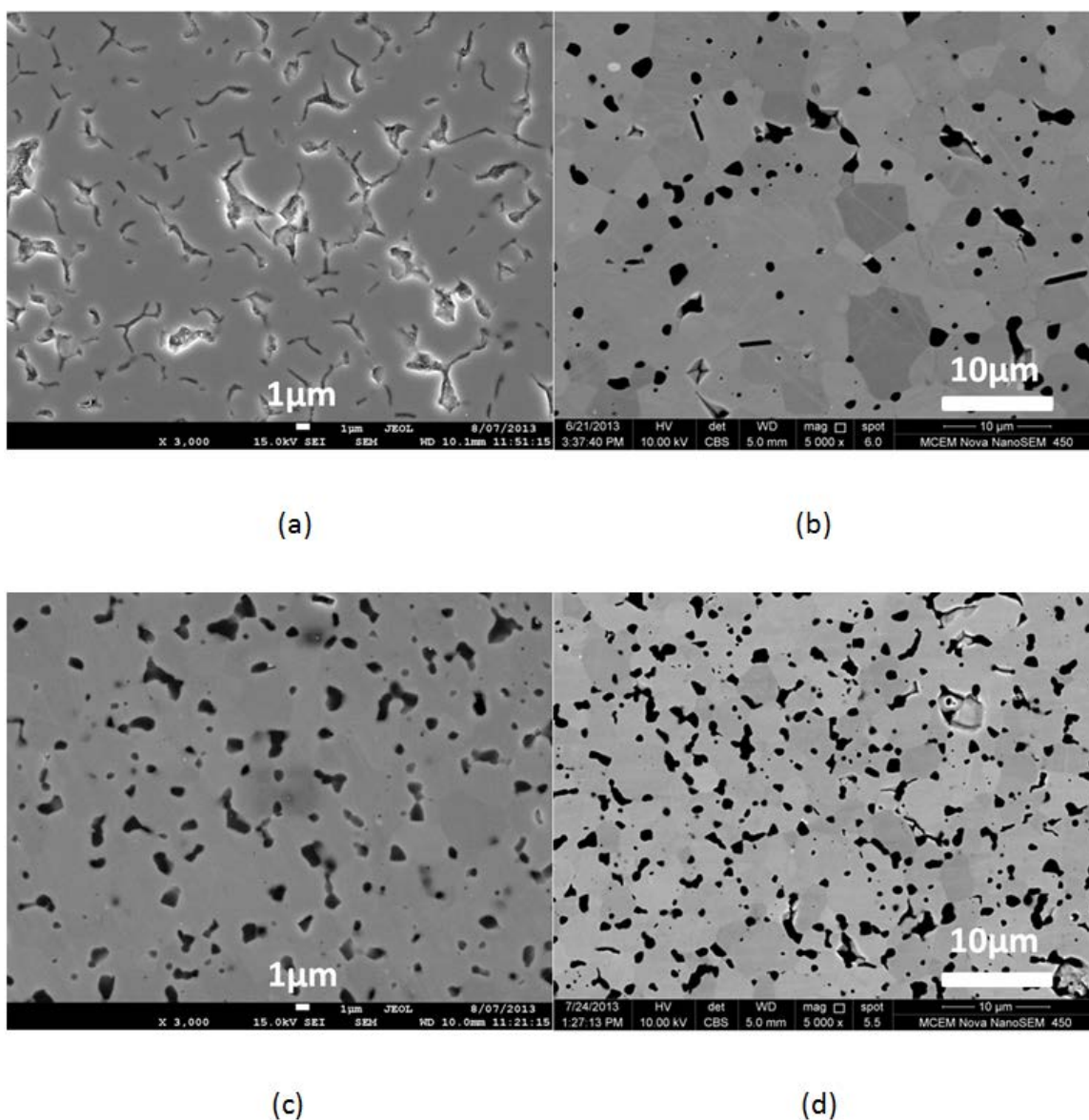
Figure 7.9 SEI SEM micrographs of the ZrB_2/SiC composites with different SiC/ZrB_2 ratios sintered by SPS at 1900 °C for 5 min. (a) SiC/ZrB_2 =0 (b) SiC/ZrB_2 =0.15 (c) SiC/ZrB_2 =0.2 (d) SiC/ZrB_2 =0.3

To compare the microstructure of dense ZrB_2 and ZrB_2/SiC composites, two samples were further sintered by SPS at 2000 °C, and their SEM micrographs are shown in Figure 7.10. We can find that the pore shape, pore size and porosity of the ZrB_2 sample sintered at 2000 °C are greatly different compared to the one sintered at 1900 °C

(Figure 7.9a and 7.10a). The pore size here is smaller, and the porosity is lower. The porosity has also changed in nature, with most of the pores being round and entrapped in the ZrB_2 grains. This is compared to the 1900°C sample, where the pores are mostly narrow gaps and on the grain boundaries. These differences arise because the ZrB_2 grains grow very fast at 2000 °C. The movement of the ZrB_2 grain boundaries is much faster than that of eliminating of pores, so that most of the pores are entrapped inside the ZrB_2 grains and become round in shape for minimizing the energy of the system. The grain size of the ZrB_2 control sample is about 20-30 μm (Figure 7.10a). On the contrary, the grain size and porosity of the ZrB_2/SiC composites sintered at 2000 °C (Figure 7.10b) are still less than 5 μm and similar to the one sintered at 1900 °C (Figure 7.9c). This means that the ZrB_2/SiC composite has been quite densified, but can be more densified, at 1900 °C and there is very little grain growth even at 2000 °C.
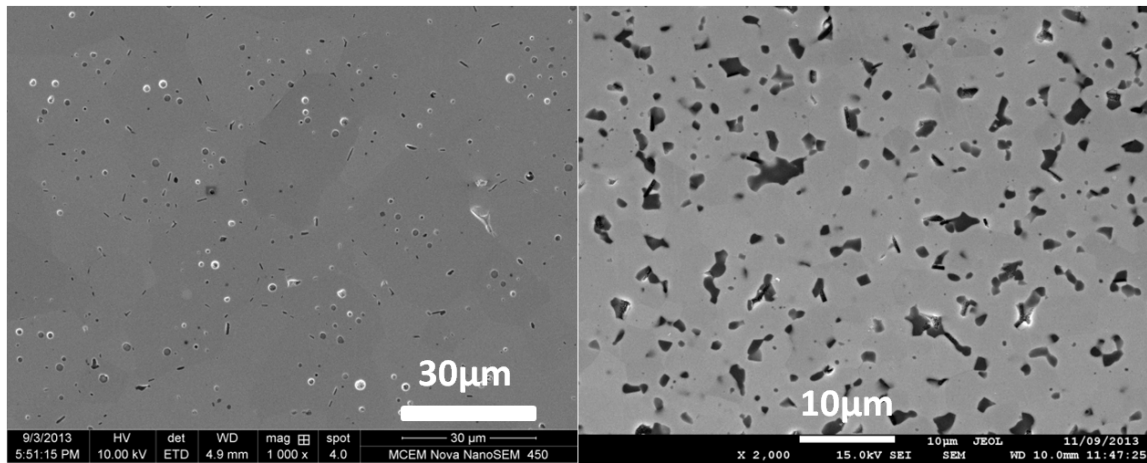
(a)   (b)

Figure 7.10 SEI SEM micrographs of the ZrB_2 ceramic and ZrB_2/SiC composites sintered by SPS at 2000 °C for 5 min. (a) ZrB_2 (b) ZrB_2/SiC composites (SiC/ZrB_2 ratio=0.2)

All these results indicate that the introduction of SiC by sol-gel coating not only greatly suppresses the grain growth of ZrB_2, but also improves its densification. One reason for this is that nano SiC particles introduce a pinning effect on the grain boundaries of ZrB_2,

which hinders the movement of the grain boundaries and thus the grain growth. Another reason is that there is some solid dissolution between the SiC and ZrB_2 two phases below 2000 °C according to the binary phase diagram of SiC and ZrB_2 (Figure 7.11), which can improve densification of the ZrB_2/SiC composite. In addition, the eutectic nature of SiC and ZrB_2 may be associated, which can also improve the densification of the ZrB_2/SiC composite.
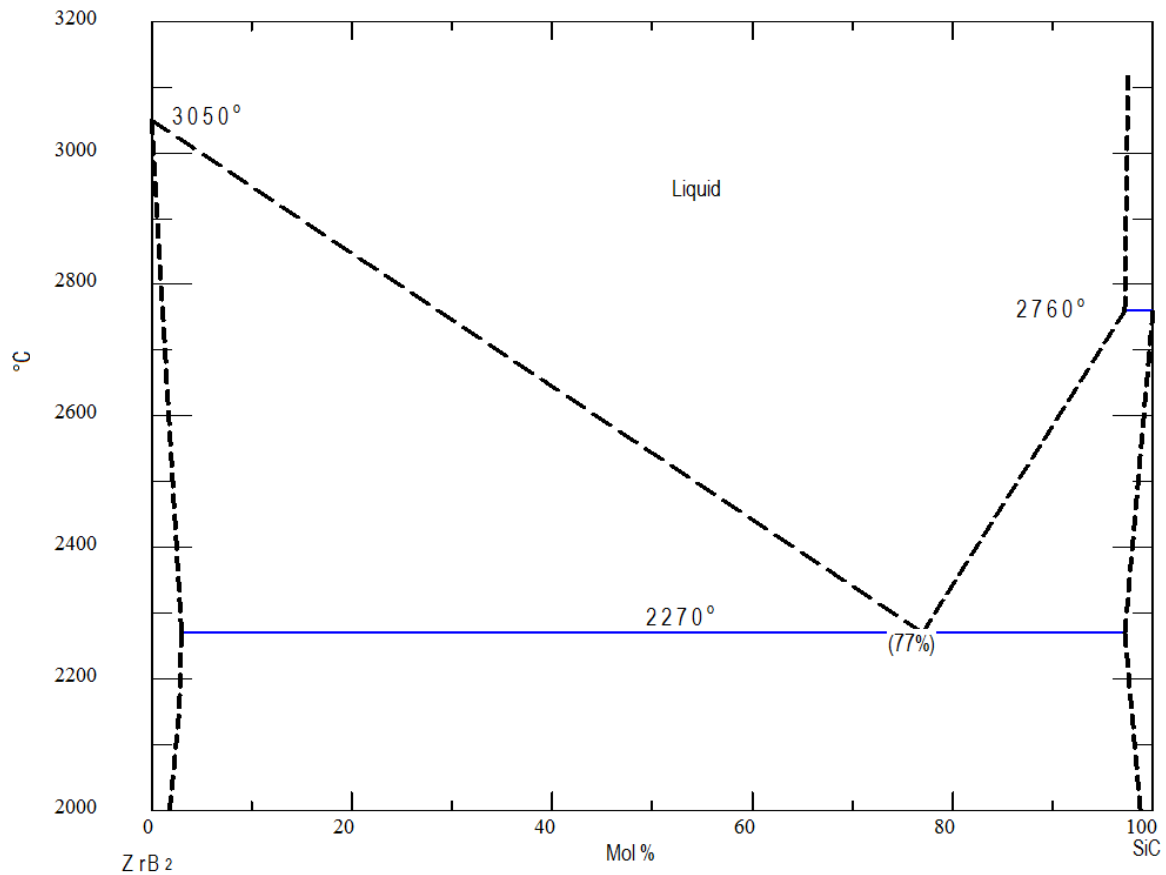
Figure 7.11 Binary phase diagram of ZrB_2 and SiC[208]

7.4 Effect of the carbon ratio on the phases and microstructures of the ZrB$_2$/SiC composites

The effect of the carbon ratio in the SiC sol-gel precursor on the phases and microstructures of the ZrB$_2$/SiC composites was studied. The amount of carbon to completely reduce the oxide in the sol-gel precursor and the oxide impurity in the starting ZrB$_2$ powder depends on the SiC sol-gel to ZrB$_2$ ratio. Less SiC added, more excess carbon is required to convert all the oxide on the ZrB$_2$ powder. To simplify the matter, the SiC to ZrB$_2$ molar ratio is fixed as 15/85. The carbon to SiO$_2$ molar ratio in the sol-gel precursor ranged from 6 to 10.

7.4.1 Effect of the carbon ratio on the phases of the ZrB$_2$/SiC composites

The XRD patterns of the ZrB$_2$/SiC composites with different carbon ratios after carbothermal reduction at 1450 °C are shown in Figure 7.12. The results show a big difference in the phases of the ZrB$_2$/SiC composites with different carbon ratios. There is some oxide left and no SiC was found in the sample with a carbon ratio of 6, which means 6C is clearly insufficient for the carbothermal reduction reaction. In the samples with carbon ratio of 7 and 8, there is the existence of the SiC phase, along with the ZrB$_2$. However, in the sample with a carbon ratio of 10, the ZrC phase begins to appear as well as SiC and ZrB$_2$. This means that carbon ratio of 8 is sufficient for the complete carbothermal reduction reaction for the sample with the SiC/ZrB$_2$ molar ratio of 15/85.

In this carbothermal reduction process, the following reactions could take place from thermodynamic point of view:

$$SiO_2(s) + 3C(s) \rightarrow SiC(s) + 2CO(g) \qquad\qquad (7\text{-}4)$$

$$ZrO_2(s) + 3C(s) \rightarrow ZrC(s) + 2CO(g) \qquad\qquad (7\text{-}5)$$

The temperatures for the reaction 7-4 and 7-5 to take place are 1781K and 1926K respectively according to the calculation of free energy of the two reactions[179]. There

are two reasons why there is ZrC phase in the sample with 10C in the SiC sol-gel precursor instead of those with carbon ratio of 8 and below. One is that the reaction temperature for carbothermal reduction of silica is lower than zirconia, so that the silica was first reduced before zirconia, if there was insufficient carbon. The other is that some zirconium diboride was oxidized depending on the oxygen partial pressure, followed by being reduced to zirconium carbide, if there was excess carbon during the carbothermal reduction process. Therefore the amount of zirconium carbide in the sample with excess carbon (10C) was larger than that in the samples with just sufficient (8C) or less carbon (7C and 6C).
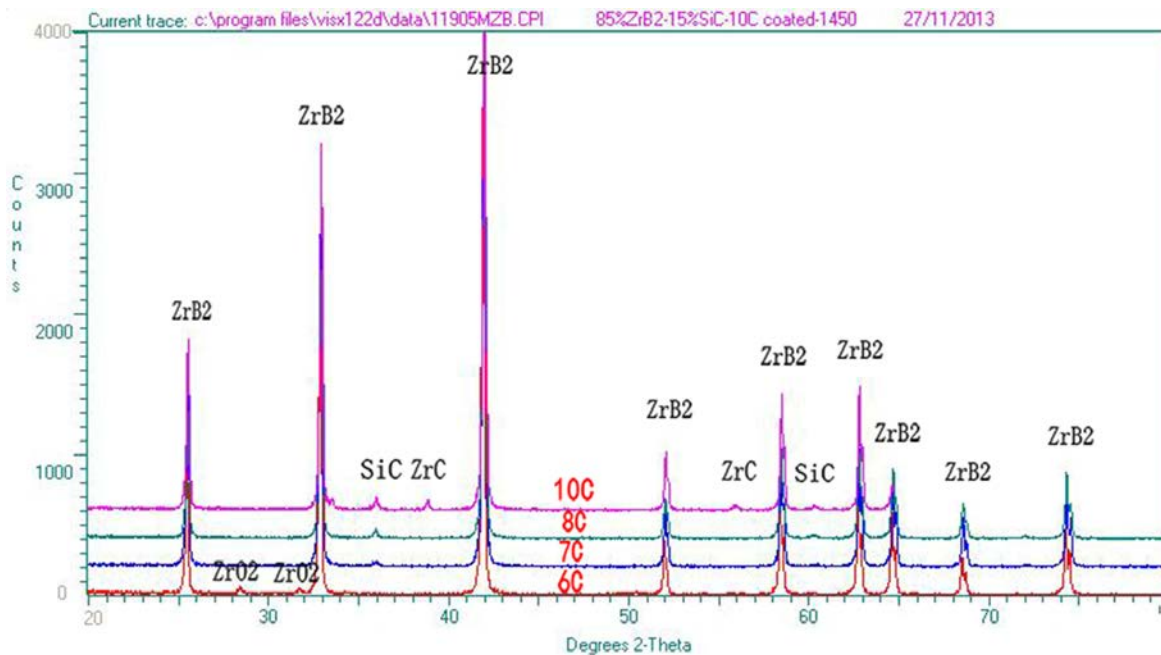
Figure 7.12 XRD patterns of the ZrB$_2$/SiC (SiC/ZrB$_2$ ratio=15/85) composites with different carbon ratios in the SiC sol-gel precursors after firing at 1450 °C for 5 hours in Ar

7.4.2 Effect of the carbon ratio on the microstructure of ZrB$_2$/SiC composites

The SEM micrographs of the ZrB$_2$/SiC composites with different carbon ratios are shown in Figure 7.13. The big micron-sized particles in the pictures are ZrB$_2$ particles, and the

small nano-sized ones are SiC. The result also shows that 6C is not sufficient for the carbothermal reduction reaction. This is highlighted by some silica layers present and the low amount of silicon carbide that can be found on the surfaces of the ZrB_2 particles (Figure 7.13a). The EDX result confirms that the layers covered on the ZrB_2 particles are mainly Si and O (Figure 7.13e). This is consistent with the XRD results in Figure 7.12, in which no carbides but oxides (zirconia) are detected (silica is a glass phase and cannot be detected by XRD). Compared with the starting ZrB_2 powders, zirconia was found in this ZrB_2/SiC composite sample but not in the starting ZrB_2 powder because the oxidation of ZrB_2 at 1450 °C due to the coated carbon deficient Si-O-C composite on the surface of ZrB_2 powders.
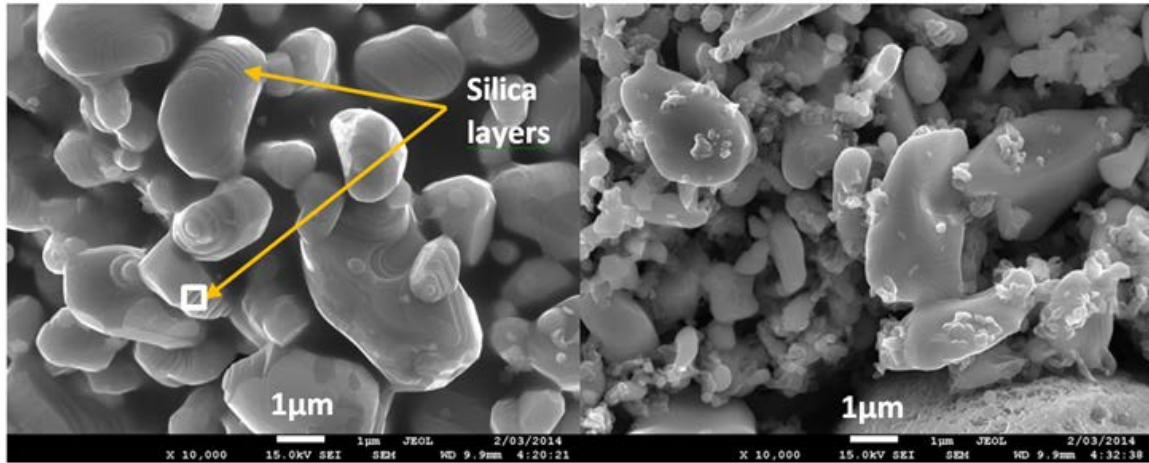
(a)

(b)
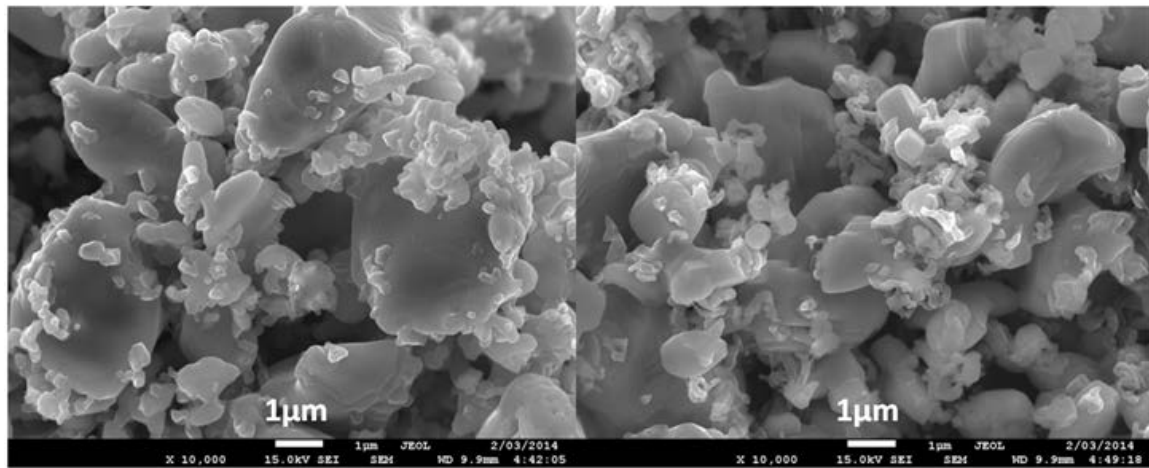
(c)

(d)
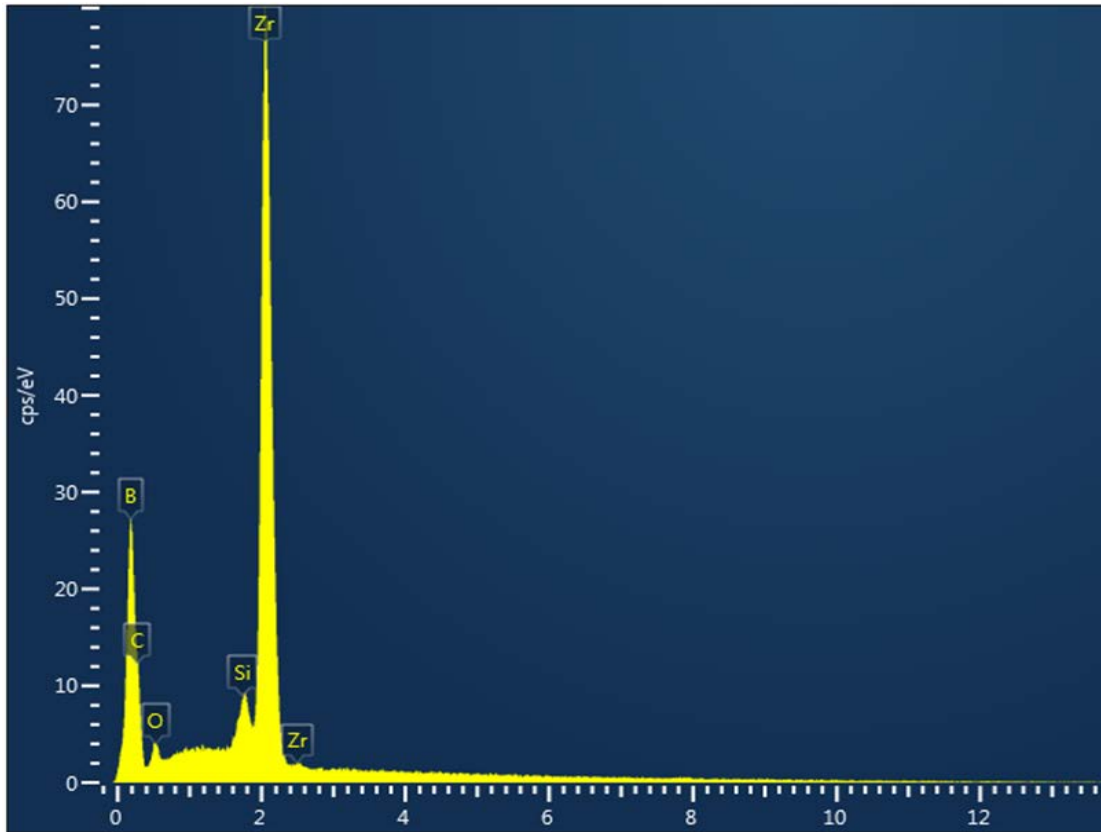
(e)

Figure 7.13 SEM micrographs of the ZrB$_2$/SiC composites (SiC/ZrB$_2$ ratio=15/85) with the carbon ratio of (a) 6 (b) 7 (c) 8 (d) 10 (e) EDX result at the spot in (a) after firing at 1450 °C for 5 hours in Ar

More nano-sized SiC particles can be found on the surfaces of ZrB$_2$ grains with increasing carbon ratio (Figure 7.13b and 7.13c). This is because more silica was converted to silicon carbide with the increasing amount of carbon in the sol-gel precursor. With the changing carbon ratio, the grain size of SiC also increases from about 100 nm in the 7C sample, to 200-300 nm in the 8C one. However the morphology of SiC grains remains similar in these two samples and both are equiaxed particles. In the sample with a carbon ratio of 10, the morphology of SiC looks more like short whiskers than particles. This is because of the nature of the gas reaction that

characterizes the carbothermal reduction of SiC gel. In this reaction the SiC grains grow up along the direction of gas evaporation. This result is also consistent with the analysis in section 7.1.2.

7.5 Effect of SiC on the oxidation resistance of the ZrB$_2$/SiC composites

UTHCs are receiving more attention and interest due to their potential ability as the material for the reusable thermal protection system and other components for the next generation of hypersonic aerospace vehicles. These components will experience extreme re-entering environment such as oxidizing atmosphere, high velocities and pressures, and temperatures from 1500°C-2400°C[197]. Currently the oxidation behavior of UHTCs at higher temperatures ($\geqslant$1600°C) is not well understood and the majority of the recent oxidation studies on ZrB$_2$ based UHTCs have been done at temperatures below 1600°C[4-7,162,163,209-211]. This is primarily due to the complexity of the oxide scale and limited information of the oxidation mechanism at higher temperatures as well as challenges and difficulties in achieving the necessary high temperatures above 1600°C in conventional laboratory furnaces. In this section, the oxidation property of ZrB$_2$/SiC composites prepared by both sol-gel infiltration and powder coating methods are compared with that of a monolithic ZrB$_2$ control sample. The SiC contents in the infiltrated and pre-coated ZrB$_2$/SiC composites are about 3.5 wt% and 6 wt% respectively. The two ZrB$_2$/SiC composites and ZrB$_2$ control sample were sintered by SPS at 1900 °C for 5 minutes under a uniaxial pressure of 40 MPa in vacuum. The oxidation experiments were carried out by an ablation test via a propylene torch at 2200 °C (measured by pyrometer on the surface of the sample during the ablation test) for 20s, 60s and 120s respectively. The distance between the nozzle of the torch and the sample surface was about 15 mm (referring the torch experiment in Section 3.2.6 in Chapter 3). The sample size is 10mm in diameter and about 6mm in thickness. The temperature of the flame was confirmed to be higher than 2000 °C by the melting of an alumina ceramic, whose melting point is 2000 °C.

7.5.1 Oxidation behavior of the ZrB_2/SiC composites prepared by the sol-gel infiltration

The ZrB_2/SiC composite samples were sintered by SPS at 1900 °C after 2 cycles of infiltration with a SiC sol-gel precursor. The preparation, phases and microstructures of the material can be found in Section 6.6, Chapter 6. According to the study in Section 6.3.2, the thickness of the surface layer of the scaffold after 2 cycles of infiltration is close to the maximum thickness that the infiltration technique can achieve under the conditions used in this thesis. The microstructure of the sintered sample shows that it was a functionally gradient material consisting of a relatively dense ZrB_2/SiC surface layer of about 500μm and a porous ZrB_2 core (Figure 6.16). The EDX and XRD results in Section 6.6 also confirmed this functionally gradient structure. A ZrB_2 control sample was also sintered at the same conditions as the ZrB_2/SiC composite sample for a comparison. The samples were cut after the ablation test and the cross sections were examined.

The weight change, change of the sample thickness and oxidation layer thickness of the three samples after the ablation tests for different times are shown in Table 7.2. The weight and thickness of the samples before and after ablation testing were measured by a balance and digital caliper respectively. The oxidation layer thickness was measured from the SEM micrographs of the samples. The weight change for the infiltrated ZrB_2/SiC composite sample after an ablation test for 20s was negative because a small piece of the oxidation layer fell off accidently during the test. From the results in Table 7.2, we can see that both the infiltrated and coated ZrB_2/SiC composite samples have less weight and thickness changes, and thinner oxidation layers than the monolithic ZrB_2 control sample. This indicates that the introduction of SiC by either infiltration or powder coating technique can successfully improve the oxidation resistance of ZrB_2 ceramics. Moreover, the ZrB_2/SiC composite made by the powder coating method has a lower weight change, thickness change and oxidation layer thickness than the infiltrated

one. This is because the SiC concentration in the coated composite sample (6 wt%, calculated according to the SiC/ ZrB$_2$ molar ratio=15/85) is higher than that in the surface layer of the infiltrated composite sample (3.5 wt%, refer to the EDX result in Section 6.6.1 of Chapter 6).

Table 7.2 Weight change, thickness change and oxidation layer thickness of monolithic ZrB$_2$ control sample, sol-gel infiltrated and coated ZrB$_2$/SiC composite samples sintered by SPS at 1900 °C for 5min after an ablation test for 20s, 60s and 120s respectively

Material	Time duration for ablation test (s)	Weight change Δw (mg)	Change in sample thickness Δh (μm)	Oxidation layer thickness (μm)
ZrB$_2$ control sample	20	4	260	100
	60	31	430	300
	120	34	510	400
Sol-gel infiltrated ZrB$_2$/SiC composite sample	20	-2	170	120
	60	13	300	180
	120	18	430	300
Sol-gel coated ZrB$_2$/SiC composite sample	20	5	100	200
	60	13	210	250
	120	12	230	230

During the ablation tests over 2200°C, the following reactions took place in the ZrB$_2$/SiC composites:

$$ZrB_2(s) + 5/2O_2(g) \rightarrow ZrO_2(s) + B_2O_3(l) \qquad (7\text{-}6)$$

$$B_2O_3(l) \rightarrow B_2O_3(g) \qquad (7\text{-}7)$$

$$SiC(s) + 3/2O_2(g) \rightarrow SiO_2(l) + CO(g) \qquad (7\text{-}8)$$

$$SiC(s) + O_2(g) \rightarrow SiO(g) + CO(g) \tag{7-9}$$

$$SiO_2(l) \rightarrow SiO_2(g) \tag{7-10}$$

The weight change of the samples after the ablation test is the combination of the weight gains due to the oxidation of zirconium diboride (7-6) and silicon carbide (7-8) and weight losses caused by the evaporation of boron trioxide (7-7) and silicon monoxide (7-9). This is because the boiling points of boron trioxide and silicon monoxide are 1860°C[212] and 1880°C[213] respectively and both are lower than the ablation test temperature. Because the low concentration of SiC in the ZrB_2/SiC composite, reaction 7-6 is the main reaction during the ablation test and the weight gain of this reaction contributes to the major part of weight change of the ZrB_2/SiC composite. This is why the weight change of the ZrB_2/SiC composite after the ablation test can be used to describe the degree of oxidation of the samples.

The low magnification SEM micrographs of the ZrB_2 control sample and the infiltrated ZrB_2/SiC composite sample after the ablation tests are shown in Figure 7.14 and Figure 7.15 respectively. The results show that the oxidation layer thickness of ZrB_2 control sample after ablation for 20s, 60s and 120s are about 100 μm, 300 μm and 400 μm respectively (Figure 7.14a, 7.14b and 7.14c). The ZrB_2 control sample after ablation for 60s has an ablation pit of about 100 μm depth and a few cracks (circle region in Figure 7.14b). However, the oxidation layer thickness of the infiltrated ZrB_2/SiC composite sample are only about 120 μm, 180 μm and 300 μm (Figure 7.15a, 7.15b and 7.15c). These results also indicate that the presence of SiC in the ZrB_2/SiC composite introduced by the sol-gel infiltration improves the oxidation resistance of ZrB_2.

(a)

(b)

(c)
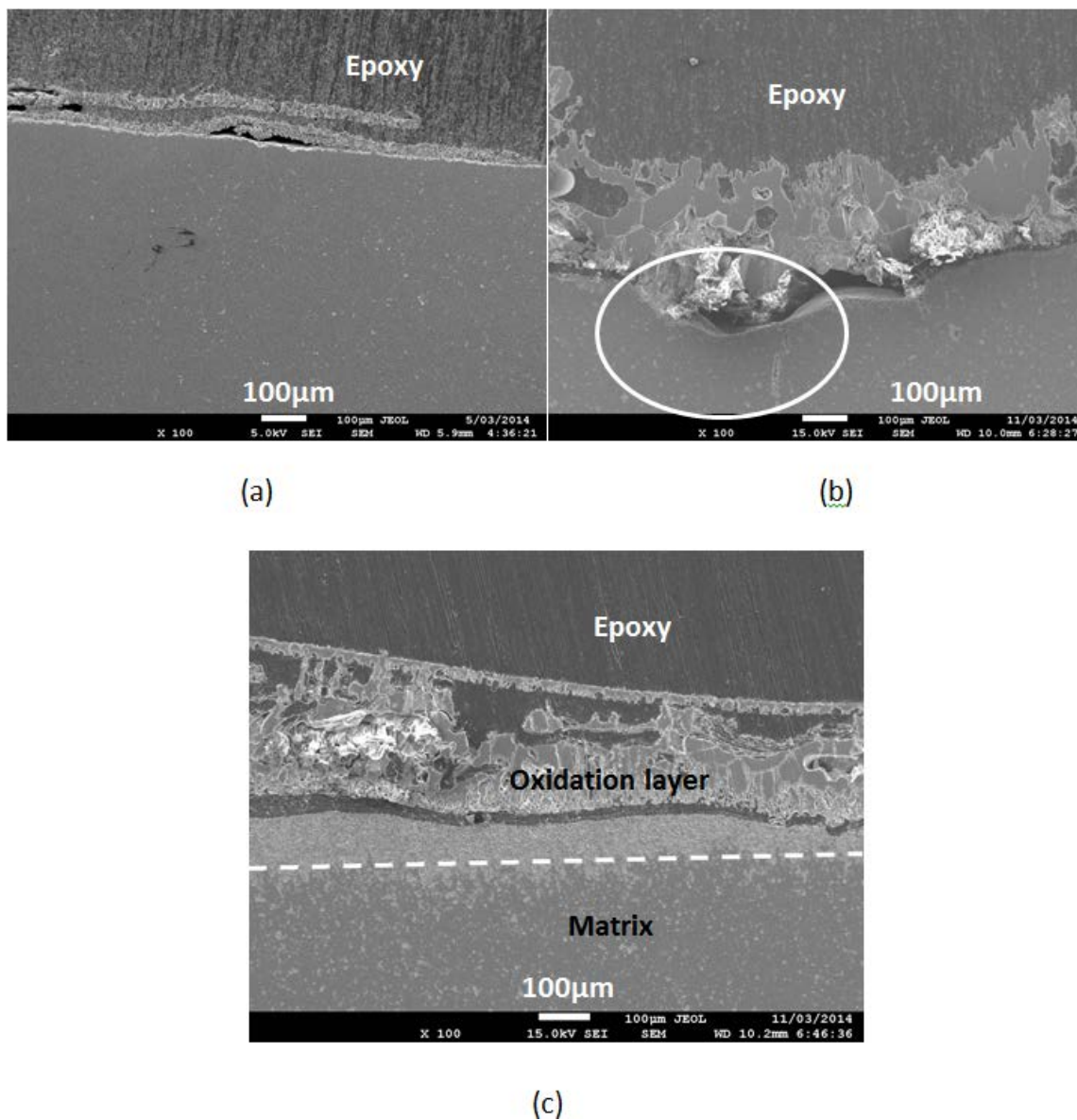
Figure 7.14 SEM micrographs of the ZrB$_2$ control sample oxidized for (a) 20s (b) 60s (c) 120s over 2200 °C. An ablation pit with a crack can be found in the circle region in (b). The samples were cold mounted by epoxy before grinding.
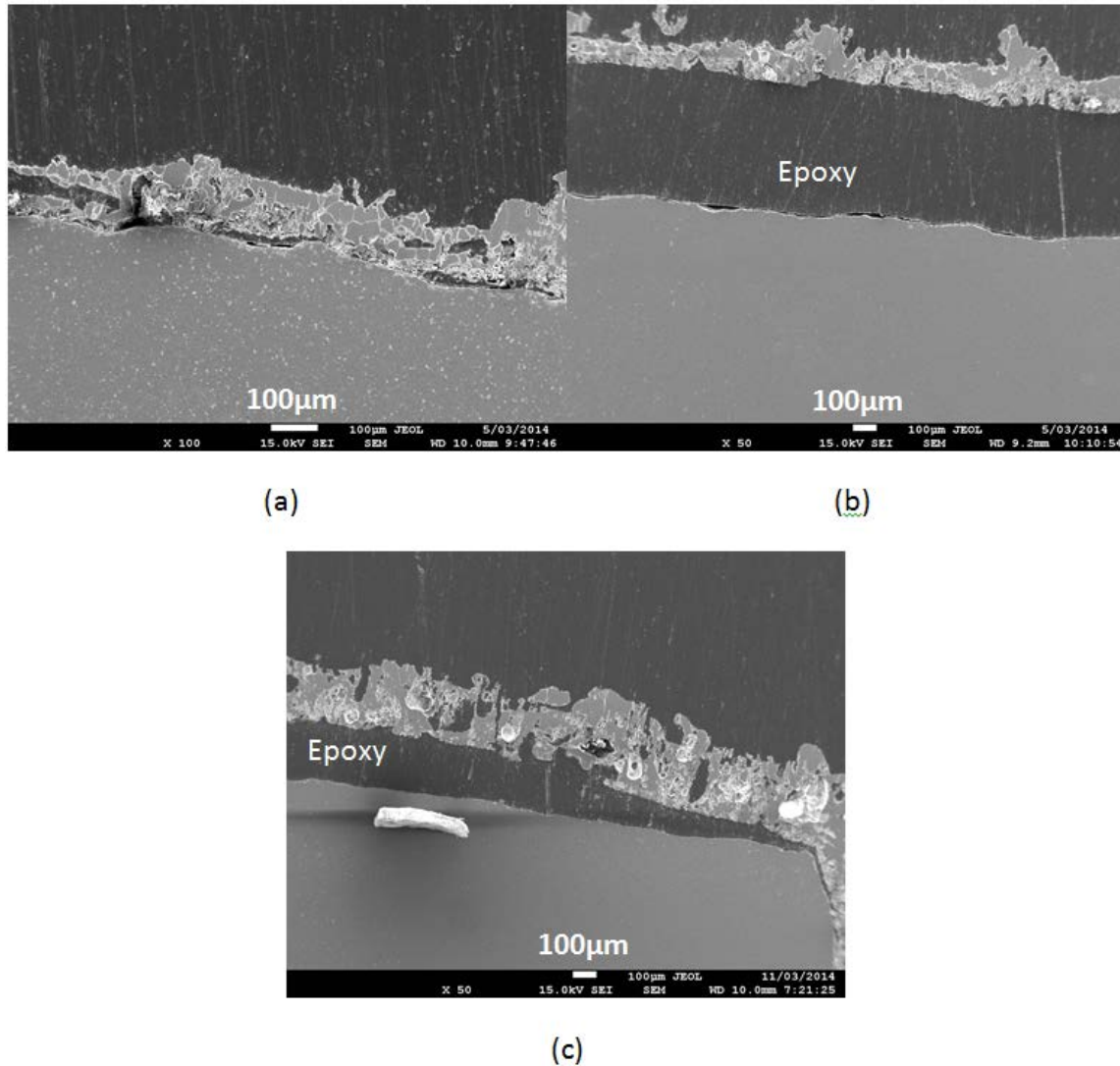
Figure 7.15 SEM micrographs of the infiltrated ZrB_2/SiC composite sample oxidized for (a) 20s (b) 60s (c) 120s at 2200°C.

The EDX analysis of the oxidation layer and matrix of the infiltrated ZrB_2/SiC composite sample after the ablation test for 60s is shown in Figure 7.16. The results indicate that SiC was left in the matrix of the infiltrated ZrB_2/SiC composite but could not be detected in the oxidation layer after ablation. This is because the SiC in the oxidation layer was oxidized and then lost in the form of SiO according to reaction 7-9. This also confirms that the SiC left in the matrix can protect the ZrB_2/SiC composite from further oxidizing.
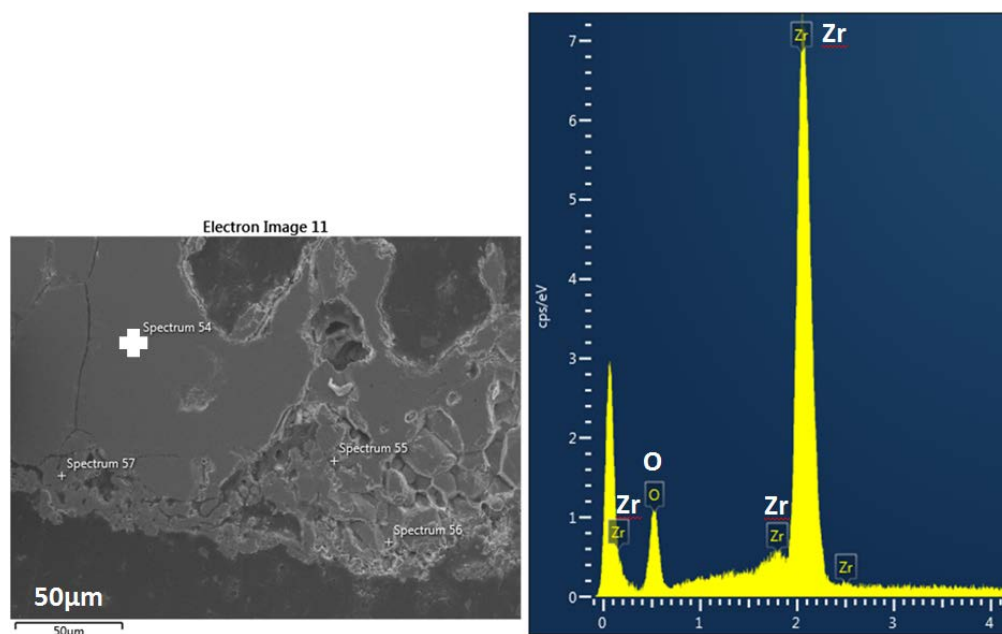
(a)
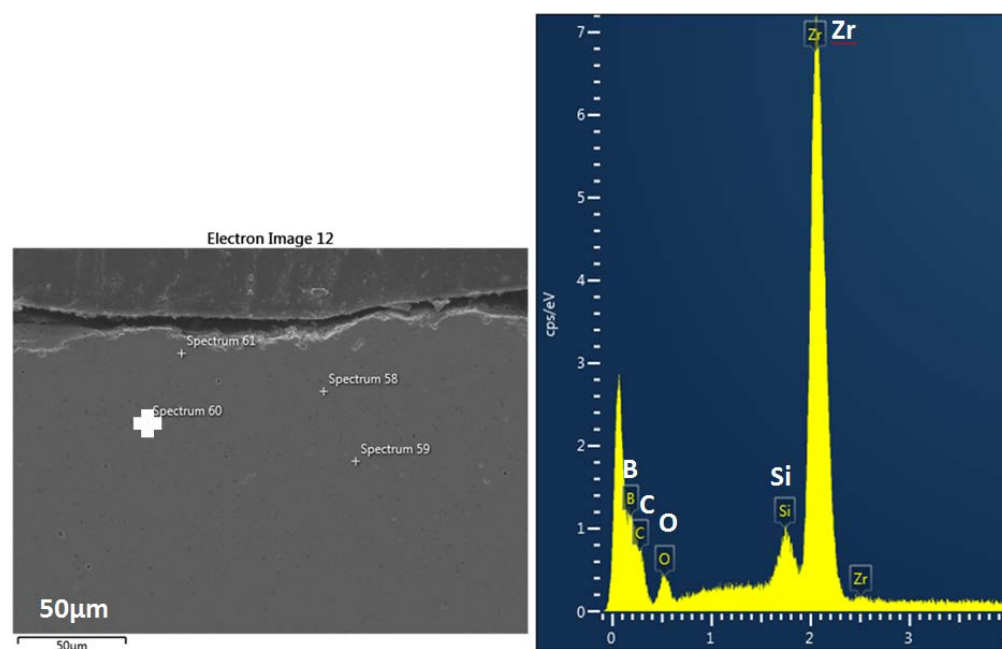
(b)

Figure 7.16 EDX analyses of the oxidation layer and matrix of the infiltrated ZrB_2/SiC composite sample oxidized for 60s, (a) the oxidation layer (b) the matrix

The XRD spectra of the oxidation layers of the infiltrated and powder coated ZrB_2/SiC composite samples and the ZrB_2 control sample after the ablation tests for 60s are shown in Figure 7.17. The only crystalline phase exists in the oxidation layers of all three samples is monoclinic zirconia. It indicates that zirconium diboride has been completely oxidized at the test temperature. The broad peak at around 20 degree may suggest the formation of amorphous phase (silica and borosilicate).
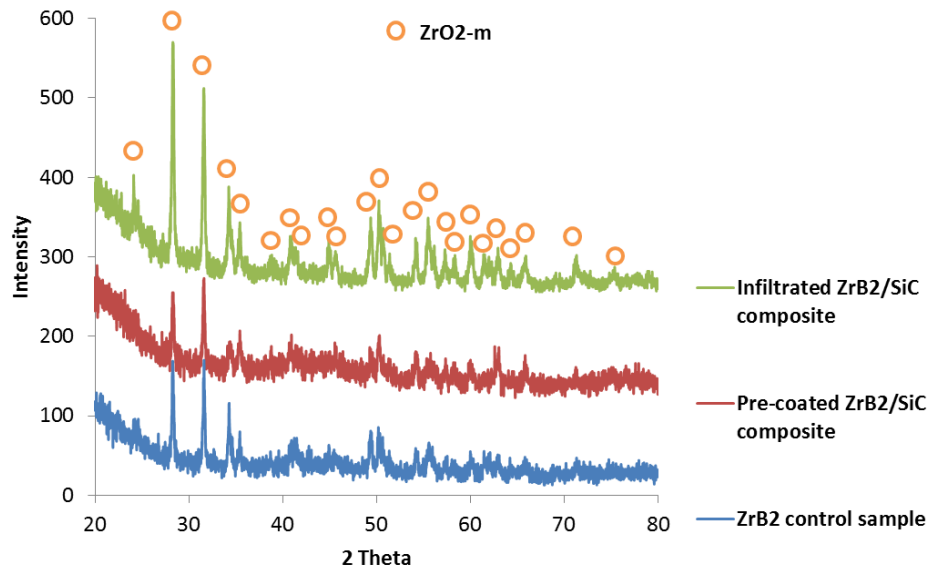
Figure 7.17 XRD spectra of the oxidation layer of the infiltrated ZrB_2/SiC composite and ZrB_2 control sample oxidized for 60s (a) ZrB_2 (b) ZrB_2/SiC

7.5.2 Oxidation behavior of the ZrB_2/SiC composites prepared by sol-gel coating of ZrB_2 powders

The preparation process of the ZrB_2/SiC composites made by the sol-gel coated ZrB_2 powder is described in Section 7.1. The SiC concentration in the coated composite is 15 at% and the carbon/metal ratio in the Si-O-C sol-gel is 8C. The low magnification SEM micrographs of the pre-coated ZrB_2/SiC composites after the ablation tests are shown in Figure 7.18. The results show that the thickness of the oxidation layer for the pre-coated ZrB_2/SiC composite samples after the ablation for 20s, 60s and 120s are about 200 µm,

250 μm and 230 μm respectively (Figure 7.18a, 7.18b and 7.18c). The oxidation layer thickness for the ZrB_2 control sample increases greatly with increasing time of the ablation tests (Figure 7.14a, 7.14b and 7.14c), which are 100 μm, 300 μm and 400 μm respectively. However, the thicknesses of the oxidation layers for the pre-coated ZrB_2/SiC composite samples are not only clearly less than those of the ZrB_2 control samples under the same testing condition, but does not change much with the increase of testing time either, indicating the significant role of SiC in improving the oxidation resistance of the ZrB_2 composites.

(a)

(b)

(c)
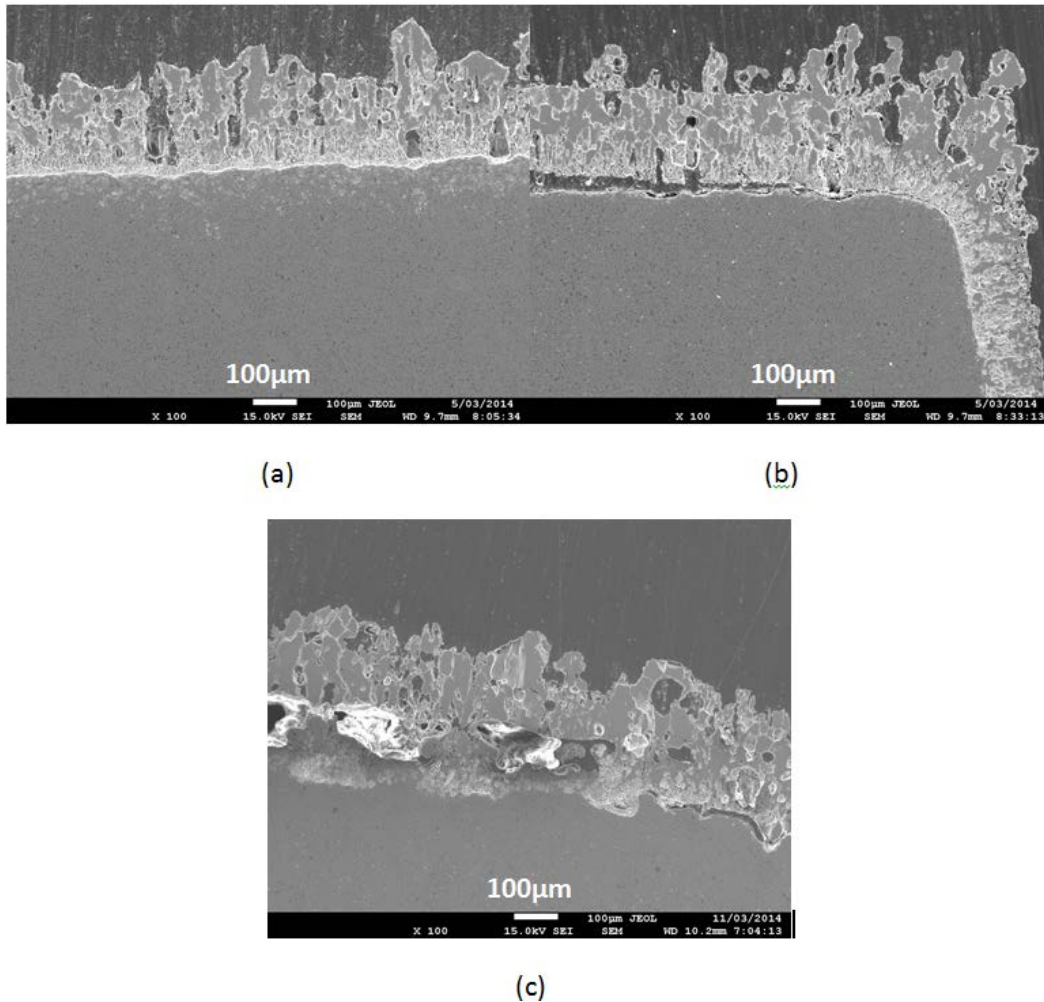
Figure 7.18 Low magnification SEM micrographs of the coated ZrB_2/SiC composite sample oxidized for (a) 20s (b) 60s (c) 120s

177

The microstructures of the oxidation layer of the pre-coated ZrB_2/SiC composites and ZrB_2 control sample are shown in Figure 7.19. We can find some porous ZrO_2 structures with fine grains in the ZrB_2 control sample (Figure 7.19a) and some pores with smooth boundaries, which could be formed after the vaporizing of a liquid phase in the ZrB_2/SiC composite (circle region in Figure 7.19b). This is because the oxidized silicon carbide became silica which was in a liquid phase at the temperature high than 1800 °C (melting point of silica is 1600-1725 °C[214]). At high temperatures, B_2O_3 vaporized quickly due to its low melting point (450 °C) and high vapor pressure. The rapid evaporation of B_2O_3 resulted in increased oxidation of ZrB_2 since ZrO_2 was not a perfect protective oxide and the porous ZrO_2 structure (Figure 7.19a) did not provide a good protection to the ZrB_2 material[195,196,199]. However, by introducing SiC, the oxidation resistance was improved due to the formation of a glassy silica layer during the ablation (formula 7-8). The ZrB_2/SiC composite had an improvement in oxidation resistance below 2200 °C because of the formation of a silica glassy layer with low oxygen permeability, which provided a protective oxidation barrier. Above 2230 °C, silica will evaporate very fast and the oxidation resistance ability of the ZrB_2/SiC composite significantly decreases because the boiling point of the silica is 2230 °C[215,216]. All these results indicate that the introduction of SiC by a sol-gel technique (infiltration or coating) improves the oxidation resistance of the ZrB_2 at high temperatures up to 2200 °C.
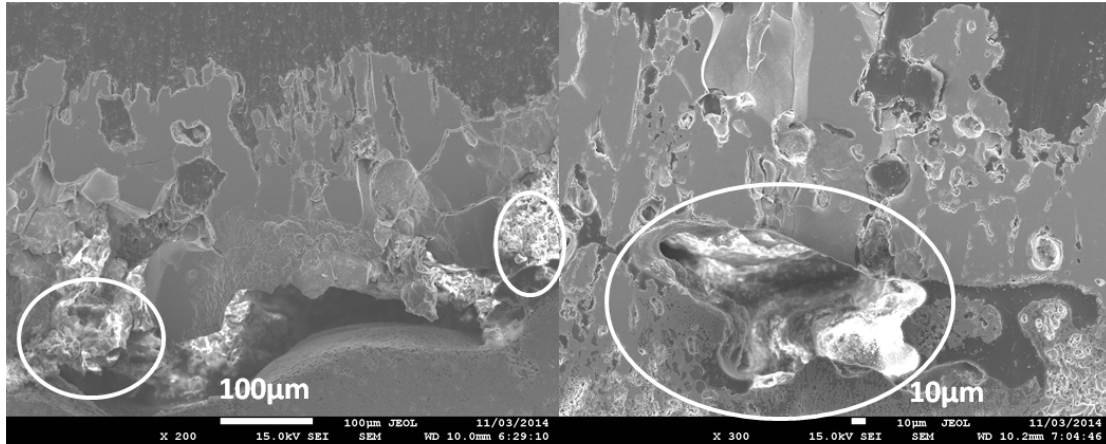
(a)   (b)

Figure 7.19 SEM micrographs of the oxidation layer of the (a) ZrB_2 and (b) pre-coated ZrB_2/SiC composite oxidized at 2200 °C for 120s, liquid silica can be found in the circle region in (b)

The EDX analysis of the pre-coated ZrB_2/SiC composite sample after the ablation testing for 60s is shown in Figure 7.20. The results indicate that SiC can be detected in the bottom of the oxidation layer and the matrix of the ZrB_2/SiC composite but not in the middle of the oxidation layer. The concentration of silicon in the matrix is also higher than that in the oxidation layer. Compared with the result in Figure 7.16 (no SiC left in the oxidation layer of the infiltrated ZrB_2/SiC composite), the oxidation resistance of the pre-coated ZrB_2/SiC composite is better than that of infiltrated ZrB_2/SiC composite. This is because the concentration of SiC in the infiltrated ZrB_2/SiC composite (3.5 wt%) is lower than that of pre-coated ZrB_2/SiC composite (6 wt%). In addition, the sol-gel coated powders also gave a more uniform and fine distribution of SiC in the composite than the infiltrated one, which also made the pre-coated ZrB_2/SiC composite have better oxidation resistance than the infiltrated one. This also shows that the sol-gel coating is a promising technique for introducing a secondary nano phase, such as SiC, to efficiently improve the oxidation resistance of UHTCs and we can further improve the oxidation resistance of UHTCs by infiltrating more SiC on the surface layer of the scaffold.
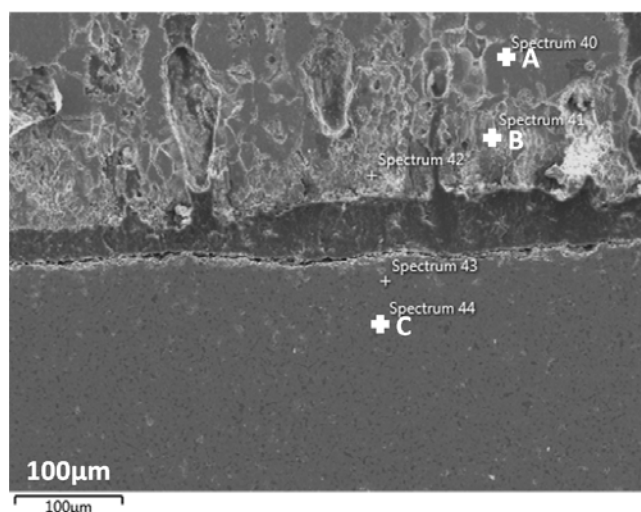
(a)
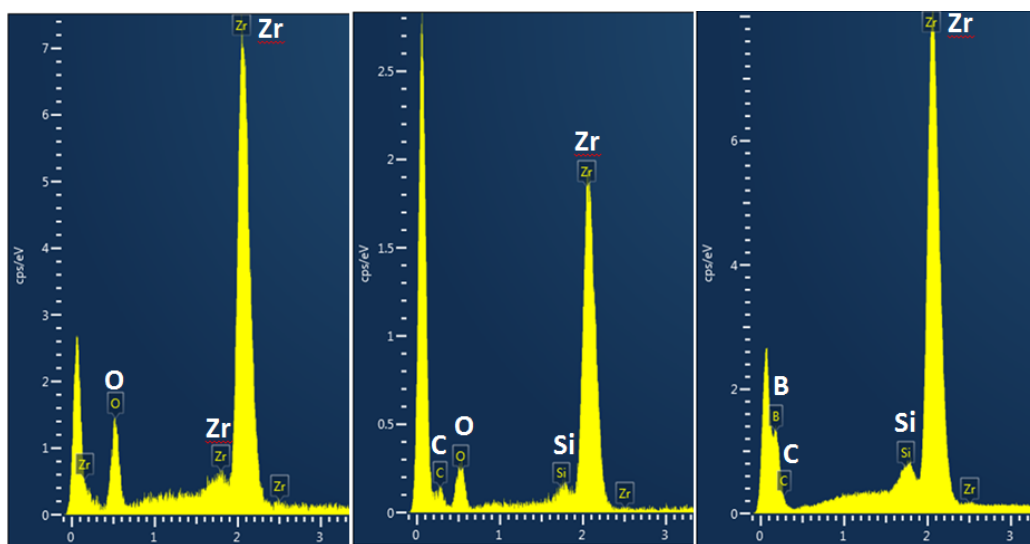
(b)   (c)   (d)

Figure 7.20 EDX analyses of the oxidation layer and the matrix of the pre-coated ZrB_2/SiC composite sample oxidized for 60s. (a) SEM image, and EDX results at spot A (b), spot B (c) and spot C (d).

The EDS mapping and compositional analysis results of the ZrB_2 control sample, infiltrated and pre-coated ZrB_2/SiC composite samples after the ablation test for 120s

are shown in Figure 7.21, 7.22 and 7.23 respectively. The carbon rich regions in the images are epoxy which was used to mount the samples. From the SEM image and EDS layered image of the ZrB_2 control sample, we can see the top of the matrix (about 150µm thick) was also oxidized besides the porous oxidation layer (Figure 7.21). However, the infiltrated and pre-coated ZrB_2/SiC composite samples do not have such an oxidized layer in the matrix (Figure 7.22 and 7.23).

Compared with the infiltrated ZrB_2/SiC composite sample, the pre-coated one has three distinct oxidation layers after ablation due to its relatively higher concentration of SiC. The outmost layer is porous and mainly composed of ZrO_2 and many voids, which were formed due to the formation and vaporization of B_2O_3 at elevated temperature (equations 7-6 and 7-6). Underneath this layer, there is a SiC depletion layer, which was mainly composed of SiO_2 and some recrystallized ZrO_2 (Figure 7.23). Underneath, there is the unaltered ZrB_2/SiC matrix layer. This SiC depletion layer is believed to be a SiO_2-rich borosilicate layer which is known to form at temperatures around 1200°C for ZrB_2/SiC composites[162,199,217]. At higher temperatures (>1200°C) the B_2O_3(l) in the borosilicate is presumed to start evaporating from the borosilicate surface layer, leaving a SiO_2 rich borosilicate as the external layer, due to the much higher vapor pressure of B_2O_3 at these temperatures compared to SiO_2[199,218,219]. This SiO_2-rich borosilicate layer can provide increased oxidation resistance due to its lower vapor pressure, higher melting temperature and viscosity, which can decrease the oxygen diffusion rate through the layer and suppress B_2O_3 evaporation at these temperatures. From the electronic image and EDS mapping of the pre-coated ZrB_2/SiC composite sample we can see the liquid SiO_2-rich borosilicate glass and the concentration of silicon (marked by ellipses in Figure 7.23). All these results indicate that the introduction of SiC by the sol-gel techniques efficiently improves the oxidation resistance of the ZrB_2 at high temperatures above 2000°C.
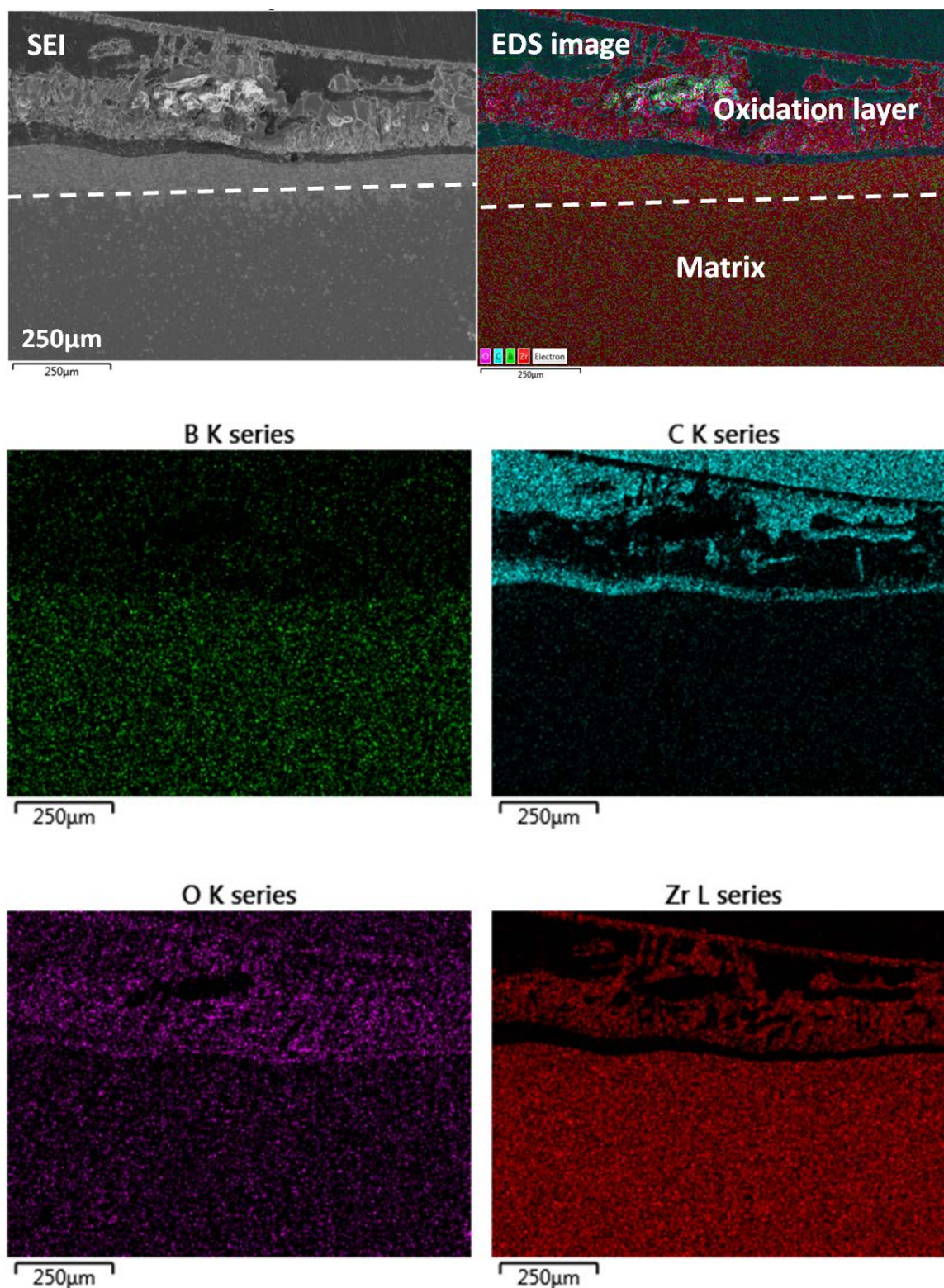
Figure 7.21 SEM image and EDS analysis of the ZrB_2 control sample oxidized for 120s
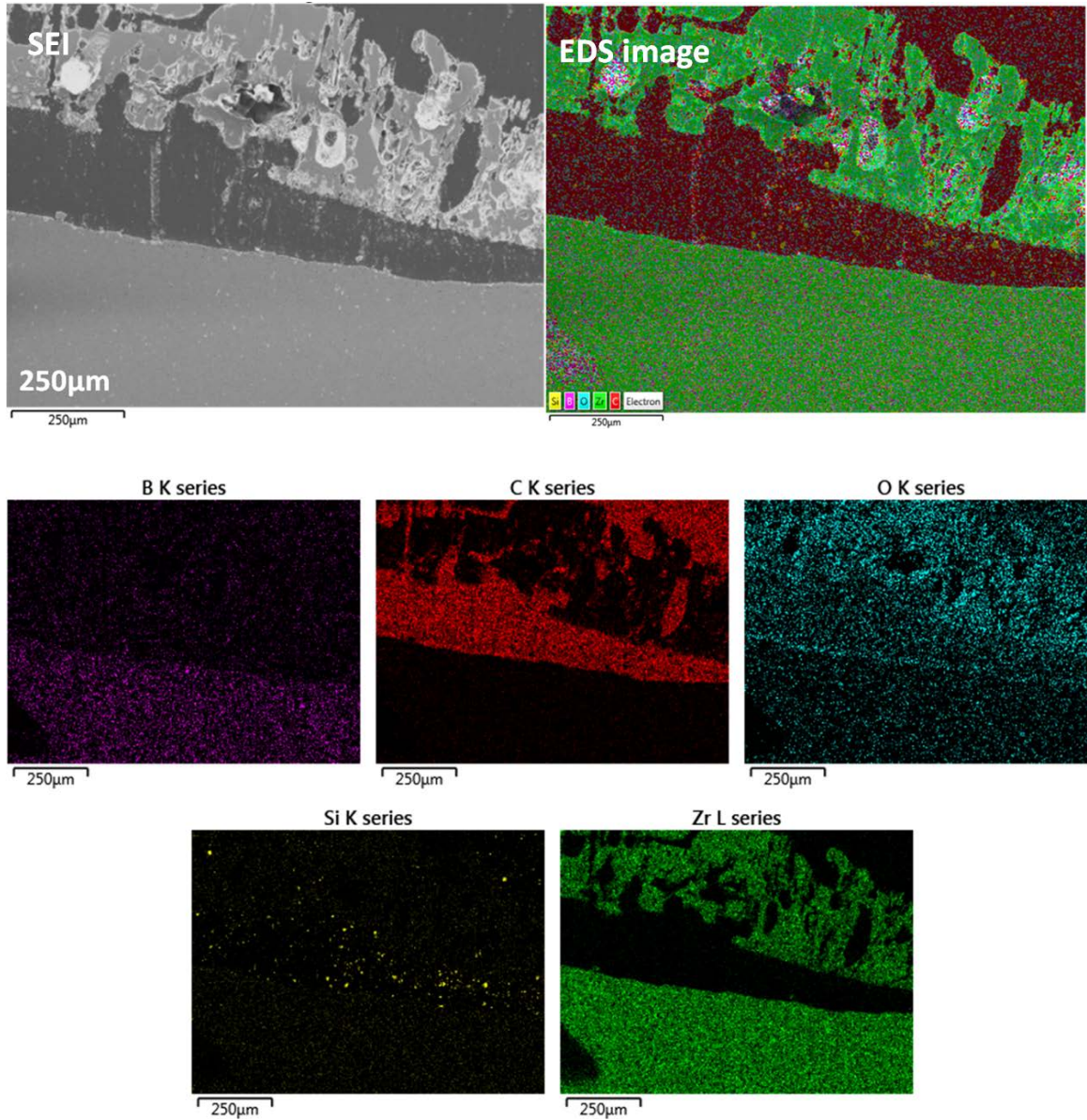
Figure 7.22 SEM image and EDS analysis of the infiltrated ZrB_2/SiC composite sample oxidized for 120s
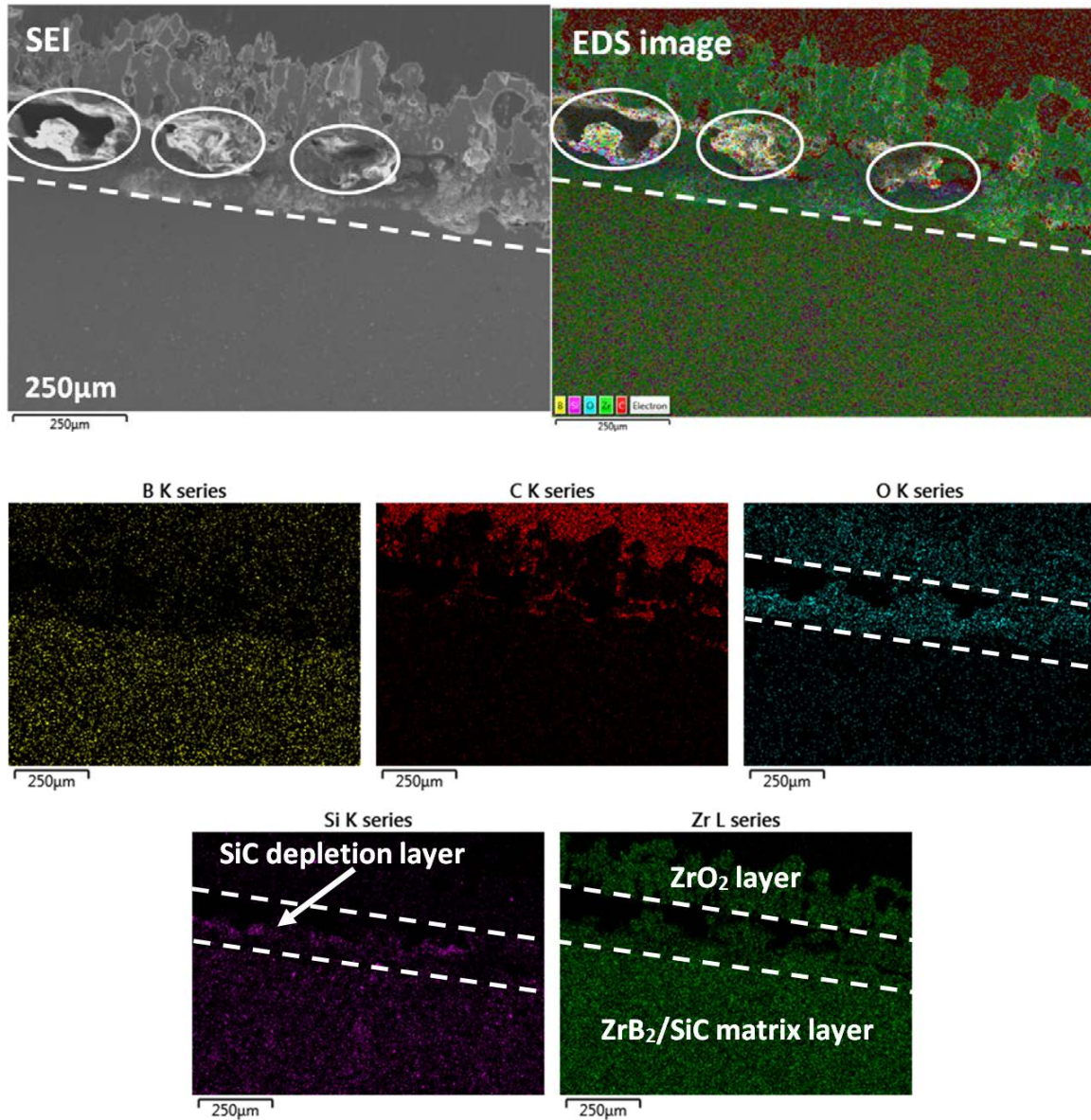
Figure 7.23 SEM image and EDS analysis of the pre-coated ZrB_2/SiC composite sample oxidized for 120s

7.6 Discussion

The introduction of nano SiC particles evenly on the surface of ZrB_2 powders by sol-gel coating improves the densification of the ZrB_2/SiC composites during spark plasma sintering compared with the monolithic ZrB_2 ceramic prepared at the same sintering conditions (Sections 7.3.3 and 7.3.4). There are several mechanisms for the improvement in densification.

Sol-gel coating can remove the oxygen impurity in the starting ZrB_2 powders by adjusting the carbon/metal ratio during the sol-gel preparing process. The addition of carbon (less than 4 wt%) was found to improve the densification of the ZrB_2-C composite[184]. The increased densification with the carbon addition was due to the removal of oxygen impurities on the ZrB_2 powder surfaces that prevented the commonly observed exaggerated grain growth through evaporation condensation of oxide phases during sintering of boride ceramics[184].

The solid dissolution between SiC and ZrB_2 (Figure 7.11), although it's only a very small amount of the solubility, not only can improve the densification of ZrB_2/SiC composites itself but also promote the coalescence of nano SiC particles on the surface of ZrB_2 powders, which can also facilitate the densification of ZrB_2/SiC composites by SiC nano particle agglomeration during sintering[201]. The intimate coating of SiC nano particles on the surface of ZrB_2 would ensure solid state diffusion to occur at the interface due to the high surface energy of the SiC nano particles (Figure 7.24).
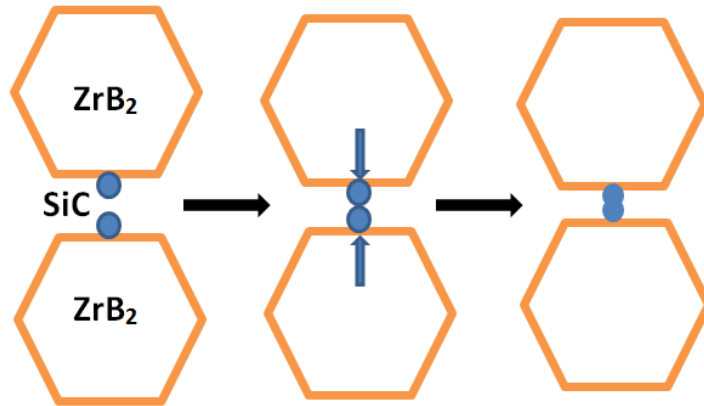
Figure 7.24 Densification of ZrB_2 facilitated by the agglomeration of nano-sized SiC coated on the surface of ZrB_2 powders

The carbothermal reduction reaction during the SPS sintering process can also improve the densification of ZrB_2/SiC composites by facilitating the mass transport process. From the TEM results of the coated ZrB_2 powders (Figure 7.5), a small amount of oxides and carbon could still exist in the ZrB_2/SiC composites after the carbothermal reduction at 1450 ^{o}C. These oxides and carbon will further react at the elevated temperature during the SPS sintering and these chemical reactions can facilitate the mass transport, so to improve densification. From the carbothermal reduction reactions (equations 7-4 and 7-5) described in Section 7.4.1, gas products are produced during the reactions so that the chamber pressure will increase. This is confirmed by the change of the chamber pressure during the SPS sintering (Figure 7.25). There are two veterxes on the curve of chamber pressure, one occurs at about 1500 ^{o}C and the other at around 1700 ^{o}C, which are caused by the carbothermal reduction reactions of silica and zirconia respectively.
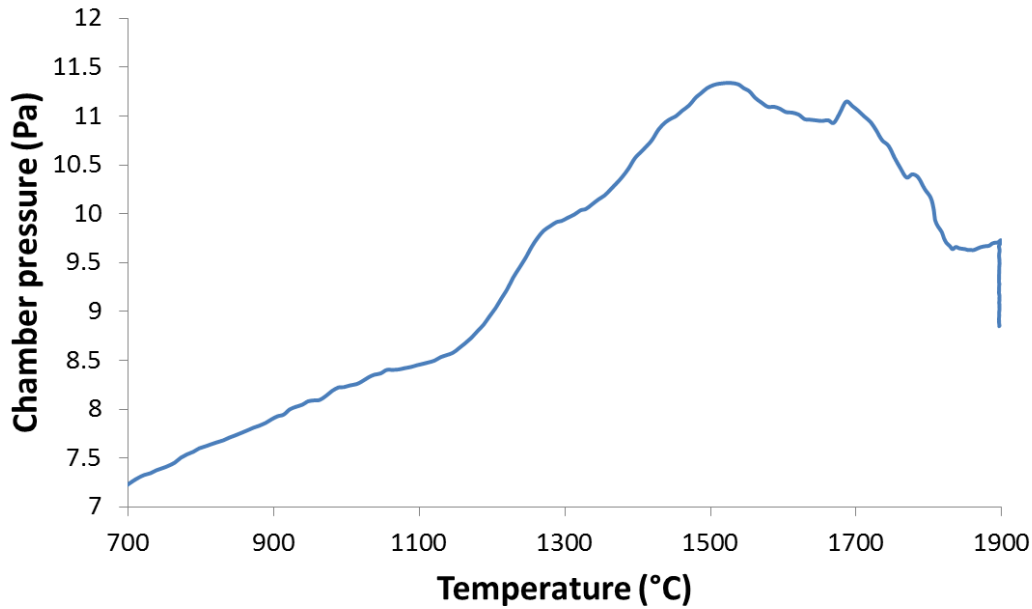
Figure 7.25 Change of the chamber pressure during the sintering process of the pre-coated ZrB_2/SiC composite SPSed at 1900^oC

The pinning effect of the SiC nano particles introduced by the sol-gel coating not only significantly hinders the grain growth of ZrB_2, but also helps to improve the densification. In the final stage of sintering, the coating of nano SiC particles on ZrB_2 resulted in a significant increase in the Zener pinning pressure. The nano-sized pinning particles at the grain boundary of every ZrB_2 grain would exert a strong dragging force to slow down the grain boundary movement, minimising grain growth at elevated temperatures. In addition, the SiC pinning particles would create intergranular channels, which help the elimination of the air and the gas products of the carbothermal reduction reactions, so that the densification is facilitated.

In summary, the SPS densification of the pre-coated ZrB_2/SiC composite is a result of combined mechanisms, including removing the oxygen impurity in the starting ZrB_2 powders, carbothermal reduction, coalescence of nanoparticles coated on ZrB_2 grains, and diffusion assisted by SiC solubility in ZrB_2. The uniform dispersion of SiC

nanoparticles was responsible for pore removal and retarding of ZrB_2 grain growth during the SPS sintering.

7.7 Summary

In this chapter, the sol-gel processing technique was used to coat fine SiC particles on the surface of ZrB_2 particles, which were then sintered by SPS. The phases, microstructures and oxidation resistance of the ZrB_2/SiC composites produced from the sol-gel modified powder were studied. All results from XRD, SEM and TEM analysis show that nano-sized SiC particles were successfully and evenly coated on the surface of ZrB_2 grains via the sol-gel coating process. The morphology and size of SiC grains varies with the increase of SiC content. The morphology of SiC grains is mostly equiaxed particles in the composites with low SiC contents (SiC/ZrB_2 ≤0.2), and becomes elongated ones in the sample with a high SiC content (SiC/ZrB_2 =0.3). The grain size of SiC increases from about 100 nm in the sample with a low (SiC/ZrB_2 ≤0.15) SiC content, to larger than 300 nm in the one with a high (SiC/ZrB_2 ≥0.2) SiC content. These differences are partly due to the nature of the gas phase reaction during the carbothermal reduction of the Si-O-C gel.

The ZrB_2/SiC powders prepared via the sol-gel coating can be almost completely densified without obvious grain growth after being sintered at 1900 °C by SPS, without any sintering additives. The introduction of SiC can improve the sintering of ZrB_2 and greatly suppress its grain growth. The grain size of the ZrB_2/SiC composite sintered at 2000 °C is still less than 5 μm compared with the grain size of 20-30 μm of the ZrB_2 control sample sintered at the same condition. The reason for this is that the great pinning effect of the nano SiC particles on the grain boundaries of ZrB_2 hinders the movement of the grain boundaries, and thus the grain growth. The shrinkage curves of the ZrB_2/SiC composites during spark plasma sintering also confirm that densification of the ZrB_2/SiC composites is improved with the increase of SiC contents. The ablation test

at 2200 °C by a propylene torch shows that the introduction of SiC by sol-gel coating efficiently improves the oxidation resistance of the ZrB_2 at high temperatures above 2000 °C due to the formation of a SiO_2-rich borosilicate layer. This SiO_2-rich borosilicate layer can provide increased oxidation resistance due to its lower vapor pressure, higher melting temperature and viscosity, which can decrease the oxygen diffusion rate through the layer and suppress B_2O_3 evaporation at these temperatures. Compared with the normal powder mixing method, the sol-gel coating has its unique advantages, such as homogenous dispersion of the minor phase, individual SiC grains attached evenly on the surface of ZrB_2 particles, providing the most effective grain boundary pinning effect and improving densification due to the coalescence of SiC on ZrB_2 by SiC nano particle agglomeration in sintering and oxidation performance of the composites.

Chapter 8 Conclusions

8.1 Conclusions

While the UHTCs have many unique advantages for high temperature applications, their strong covalent bonds render the materials very low atomic diffusion rate and are thus very difficult to densify. Conventional methods for processing of UHTC composites use powder as a starting material. A major issue with the conventional method is the poor mixing/processing of powders with different densities and sizes. This is especially true with nano-sized powders. The sol-gel based wet chemistry method offers unique advantages for the production of UHTCs, such as improved microstructures, properties and surface coatings of the materials, when compared with conventional powder mixing approaches. Even with these advantages, to the best of our knowledge, little research has been done on preparing dense UHTCs by the sol-gel process. In this thesis, sol-gel based wet chemistry approaches coupled with spark plasma sintering (SPS) are used to prepare dense UHTC composites with modified/improved microstructures and properties. Research in this thesis shows that the proposed novel sol-gel based wet chemistry approaches for synthesizing and modifying UHTC composites are successful. The sol-gel approach has many advantages over the conventional powder mixing techniques, including the retention of homogeneous fine-grained microstructures, hindering grain growth, avoiding intermediate transit phase/liquid phase, improving densification, filling pores to improve density, avoiding handling of nano-sized starting powders and allowing infiltration of complex shaped samples.

The effects of the pulsed DC current during SPS on the densification, phase transformation, microstructure and mechanical properties of conductive Si_3N_4/TiN composites and non-conductive monolithic Si_3N_4 were studied. The introduction of TiN into Si_3N_4 increases the electrical conductivity of the composite materials, and consequently affects their sintering behavior, microstructure and mechanical properties

after SPS densification. The densification and α-β transformation of the Si$_3$N$_4$/TiN composites are significantly improved by the passage of a high current through the sample during the SPS process. The shrinkage curves of the samples also showed that the densification for the conductive Si$_3$N$_4$/TiN composites started about 120°C lower than that for the non-conductive monolithic Si$_3$N$_4$. The results of the mechanical property tests show that the introduction of TiN in Si$_3$N$_4$/TiN composite samples, especially with 50% TiN, greatly increases the fracture toughness. It does this without causing a decrease to the hardness of the Si$_3$N$_4$. This study shows that increasing the current that is passing through a sample is a possible means for improving the sintering behavior of the material.

Dense TiC/SiC composites with uniform nanostructures are successfully prepared by a combination of sol-gel processing and SPS. Ultra-fine TiC/SiC nanopowders were first synthesized from direct carbothermal reduction of monolithic Ti–Si–O–C precursors. The grain size of the TiC/SiC composites not only decreases markedly with the increase of SiC content (from a few hundred nanometres in monolithic TiC to less than 50 nanometres in the 50%TiC-50%SiC composite) but also decreases in some degree with the increase of the carbon/metal ratio after carbothermal reduction. The densification of the TiC/SiC composites is also improved with the increase of the concentration of SiC in the TiC/SiC composites. Almost fully dense TiC/SiC composites with uniform nanostructures were prepared successfully through SPS at 1700 °C without significant grain growth. This ia a significant improvement compared with monolithic TiC, which still had some pororsity after SPS at 1800 °C with grain size larger than 10 μm. Grain growth of the TiC/SiC composites is damatically suppressed with increasing SiC content due to the pinning effect of SiC grains at the boundaries of TiC grains.

TiC/SiC composites of near full density with homogeneous nanostructures were produced successfully through a novel sol-gel infiltration and SPS with multi-cycles of infiltration of a Si-O-C sol into porous TiC scaffolds. This compares favorably with the 95

percent density achieved with a controlled monolithic TiC sample sintered at the same condition. Functionally gradient TiC/SiC nanocomposites were also formed successfully by the sol-gel infiltration of porous TiC scaffolds. The porosity declines from 30% for the starting scaffold to a few percent after three or more cycles of infiltration. The introduction of SiC as a very fine dispersion into the TiC scaffold hinders the grain growth of TiC due to the grain boundary pinning effect. This sol-gel infiltration technique is also successfully used to control the residual carbon in the TiC scaffold, which helps create fully dense composites.

XRD, SEM and TEM analyses show that nano-sized SiC particles were successfully coated on the surface of ZrB_2 grains uniformly via the sol-gel coating process. The morphology and size of SiC grains also variy with the increasing of SiC content. The morphology of SiC grains changes from mostly particles to short whiskers with increasing SiC content in the composites. The grain size of SiC increases from about 100 nm in the sample with 9 at% SiC to larger than 300 nm in the one with 23 at% SiC. These differences are due to the nature of gas reaction during the carbothermal reduction of the Si-O-C gel, in which the SiC grains grow up from the gas phases. ZrB_2/SiC composites prepared via sol-gel coating can be almost completely densified without obvious grain growth after being sintered at 1900 °C, without any sintering additives. The introduction of SiC improves the densification of the ZrB_2 and greatly suppresses its grain growth due to the solid solution of SiC and ZrB_2 and the pinning effect of the nano SiC particles on the grain boundaries of ZrB_2. The results of the ablation test at 2200 °C in air show that the introduction of SiC by both sol-gel infiltration and coating greatly improves the oxidation resistance of the ZrB_2/SiC composite at high temperatures compared with the monolithic ZrB_2 control sample.

8.2 Outlook

The potential for future direction and improvement are brieftly highlighted. The novel sol-gel infiltration technique developed in this study has great potential for modifying/improving the surface of UHTC powders and bulk materials and producing functionally graded materials with complicated shapes, which are very difficult or even impossible in some cases to achieve by conventional manufacturing methods. However, the effects of the pore size and distribution in the scaffolds on the thickness of the infiltration layer and the density of the final products after sintering have not been investigated due to the limitation of faciclities and time. This is important for the fabrication of functionally graded material objects. One key point for this sol-gel infiltration technique to succeed is the preparation of porous scaffolds with sufficient strength to allow smooth infiltration but to survive the sol-gel infiltration process as well. One possible approach could be to prepare the porous scaffold containing binders at room temperature so that the scaffold can have high open porosity and enough bonding strength between the grains after calcination. This approach would be particularly useful for the scaffolds prepared from nano-sized powders. The residual carbon in the scaffold can be tailored by carbothermal reaction with the oxygen in the sol during the subsequent firings, which has been confirmed as completely practicable in section 6.4 Chapter 6.

One potential for the improvement of the sol-gel coating approach for the preparation of UHTCs is the coating of nano-sized SiC whiskers *in situ* on the surface of the ZrB_2 powders, which may have a great positive effect on the improvement of the microstructure and mechanical properties of the final sintered ZrB_2/SiC composite. The temperature of the ablation test of the ZrB_2/SiC composite in this study was only about 2200 °C due to the limitation of facilities. Testing of UHTCs in more severe environments, e.g. arc jet condition, will be an important future work. In general more

property tests, such as thermal, chemical and mechanical properties, must be carried out for future applications of the sol-gel derived UHTCs.

Publications

1. **Manyuan Zhou**, Don Rodrigo, Xiaojing Wang, Jianbao Hu, Shaoming Dong, Yi-Bing Cheng, A novel approach for preparation of dense TiC–SiC nanocomposites by sol–gel infiltration and spark plasma sintering, Journal of the European Ceramic Society 34 (2014) 1949–1954.

2. Jianbao Hu, Shaoming Dong, Qian Feng, **Manyuan Zhou**, Xiaojing Wang, Yibing Cheng, Tailoring carbon nanotube/matrix interface to optimize mechanical properties of multiscale composites, CARBON 69 (2014) 621–625.

3. Jie Zhong, Yong Peng, **Manyuan Zhou**, Juan Zhao, Shuquan Liang, Huanting Wang, Yi-Bing Cheng, Facile synthesis of nanoporous TiC–SiC–C composites as a novel counter-electrode for dye sensitized solar cells, Microporous and Mesoporous Materials 190 (2014) 309–315.

4. **Manyuan Zhou**, Don Rodrigo, Yi-Bing Cheng, Effects of the electric current on conductive Si_3N_4/TiN composites in spark plasma sintering, Journal of Alloys and Compounds 547 (2013) 51–58.

5. **Manyuan Zhou**, Jie Zhong, Juan Zhao, Don Rodrigo, Yi-Bing Cheng, Microstructures and properties of Si_3N_4/TiN composites sintered by hot pressing and spark plasma sintering, Materials Research Bulletin 48 (2013) 1927–1933.

6. Jie Zhong, Juan Zhao, Shuquan Liang, Xiaoping Tan, **Manyuan Zhou**, Guowei Zhang, Synthesis of spherical (30 nm) and rod-like (200 nm) zirconia co-reinforced mullite nanocomposites, Ceramics International, 39 (2013) 4163-4170.

References

1   Loehman, R., Corral, E., Dumm, H. P., Kotula, P. & Tandon, R. Ultra High Temperature Ceramics for hypersonic Vehicle application. *Sandia report* (2006).

2   Rödel, J. *et al.* Development of a roadmap for advanced ceramics: 2010–2025. *Journal of the European Ceramic Society* **29**, 1549-1560, doi:10.1016/j.jeurceramsoc.2008.10.015 (2009).

3   Giordano, C. & Antonietti, M. Synthesis of crystalline metal nitride and metal carbide nanostructures by sol–gel chemistry. *Nano Today* **6**, 366-380, doi:10.1016/j.nantod.2011.06.002 (2011).

4   Han, J., Hu, P., Zhang, X. & Meng, S. Oxidation behavior of zirconium diboride–silicon carbide at 1800°C. *Scripta Materialia* **57**, 825-828, doi:10.1016/j.scriptamat.2007.07.009 (2007).

5   Marschall, J. *et al.* Oxidation of ZrB_2-SiC Ultrahigh-Temperature Ceramic Composites in Dissociated Air. *Journal of Thermophysics and Heat Transfer* **23**, 267-278, doi:10.2514/1.39970 (2009).

6   Karlsdottir, S. N. & Halloran, J. W. Oxidation of ZrB_2-SiC: Influence of SiC Content on Solid and Liquid Oxide Phase Formation. *Journal of the American Ceramic Society* **92**, 481-486, doi:10.1111/j.1551-2916.2008.02874.x (2009).

7   Karlsdottir, S. N., Halloran, J. W. & Grundy, A. N. Zirconia Transport by Liquid Convection during Oxidation of Zirconium Diboride-Silicon Carbide. *Journal of the American Ceramic Society* **91**, 272-277, doi:10.1111/j.1551-2916.2007.02142.x (2007).

8   Johnson, S. M. Ultra High Temperature Ceramics-Application, issues and prospects. *2nd Ceramic Leadership Summit* (2011).

9   Tokita, M. Mechanism of spark plasma sintering (SPS). *PM2000 Powder Metallurgy World Congress, Kyoto, Japan*, 729-732 (2001).

10   Tokita, M. Development of advanced spark plasma sintering (SPS) systems and its industrial applications. *Am Ceram Soc. , ceramic transaction* **194**, 51-60 (2006).

11   Munir, Z. A., Anselmi-Tamburini, U. & Ohyanagi, M. The effect of electric field and pressure on the synthesis and consolidation of materials, synthesis and consolidation of materials: a review of the spark plasma sintering method. *J Mater Sci* **41**, 763-777 (2006).

12   Makino, Y. Crystallographic behaviors of nanopowder anatase consolidated by SPS method. *Am Ceram Soc., ceramic transaction* **194**, 301-312 (2006).

13   Grasso, S., Sakka, Y. & Maizza, G. Electric current activated/assisted sintering(ECAS): a review of patents 1996-2008. *Sci Tech Adv Mater* **10**, 1-24 (2009).

14   Hungria, T., Galy, J. & Castro, A. Spark plasma sintering as a useful technique to the nanostructuration of piezo-ferroelectric materials. *Adv Eng Mater* **11**, 615-631 (2009).

15   Tokita, M. Spark Plasma Sintering (SPS) Method, Systems, and Applications. *Handbook of Advanced Ceramic* **Chapter 11.2.3**, 1149-1177, doi:10.1016/b978-0-12-385469-8.00060-5 (2013).

16   Inoue, K. *US Patent No. 3* **241** (1966).

17   Tokita, M. Trends in Advanced SPS Spark Plasma Sintering Systems and Technology. *J. Soc. Powder Technol.* **30**, 790-804 (1993).

18   Yamazaki, K., Risbud, S. H., Aoyama, H. & Shoda, K. PAS (Plasma activated sintering): Transient sintering process control for rapid consolidation of powders. *J. Mater. Proc. Tech.* **65**, 955-965 (1996).

19   Anderson, K. R., Groza, J. R., Fendorf, M. & Echer, C. J. Surface oxide debonding in field assisted powder sintering. *Mater. Sci. Eng. A* **270**, 278-282 (1999).

20   Matsugi, K., Hatayama, T. & Yanagisawa, O. Effect of direct current pulse discharge on specific resistivity of copper and iron powder compacts. *J Jpn Inst Metals* **59**, 740-745 (1995).

21   Ozaki, K., Kobayashi, K., Nishio, T., Matsumoto, A. & Sugiyama, A. Sintering phenomena on initial stage in pulsed current sintering. *J Jpn Soc Powder Powder Metall* **47**, 293-297 (2000).

22   Shen, Z., Johnsson, M., Zhao, Z. & Nygren, M. Spark plasma sintering of alumina. *J Am Ceram Soc* **85**, 1921-1927 (2002).

23   Schmidt, J., Niewa, R., Schmidt, M. & Grin, Y. Spark plasma sintering effect on the decomposition of MgH_2. *J Am Ceram Soc* **88**, 1870-1874 (2005).

24   Song, X., Liu, X. & Zhang, J. Neck formation and self-adjusting mechanism of neck growth of conducting powders in spark plasma sintering. *J Am Ceram Soc* **89**, 494-500 (2006).

25   Chaim, R. Densification mechanisms in spark plasma sintering of nanocrystalline ceramics. *Mater Sci Eng A* **443** (2007).

26   Misawa, T., Shikatani, N., Kawakami, Y., Enjoji, T. & Ohtsu, Y. Influence of internal pulsed current on the sintering behavior of pulsed current sintering process. *Mater Sci Forum* **638-642**, 2109-2114 (2010).

27   Nanko, M., Maruyama, T. & Tomino, H. Neck growth on initial stage of pulse current pressure sintering for coarse atomized powder made of cast-iron. *J Jpn Inst Metals* **63**, 917-923 (1999).

28   Kumeta, K., Nakamura, Y., Takada, A. & Ishizaki, K. Surface observation of pulsed electric sintered alumina balls. *J Jpn Ceram Soc* **107**, 187-189 (1999).

29   Kim, H. T., Kawahara, M. & Tokita, M. Specimen temperature and sinterability of Ni powder by spark plasma sintering. *J Jpn Soc Powder Powder Metall* **47**, 887-891 (2001).

30   Guyot, P. *et al.* Does the Branly effect occur in spark plasma sintering. *J. Phys. D: Appl. Phys.* **45**, 1-4 (2012).

31   Belmonte, M., González-Julián, J., Miranzo, P. & Osendi, M. I. Spark plasma sintering: A powerful tool to develop new silicon nitride-based materials. *Journal of the European Ceramic Society* **30**, 2937-2946, doi:10.1016/j.jeurceramsoc.2010.01.025 (2010).

32   Suárez, M. *et al.* Challenges and Opportunities for Spark Plasma Sintering: A Key Technology for a New Generation of Materials. *http://www.intechopen.com/books/sintering-applications/challenges-and-opportunities-for-spark-plasma-sintering-a-key-technology-for-a-new-generation-of-mat* (2013).

33   JR, G., M, G. & JA, S. Surface effects in field-assisted sintering. *J Mater Res* **16**, 286-292 (2001).

34   Z, S. & M, N. Kinetic aspects of superfast consolidation of silicon nitride based ceramics by spark plasma sintering. *J Mater Chem* **11**, 204-207 (2001).

35   ZJ, S., Z, Z., H, P. & M, N. Formation of tough interlocking microstructures in silicon nitride ceramics by dynamic ripening. *Nature* **417**, 266-269 (2002).

36   Salamon, D., Shen, Z. & Šajgalík, P. Rapid formation of α-sialon during spark plasma sintering: Its origin and implications. *Journal of the European Ceramic Society* **27**, 2541-2547, doi:10.1016/j.jeurceramsoc.2006.09.008 (2007).

37   Sarin, V. K. On the α-to-β phase transformation in silicon nitride. *Materials Science and Engineering A* **105/106**, 151-159 (1988).

38   Wada, S., Suganuma, M., Kitagawa, Y. & Murayama, N. Delay of alpha to beta transformation of Si3N4 contacting with carbon during hot-pressing and PECS. *J. Ceram. Soc. Jpn.* **106**, 924-926 (1998).

39   Nishimura, T., Mitomo, M., Hirotsuru, H. & Kawahara, M. Fabrication of silicon-nitride nano-ceramics by spark plasma sintering. *J. Mater. Sci. Lett.* **14**, 1046-1047 (1995).

40   Schneider, J. A., Mukherjee, A. K., Yamazaki, K. & Shoda, K. Mechanism of plasma assisted sintering in Si_3N_4 ceramic system. *Mater. Lett.* **25**, 101-104 (1995).

41   Chen, C., Chen, F., Shen, Q. & L. Zhang, F. Y. Liquid phase sintering (LPS) and dielectric constant of α-silicon nitride ceramic. *J. Wuhan Univ. Technol. Mater. Sci. Eng. Ed.* **21**, 98-100 (2006).

42   Lu, X., Ning, X. S., Xu, W., Zhou, H. P. & Chen, K. X. Study on Thermal Conductivity of SPS-Sintered Si_3N_4 Ceramics after Heat-Treatment. *Materials Science Forum* **475-479**, 1279-1282, doi:10.4028/www.scientific.net/MSF.475-479.1279 (2005).

43   Suganuma, M., Kitagawa, Y., S.Wada & N.Murayama. Pulsed Electric Current Sintering of Silicon Nitride. *J. Am. Ceram. Soc.* **86**, 387-394 (2003).

44   Xu, X. *et al.* New Strategies for Preparing NanoSized Silicon Nitride Ceramics. *Journal of the American Ceramic Society* **88**, 934-937, doi:10.1111/j.1551-2916.2005.00187.x (2005).

45   Hotta, M. & Hojo, J. Nanostructure control of liquid-phase sintered Si_3N_4 ceramics by spark plasma sintering. *J. Ceram Soc Japan.* **117**, 1302-1305 (2009).

46   Wei, P., Chen, L., Okubo, A. & Hirai, T. Tough multilayered α–β SI3N4 ceramics prepared by spark plasma sintering. *Materials Letters* **49**, 239-243 (2001).

47   Wada, S., Suganuma, M., Kitagawa, Y. & Murayama, N. Comparison between Pulse Electric Current Sintering and Hot Pressing of Silicon Nitride Ceramics. *J. Ceram. Soc. Jpn.* **107**, 887-890 (1999).

48   Bai, L., Mao, X., Shen, W. & Ge, C. Comparative study of β- Si_3N_4 powders prepared by SHS sintered by spark plasma sintering and hot pressing. *Journal of University of Science and Technology Beijing, Mineral, Metallurgy, Material* **14**, 271-275, doi:10.1016/s1005-8850(07)60052-8 (2007).

49   Kurama, S., Schulz, I. & Herrmann, M. Wear properties of α- and α/β-SiAlON ceramics obtained by gas pressure sintering and spark plasma sintering. *Journal of the European Ceramic Society* **31**, 921-930, doi:10.1016/j.jeurceramsoc.2010.11.010 (2011).

50   Wang, S. W., Chen, L. D. & Hirai, T. Effect of plasma activated sintering(PAS) parameters on densification of copper powder. *Mater. Res. Bull.* **35**, 619-628 (2000).

51   Kim, H. T., Kawahara, M. & Tokita, M. Specimen temperature and sinterability of Ni powder by spark plasma sintering. *J. Jpn. Soc. Powder Metall.* **47**, 887-891 (2000).

52   Stanciu, L. A., Kodash, V. Y. & Groza, J. R. Effects of heating rate on densification and grain growth during field-assisted sintering of α-Al$_2$O$_3$ and MoSi$_2$ powders. *Metall. Mater. Trans. A* **32**, 2633-2638 (2001).

53   Omori, M. Sintering, consolidation, reaction and crystal growth by the spark plasma system (SPS). *Mater. Sci. Eng. A* **287**, 183-188 (2000).

54   Wang, S. W., Chen, L. D. & Hirai, T. Densification of Al$_2$O$_3$ powder using spark plasma sintering. *J. Mater. Res.* **15**, 982-987 (2000).

55   Dobedoe, R. S., Wost, G. D. & Lewis, M. H. Spark plasma sintering of ceramics. *, Bull. Eur. Ceram. Soc.* **1**, 19-24 (2003).

56   Shearwood, C., Fu, Y. Q., Yu, L. & Khor, K. A. Spark plasma sintering of TiNi nano-powder. *Scripta Mater.* **52**, 455-460 (2005).

57   Lee, J.-M., Kang, S.-B., Sato, T., Tezuka, H. & Kamio, A. Fabrication of Al/Al3Fe composites by plasma synthesis method. *Mater. Sci. Eng. A* **343**, 199-209 (2003).

58   Zavaliangos, A., Zhang, J., Krammer, M. & Groza, J. R. Temperature evolution during field activated sintering. *Mater. Sci. Eng. A* **379**, 218-228 (2004).

59   Yucheng, W. & Zhengyi, F. Study of Temperature Field in Spark Plasma Sintering. *Mater. Sci. Eng. B* **90**, 34-37 (2002).

60   Kawano, S., Takahashi, J. & Shimada, S. The preparation and spark plasma sintering of silicon nitride-based materials coated with nano-sized TiN. *Journal of the European Ceramic Society* **24**, 309-312, doi:10.1016/s0955-2219(03)00229-2 (2004).

61   Lee, C.-H., Lu, H.-H., Wang, C.-A., Nayak, P. K. & Huang, J.-L. Microstructure and mechanical properties of TiN/Si3N4 nanocomposites by spark plasma sintering (SPS). *Journal of Alloys and Compounds* **508**, 540-545, doi:10.1016/j.jallcom.2010.08.116 (2010).

62   Ayas, E., Kara, A. & kara, F. A novel approach for preparing electrically conductive α-β SiAlON-TiN composites by spark plasma sintering. *J. Ceram. Soc. Jpn.* **116**, 812-814 (2008).

63   Kawano, S., Takahashi, J. & Shimada, S. Highly electroconductive TiN/Si3N4 composite ceramics fabricated by spark plasma sintering of Si3N4 particles with a nano-sized TiN coating. *Journal of Materials Chemistry* **12**, 361-365, doi:10.1039/b107058b (2002).

64   Kawano, S., Takahashi, J. & Shimada, S. Fabrication of TiN-Si3N4 ceramics by spark plasma sintering of Si3N4 particles coated with nanosized TiN prepared by controlled hydrolysis of Ti O-i-C3H7. *J. Am. Ceram. Soc.* **86**, 701-705 (2003).

65   Ahmad, N. & Sueyoshi, H. Properties of Si3N4–TiN composites fabricated by spark plasma sintering by using a mixture of Si3N4 and Ti powders. *Ceramics International* **36**, 491-496, doi:10.1016/j.ceramint.2009.09.029 (2010).

66   Ahmad, N. & Sueyoshi, H. Microstructure and mechanical properties of silicon nitride–titanium nitride composites prepared by spark plasma sintering. *Materials Research Bulletin* **46**, 460-463, doi:10.1016/j.materresbull.2010.11.021 (2011).

67   Guo, Z. *et al.* Microstructure and electrical properties of Si3N4–TiN composites sintered by hot pressing and spark plasma sintering. *Ceramics International* **33**, 1223-1229, doi:10.1016/j.ceramint.2006.03.029 (2007).

68   Giordano, C. & Antonietti, M. Synthesis of crystalline metal nitride and metal carbide nanostructures by sol-gel chemistry. *Nano Today* **6**, 366-380 (2011).

69   Andrievski, R. A. Review-Films of interstitial phases: synthesis and properties. *J. Mater. Sci* **32**, 4463-4484 (1997).

70   Knotek, O., Loffler, F., Schrey, A. & Bosserhoff, B. Diffusion barrier design against rapid interdiffusion of mcraly and ni-base material. *Surf. Coat. Technol.* **61**, 133-138 (1993).

71   Hirai, T. & Sasaki, M. Vapor-deposited functionally gradient materials. *JSME International Journal, Series I-Solid Mech. Strength Mater.* **34**, 123-129 (1991).

72 Schaaf, P., Kahle, M. & Carpene, E. Reactive laser synthesis of carbides and nitrides. *Appl. Surf. Sci.* **247**, 607-615 (2005).

73 Vissokov, G., Grancharov, I. & Tsvetanov, T. On the plasma-chemical synthesis of nanopowders. *Plasma Sci. Technol.* **5**, 2039-2050 (2003).

74 S.V. Petrov. Plasma synthesis in the technology of gasothermic spraying. *Powder Metall. Met. Ceram.* **36**, 483-486 (1997).

75 Todas, T. T. *Angew. Chem. Adv. Mater.* **101**, 814 (1989).

76 Liu, T. Q., Sakurai, O., Kieda, N., Kato, M. & Mizutani, N. *Nippon Seramikkusu Kyokai Gakujutsu Ronbunshi* **97**, 1321 (1989).

77 Wachtmann, J. B. J. & Haber, R. A. *Chem. Engng Prog.* **39**, 46 (1986).

78 FLAGAN, R. C. Aerosol routes for powder synthesis. *American Ceramic Society Ceramic Transactions* **1A**, 229 (1988).

79 Flint, J. H. & Haggerty, J. S. Models for synthesis of ceramic powders by vapor phase reaction. *American Ceramic Society Ceramic Transactions* **1A**, 244 (1988).

80 Rhine, W. E. & Bowen, H. K. An Overview of Chemical and Physical Routes to Advanced Ceramic Powders. *Ceramics international* **17**, 143-152 (1991).

81 Nikzada, L., Ebadzadehb, T., Vaezia, M. R. & Tayebifard, A. High-energy ball milling of B-C-Ti mixtures for the fabrication of B4C and TiB2 nanocomposite powder. *Journal of Ceramic Processing Research* **13**, 5 (2012).

82 Wang, J. J., Grocholl, L. & Gillan, E. G. Facile azidothermal metathesis route to gallium nitride nanoparticles. *Nano Lett.* **2**, 899-902 (2002).

83 Micic, O. I., Ahrenkiel, S. P., Bertram, D. & Nozik, A. J. Synthesis, structure, and optical properties of colloidal GaN quantum dots. *Appl. Phys. Lett.* **75**, 478-480 (1999).

84 Li, J. G. *et al.* Synthesis of nanocrystalline titanium nitride powders by direct nitridation of titanium oxide. *J. Am. Ceram. Soc.* **84**, 3045-3047 (2001).

85 Jackson, A. W., Shebanova, O., Hector, A. L. & McMillan, P. F. *J. Solid State Chem.* **179**, 1383-1393 (2006).

86   Choi, D., Blomgren, G. E. & Kumta, P. N. Fast and reversible surface redox reaction in nanocrystalline vanadium nitride supercapacitors. *Adv. Mater.* **18**, 1178-1182 (2006).

87   Kaskel, S., Schlichte, K., Chaplais, G. & Khanna, M. Synthesis and Characterisation of Titanium Nitride Based Nanoparticles. *J. Mater. Chem.* **13**, 1496-1499 (2003).

88   Schwartz, V. & Oyama, S. T. Study of niobium oxynitride - synthesis, characterization, and reactivity. *Chem. Mater.* **9**, 3052-3059 (1997).

89   Huang, Y. L. *et al.* Synthesis of nanocrystalline titanium nitride by reacting titanium dioxide with sodium amid. *Mater. Lett.* **61**, 1056-1059 (2007).

90   Kawaguchi, M. & Nozaki, K. Synthesis, structure, and characteristics of the new host material [(C3N3)(2)(NH)(3)](N). *Chem. Mater.* **7**, 257-264 (1995).

91   Fischer, A., Antonietti, M. & Thomas, A. Growth Confined by the Nitrogen Source: Synthesis of Pure Metal Nitride Nanoparticles in Mesoporous Graphitic Carbon Nitride. *Adv. Mater.* **19**, 264-267 (2007).

92   Zhao, H. Z., Lei, M., Chen, X. L. & Tang, W. H. Facile route to metal nitrides through melamine and metaloxides. *J. Mater. Chem.* **16**, 4407-4412 (2006).

93   Zhao, H. Z., Lei, M., Yang, X., Jian, J. K. & Chen, X. L. Route to GaN and VN assisted by carbothermal reduction process. *J. Am. Chem. Soc.* **127**, 15722-15723 (2005).

94   Rahaman, M. N. Ceramic Processing and Sintering Second Edition. *CRC Press*, 18 (2003).

95   Livage, J. & Sanchez, C. Sol-gel chemistry. *J. Non-Cryst. Solids* **145**, 11-19 (1992).

96   Sanchez, C. *et al.* Designed hybrid organic-inorganic nanocomposites from functional nanobuilding blocks. *Chem. Mater.* **13**, 3061-3083 (2001).

97   Brinker, C. J. & Scherer, G. W. Sol-Gel Science: the physics and chemistry of sol-gel processing. *Academic Press Inc.*, 1 (1990).

98   Berger, W. G. E. Jenaer Glaswerk Schott und Gen. *Jena GDR*, 411 (1939).

99   Dislich, H. & Hinz, P. History and principles of the sol-gel process and some new multicomponent oxide coatings. *J. Non-Cryst. Solids* **48**, 11-16 (1982).

100   Sanchez, C., Belleville, P., Popall, M. & Nicole, L. Applications of advanced hybrid organic-inorganic nanomaterials: from laboratory to market. *Chem. Soc. Rev.* **40**, 696-753 (2011).

101   Brown, G. M. & Maya, L. Ammonolysis Products of the Dialkylamides of Titanium, Zirconium, and Niobium as Precursors to Metal Nitrides. *J. Am. Ceram. Soc.* **71**, 78-82 (1988).

102   Maya, L. Ammonolysis of niobium(V) bromide. *Inorg. Chem.* **26**, 1459-1462 (1987).

103   Maya, L. A mixed-valence titanium(III)-titanium(IV) tetramer and related compounds. *Inorg. Chem.* **25**, 4213-4217 (1986).

104   Sardar, K., Deepak, F. L., Govindaraj, A., Seikh, M. M. & Rao, C. N. R. InN nanocrystals, nanowires and nanotubes. *Small* **1**, 91-94 (2005).

105   Desmoulins-Krawiec, S. *et al.* Synthesis of nanostructured materials in supercritical ammonia : nitrides, metals and oxides. *J. Mater. Chem.* **14**, 228-232 (2004).

106   Grocholl, L., Wang, J. J. & Gillan, E. G. Solvothermal azide decomposition route to GaN nanoparticles, nanorods, andfaceted crystallites. *Chem. Mater.* **13**, 4290-4296 (2001).

107   Eick, B. M. & Youngblood, J. P. Carbothermal reduction of metal-oxide powders by synthetic pitch to carbide and nitride ceramics. *J. Mater. Sci.* **44**, 1159-1171 (2009).

108   Vaidhyanathan, B. & Rao, K. J. Synthesis of Ti, Ga and V Nitrides : Microwave assisted carbothermal reduction and nitridation. *Chem. Mater.* **9**, 1196-1200 (1997).

109   Bača, Ľ. & Stelzer, N. Adapting of sol–gel process for preparation of TiB2 powder from low-cost precursors. *Journal of the European Ceramic Society* **28**, 907-911, doi:10.1016/j.jeurceramsoc.2007.09.028 (2008).

110   Jung, W. S. & Ahn, S. K. Monitoring the conversion of α-alumina to AlN under a flow of nitrogen by Al-27 MAS NMR spectroscopy. *J. Mater. Sci. Lett.* **16**, 1573-1575 (1997).

111   Zhong, J. *et al.* Formation of novel mesoporous TiC microspheres through a sol–gel and carbothermal reduction process. *Journal of the European Ceramic Society* **32**, 3407-3414, doi:10.1016/j.jeurceramsoc.2012.04.047 (2012).

112   Li, F., Kang, Z., Huang, X. & Zhang, G.-J. Synthesis of ZrB2 nanofibers by carbothermal reduction via electrospinning. *Chemical Engineering Journal* **234**, 184-188, doi:10.1016/j.cej.2013.08.100 (2013).

113   Gotoh, Y. *et al.* Synthesis of titanium carbide from a composite of TiO2 nanoparticles-methyl cellulose by carbothermal reduction. *Materials Research Bulletin* **36**, 2263-2275 (2001).

114   Xiang, J., Xie, Z., Huang, Y. & Xiao, H. Synthesis of Ti(C,N) ultrafine powders by carbothermal reduction of TiO2 derived from sol–gel process. *Journal of the European Ceramic Society* **20**, 933-938 (2000).

115   Raman, V., Bhatia, G., Mishra, A. K., Bhardwaj, S. & Sood, K. N. Synthesis of silicon carbide nanofibers from pitch blended with sol–gel derived silica. *Materials Letters* **60**, 3906-3911, doi:10.1016/j.matlet.2006.03.138 (2006).

116   Nishimura, T., Ishihara, S., Yoshioka, Y. & Tanaka, H. Synthesis of Non-Oxide Ceramic Fine-Powders from Organic Precursors. *Key Engineering Materials* **403**, 269-272, doi:10.4028/www.scientific.net/KEM.403.269 (2009).

117   Wang, K., Wang, H. & Cheng, Y. B. Synthesis of nanostructured silicon carbide spheres from mesoporous C-SiO2 nanocomposites. *Chem Commun (Camb)* **46**, 303-305, doi:10.1039/b912326a (2010).

118   Xie, J., Fu, Z., Wang, Y., Lee, S. W. & Niihara, K. Synthesis of nanosized zirconium carbide powders by a combinational method of sol–gel and pulse current heating. *Journal of the European Ceramic Society* **34**, 13.e11-13.e17, doi:10.1016/j.jeurceramsoc.2013.07.003 (2014).

119   Dollé, M. *et al.* Synthesis of nanosized zirconium carbide by a sol–gel route. *Journal of the European Ceramic Society* **27**, 2061-2067, doi:10.1016/j.jeurceramsoc.2006.06.005 (2007).

120   Li, Y., Han, W., Li, H., Zhao, J. & Zhao, T. Synthesis of nano-crystalline ZrB2/ZrC/SiC ceramics by liquid precursors. *Materials Letters* **68**, 101-103, doi:10.1016/j.matlet.2011.10.060 (2012).

121   Kim, I. S. & Kumta, P. N. Hydrazide sol-gel synthesis of nanostructured titanium nitride: precursor chemistry and phase evolution. *J. Mater. Chem.* **13**, 2028-2035 (2003).

122   Livage, J., Henry, M. & Sanchez, C. Sol-gel chemistry of transition metal oxides. *Prog. Solid State Chem.* **18**, 259-341 (1988).

123   Niederberger, M., Bartl, M. H. & Stucky, G. D. Benzyl alcohol and titanium tetrachloride - a versatile reaction system for the nonaqueous and low-temperature preparation of crystalline and luminescent titania nanoparticles. *Chem. Mater.* **14**, 4364-4370 (2002).

124   Bilecka, I. & Niederberger, M. New developments in the nonaqueous and/or non-hydrolytic sol-gel synthesis of inorganic nanoparticles. *Electrochim. Acta* **55**, 7717-7725 (2010).

125   J. Buha, I. D., Antonietti, M. & Niederberger, M. Thermal transformation of metal oxide nanoparticles into nanocrystalline metal nitrides using cyanamide and urea as nitrogen source. *Chem. Mater.* **19**, 3499-3505 (2007).

126   Giordano, C., Erpen, C., Yao, W. T. & Antoniett, M. Synthesis of Mo and W Carbide and Nitride Nanoparticles via a Simple "Urea Glass" Route". *Nano Lett.* **8**, 4659-4663 (2008).

127   Sardar, K., Dan, M., Schwenzer, B. & Rao, C. N. R. A simple single-source precursor route to the nanostructures of AlN, GaN and InN. *J. Mater. Chem.* **15**, 2175-2177 (2005).

128   Qiu, Y. & Gao, L. Metal-urea complex-a precursor to metal nitrides. *J. Am. Ceram. Soc.* **87**, 352-357 (2004).

129   Qiu, Y. & Gao, L. Novel synthesis of nanocrystalline gallium nitride powder from gallium(III)-urea complex. *Chem. Lett.* **32**, 774-775 (2003).

130   Preiss, H., Berger, L.-M. & Schultze, D. Studies on the Carbothermal Preparation of Titanium Carbide from Different Gel Precursors. *Journal of the European Ceramic Society* **19**, 195-206 (1999).

131   Chandra, N., Sharma, M., Singh, D. K. & Amritphale, S. S. Synthesis of nano-TiC powder using titanium gel precursor and carbon particles. *Materials Letters* **63**, 1051-1053, doi:10.1016/j.matlet.2009.02.004 (2009).

132   Biedunkiewicz, A. Manufacturing of ceramic nanomaterials in Ti–Si–C–N system by sol–gel method. *Journal of Sol-Gel Science and Technology* **59**, 448-455, doi:10.1007/s10971-010-2237-2 (2010).

133   Rambo, C. R., Cao, J., Rusina, O. & Sieber, H. Manufacturing of biomorphic (Si,Ti,Zr)-carbide ceramics by sol–gel processing. *Carbon* **43**, 1174-1183, doi:10.1016/j.carbon.2004.12.009 (2005).

134   Li, S. *et al.* In situ synthesis and microstructure characterization of TiC–TiB2–SiC ultrafine composites from hybrid precursor. *Materials Chemistry and Physics* **133**, 946-953, doi:10.1016/j.matchemphys.2012.01.121 (2012).

135   Nakamura, I. H. a. T. <Synthesis of continuous silicon carbide-titanium carbide hybrid fibers through sol-gel processing.pdf>. *Materials Rcscarch Buktin* **31**, 869-875 (1996).

136   Wang, K., Yao, J., Wang, H. & Cheng, Y. B. Effect of seeding on formation of silicon carbide nanostructures from mesoporous silica-carbon nanocomposites. *Nanotechnology* **19**, 175605, doi:10.1088/0957-4484/19/17/175605 (2008).

137   Ang, C. *et al.* Synthesis and Evolution of Zirconium Carbide via Sol-Gel Route: Features of Nanoparticle Oxide-Carbon Reactions. *Journal of the American Ceramic Society* **96**, 1099-1106, doi:10.1111/jace.12260 (2013).

138   Lin, T.-T., Chang, J.-F. & Hon, M.-H. The growth and characteristics of CVD SiC TiC in-situ composites. *Ceramics International* **24**, 265-272 (1998).

139   Touanen, M., Teyssandier, F. & Ducarroir, M. SiC-TiC multiphased materials obtained by CVD. *Materials Science and Engineering A* **147**, 239-247 (1991).

140   Liu, G., Li, J., Chen, K. & Zhou, H. Combustion synthesis of (TiC+SiC) composite powders by coupling strong and weak exothermic reactions. *Journal of Alloys and Compounds* **492**, L82-L86, doi:10.1016/j.jallcom.2009.12.033 (2010).

141   Jiang, D. L., Wang, J. H., Li, Y. L. & Ma, L. T. Studies on the strengthening of silicon carbide-based multiphase ceramics I- The Si-TiC system. *Materials Science and Engineering A* **109**, 401-406 (1989).

142   Endo, H., Ueki, M. & Kubo, H. Hot pressing of SiC-TiC composites. *Journal of Materials Science* **25**, 2503-2506 (1990).

143   Endo, H., Ueki, M. & Kubo, H. Microstructure and mechanical properties of hot-pressed SiC-TiC composites. *Journal of Materials Science* **26**, 3769-3774 (1991).

144   Robayie, J. A., Kiipp, C. & Hausner, H. The influence of processing parameters on microstructure and mechanical properties of SiC-TiCp ceramics. *Ceramics International* **21**, 297-301 (1995).

145   Cho, K., Kim, Y., Choi, H. & Lee, J. In Situ-Toughened Silicon Carbide-Titanium Carbide Composites. *J. Am. Ceram. Soc.* **79**, 1711-1713 (1996).

146   An, H.-G., Kim, Y.-W. & Lee, J.-G. Effect of initial α-phase content of SiC on microstructure and mechanical properties of SiC–TiC composites. *Journal of the European Ceramic Society* **21**, 93-98 (2008).

147   Cabrero, J., Audubert, F. & Pailler, R. Fabrication and characterization of sintered TiC–SiC composites. *Journal of the European Ceramic Society* **31**, 313-320, doi:10.1016/j.jeurceramsoc.2010.10.010 (2011).

148   Chaim, R., Kleiner, L. & Kalabukhov, S. Densification of nanocrystalline TiC ceramics by spark plasma sintering. *Materials Chemistry and Physics* **130**, 815-821, doi:10.1016/j.matchemphys.2011.07.072 (2011).

149   Cheng, L., Xie, Z., Liu, G., Liu, W. & Xue, W. Densification and mechanical properties of TiC by SPS-effects of holding time, sintering temperature and pressure condition. *Journal of the European Ceramic Society* **32**, 3399-3406, doi:10.1016/j.jeurceramsoc.2012.04.017 (2012).

150   Chen, J., Li, W. & Jiang, W. Characterization of sintered TiC–SiC composites. *Ceramics International* **35**, 3125-3129, doi:10.1016/j.ceramint.2009.04.022 (2009).

151   Wang, L., Jiang, W. & Chen, L. Fabrication and characterization of nano-SiC particles reinforced TiC/SiCnano composites. *Materials Letters* **58**, 1401-1404, doi:10.1016/j.matlet.2003.09.053 (2004).

152   You, C., Jiang, D. & Tan, S. Deposition of silicon carbide-titanium carbide laminar ceramics by electrophoresis and densification by spark plasma sintering. *J. Am. Ceram. Soc.* **87**, 759-761 (2004).

153   Yan, Y., Zhang, H., Huang, Z., Liu, J. & Jiang, D. In Situ Synthesis of Ultrafine ZrB2–SiC Composite Powders and the Pressureless Sintering Behaviors. *Journal of the American Ceramic Society* **91**, 1372-1376, doi:10.1111/j.1551-2916.2008.02296.x (2008).

154   Ortona, A., Lagos, M. A., Scocchi, G. & Barcena, J. Spark plasma sintering of ZrB2–SiC composites with in-situ reaction bonded silicon carbide. *Ceramics International* **40**, 821-826, doi:10.1016/j.ceramint.2013.06.074 (2014).

155   Zou, J., Zhang, G.-J., Vleugels, J. & Van der Biest, O. High temperature strength of hot pressed ZrB2–20vol% SiC ceramics based on ZrB2 starting powders prepared by different carbo/boro-thermal reduction routes. *Journal of the European Ceramic Society* **33**, 1609-1614, doi:10.1016/j.jeurceramsoc.2013.03.001 (2013).

156   Zamora, V., Ortiz, A. L., Guiberteau, F. & Nygren, M. On the enhancement of the spark-plasma sintering kinetics of ZrB2–SiC powder mixtures subjected to high-energy co-ball-milling. *Ceramics International* **39**, 4191-4204, doi:10.1016/j.ceramint.2012.11.001 (2013).

157   Zhu, S., Fahrenholtz, W. G. & Hilmas, G. E. Influence of silicon carbide particle size on the microstructure and mechanical properties of zirconium diboride–silicon carbide ceramics. *Journal of the European Ceramic Society* **27**, 2077-2083, doi:10.1016/j.jeurceramsoc.2006.07.003 (2007).

158   Zhang, S. C., Hilmas, G. E. & Fahrenholtz, W. G. Mechanical properties of sintered ZrB2–SiC ceramics. *Journal of the European Ceramic Society* **31**, 893-901, doi:10.1016/j.jeurceramsoc.2010.11.013 (2011).

159   Neuman, E. W., Hilmas, G. E. & Fahrenholtz, W. G. Mechanical behavior of zirconium diboride–silicon carbide ceramics at elevated temperature in air. *Journal of the European Ceramic Society* **33**, 2889-2899, doi:10.1016/j.jeurceramsoc.2013.05.003 (2013).

160   Bird, M. W., Aune, R. P., Thomas, A. F., Becher, P. F. & White, K. W. Temperature-dependent mechanical and long crack behavior of zirconium diboride–silicon carbide composite. *Journal of the European Ceramic Society* **32**, 3453-3462, doi:10.1016/j.jeurceramsoc.2012.03.029 (2012).

161   Jin, X., He, R., Zhang, X. & Hu, P. Ablation behavior of ZrB2–SiC sharp leading edges. *Journal of Alloys and Compounds* **566**, 125-130, doi:10.1016/j.jallcom.2013.03.067 (2013).

162   Rezaie, A., Fahrenholtz, W. G. & Hilmas, G. E. Evolution of structure during the oxidation of zirconium diboride–silicon carbide in air up to 1500°C. *Journal of the European Ceramic Society* **27**, 2495-2501, doi:10.1016/j.jeurceramsoc.2006.10.012 (2007).

163   Seong, Y.-H., Lee, S. J., Kim, D. K. & Fahrenholtz, W. TEM Study of the High-Temperature Oxidation Behavior of Hot-Pressed ZrB2-SiC Composites. *Journal of the American Ceramic Society* **96**, 1570-1576, doi:10.1111/jace.12246 (2013).

164   Bird, M. W., Aune, R. P., Yu, F., Becher, P. F. & White, K. W. Creep behavior of a zirconium diboride–silicon carbide composite. *Journal of the European Ceramic Society* **33**, 2407-2420, doi:10.1016/j.jeurceramsoc.2013.03.022 (2013).

165   Gangireddy, S., Halloran, J. W. & Wing, Z. N. Flexural creep of zirconium diboride–silicon carbide up to 2200°C in minutes with non-contact

electromagnetic testing. *Journal of the European Ceramic Society* **33**, 2901-2908, doi:10.1016/j.jeurceramsoc.2013.05.031 (2013).

166   Kall, P.-O. Quantitative phase analysis of Si3N4-based materials. *Chem. Scripta* **28**, 8 (1988).

167   G.R., A., P., C., B.R., l. & D.B, m. A critical evaluation of indentation techniques for measuring fracture toughness. I. Direct crack measurements. *J. Am. Ceram. Soc.* **64** (1981).

168   Locci, A. M., Cincotti, A., Todde, S., Orrù, R. & Cao, G. A methodology to investigate the intrinsic effect of the pulsed electric current during the spark plasma sintering of electrically conductive powders. *Science and Technology of Advanced Materials* **11**, 045005, doi:10.1088/1468-6996/11/4/045005 (2010).

169   Kingery, W. D., Bowen, H. K. & Uhlmann, D. R. Introduction to Ceramics, second ed. *Wiley, Interscience* (1976).

170   Räthel, J., Herrmann, M. & Beckert, W. Temperature distribution for electrically conductive and non-conductive materials during Field Assisted Sintering (FAST). *Journal of the European Ceramic Society* **29**, 1419-1425, doi:10.1016/j.jeurceramsoc.2008.09.015 (2009).

171   Falk, L. K. L. Imaging and microanalysis of liquid phase sintered silicon-based ceramic microstructures. *Journal of Materials Science* **39**, 9 (2004).

172   Choi, H.-J., Cho, K.-S. & Lee, J.-G. R-Curve Behavior of Silicon Nitride–Titanium Nitride Composites. *J. Am. Ceram. Soc.* **80**, 2681-2684 (1997).

173   WEI, G. C. & BECHER, P. F. Improvements in mechanical properties in SiC by the addition of TiC particles. *J Am Ceram Soc* **67**, 4 (1984).

174   Chae, K. W., Niihara, K. & Kim, D.-Y. Improvements in the mechanical properties of TiC by the dispersion of fine SiC particles. *Journal of Materials Science Letters* **14**, 3 (1995).

175   K., U., J.-M., Y. & P., H. W. Materials for ultrahigh temperature structural applications. *Am. Ceram. Soc. Bull.* **76**, 6 (1997).

176   B., B., P., B. M., D., D. & J., L. High-temperature oxidation of silicon carbide in simulated atmospheric re-entry conditions. *J. Mater. Sci.* **27**, 5 (1992).

177   Hasegawa, I., Fukuda, Y. & Kajiwarab, M. An improved procedure for fabricating SiO2-TiO2-phenolic resin hybrid fibers as precursors for long Si-Ti-C fibers by sol-gel processing. *Journal of the European Ceramic Society* **17**, 7 (1997).

178   Zhong, J. *et al.* Synthesis of Mesoporous Carbon-Bonded TiC/SiC Composites by Direct Carbothermal Reduction of Sol-Gel Derived Monolithic Precursor. *Journal of the American Ceramic Society* **94**, 4025-4031, doi:10.1111/j.1551-2916.2011.04662.x (2011).

179   Turkdogan, E. T. Physical chemistry of high temperature technology. *New York : Academic Press* (1980).

180   Loos, J., Alexeev, A., Grossiord, N., Koning, C. E. & Regev, O. Visualization of single-wall carbon nanotube (SWNT) networks in conductive polystyrene nanocomposites by charge contrast imaging. *Ultramicroscopy* **104**, 8 (2005).

181   Beketov, A. R., Shabalin, I. L. & Fedorenko, O. V. Hot-pressed and fused carbide-carbon materials. *Tsvetn. Met.* **3**, 4 (1979).

182   Shabalin, I. L., Tomkinson, D. M. & Shabalin, L. I. High-temperature hot-pressing of titanium carbide-graphite hetero-modulus ceramics. *Journal of the European Ceramic Society* **27**, 11 (2007).

183   Stobierski, L. & Gubernat, A. Sintering of silicon carbide I. Effect of carbon. *Ceramics International* **29**, 6 (2003).

184   Mishra, S. K. & Pathak, L. C. Effect of carbon and titanium carbide on sintering behaviour of zirconium diboride. *Journal of Alloys and Compounds* **465**, 9 (2008).

185   Taylor, R. E. Thermal Conductivity of Titanium Carbide at High Temperatures. *Journal of the American Ceramic Society* **44**, 1 (1961).

186   Lezhenin, F. F. & Gnesin, G. G. Thermal conductivity of silicon carbide at high temperatures. *Soviet Powder Metallurgy and Metal Ceramics* **6**, 3 (1967).

187   IV, B. & GE., M. Monte Carlo simulation of the effective thermal conductivity in two-phase material. *J Mater Proc Technol* **153-154** (2004).

188   M, L. F., A, A., S, U., D, C. & C, R. Microstructure and thermal conductivity of Mo–TiC cermets processed by hot isostatic pressing. *J Nucl Mater* **380**, 8 (2008).

189   Safaraliev, G. K., Tairov, Y. M., Tsvetkov, V. F. & Shabanov, S. S. Solubility and Diffusion in the Systems SiC-NbC, SiC-TiC and SiC-ZrC. *Pis'ma Zh. Tekh. Fiz.* **17**, 4 (1991).

190   Calleja, G., Serrano, D. P., Sanz, R. & Pizarro, P. Mesostructured SiO2-Doped TiO2 with Enhanced Thermal Stability Prepared by a Soft-Templating Sol-Gel Route. *Micropor. Mesopor. Mater.* **111**, 12 (2008).

191   Beketov, A. R., Podkovyrkin, M. I. & Shabalin, I. L. A study into the strength of hot-pressed titanium carbide-silicon carbide-carbon materials. *Alloys of High-Melting and Rare Metals for Use at High Temperatures. Collection of Research Papers*, 4 (1984).

192   Nishizawa, T. Thermodynamics of Microstructures. *ASM International* (2008).

193   Mallik, M., Roy, S., Ray, K. K. & Mitra, R. Effect of SiC content, additives and process parameters on densification and structure–property relations of pressureless sintered ZrB2–SiC composites. *Ceramics International* **39**, 2915-2932, doi:10.1016/j.ceramint.2012.09.066 (2013).

194   LU, T. J. & FLECK, N. A. THE THERMAL SHOCK RESISTANCE OF SOLIDS. *Acta mater.* **46**, 14 (1998).

195   Tripp, W. C. & Graham, H. C. Thermogravimetric Study of Oxidation of ZrB2 in Temperature Range of 800 Degrees to 1500 Degrees. *Journal of the Electrochemical Society* **118**, 1195-1971 (1971).

196   Chamberlain, Fahrenholtz, W., Hilmas, G. & Ellerby, D. Oxidation of ZrB2-SiC Ceramics under Atmospheric and Reentry Conditions. *Refractories Applications Transactions* **1**, 2-8 (2005).

197   Opeka, M. M., Talmy, I. G. & Zaykoski, J. A. Oxidation-Based Materials Selection for 2000ºC + Hypersonic Aerosurface: Theoretical Considerations and Historical Experience. *J. of Mater. Sci.* **39**, 5887-5904 (2004).

198   Opeka, M. M., Talmy, I. G., Wuchina, E. J., Zaykoski, J. A. & Causey, S. J. Mechanical, Thermal, and Oxidation Properties of Refractory Hafnium and Zirconium Compounds. *J. Eur. Ceram. Soc.* **19**, 2405-2414 (1999).

199   Fahrenholtz, W. G. Thermodynamics of ZrB2-SiC oxidation: the formation of a SiC-depleted region. *J. Am. Ceram. Soc.* **90**, 143-148 (2007).

200   Zhou, M. *et al.* A novel approach for preparation of dense TiC–SiC nanocomposites by sol–gel infiltration and spark plasma sintering. *Journal of the European Ceramic Society* **34**, 1949-1954 (2014).

201 Ang, C., Seeber, A., Williams, T. & Yi-BingCheng. SPS densification and microstructure of ZrB2 composites derived from sol–gel ZrC coating. *Journal of the EuropeanCeramic Society* **34**, 2875-2883 (2014).

202 Hu, C. *et al.* Microstructure and properties of ZrB2-SiC composites prepared by spark plasma sintering using TaSi2 as sintering additive. *J. Eur. Ceram. Soc.* **30**, 7 (2010).

203 Guo, S.-Q., Kagawa, Y., Nishimura, T. & Tanaka, H. Pressureless sintering and physical properties of ZrB2-based composites with ZrSi2 additive. *Scr. Mater.* **58**, 4 (2008).

204 Sciti, D., Silvestroni, L. & Nygren, M. Spark plasma sintering of Zr- and Hf-borides with decreasing amounts of MoSi2 as sintering aid. *J. Eur. Ceram. Soc.* **28**, 10 (2008).

205 Fahrenholtz, W. G., Hilmas, G. E., Talmy, I. G. & Zaykoski, J. A. Refractory Diborides of Zirconium and Hafnium. *Journal of the American Ceramic Society* **90**, 1347-1364, doi:10.1111/j.1551-2916.2007.01583.x (2007).

206 Monteverde, F. & Bellosi, A. Effect of the addition of silicon nitride on sintering behaviour and microstructure of zirconium diboride. *Scr. Mater.* **46**, 223-228 (2002).

207 Ang, C., Seeber, A., Wang, K. & Cheng, Y.-B. Modification of ZrB2 powders by a sol–gel ZrC precursor—A new approach for ultra high temperature ceramic composites. *Journal of Asian Ceramic Societies* **1**, 77-85, doi:10.1016/j.jascer.2013.03.004 (2013).

208 Ordan'yan, S. S., Dmitriev, A. I. & Moroshkina, E. S. Synthesis and properties of ceramics in the SiC. *Izv. Akad. Nauk SSSR, Neorg. Mater.* **25**, 1487-1489 (1989).

209 Gangireddy, S., Karlsdottir, S. N., Norton, S. J., Tucker, J. C. & Halloran, J. W. In situ microscopy observation of liquid flow, zirconia growth, and CO bubble formation during high temperature oxidation of zirconium diboride–silicon carbide. *Journal of the European Ceramic Society* **30**, 2365-2374, doi:10.1016/j.jeurceramsoc.2010.01.034 (2010).

210 Gao, D., Zhang, Y., Xu, C., Song, Y. & Shi, X. Oxidation kinetics of hot-pressed ZrB2–SiC ceramic matrix composites. *Ceramics International* **39**, 3113-3119, doi:10.1016/j.ceramint.2012.09.091 (2013).

211   Monteverde, F. & Scatteia, L. Resistance to Thermal Shock and to Oxidation of Metal Diborides?SiC Ceramics for Aerospace Application. *Journal of the American Ceramic Society* **90**, 1130-1138, doi:10.1111/j.1551-2916.2007.01589.x (2007).

212   http://en.wikipedia.org/wiki/Boron_trioxide. (2014).

213   http://en.wikipedia.org/wiki/Silicon_monoxide. (2014).

214   http://en.wikipedia.org/wiki/Silicon_dioxide. (2014).

215   Hu, P., Zhang, X. H. & Meng, S. H. Oxidation behavior of zirconium diboride-silicon carbide at 1800°C. *Scripta Materialia* **57**, 825-828 (2007).

216   Zhang, X., Hu, P., Han, J. & Meng, S. Ablation behavior of ZrB2-SiC ultra high temperature ceramics under simulated atmospheric re-entry conditions. *Composites Science and Technology* **68**, 1718-1726 (2008).

217   Levine, S. R. *et al.* Evaluation of Ultra-High Temperature Ceramics for Aeropropulsion Use. *J. Eur. Ceram. Soc.* **22**, 2757-2767 (2002).

218   Opila, E. J., Levine, S. R. & Lorincz, J. Oxidation of ZrB2-and HfB2 based Ultra-High Temperature Ceramics: Effect of Ta Additions. *J. of Materials Science* **39**, 5969-5977 (2004).

219   Fahrenholtz, W. G. The ZrB2 Volatility Diagram. *J. Am. Ceram. Soc.* **88**, 3509-3512 (2005).